Detonation Stability with Reversible Kinetics

Thesis by

Shannon Kao

In Partial Fulfillment of the Requirements

for the Degree of

Doctor of Philosophy

California Institute of Technology

Pasadena, California

2008

(Defended June 2, 2008)

Acknowledgments

It seems like only a little while ago I arrived in southern California to start graduate studies at Caltech. My six years here have been very rewarding because with great challenge comes great satisfaction. Many of the people here at Caltech and away from campus have contributed to my successes.

As most students do, I must start with my adviser Joe Shepherd. An adviser, or more appropriately a mentor, colors a student's experience, and my adviser gave me a very well-rounded one. During my tenure, there were shared triumphs and frustrations. He was always available as a sounding board and showed a true interest in being involved with every step of my project. He was stern when appropriate, but also good at giving support and praise when warranted. He instilled a team attitude among our group, and for that reason, I learned about projects other than mine. This has definitely prepared me to attack new topics with gusto.

I also must thank the members of my committees. Dr Pullin and Dr Meiron provided necessary expertise concerning several of the details of my project. Dr Hunt and Dr Colonius graciously agreed, at the last minute, to serve on my candidacy committee. Dr Colonius additionally served on my defense committee. Their outside perspective was essential to assuring that my thesis work is complete and well presented.

Although he was not able to serve on my defense committee, Dave Goodwin has been invaluable. His thermodynamic library, Cantera, made our implementation possible and he provided valuable technical support.

Besides these Caltech professors, several additional professors have provided necessary expertise. Mark Short and Scott Stewart provided insight from years of working with this

specific problem. Anatoli Tumin, more recently, has been looking at the problem from a different perspective. Discussions with him have illuminated new interesting aspects of the problem to investigate.

Although professors offer years of experience and a big picture view, often peers have been the most helpful with day to day details. Caltech offers a very special environment where students of different disciplines are encouraged to work together, and I have never hesitated to bounce an idea off any of my colleagues. I would like to thank all the members of my group who have been so helpful. Specifically, Dan Lieberman, Florian Pintgen, Jim Karnesky, Sally Moffett, and Philipp Boettcher have been fantastic collaborators and given me a view into the experimental world. Rita Liang, one of our post-docs, was invaluable in the beginnings of my project because she had also worked on this topic.

Possibly the most helpful student was Kazuaki Inaba, another post-doc. We used his software to confirm the predictions from our method. He spent many hours helping me to modify his software to work with our model, and then he graciously ran many of the simulations. Without his input, the confirmation would not have gone as smoothly.

Besides group members, Vaughan Thomas patiently helped me learn to program and work through the mysteries of Cantera; Theresa Kidd, Sharlotte Kramer, and Richard Kramer were wonderful sounding boards; and Mike Rubel provided Linux expertise. In addition to being supportive scientifically, each of these students also made studying at Caltech a memorable experience.

Caltech can be a very one-dimensional place. Thankfully I have had many outlets here in Pasadena to offset the extreme environment. I want to thank Desiree LaVertu, the Glee Club director and my voice teacher. She has been a source of fun and an additional mentor. She hasn't taught me about science but has kept my view of life more normal. I also want to thank the members of my church choir. Each week, they remind me that there are millions of people in the world who do not do what we do here at Caltech. It is an important reality check and de-stresser.

Finally, I acknowledge my family. My parents encouraged my successes at every stage. Although their areas of expertise are vastly different than mine, they have expressed

interest in my thesis work because it is important to me. Without their constant love and support, I would not have accomplished so much. I also want to thank my husband, Pete. He regularly reminds me how proud he is of me – a daily reminder that I am blest.

This work was supported by a National Science Foundation fellowship and then by the Department of Energy ASC Center grant.

Abstract

Detonation propagation is unsteady due to the innate instability of the reaction zone structure. Up until the present, investigations of detonation stability have been exclusively concerned with model systems using the perfect gas equation of state and primarily single-step irreversible reaction mechanisms.

This study investigates detonation stability characteristics with reversible chemical kinetics models. To allow for more general kinetics models, we generalize the perfect gas, one-step irreversible kinetics, linear stability equations to a set of equations using the ideal gas equation of state and a general reaction scheme. We linearly perturb the reactive Euler equations following the method of Lee and Stewart (1990) and Short and Stewart (1998). Our implementation uses Cantera (Goodwin, 2005) to evaluate all thermodynamic quantities and evaluate generalized analytic derivatives of quantities dependent on the kinetics model.

The computational domain is the reaction zone in the shock-fixed frame such that the left boundary conditions are the perturbed shock jump conditions which we have derived for a general equation of state and implemented for an ideal gas equation of state. At the right boundary, the system must satisfy a radiation condition requiring that all waves travel out of the domain. Unlike the case of a single reversible reaction, in a truly multistep kinetics model, the radiation boundary condition cannot be solved analytically. In this work, we provide a general methodology for satisfying the appropriate boundary condition.

We then investigate the effects of reversibility on the characteristics of the instability in one and two dimensions. These characteristics are quantified by the unstable eigen-

values as well as the shape of the base flow and eigenfunctions. We show that there is an exchange of stability as a function of reversibility. To confirm the results our work, we have performed unsteady calculations. We show that we can match the frequencies predicted by our linear stability calculations near the stability threshold.

Contents

List of Figures

List of Tables

Nomenclature

Calligraphic characters

$\mathcal{A}$	generic reactant species, Eq. (1.4.6)	
$\mathcal{B}$	generic product species, Eq. (1.4.6)	
$\mathcal{C}$	Eq. (F11)	
$\mathcal{D}$	Eq. (F12)	
$\mathcal{E}$	Eq. (F13)	
$\mathcal{F}$	Eq. (F14)	
$\mathcal{R}$	universal gas constant, Eq. (1.1.11)	J/K/mol
$\mathcal{G}$	Eq. (F15)	
$\mathcal{H}(\omega)$	eigenvalue selection criterion, Eq. (3.4.20)	
$\mathcal{P}$	discrete Fourier transform of $P(t)$, Eq. (6.2.2)	Pa

Greek symbols

α_T	coefficient of thermal expansion, Eq. (B1.5)	1/K
α	simplifying function, Eq. (4.2.12)	1/s
$\Delta\dot{\Omega}$	$\dot{\Omega}_{\mathcal{B},Y_\mathcal{B}} - \dot{\Omega}_{\mathcal{B},Y_\mathcal{A}}$, Eq. (F2)	1/s
$\Delta\nu$	reaction order, Eq. (D1.2)	

$\Delta_f h^\circ$	specific heat of formation at standard state, Eq. (2.1.5)	J/kg
Δe	$e_{\mathcal{B}} - e_{\mathcal{A}}$, Eq. (4.2.13)	J/kg
Δh, $\Delta_R h$	heat of reaction, Eq. (D1.15)	J/kg
$\Delta s/R$	reversibility parameter (Δa_6), Eq. (2.2.16)	
ΔZ	$Z_{,Y_{\mathcal{B}}} - Z_{,Y_{\mathcal{A}}}$, Eq. (F3)	Pa/s
$\Delta_{e,ZND}$	exothermic pulse width, Fig. 1.7	m
$\Delta_{i,ZND}$	induction length, Eq. (1.3.1)	m
$\dot{\Omega}$	net rate of production, Eq. (1.1.6)	1/s
$\dot{\omega}_i$	net molar rate of production, Eq. (D1.9)	mole/m^3/s
$\dot{\sigma}$	thermicity, Eq. (1.2.11)	1/s
ϵ	Angle, Eq. (B6.1)	
ϵ_i	efficiency, Eq. (D1.4)	
η	sonic parameter, Eq. (1.2.12)	
γ	isentropic ratio, Eq. (1.1.13)	
λ	wave length, Eq. (5.7)	m
$\lambda_{k\mathbf{N}}$	eigenvalue of $\mathbf{N}$, Eq. (3.4.8)	1/m
λ	cell width, Figure 1.8b	m
μ	chemical potential, Eq. (D1.12)	J/kg
ν_i	stoichiometric coefficient, Eq. (D1.1)	
ω	complex growth rate, Eq. (3.2.6)	1/s

ϕ	equivalence ratio, pg 26	
ψ	shock speed perturbation, Eq. (3.2.6), Eq. (3.1.1)	m
ψ^1	constant coefficient, Eq. (3.2.6)	m
ρ	density, Eq. (1.2.4)	kg/m^3
θ	argument of α, Eq. (F10)	
θ	reduced effective activation energy, pg 20	
$\tilde{\beta}$	nondimensional heat release, pg 35	
$\tilde{\kappa}$	nondimensional normal wave number, Eq. (4.2.18)	
$\tilde{\kappa}_*$	function of nondimensional normal wave number $\tilde{\kappa}$, Eq. (4.2.19)	
ζ	specific acoustic impedance, Eq. (5.19)	

Roman characters

$[M]$	concentration of chaperon molecule, Eq. (D1.4)	moles/m^3
$\overline{W}$	mean molecular weight, Eq. (1.1.11)	g/mol
A	pre-exponential, Eq. (1.4.5)	varies
A'	modified A, Eq. (2.2.16)	varies
a_e	equilibrium soundspeed, Eq. (C1.7)	m/s
a_f	frozen soundspeed, Eq. (C1.6)	m/s
a_k, b_k	polynomial coefficients, Eq. (3.4.3), Eq. (1.4.1)	
c_P	specific heat capacity at constant pressure, Eq. (B1.6)	J/K/kg
c_v	specific heat capacity at constant volume, Eq. (1.1.13)	J/K/kg

c_ϕ	phase speed, Eq. (4.3.25)	m/s
$c_{k\mathbf{N}}$	characteristic speeds of matrix $\mathbf{N}$, Eq. (4.1.3)	m/s
e	specific energy, Eq. (1.1.7), Eq. (1.1.12)	J/kg
E_a	effective activation energy, Eq. (1.3.1)	J/kg
E'_a	modified E_a, Eq. (2.2.16)	J/kg
f	generic function, Eq. (B2.1)	
f	overdrive, Eq. (1.2.23)	
F_k	generic wave function, Eq. (4.2.15)	
G	Gruüneisen coefficient, Eq. (B1.4)	
g_i	specific Gibbs free energy, Eq. (D1.13)	J/kg
g_k	transformed function, Eq. (3.4.9), Eq. (3.4.8)	
h	specific enthalpy, Eq. (1.2.11)	1/s
i	$\sqrt{-1}$, Eq. (3.2.6)	
K_C	concentration based equilibrium constant, Eq. (2.2.11)	
k_f	forward reaction rate coefficient, Eq. (1.4.5)	varies
K_P	pressure based equilibrium constant, Eq. (2.2.13)	
k_r	reverse reaction rate coefficient, Eq. (2.2.10)	varies
k_y	transverse wave number, Eq. (3.2.6)	1/m
M	Mach number, Eq. (1.2.10)	
n	temperature power, Eq. (1.4.5)	

N_Y	number of species, Eq. (1.1.4)	
P	pressure, Eq. (1.1.3)	Pa
$P_{\text{synthetic}}$	synthetic pressure history, Eq. (6.2.1)	
$P_{\text{mode } k}$	constant coefficient, Eq. (6.2.1)	
R	species specific gas constant, Eq. (1.1.11)	kJ/K/kg
r	magnitude of α, Eq. (F9)	
r	reaction rate, Eq. (E1.2)	1/s
S	characteristic surface, Eq. (H3)	
$s_\circ$	standard state specific entropy, Eq. (2.1.12)	J/kg/K
T	temperature, Eq. (1.1.9)	K
t	time, Eq. (1.1.1)	s
T°	standard state temperature, Eq. (2.1.12)	K
v	specific volume, Eq. (1.1.1)	m^3/kg
W	molecular weight, Eq. (1.1.6)	g/mol
X	mole fraction, Eq. (D1.4)	
x	Cartesian coordinate, Eq. (1.2.2)	
x_R	point where radiation condition is evaluated, pg 51	
Y	mass fraction, Eq. (1.1.4)	
y	Cartesian coordinate, Eq. (1.2.1)	
$Y_{\mathcal{B}}^{*'}$	equilibrium value of $Y'_{\mathcal{B}}$, Eq. (4.3.22)	

Z	pseudo-thermodynamic function, Eq. (3.2.13)	Pa/s
U	shock speed, Eq. (1.2.23)	m/s
u	velocity component in x direction, Eq. (3.1.3)	m/s
v	velocity component in y direction, Eq. (3.1.4)	m/s
w	velocity component in x direction in the shock-fixed frame, Eq. (1.2.2)	m/s
D	unsteady shock velocity, Eq. (3.1.1)	m/s

Sub-scripts $ Super-scripts

$(\ )'$	perturbation quantity, Eqs. (3.2.1)–(3.2.5)
$(\ )^*$	complex conjugate, Eq. (6.2.2)
$(\ )^1$	eigenfunction, Eq. (3.2.8)
$(\ )^L$	laboratory frame, pg 43
$(\ )^o$	base flow quantity, Eqs. (3.2.1), (3.2.3)–(3.2.5)
$(\ )_1$	pre-shock state, Eq. (1.2.17)
$(\ )_2$	post-shock state, Eq. (1.2.17)
$(\ )_c$	characteristic scale
$(\ )_f$	fluid dynamic components only, Eq. (E6.1)
$(\ )_I$	inhomogeneous solution, Eq. (E6.11)
$(\ )_i$	species index, Eq. (1.1.4)
$(\ )_j$	free index
$(\ )_k$	free index

$(\ )_n$ normal component, Eq. (B6.4)

$(\ )_p$ reaction index

$(\ )_{,m}$ derivative wrt m, Eq. (1.2.2)

$(\ )_{1/2}$ value when $Y_{\mathcal{B}=0.5}$

$(\ )_{\mathcal{I}}$ imaginary component

$(\ )_{\mathcal{R}}$ real component

$(\ )_{CJ}$ Chapman-Jouguet quantity, Eq. (1.2.23)

$(\ )_{n\times n}$ top left $n \times n$ of matrix

$(\ )_{shock}$ of the shock, Eq. (3.1.1)

$(\ )_{x_R}$ base flow quantity far from the reaction zone, pg 51

$\hat{(\ )}$ constant coefficient, Eq. (3.4.15)

$\mathcal{I}m(\ )$ real component

$\mathcal{R}e(\ )$ real component

$\tilde{(\ )}$ nondimensional quantity

Vectors and Matrices

$\mathbf{u}$	velocity vector, Eq. (1.1.2)	m/s
$\mathbf{\Lambda_N}$	matrix of eigenvalues of $\mathbf{N}$, Eq. (3.4.7)	
$\mathbf{A}$	x convective derivative, Eq. (3.2.11)	
$\mathbf{B}$	y convective derivative, Eq. (3.2.11)	
$\mathbf{b}$	vector of derivatives, pg 47	

$\mathbf{C}$ source matrix, Eq. (3.2.12)

$\mathbf{F}$ vector of fluxes, Eq. (6.1.2)

$\mathbf{I}$ identity matrix, Eq. (3.2.10)

$\mathbf{J}$ Jacobian matrix, Eq. (4.4.1), Eq. (3.5.3)

$\mathbf{L}$ matrix of left eigenvectors, Eq. (3.4.7)

$\mathbf{m}_k$ left eigenvector, Eq. (3.4.11)

$\mathbf{N}$ matrix summation, Eq. (3.4.6)

$\mathbf{n}_k$ right eigenvector, Eq. (3.4.3)

$\mathbf{S}$ vector of source terms, Eq. (6.1.2)

$\mathbf{Y}$ vector of mass fractions, Eq. (1.1.7)

$\mathbf{z}$ solution vector, Eq. (3.2.7)

$\mathbf{z}_c$ vector of conserved variables, Eq. (6.1.2)

Chapter 1

Introduction

A detonation is a supersonic combustion wave in which a shock wave and a reaction zone are coupled. The leading shock raises the temperature and pressure of a mixture of fuel and oxidizer initiating a coupled thermal branching-chain explosion. After an induction time, exothermic recombination reactions create product species whose expansion acts as a piston propelling the shock wave forward. The interaction between the leading shock and consequent reaction zone is a defining characteristic of self-sustained detonations.

Experiments and numerical simulations of detonation propagation problems are also characterized by unsteady motion due to the intrinsic instability of the reaction zone structure. This instability may arise due to the sensitivity of the reaction rates to temperature fluctuations. Arrhenius (1889) proposed that the reaction rate k depends on temperature in the following way

$$k \propto \exp\left(-\frac{E_a}{RT}\right). \tag{1.1}$$

From this, we see that small fluctuations in the leading shock speed which are manifested as small changes in temperature lead to large changes in the reaction rate. While this is the most commonly discussed cause for the instability, several other mechanisms have been proposed. Despite the fact that we only observe the nonlinear stages of this instability in experimental studies, we can numerically examine the linear stages.

To date, investigations of the detonation linear stability problem have almost exclu-

sively been concerned with model systems using the perfect gas equation of state and reaction mechanisms consisting of a small number (usually one) of irreversible reactions. Starting from the one-step model used in the pioneering studies of Erpenbeck (1962) and the reformulated numerical approach in Lee and Stewart (1990), Short (1997), and Short and Stewart (1998), researchers have been making steady progress by considering more complex chemical reaction models and equations of state (Short and Quirk, 1997, Liang and Bauwens, 2005, Liang et al., 2007). While these multi-step models are an improvement on the one-step model, realistic chemical kinetics involves multiple reversible reactions.

The scope of this study is the linear stage of the instability of an initially steady, one-dimensional base flow based on the ZND model of detonation structure. We focus our attention on the role reversibility plays in this instability. To this end, we develop numerical tools that enable the computation of stability characteristics for multi-step reaction mechanisms with reversible reactions, realistic rate constant representation, and mixture thermodynamics with variable specific heat. We investigate reversibility by using an artificial chemical mechanism consisting of a single reaction between two perfect gases. Although this model is contrived, it gives insight into the effect reversibility has on the nature of the instability. An additional complication is that, unlike the irreversible models studied previously, there is not an analytic expression for the required downstream boundary condition. To address this, we have devised a general numerical formulation. The governing equations for detonations and a simplified detonation model are presented in Sections 1.1 and 1.2. Then a detailed discussion of detonation instability is presented in Section 1.3. Finally we give a review of the simplified chemistry research and its relationship to the stability problem in Section 1.4.

1.1 Governing Equations

The equations of inviscid motion of a real fluid are the so-called reactive Euler equations, which are simply the conservation of mass, momentum, energy, and species. In a fixed (inertial) reference frame, these are:

$$\frac{\mathrm{D}v}{\mathrm{D}t} = v\boldsymbol{\nabla}\cdot\mathbf{u} \tag{1.1.1}$$

$$\frac{\mathrm{D}\mathbf{u}}{\mathrm{D}t} = -v\boldsymbol{\nabla}P \tag{1.1.2}$$

$$\frac{\mathrm{D}e}{\mathrm{D}t} = -P\frac{\mathrm{D}v}{\mathrm{D}t} \tag{1.1.3}$$

$$\frac{\mathrm{D}Y_i}{\mathrm{D}t} = \dot{\Omega}_i \qquad i = 1,\ldots,N_Y \tag{1.1.4}$$

$$\frac{\mathrm{D}}{\mathrm{D}t} = \frac{\partial}{\partial t} + \mathbf{u}\cdot\boldsymbol{\nabla}. \tag{1.1.5}$$

The symbols are: v specific volume, $\mathbf{u}$ fluid velocity, P pressure, e specific internal energy, Y_i mass fraction of species i, and $\dot{\Omega}_i$ net production rate of species i. In more traditional chemical notation (Kee et al., 1987) the net production rate can be expressed

$$\dot{\Omega}_i = vW_i\dot{\omega}_i \tag{1.1.6}$$

where $\dot{\omega}_i$ is the net molar production rate of species i per unit volume and W_i is the molar mass of species i.

Real gas equations of state take many forms. One popular formulation used in Euler flow simulations is

$$e = e(P, v, \mathbf{Y}). \tag{1.1.7}$$

In nonreactive flow problems, this is adequate to close the problem in terms of the primitive variable set $(v, \mathbf{u}, P)$. However, this is not a complete equation of state and additional thermodynamic information may be required. One potential difficulty is that the net production rate expressions are commonly given in terms of the temperature T

$$\dot{\Omega}_i(T, v, \mathbf{Y}). \tag{1.1.8}$$

This requires the construction of a temperature function

$$T = T(P, v, \mathbf{Y}) \tag{1.1.9}$$

that is thermodynamically consistent with the $e(P, v, \mathbf{Y})$ function. This problem is discussed at some length by McCahan (1992) and solved for some specific cases. A methodology for systematically extending the ideal gas properties to real gases has been developed by the chemical engineering community (Smith et al., 1996) and has also found application to problems of this type, i.e., the CHEMKIN-RG package (Butler, 1989).

Using appropriate thermodynamic identities, we can re-express the energy equation (see Appendix B.1) as

$$\frac{\mathrm{D}P}{\mathrm{D}t} + \frac{a_f^2}{v}\boldsymbol{\nabla}\cdot\mathbf{u} = -\frac{G}{v}\sum_{i=1}^{N_Y}\left.\frac{\partial e}{\partial Y_i}\right|_{P,v,Y_{j\neq i}}\dot{\Omega}_i \tag{1.1.10}$$

where a_f is the frozen soundspeed discussed in Appendix C.1.

A simple but important case is the ideal gas equation of state:

$$Pv = RT \qquad R = \frac{\mathcal{R}}{\overline{W}} \qquad \overline{W} = \left(\sum_{i=1}^{N_Y}\frac{Y_i}{W_i}\right)^{-1} \tag{1.1.11}$$

$$e = \sum_{i=1}^{N_Y} Y_i e_i(T). \tag{1.1.12}$$

This model is appropriate for a wide range of low-pressure combustion problems such as

gaseous detonations. The individual species specific energy functions e_k are determined from thermochemical data (see the JANNAF compilation, Gurvich et al. 1989), statistical mechanics, and spectroscopic studies of molecular structure.

For an ideal gas, $G = \gamma - 1$, $\alpha_T = 1/T$, and $c_P = \gamma R/(\gamma - 1)$ where

$$\gamma(T) = \frac{c_P}{c_v} \tag{1.1.13}$$

is the temperature-dependent ratio of specific heat capacities. The reactive Euler equations in the laboratory frame for an ideal gas are summarized in Appendix A.1.1.

1.2 ZND Detonation Model

The equations that result as a consequence of transforming to the shock-fixed frame and assuming that the flow is one-dimensional and time-independent, i.e., steady

$$\frac{\partial}{\partial t} = 0 \quad \frac{\partial}{\partial y} = 0, \tag{1.2.1}$$

are the set of ordinary differential equations that describe the idealized, steady, reaction zone structure first studied by Zel'dovich (1940), von Neumann (1942), and Doering (1943) and now commonly referred to as the ZND model given below.

$$\mathrm{w}v_{,x} = v\mathrm{w}_{,x} \tag{1.2.2}$$

$$\mathrm{w}\mathrm{w}_{,x} = -vP_{,x} \tag{1.2.3}$$

$$\mathrm{w}P_{,x} + \rho a_f^2 \mathrm{w}_{,x} = -\frac{G}{v}\sum_{i=1}^{N_Y} e_{,Y_i}\dot{\Omega}_i \tag{1.2.4}$$

$$\mathrm{w}Y_{i,x} = \dot{\Omega}_i \tag{1.2.5}$$

These equations can also be expressed as

$$\mathrm{w}_{,x} = -\frac{1}{1-M^2}\frac{G}{a_f^2}\sum_{i=1}^{N_Y} e_{,Y_i}\dot{\Omega}_i \tag{1.2.6}$$

$$P_{,x} = \rho \mathrm{w}\frac{1}{1-M^2}\frac{G}{a_f^2}\sum_{i=1}^{N_Y} e_{,Y_i}\dot{\Omega}_i \tag{1.2.7}$$

$$\rho_{,x} = \frac{\rho}{\mathrm{w}}\frac{1}{1-M^2}\frac{G}{a_f^2}\sum_{i=1}^{N_Y} e_{,Y_i}\dot{\Omega}_i \tag{1.2.8}$$

$$\mathrm{w}Y_{i,x} = \dot{\Omega}_i \tag{1.2.9}$$

where, the Mach number is

$$M = \frac{\mathrm{w}}{a_f} \tag{1.2.10}$$

Transforming to the shock-fixed reference frame is similar to the coordinate transformation described in Section 3.1 and Appendix B.2. Note that for exothermic reactions, the term $\sum_k e_{,Y_k}\dot{\Omega}_k$ is negative. The solution for CJ detonation (see Section 1.2.1) in an initially stoichiometric mixture of hydrogen and air at 300 K and 1 atm is depicted in Figure 1.1. This simulation was performed with the Shock and Detonation toolbox (Browne et al., 2007b) with `h2air_highT.cti`, a hydrogen-air mechanism derived from the GRI 3.0 detailed chemical mechanism (Smith et al., 1999), which contains 12 species and 24 reactions. Detailed mechanisms are discussed further in Section 1.4 and Appendix D.4.

We can also express these equations in terms of thermicity,

$$\dot{\sigma} = \sum_k \left(\frac{\overline{W}}{W_k} - \frac{h_k}{c_P T}\right)\dot{\Omega}_k, \tag{1.2.11}$$

which is the sum of two terms: the difference in the number of moles of products and reactants and the energy absorbed or released from chemical bonds. In terms of thermicity

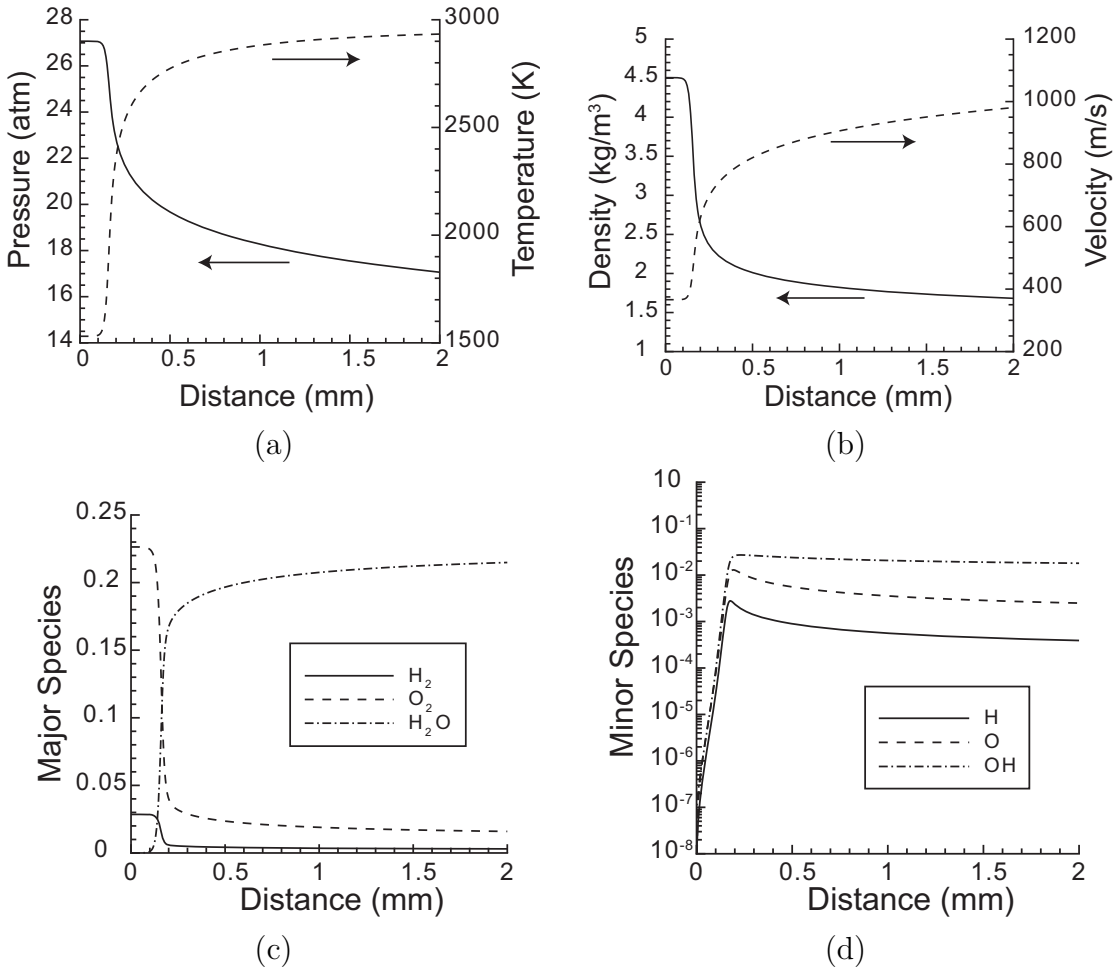

Figure 1.1: ZND structure for stoichiometric hydrogen-air initially at 300 K and 1 atm. (a) temperature and pressure profiles, (b) density and velocity profiles, (c) major species profiles, (d) minor species profiles

and the sonic parameter,

$$\eta = 1 - M^2, \tag{1.2.12}$$

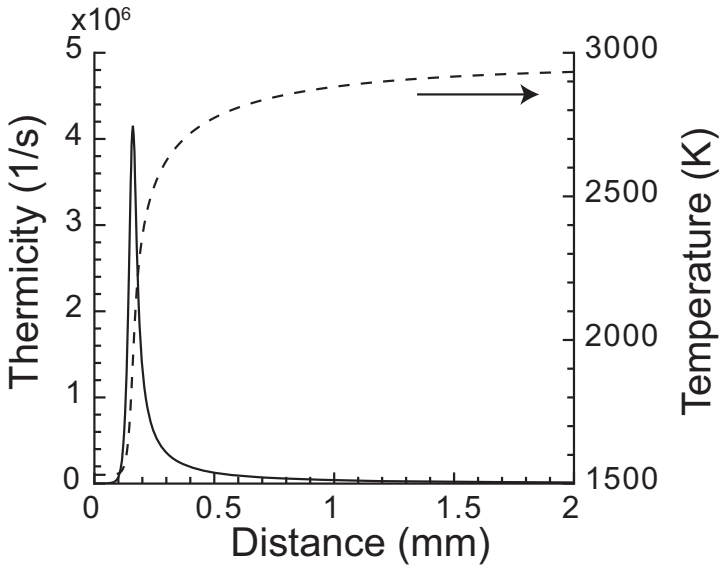

Figure 1.2: Thermicity ($\dot{\sigma}$) and temperature ZND structure for stoichiometric hydrogen-air initially at 300 K and 1 atm.

(1.2.6)–(1.2.9) are

$$\mathrm{w}_{,x} = \frac{\dot{\sigma}}{\eta} \tag{1.2.13}$$

$$P_{,x} = -\rho \mathrm{w} \frac{\dot{\sigma}}{\eta} \tag{1.2.14}$$

$$\rho_{,x} = -\frac{\rho}{\mathrm{w}} \frac{\dot{\sigma}}{\eta} \tag{1.2.15}$$

$$\mathrm{w} Y_{i,x} = \dot{\Omega}_i. \tag{1.2.16}$$

A more detailed derivation is presented in Appendix B.3. A solution technique for the ZND equations (1.2.13)–(1.2.16) is discussed in detail in Browne et al. (2005).

The thermicity profile for a CJ detonation in stoichiometric hydrogen-air is superposed on the temperature profile and shown in Figure 1.2.

1.2.1 Chapman-Jouguet Detonation Velocity

The initial conditions for a ZND calculation are determined from the frozen shock jump conditions in an instantaneous shock-fixed frame which fixes the shock location at $x = 0$, but focuses on one moment in time.

$$\rho_1 \mathrm{w}_1 = \rho_2 \mathrm{w}_2 \tag{1.2.17}$$

$$P_1 + \rho_1 \mathrm{w}_1^2 = P_2 + \rho_2 \mathrm{w}_2^2 \tag{1.2.18}$$

$$h_1 + \frac{\mathrm{w}_1^2}{2} = h_2 + \frac{\mathrm{w}_2^2}{2} \tag{1.2.19}$$

This situation is illustrated in Figure 1.3. In this case, we use w to represent the normal

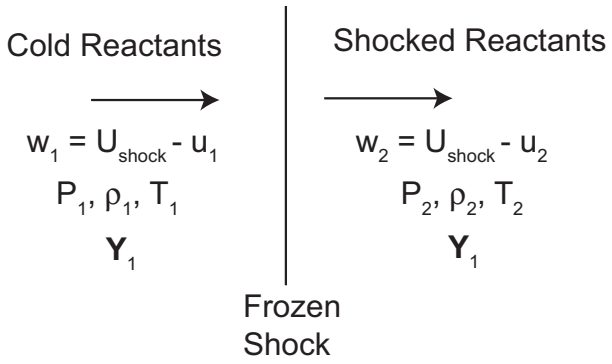

Figure 1.3: Cartoon depicting the instantaneous shock-fixed frame.

velocity component relative to the shock in this frame.

The jump conditions are often transformed so that they can be represented in the P-v thermodynamic coordinates. The Rayleigh line is a consequence of combining the mass (1.2.17) and momentum (1.2.18) conservation relations

$$P_2 = P_1 - \rho_1^2 \mathrm{w}_1^2 \left(v_2 - v_1\right). \tag{1.2.20}$$

The Rayleigh line must pass through both the initial state 1 and final state 2. If we eliminate the post-shock velocity, energy conservation (1.2.19) can be rewritten as a purely thermodynamic relation known as the Hugoniot or shock adiabat.

$$h_2 - h_1 = (P_2 - P_1)\frac{(v_2 + v_1)}{2} \tag{1.2.21}$$

or

$$e_2 - e_1 = \frac{(P_2 + P_1)}{2}(v_1 - v_2). \tag{1.2.22}$$

We can solve either (1.2.21) or (1.2.22) to obtain the locus of all possible downstream states $P_2(v_2)$ for a fixed upstream state. The result $P(v)$ is referred to as the Hugoniot curve or simply Hugoniot. For a frozen composition or an equilibrium composition in a non-exothermic mixture like air, Figure 1.4a, the Hugoniot curve passes through the initial state. For an equilibrium composition in an exothermic mixture like hydrogen-air, Figure 1.4b, the chemical energy release displaces the Hugoniot curve from the initial state. The Rayleigh line slope is always negative and dictates that the portion of the Hugoniot curve between the dashed vertical and horizontal lines (Figure 1.4b) is nonphysical. The nonphysical region divides the Hugoniot into two branches: the upper branch represents supersonic combustion waves or detonations, and the lower branch represents subsonic combustion waves or deflagrations.

The advantage of using the Rayleigh line and Hugoniot formulation is that solutions of the jump conditions for a given shock speed can be graphically interpreted in P-v diagram as the intersection of the Hugoniot and a particular Rayleigh line.

The detonation branch of the Hugoniot for a stoichiometric hydrogen-air mixture and three example Rayleigh lines are shown in Figure 1.5. The possible solutions to the jump conditions are shown graphically as the intersection points of the Rayleigh lines and Hugoniot. In general, there are two solutions (S, W) possible on the detonation branch for a given wave speed, $\infty > \mathrm{U} > \mathrm{U}_{CJ}$. Only one of the two solutions (S) is

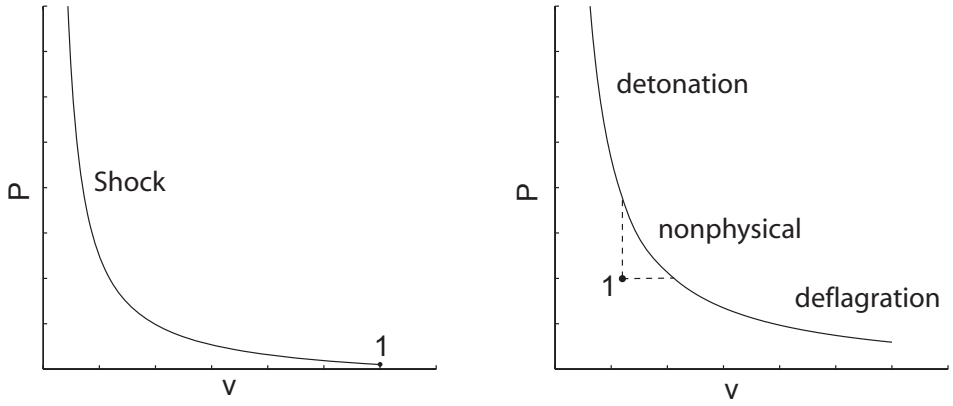

Figure 1.4: Hugoniots (a) Shock wave propagating in a non-exothermic mixture or a mixture with frozen composition. (b) Shock wave propagating in an exothermic mixture.

considered to be physically acceptable. According to Jouguet's rule (Fickett and Davis, 1979), this solution has two distinct features. First the flow behind the wave is subsonic, i.e., $w_2 < a_2$ where a_2 is the sound speed behind the wave (see Appendix C.1). The flow also satisfies the condition of causality, which is that disturbances behind the wave can catch up to the wave and influence its propagation.

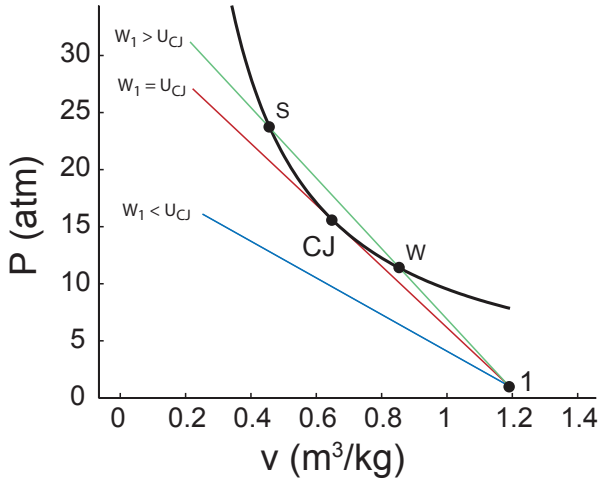

Figure 1.5: Hugoniot and three representative Rayleigh lines illustrating $w_1 = U_{CJ}$ as the minimum wave speed and tangency of Rayleigh line and Hugoniot at the CJ point.

As first recognized by Chapman (1899), the geometry (Figure 1.5) of the Hugoniot and Rayleigh line impose restrictions on the possible values of the detonation velocity. Below a minimum wave speed, $w_1 < U_{CJ}$, the Rayleigh line and equilibrium Hugoniot do not intersect and there are no steady solutions. For a wave traveling at the minimum wave speed $w_1 = U_{CJ}$, there is a single intersection with the equilibrium Hugoniot. Above this minimum wave speed $w_1 > U_{CJ}$, the Rayleigh line and equilibrium Hugoniot intersect at two points, usually known as the strong (S) and weak (W) solutions. Based on these observations, Chapman proposed that the measured speed of detonation waves corresponds to that of the minimum wave speed solution, which is unique. This leads to the following definition:

Definition I: *The Chapman-Jouguet detonation velocity is the minimum wave speed for which there exists a solution to the jump conditions from reactants to equilibrium products traveling at supersonic velocity.*

From the geometry (Figure 1.5), it is clear that the minimum wave speed condition occurs when the Rayleigh line is tangent to the Hugoniot. The point of tangency is the solution for the equilibrium downstream state and is referred to as the CJ state, as indicated on Figure 1.5. Jouguet (1905) showed that at the CJ point, the entropy is an extreme value and that as a consequence, the isentrope passing through the CJ point is tangent to the Hugoniot and therefore also tangent to the Rayleigh line, as indicated in Figure 1.6 (see Browne et al., 2007a). We conclude that at the CJ point, the flow in the products is moving at the speed of sound (termed *sonic* flow) relative to the wave. This leads to the alternative formulation (due to Jouguet) of the definition of the CJ condition.

Definition II: *The Chapman-Jouguet detonation velocity occurs when the flow in the products is sonic relative to the wave. This is equivalent to the tangency of the Rayleigh line, Hugoniot, and equilibrium isentrope at the CJ point.*

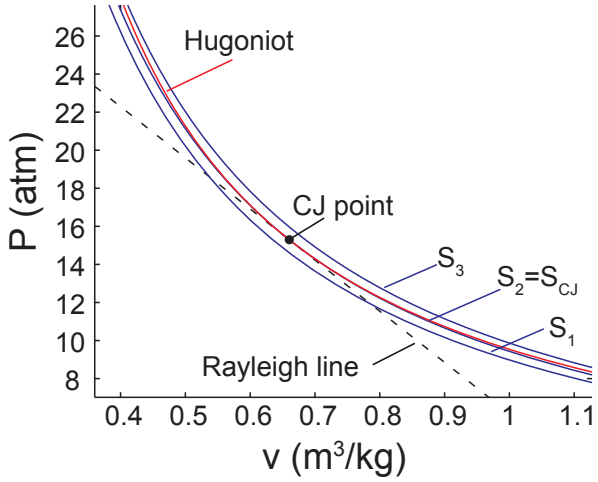

Figure 1.6: Hugoniot, Rayleigh line, and three representative isentropes (equilibrium) illustrating the tangency conditions at the CJ point.

1.2.2 Overdrive Factor

As discussed in the previous section, CJ detonations are characterized by a sonic plane at the end of the reaction zone. As indicated in by Figure 1.5, detonations can propagate at speeds greater than U_{CJ}. The overdrive factor, f, defined as

$$f = \left(\frac{\mathrm{U}}{\mathrm{U}_{CJ}}\right)^2 = \left(\frac{M}{M_{CJ}}\right)^2 \tag{1.2.23}$$

is a nondimensional measure of the detonation speed. The necessary downstream boundary condition is challenging to determine in the case of a CJ wave (see Section 1.3.2), and for this reason, we will concern ourselves strictly with overdriven detonations. In the programs that accompany this document, the shock speed can be specified three different ways: f, U, or M. In the case that f is specified, U_{CJ} is determined using methods discussed in Browne et al. (2007a).

1.2.3 Induction Zone

In high-temperature, shock-induced combustion, the temporal evolution of the species usually consists of an induction period that is almost thermally neutral followed by an

exothermic recombination period (Figure 1.7). The induction length, $\Delta_{i,ZND}$, is determined by the location of maximum thermicity while the energy release pulse width, $\Delta_{e,ZND}$, is the full-width at half-maximum thermicity locations.

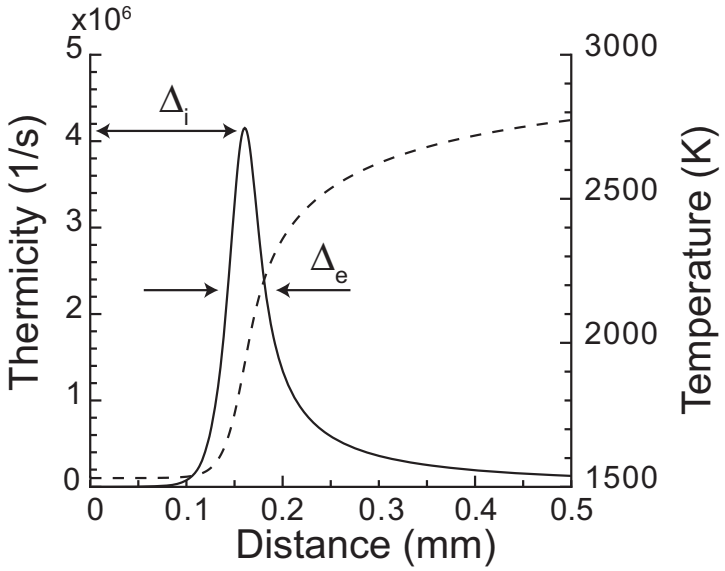

Figure 1.7: Cartoon defining induction length ($\Delta_{i,ZND}$) and energy release pulse width ($\Delta_{e,ZND}$) of CJ detonation in stoichiometric hydrogen-air initially at 1 atm and 300 K. In this case, $\Delta_{i,ZND} \approx 161$ μm and $\Delta_{e,ZND} \approx 43$ μm.

1.3 Detonation Instability

An interest in detonation instability arose in the 1960s when experimental results showed that detonations were inherently unstable. White (1961) first observed this instability with interferometry. At the same time, Denisov and Troshin (1959) and Shchelkin and Troshin (1965) used the popular soot foil technique to record histories of the detonation instability. A full review of the early experimental detonation instability studies is given in Fickett and Davis (1979). The results of these experiments indicated that detonations were complex three-dimensional phenomena with nonplanar shock fronts and turbulent reaction zones.

Early experimental investigations of the nonlinear stages of detonation instability provided the historic physical model which relies on the coupling between the fluid mechanics and the chemical reactions. Once the instability is fully developed, in two dimensions, the leading shock speed is a piecewise function of y as shown in Figure 1.8a. Classically, the alternating segments are referred to as the slower "incident shock" and faster "Mach stem." These names are not precise but arise from the shock-wedge interaction problem which was considered analogous. Because the induction length is sensitive to the post-shock temperature which is determined by the shock front speed, the distance between the exothermic pulse (see Figure 1.7) and the "Mach stem" is shorter than the distance between the exothermic pulse and the "incident shock." Figures 1.8 and 1.9 indicate that at each piecewise intersection between segments of "incident shock" and "Mach stem," a transverse wave propagating perpendicular to the front appears.

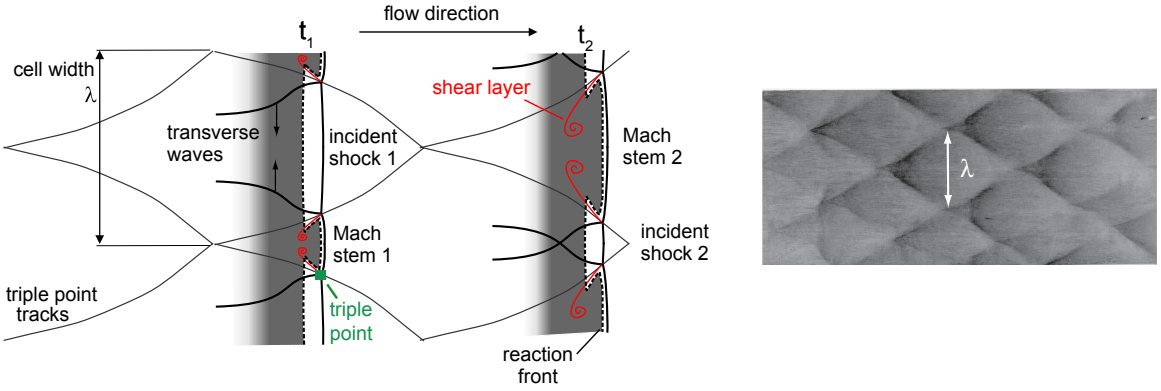

(a) (b)

Figure 1.8: (a) Schematic of detonation cellular structure. (Reprinted with permission from Pintgen (2004), Figure 1.3.) (b) Soot foil history of cellular structure (initial conditions: $2H_2$-O_2-17Ar, $P_1 = 20$ kPa). (Reprinted with permission from Austin (2003), Figure 4.2.)

As the detonation propagates, pairs of transverse waves move toward each other and weaken their corresponding Mach stem. They collide creating a region of high temperature and pressure increasing the chemical reaction rate. Products of this rapid combustion act as a piston to accelerate the neighboring shock segment. At this point,

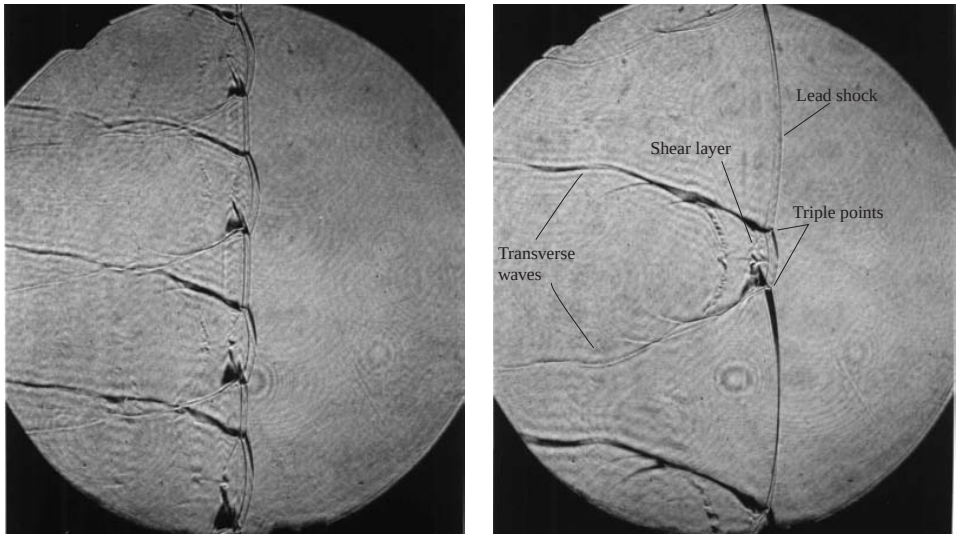

Figure 1.9: Schlieren images of detonation with initial conditions: $2H_2$-O_2-17Ar, $P_1 = 20$ kPa. Detonation is propagating from left to right, and the image size is $\approx$ 146 mm. (Reprinted with permission from Austin (2003) Figure 4.2)

the segment which was originally traveling faster has decayed significantly ("Mach stem 1" becomes "incident shock 2"), and the portion of the segment that was originally moving more slowly has accelerated ("incident shock 1" becomes "Mach stem 2"). After collision, the transverse waves begin to propagate away from each other, and the cycle begins again. Simulations based on simplified mechanisms and estimates from laboratory experiments suggest that a typical range for shock front velocities is $0.8U_{CJ}$ to $1.4U_{CJ}$.

A triple point occurs at the intersection of a transverse wave with the piecewise shock front. The soot foil technique is commonly used to record the instability's features by tracking the triple points. A cellular pattern is traced in the soot as depicted in Figure 1.8b. Each diamond element corresponds to a cell, and each of the vertices corresponds to the intersection of two triple points. Pintgen et al. (2003) used the PLIF technique (planar laser induced florescence) to observe the location of OH radicals. These radicals are indicative of the location of the exothermic pulse. This technique, shown in Figure 1.10, supports the historic description.

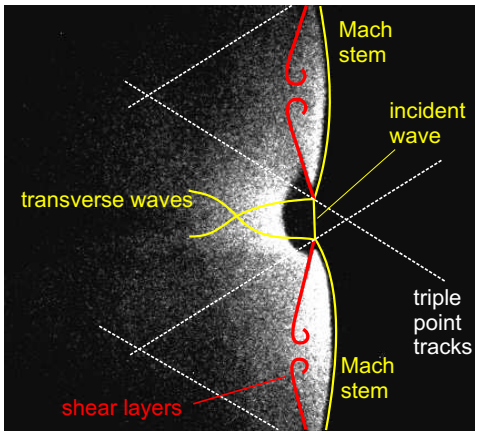

Figure 1.10: PLIF image of detonation with initial conditions: $2H_2$-O_2-17Ar, $P_1 = 20$ kPa, $T_1 = 300$ K. Flow direction is left to right, and the image height 75 mm. (Reprinted with permission from Pintgen (2004), Figure 1.4.)

1.3.1 Experimental Investigations

Clearly, detonations have a somewhat periodic instability which varies with chemical mixture. This prompted researchers to investigate the character of the instability and the important parameters governing the behavior. Shown in Figure 1.11 are two soot foils; Figure 1.11a depicts a "regular" cellular structure and Figure 1.11b depicts a very "irregular" structure. "Regularity" is a subjective classification related to the consistency of the cell size and shape. The cell width λ, defined in Figure 1.8, is a characteristic length scale which is usually an average of several cell widths. If all cells are relatively the same size, the mixture is deemed "regular," but if many different cell sizes and shapes are apparent, the mixture is deemed "irregular." The appearance of soot foils was used by both Strehlow and Biller (1969) and Libouton et al. (1981) to subjectively characterize detonation stability.

In an effort to investigate the most influential parameters, researchers investigated the linear stages of detonation instability. Strehlow et al. (1967) observed transition from a stable structure to a regular structure to an irregular structure shown in Figure 1.12. He commented that "transverse waves appear spontaneously even during the most nicely controlled one-dimensional initiations." He further observed that transverse waves "can

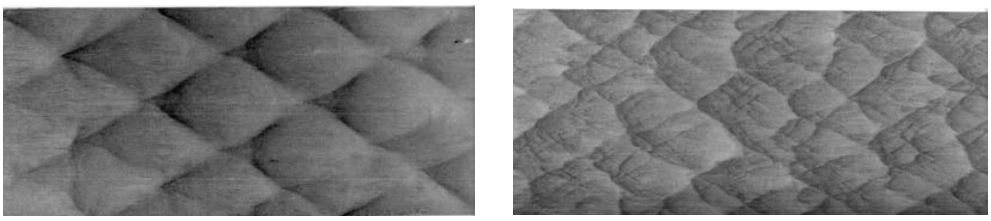

(a) (b)

Figure 1.11: Sample soot foils with (a) regular cellular structure (initial conditions: $2H_2$-O_2-17Ar, $P_1 = 20$ kPa) and (b) irregular structure (initial conditions: C_3H_8-$5O_2$-$9N_2$, $P_1 = 20$ kPa). Detonation propagated from left to right, and the image height is 152 mm. (Reprinted with permission from Austin (2003), Figure 1.3.)

appear spontaneously on a shock which is simply followed by an exothermic reaction," and that "the transverse waves appear with a regular spacing which has no relation to the tube's geometry."

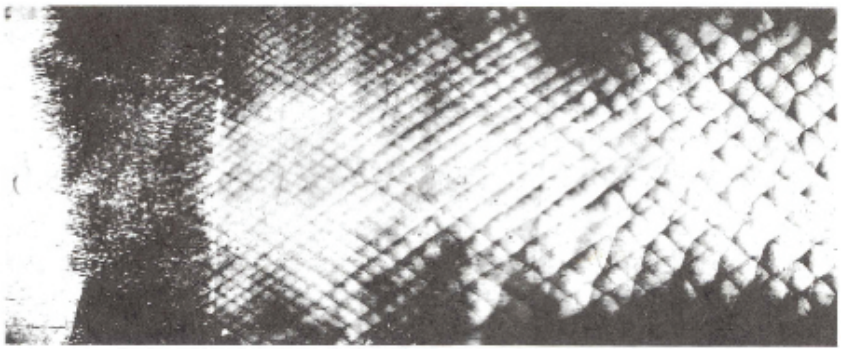

Figure 1.12: Soot foil record of the initiation of $2H_2$-O_2-70%Ar mixture. Back wall is to the left.(Reprinted with permission from Strehlow et al. (1967), Figure 1. Copyright 1967, American Institute of Physics.)

Contemporarily, the linear stages of detonation stability were being studied numerically (see Section 1.3.2), and experimentalists were investigating how parameters governing linear stability manifest themselves in the nonlinear stages. Cell width λ, the original classification parameter (Strehlow and Biller, 1969, Libouton et al., 1981) has been correlated to induction length $\Delta_{i,ZND}$. The temperature sensitivity of the induction length is conventionally characterized by an effective activation energy, E_a, which can

be obtained from an Arrhenius plot ($\ln(\Delta_{i,ZND})$ vs. $1/T$). For a one-step model or an elementary reaction with a single activation energy,

$$\ln(\Delta_{i,ZND}) = \frac{E_a}{R}\frac{1}{T} + \text{constant}. \tag{1.3.1}$$

For a multi-step model, E_a/R can be defined as the local slope of the Arrhenius curve as depicted in Figure 1.13. Schultz and Shepherd (2000) and Pintgen and Shepherd (2003) discuss methods for determining the effective activation energy for multi-step kinetics.

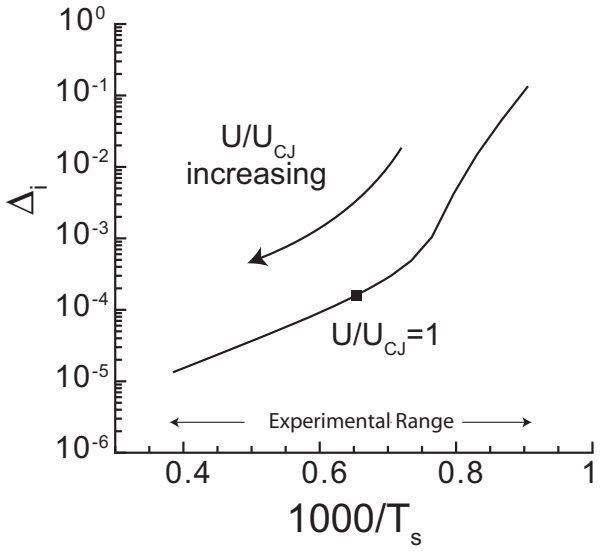

Figure 1.13: Arrhenius plot of induction time for a range of post-shock states in stoichiometric H_2-Air initially at standard conditions. The determination of E_a/R as the slope is shown.

Numerical studies of linear stability indicated that as the effective activation energy increases, the perturbation growth rate increases. Strehlow (1979) recognized that this result was in agreement with his experimental finding but found describing the physics with complex mathematical methods difficult. Instead he proposed two simpler physical models to describe the instability. The first model is the interaction between a longitudinal expansion wave and an overdriven one-dimensional detonation. This model supports the result that systems with greater effective activation energy are less stable.

The larger the activation energy, the more sensitive the induction length will be to fluctuations in temperature within the reaction zone. Ul'yanitskii (1981) proposed that the effective activation energy is the parameter that governs detonation stability. Radulescu et al. (2002) specifically investigated how argon dilution influences stability. They showed that argon dilution which changes the value of the effective activation energy has a stabilizing affect on C_2H_2-O_2 detonations. Further stability computations and experimental studies of detonation structure (Austin et al., 2005) have shown that the reduced effective activation energy, $\theta = E_a/(RT_2)$, is indeed a figure of merit for judging stability, supporting Ul'yanitskii's proposal. The larger the value of θ, the more irregular the cellular structure. This is shown in Figure 1.14. Although the global activation energy plays a role in detonation stability, Shepherd (1986) showed that activation energy is not a "systematic" measure of regularity.

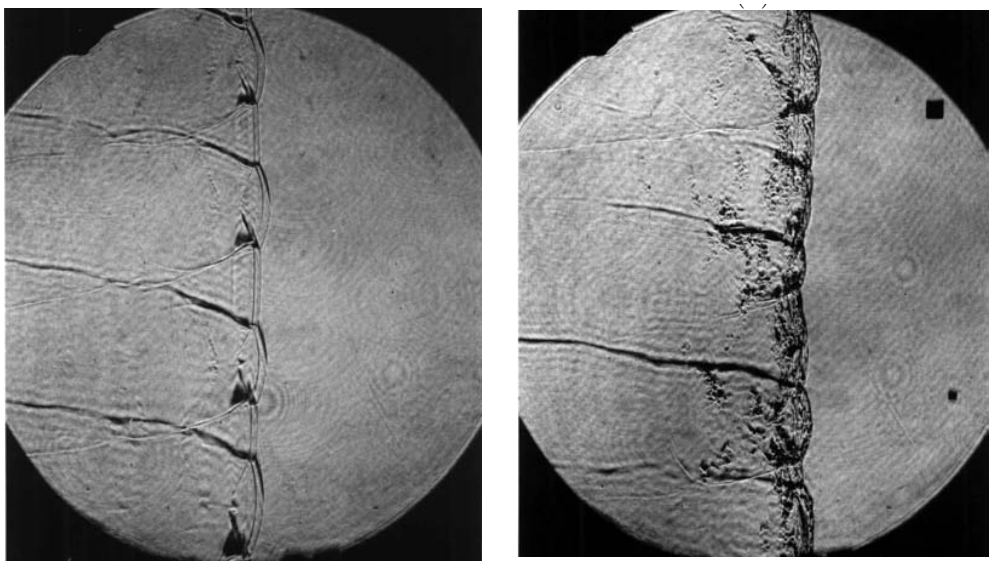

(a) (b)

Figure 1.14: Schlieren images of a (a) "weakly unstable" detonation, $\theta = 5.2$ (initial conditions: $2H_2$-O_2-$12Ar$, $P_1 = 20$ kPa) and a (b) "highly unstable" detonation, $\theta = 11.5$ (initial conditions: H_2-N_2O-$1.77N_2$, $P_1 = 20$ kPa). Detonations propagate from left to right, and the field of view is ≈ 146 mm. (Reprinted with permission from Austin (2003), Figure 5.2.)

The second model Strehlow (1979) presents is based on acoustic theory. He starts

with the steady detonation model and then introduces an acoustic source directly behind the leading shock. From these initial conditions, he observes the evolution of the wave front emanating from the acoustic source and determines that there is a specific location within the reaction zone where the wave front propagates parallel to the leading shock. Analyzing further, he concludes that high-frequency transverse waves cause all one-dimensional detonations to become unstable.

Barthel and Strehlow (1966) expand on this acoustic theory to describe the finite amplitude structure observed in experiments. They numerically integrated the ray equations for initial conditions corresponding to Strehlow's second model. From this, they found that the number of times the wave front contacts the shock front increases with time. Their ray tracing plots indicate that the gradients in soundspeed and flow velocity through the reaction zone causes folding in the ray emanating from the acoustic source (Barthel and Strehlow, 1966, see Figure 8).

Sturtevant and Kulkarny (1976) give an in depth discussion of how "wave folding" shown in Figure 1.15a arises for non-reacting acoustic waves. In their experiments, they observe that as the wave speed increases, the wave front no longer folds and instead "Mach reflexion" shown in Figure 1.15b occurs. This is a possible explanation for how the piecewise leading shock develops in detonations.

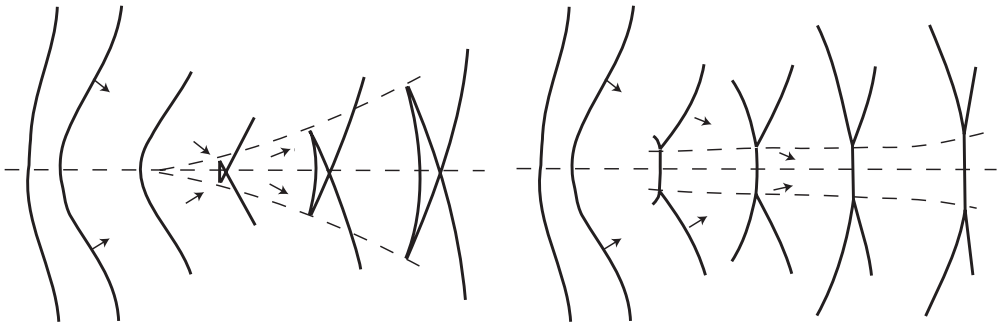

Figure 1.15: Schematic representation of the effect of shock strength on focusing for (a) sound pulses (b) strong shocks.

Hornung (1998) offered another explanation for the piecewise shock front. He in-

vestigated streamline curvature as a function of chemical reaction and found that for sufficiently exothermic reactions, no Crocco point exists. The Crocco point is the zero in the plot of streamline curvature vs. shock angle. At this point, the streamline curvature is zero for all values of the shock curvature. He concludes that in exothermic systems, transverse waves must occur as shown in Figure 1.16.

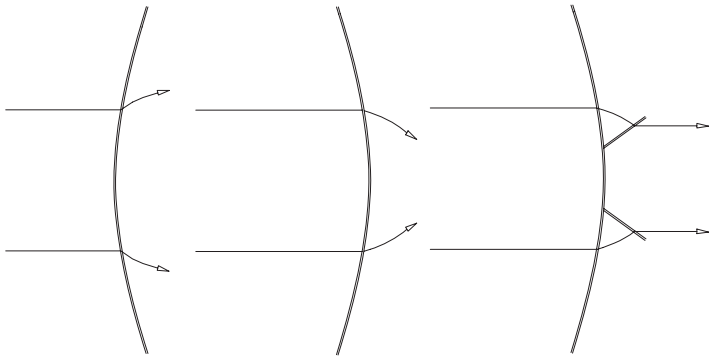

Figure 1.16: Schematic sketch of near-normal convex and concave shocks and associated streamlines for a mixture with fast exothermic reaction rate. The convex upstream shock on the left can exist with stable steady flow. The concave upstream shock shown in the center requires a pair of unsteady shocks to deflect the flow parallel to the symmetry plane shown on the far right.

McVey and Toong (1971) and Alpert and Toong (1972) offer yet another physical argument for the instability. Their proposal, like Strehlow's second model, argues that acoustic perturbations lead to temperature fluctuations. As described above, small temperature fluctuations lead to large changes in the induction length and this affects the leading shock. This model is called the "McVey-Toong short-period wave-interaction model."

As the induction time becomes long, the detonation structure transitions from the "multi-front structure" described above to the "spin detonation" or "marginal detonation." In this phenomenon, there is a single transverse wave that follows a helical path along the edge of a cylindrical tube as illustrated in Figure 1.17. Campbell and Woodhead first observed this behavior in 1926, and later Bone et al. (1935) determined that "spin" is dependent on the stability of the associated detonation. Manson (1946), Chu

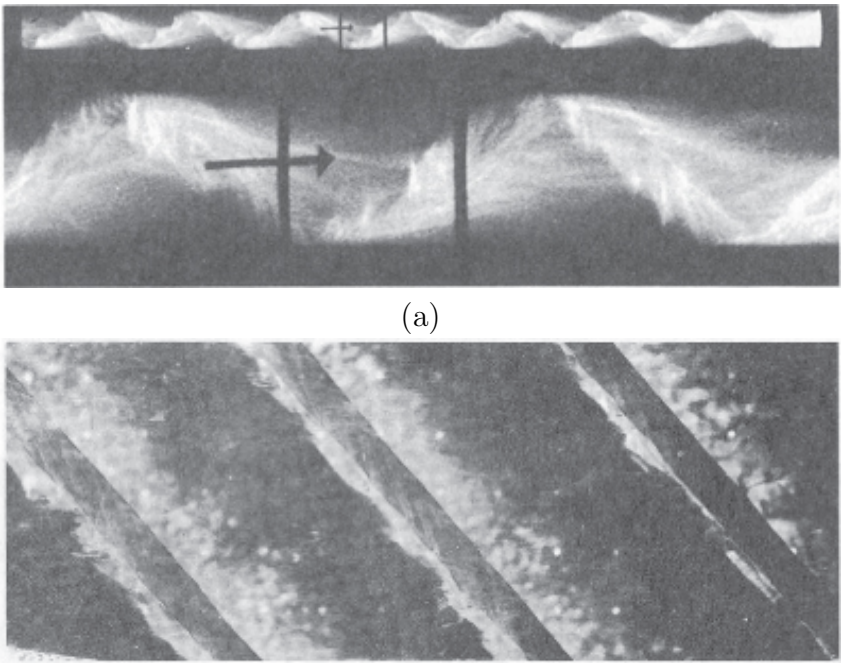

(a)

(b)

Figure 1.17: Single-spin detonation in C_2H_2-O_2-Ar mixture: (a) Open-shutter photograph, (b) Constant velocity spin soot foil. (Reprinted with permission from Schott (1965), Figures 1 and 5a. Copyright 1965, Combustion Institute.)

(1956), and Fay (1952) each developed a theory describing the "spin" behavior, but for some time, the "multi-front" detonation and "spin" detonation were considered separate phenomena. In 1959, Gordon et al. questioned:

> Is the spinning wave a completely different regime to that of the normal von Neuman experimental detonation, or can the two regimes be superimposed?...Is it possible that a spinning wave always results when a stable von Neuman structure cannot be set up?

Duff (1961) determined that the "spin" detonation is a limiting case of the "multi-front" detonation and that Manson's theory, applied appropriately, described both regimes. More recently, Kasimov and Stewart (2002) have numerically investigated the linear stability of one-dimensional steady detonations in cylindrical tubes. The found spinning unstable modes as they decreased the heat release Δh and propose that the spinning

instability starts the "spin" detonation.

1.3.2 Numerical Investigations of Stability

The model presented in Section 1.2 is unstable to small disturbances and in 1962, Erpenbeck first proposed a numerical approach to determine the hydrodynamic stability of "structurally stable" solutions (Wood and Salsburg, 1960). He focused his attention on a single irreversible reaction mechanism with a perfect gas equation of state. Using this simple model, he was able to determine unstable growth rates and corresponding frequencies with a combination of Laplace transform and Fourier transform methods. During the course of the decade, Erpenbeck published thirteen papers furthering his investigation of detonation stability. In these papers, he discussed topics including stability bounds (Erpenbeck, 1965), large activation energy asymptotic methods (Erpenbeck, 1963), and the effects of the transverse wave number (Erpenbeck, 1966).

Unfortunately although Erpenbeck's Laplace/Fourier transform methodology was exact, implementation was tedious and required inconvenient hand calculations. Erpenbeck (1969) references three studies (Pukhnachev, 1963, Zaidel, 1961, Aslanov, 1965) which propose a "normal modes" approach to the same problem, but the "normal modes" formulation became popular after Lee and Stewart (1990) presented the approach. While this assumption disregards solutions with an algebraic dependence on time, the stability problem becomes tractable. Recently Tumin (2007b) has used a spectral method and determined that there are no algebraic growth modes. In Lee and Stewart (1990), they use a shooting method to determine the unstable growth rates and corresponding frequencies which agree with those determined by Erpenbeck. Later in 1997, Short extended the normal modes formulation to two dimensions by assuming a Fourier component for the transverse direction. A comprehensive review of the linear stability problem is presented in Stewart and Kasimov (2006). These linear stability studies indicate that the effective activation energy E_a, overdrive f, isentropic ratio γ, and heat release Δh are important parameters for simplified models. Each of the studies discussed above was

carried out with single-step irreversible kinetics. Recently, Tumin (2007b) has returned to Erpenbeck's original formulation and applied spectral methods.

The detonation stability problem is a two-point boundary value problem described mathematically as a set of coupled partial differential equations. Lee and Stewart (1990) specifically address the boundary conditions for this problem. First they transform their reference frame to a "flat-shock-fixed frame" (see Section 3.1), a frame first proposed by Erpenbeck (1962). In this frame of reference, the left boundary condition is determined by the Rankine-Hugoniot equations. A radiation condition must be applied at the right boundary, and for overdriven detonations with irreversible kinetics models, there is an analytic expression for this. Unfortunately, in the case of reversible kinetics, this condition must be determined numerically. We will address this further in Chapter 4. The CJ detonation also presents complications; there is a singularity in the perturbation equations for this specific case which is discussed and addressed in Sharpe (1997). Due to this complication, we limit our study to strictly overdriven detonations ($f > 1$).

As discussed in Section 1.3.1, the linear stages of detonation instability are not easily observed in experiments. For this reason, other researchers investigated the behavior of the unsteady problem by means of direct numerical simulation. Fickett and Wood (1966) demonstrated that direct numerical simulation could reproduce the same frequencies that Erpenbeck's method determined. Bourlioux et al. (1991) improved the numerical methods used in Fickett and Wood (1966) and presented results for an extensive parameter space.

In 1984, Lee proposed four dynamic detonation parameters, and subsequently, researchers have used nonlinear simulations to investigate the effects of these parameters on detonation structure. He and Lee (1995) found three regimes of nonlinear behavior which they were able to correlate to two critical effective activation energies. Later, Gamezo et al. (1999) used two-dimensional detonation simulations to illustrate how the effective activation energy affects the "regularity" of cellular structure. Sharpe and Falle (2000) found that linear stability theory reasonably predicts minimum tube width when they compared cellular structure with linear theory predictions. Eckett et al. (2000)

used nonlinear simulations to investigate how varying point blast source energy affected detonation ignition. Using their critical decay rate model, they were able to predict the critical energy to within an order of magnitude.

The nonlinear stages of detonation stability are mainly characterized by oscillations. Matsuo and Fujii (1997) describe two modes of unsteady oscillation: high frequency/low amplitude and low frequency/low amplitude, and later Daimon and Matsuo (2003) increased the number of observed modes to four. Both Matsuo and Fujii and Daimon and Matsuo used a single-step irreversible kinetics model. Recently, Daimon and Matsuo (2007) have investigated the nature of unsteady oscillations with detailed chemical models and found that similar parameters continue to be the primary governing parameters. They conclude that initial composition (T_1, P_1, ϕ), which is akin to Δh and γ in the one-step model, effective activation energy E_a, and overdrive f most influence the nature of the nonlinear oscillations.

The nonlinear stages of detonation instability have also been studied as a nonlinear dynamical system (Short and Sharpe, 2003, Kasimov and Stewart, 2004). Ng et al. (2005a) and Yungster and Radhakrishnan (2005) present bifurcation diagrams which more clearly describe the inherent nonlinear dynamics. The bifurcation diagram in Ng et al. indicates that the period doubling follows a Feigenbaum series and eventually leads to chaotic behavior. Daimon and Matsuo (2003) also notice chaotic behavior in their simulations. Yungster and Radhakrishnan have investigated the same period doubling bifurcation with a detailed chemical model and proposed a "modified McVey-Toong short-period wave-interaction theory" which reasonably describes the nonlinear behavior.

1.4 Kinetics Models

Simplified chemical reaction mechanisms have been widely used in linear stability computations as well as multi-dimensional, unsteady simulations for detonations. Substantial progress (Fickett and Davis, 1979) was made early on by focusing on the simplest model of a one-step irreversible reaction. In the last two decades, many different approaches

have been taken to develop more realistic models that are still computationally efficient.

The most realistic set of kinetics models are detailed chemical mechanisms. These models include experimentally validated thermodynamic, transport, and kinetic data. Most commonly, these mechanisms are used within the framework of a thermo-kinetics software package such as CHEMKIN (Kee et al., 1987) or Cantera (Goodwin, 2005). The benefit of detailed mechanisms is that they are intended to represent all chemical aspects of a true system. To this end, the GRI mechanism for methane combustion (Smith et al., 1999) contains 53 species and 285 elementary reactions. Each species is modeled as an ideal gas with temperature-dependent specific heat, i.e.

$$\left(\frac{c_P}{R}\right)_{\mathrm{H_2}} = \begin{cases} \sum_{k=0}^{4} a_k T^k & 200\ \mathrm{K} < T < 1000\ \mathrm{K} \\ \\ \sum_{k=0}^{4} b_k T^k & 1000\ \mathrm{K} < T < 6000\ \mathrm{K} \end{cases} \tag{1.4.1}$$

where

$$\{a\}_{\mathrm{H_2}} = \{2.34, 7.98 \cdot 10^{-3}, -1.95 \cdot 10^{-5}, 2.02 \cdot 10^{-8}, -7.38 \cdot 10^{-12}\} \tag{1.4.2}$$

$$\{b\}_{\mathrm{H_2}} = \{2.93, 8.27 \cdot 10^{-4}, -1.46 \cdot 10^{-7}, 1.54 \cdot 10^{-11}, -6.89 \cdot 10^{-16}\}. \tag{1.4.3}$$

Additionally, each elementary reaction is reversible with a modified Arrhenius rate coefficient, i.e.,

$$\mathrm{OH} + \mathrm{H_2} \overset{k_f, k_r}{\leftrightarrow} \mathrm{H_2O} + \mathrm{H} \tag{1.4.4}$$

$$k_f = AT^n \exp\left(\frac{-E_a}{RT}\right) = 1.17000 \cdot 10^9 T^{1.3} \exp\left(\frac{-3626}{RT}\right). \tag{1.4.5}$$

A subset of the GRI mechanism was used to generate Figure 1.1. This subset contains 12 species: 3 reactants (H_2, O_2, N_2), 1 product (H_2O), 4 radicals (H, O, OH, N), 3 intermediates (HO_2, H_2O_2, NO), and 1 inert (Ar). This subset also contains 24 reactions, and Table 1.1 shows a selection of these reactions and their rate parameters. There are

four primary reaction types in a branching chain: chain initiation, chain branching, chain propagation, and chain termination. In the hydrogen mechanism (Table 1.1), reaction 1 (backwards) is the initiation reaction. Here the hydrogen molecule reacts with another molecule to produce two hydrogen radicals. Once sufficient free radicals exist, chain branching (Reactions 2–4) and chain propagating reactions (Reaction 5) continue the chain. In each of the branching reactions, two radicals are produced for each radical that reacts. The final process is chain termination which occurs when one or more radicals react to form a stable species. Reaction 6 of the hydrogen mechanism is a termination reaction. Unlike reaction 1, the extra reactant molecule removes energy from the collision between H and O_2 and allows them to bond and form HO_2.

No.	**Reaction**	A	n	E_a
1	$H + H + M \leftrightarrow H_2 + M$	$1.00{\cdot}10^{18}$	-1.00	0
2	$O + OH \leftrightarrow O_2 + H$	$4.00{\cdot}10^{14}$	-0.50	0
3	$O + H_2 \leftrightarrow OH + H$	$5.06{\cdot}10^{4}$	2.67	6290.0
4	$OH + OH \leftrightarrow O + H_2O$	$6.00{\cdot}10^{8}$	1.30	0
5	$OH + H_2 \leftrightarrow H_2O + H$	$1.17{\cdot}10^{9}$	1.30	3626.0
6	$H + O_2 + M \leftrightarrow HO_2 + M$	$3.61{\cdot}10^{17}$	-0.72	0

Table 1.1: Partial hydrogen oxidation mechanism and rate constants (Smith et al., 1999).

In general, simulations involving detailed chemistry are computationally expensive because each species adds an additional conservation equation which involves a subset of the elementary reactions. Oran et al. (1998) and Inaba and Matsuo (2001) give numerical simulation results using detailed mechanisms, providing a benchmark for simulations using simplified mechanisms.

On the other end of the spectrum is the one-step irreversible model.

$$\mathcal{A} \xrightarrow{k_f} \mathcal{B} \tag{1.4.6}$$

$$k_f = A \exp\left(\frac{-E_a}{RT}\right) \tag{1.4.7}$$

In this model, there is one irreversible reaction that transforms reactants $\mathcal{A}$ to products $\mathcal{B}$. The simplest implementations of this model assume that both species have identical

and constant specific heat and molecular weights but different heats of formation. The reaction rate coefficient k_f has an Arrhenius form. Although this model is convenient to implement numerically, it is difficult to relate to realistic systems because it only has one time scale and the following four parameters γ, E_a, Δh, A.

Both detailed chemical models and one-step models have limitations: detailed chemical mechanisms are computationally expensive and one-step models are unrealistic. Because of this, several types of reduced models have been investigated. The origins of all simplified models of combustion reactions for explosions can be traced back to the pioneering studies of Semenov (1935) who discovered the key roles of thermal feedback and branching chain reactions in explosions and proposed separate models of each process. A unified model was developed by Gray and Yang (1965) to treat explosions due to simultaneous thermal and chain mechanisms. Since then, researchers have developed two main methods of reducing detailed mechanisms: "timescale separation" methods and pseudo-species methods.

"Timescale separation" methods rely on ordering the many chemical timescales. Tomlin et al. (1997) and Eckett (2000) give reviews of this type of method. Eckett (2000) discusses the QSSA (Quasi-Steady-State Approximation, Peters (1988)) and ILDM (Intrinsic Low Density Manifold, Maas and Pope (1992)) methods extensively. In both of these methods, the chemical timescales are compared with the fluid mechanics timescale and separated into two categories. The reactions that proceed more slowly than the fluid mechanics are modeled with detailed chemistry, while a different model is proposed for those proceeding more quickly than the fluid mechanics. Varatharajan and Williams (2001) and more recently Varatharajan et al. (2005) have also presented work using reduced mechanisms. Like the QSSA and IDLM methods, they used detailed kinetics to model slow timescales and a simplified model to capture the fast timescales.

The second method of reduction is of a more ad hoc nature that addresses the underlying primary chemical pathways. These simple models are in some sense an elaboration of the one-step model, using a notional reaction scheme with multiple steps between a set of pseudo-species in order to mimic the chemical processes. These pseudo-species

mechanisms include initiation, branching, and termination steps and are designed to imitate the key features of a realistic chemical reaction mechanism without the computational expense associated with time integration of a large set of species. The two-step model (Korobeinikov et al., 1972) includes an induction region and an energy release region. Oran et al. (1981) improved upon this model by using detailed mechanisms to choose appropriate values for the induction length and maximum energy release parameters. Lefebvre et al. (1992) further improved the model by allowing the species specific heats and the average molecular weight to be functions of temperature. This generalized the model's original perfect gas equation of state.

In order to incorporate more chemical features, pseudo-species models began to include an "extended second limit" between a fully-branched mechanism and a straight-chain mechanism with rare branching, which Voevodesky and Soloukhin (1965) found was a key factor in determining ignition regimes. Dold and Kapila (1991) and Short and Quirk (1997) developed a three-step mechanism which characterizes the extended second limit by a cross-over temperature where the chain-branching and chain-termination reaction rates are equal. A simplified view of the situation is that above this temperature, branching dominates, while below, termination will slow down and possibly quench the reaction. Liang and Bauwens (2005) added a fourth step to this model to include the first explosion limit and then devised a five-step model (Liang et al., 2007) to capture the competition between chain branching pathways and peroxide pathways. The three-, four-, and five-step models are viewed as being more realistic than the traditional one-step models and therefore able to more realistically represent phenomena such as initiation and quenching of reaction in unstable detonations.

The nature of the chemical reaction model and the shape of the reaction zone structure have a clear influence on the detonation stability. The existence of multiple length scales in the reaction zone and the relevance to experimental measurements of detonation cell width and cellular regularity was examined by Strehlow and Engel (1969). To date, there have not been any linear stability studies using detailed chemical models due to their complexity, but the limitations of the one-step models motivated Short and Sharpe

(2003) and Short and Quirk (1997) to investigate stability limits for two- and three-step reactions. They concluded that detonation instability is strongly dependent on the ratio of the lengths of the induction zone $\Delta_{i,ZND}$ and energy release zone $\Delta_{e,ZND}$ (see Figure 1.7). Increasing the length of the energy release zone relative to the induction zone stabilized the detonation. In the case of the three-step reaction proposed by Short and Quirk, this ratio ($\Delta_{i,ZND}/\Delta_{e,ZND}$) is governed by the value of the post-shock temperature relative to the cross-over temperature. Ng and Lee (2003) used the same model as Short and Quirk to study detonation initiation, and they also emphasized the importance of independently varying the ratio of energy release time to induction time as well as the activation energy.

One-dimensional pulsating detonation simulations with detailed chemistry (Yungster and Radhakrishnan, 2005) for ethylene and hydrogen-air mixtures show a transition from high- to low-frequency modes with increasing equivalence ratio. This transition is associated with the changing shape of the reaction zone. Similar computations have been carried out by Ng et al. (2005b) for the hydrogen-air system. Ng et al. found that the reaction zone shape, characterized by the ratio of induction length to energy release length, was important in developing predictive correlations for detonation cell width as well as the one-dimensional stability threshold. These studies all indicate that the ability to independently specify the induction and energy release times, as well as the effective activation energies, is an important aspect of any realistic chemical reaction model.

1.5 Thesis Outline

Simple models of detonation structure and a review of previous experimental and numerical work related to the present study are given in Chapter 1. Chapter 2 describes how we implement the base flow with specific kinetics models. Chapter 3 discusses the method for determining the unstable roots during the linear stages of detonation instability for an arbitrary chemistry model. Chapter 4 gives a detailed discussion of the necessary radiation condition for the implementation presented in Chapter 3. This boundary condition

is non-trivial and significant attention has been paid.

Chapter 5 presents the results of this study and discussion in one and two dimensions using the single-step reversible model discussed in Chapter 2. We demonstrate that we can find unstable roots for varying degrees of reversibility using our numerical radiation condition. We have used direct Euler simulations to confirm the one-dimensional results given in Chapter 5. Chapter 6 provides the necessary details for determining the unstable roots with one-dimensional direct Euler simulations and comparision with linear stability predicitions. Finally, Chapter 7 gives a summary of the work done and proposes future investigation.

Chapter 2

Base Flow

The base flow for our linear stability study is the ZND model discussed in Section 1.2. In order to implement this base flow, we must specify a chemical mechanism including kinetic and thermodynamic data. As discussed in Section 1.4, traditionally, linear stability studies have focused on a single-step irreversible reaction model. In realistic kinetics, each elementary reaction is reversible, and this work seeks to determine the effect reversibility has on detonation linear stability. In this chapter, we will describe both the traditional one-step irreversible model and our one-step reversible model. Our implementation uses Cantera (Goodwin, 2005), and for this reason, we will also describe how we created the necessary `cti` files, Cantera's mechanism input file type.

2.1 One-Step Irreversible Perfect Gas Analysis

The one-step irreversible perfect gas model has been studied extensively due to its simplicity (see Section 1.3.2). The mechanism consists of perfect gas thermodynamics and a single irreversible reaction

$$\mathcal{A} \xrightarrow{k_f} \mathcal{B} \tag{2.1.1}$$

where a generic reactant species, $\mathcal{A}$, is transformed into a generic product species, $\mathcal{B}$. Unlike realistic systems, the equilibrium state consists solely of product species. Addi-

tionally, the model assumes that the specific heats and molecular weights are equal for the two species. We choose to use the molecular weight of Ar (39.9) for the molecular weight of both pseudo-species. To create a Cantera input file in `cti` format for a perfect gas with one-step kinetics, we must determine appropriate thermodynamic and reaction data. An example `cti` file is given in Appendix G.

The thermodynamic data required for a `cti` file is derived from the original NASA polynomial fit format. According to the CHEMKIN manual Kee et al. (1987), this format specifies the constant pressure specific heat as a piecewise fourth-order polynomial in the following way

$$\frac{c_{Pi}}{R} = \begin{cases} \sum_{k=0}^{4} a_{ik} T^k, & T_{\min} \leq T \leq T_{\mid} \\ \\ \sum_{k=0}^{4} b_{ik} T^k, & T_{\mid} \leq T \leq T_{\max} \end{cases} . \tag{2.1.2}$$

If we want a perfect gas, constant c_P, only a_0 and b_0 can have non-zero values. To maintain continuity at $T_{\mid}$, they must also be equal $a_0 = b_0$. Now for a perfect gas,

$$\frac{c_{Pi}}{R} = a_{i0}, \quad T_{\min} \leq T \leq T_{\max} . \tag{2.1.3}$$

We can determine the value of a_0 from the desired constant isentropic ratio, γ

$$\frac{c_{P\mathcal{A}}}{R} = \frac{c_{P\mathcal{B}}}{R} = a_0 = \frac{\gamma}{\gamma - 1}. \tag{2.1.4}$$

In addition to these five coefficients, two constants of integration are necessary to determine the enthalpy and entropy from the specific heat. The enthalpy is determined by the following equation

$$h_i = \int_{T^\circ}^{T} c_{Pi}(T')dT' + \Delta_f h_i^\circ \tag{2.1.5}$$

which with (2.1.3) becomes

$$\frac{h_i}{R_i T} = \left\{ \; a_{0i} + \frac{a_{5i}}{T} \quad T_{\min} \leq T \leq T_{\max} \right. \quad . \tag{2.1.6}$$

In a perfect gas system, all heat release is specified by the enthalpy difference between the reactants and products, i.e.,

$$h_{\mathcal{A}} = c_P T \tag{2.1.7}$$

$$h_{\mathcal{B}} = c_P T - \Delta h. \tag{2.1.8}$$

We choose to use the standard state enthalpy of argon for the reactants

$$a_{5\mathcal{A}} = \left(\frac{h(300 \text{ K})}{R} \right)_{Ar} = -1.8 \cdot 10^3. \tag{2.1.9}$$

To determine the standard state enthalpy of the products, we must subtract Δh from the standard state enthalpy of the reactants. Traditionally $\tilde{\beta}$ is the nondimensional version of Δh such that $\tilde{\beta} = \Delta h/(RT_1)$ and we can express the standard state enthalpy of the products in terms of $\tilde{\beta}$.

$$a_{5\mathcal{B}} = a_{5\mathcal{A}} - \tilde{\beta} \cdot 300 \tag{2.1.10}$$

The classic value of $\tilde{\beta}$ given in Erpenbeck's studies is 50 which gives

$$a_{5\mathcal{B}} = -1.68 \cdot 10^4. \tag{2.1.11}$$

The second constant of integration a_6 is required to determine the entropy of each species. Like the enthalpy, the entropy is also determined from the specific heat

$$s_{\circ i} = \int_{T_1}^{T} \frac{c_{Pi}(T')}{T'} dT' + s_{\circ i}(T^\circ) \tag{2.1.12}$$

which with (2.1.3) becomes

$$\frac{s_{\circ i}}{R_i} = a_{0i} \ln(T) + a_{6i} \quad T_{\min} \leq T \leq T_{\max} \ . \tag{2.1.13}$$

The species entropy is necessary to calculate the equilibrium constant for the reaction. In the case of an irreversible reaction, the reaction equilibrium constant is unnecessary. We will discuss the reaction equilibrium constant further in Section 2.2. For this model though, we can specify any value for the entropy constants of the reactant and the product. We choose the value for argon at 300 K for both species, i.e.,

$$a_{6\mathcal{A}} = a_{6\mathcal{B}} = 4.366. \tag{2.1.14}$$

Reaction data is necessary to calculate the rates of production which appear in the ZND equations. Cantera calculates these with the following expression

$$\dot{\Omega}_{\mathcal{A}} = -k_f Y_{\mathcal{A}} \tag{2.1.15}$$

$$\dot{\Omega}_{\mathcal{B}} = k_f Y_{\mathcal{A}}. \tag{2.1.16}$$

The reaction rate coefficient, k_f, is given in the modified Arrhenius form

$$k_f = A T^n \exp\left(-\frac{E_a}{RT}\right) \tag{2.1.17}$$

where the three required values are "A," the pre-exponential, n, the temperature power, and E_a, the activation energy. It is important to note that because Cantera `cti` files are often derived from CHEMKIN input files, the unit system is usually cgs instead of SI. The temperature power, n, is unitless and therefore transfers directly amongst all representations. We choose $n = 0$ which corresponds to the classical Arrhenius form.

$$k_f = A \exp\left(-\frac{E_a}{RT}\right) \tag{2.1.18}$$

The activation energy is traditionally specified nondimensionally as $\tilde{E} = E_a/RT_1$. When dimensionalizing $\tilde{E}_a$ for the Cantera `cti` file, E_a may need to be specified in calories per mole if the cgs standard is specified at the top of the `cti` file. In the case of Erpenbeck's work, $\tilde{E}_a = 50$ which translates to

$$E_a = 3 \cdot 10^4 \text{ cal/mol.} \tag{2.1.19}$$

The pre-exponential, A, determines the location of the reaction zone. We can normalize A such that the reaction zone is centered at $\tilde{t} = \dfrac{t}{t_c} = 1$ where t_c is a reference time scale. This essentially normalizes t by the half reaction time $t_c = t_{1/2}$ which is the normalization presented in Lee and Stewart (1990). Instead of building the normalization into the reaction data, we could normalize at the end of the computation. We have selected to normalize A such that $\tilde{t}_{1/2} = 1$ s, and the easiest method to determine this $\tilde{A}$ is to plot the ZND profile of the product mass fraction as a function of time. $\tilde{A}$ should be chosen in order to ensure that the product mass fraction is 0.5 when $\tilde{t} = 1$ s for a given overdrive value, f. To determine the correct value of A calculate the ZND profile for $A = 10^4$ and find the time when the product mass fraction is 0.5 ($t_{Y_{\mathcal{B}=0.5}}$). Now $\tilde{A}$ is

$$\tilde{A} = A\frac{t_{Y_{\mathcal{B}=0.5}}}{\tilde{t}_{1/2}} \tag{2.1.20}$$

which is

$$\tilde{A} = 8.6119065 \cdot 10^2 \tag{2.1.21}$$

for $\tilde{\beta} = \tilde{E}_a = 50$ and $\gamma = f = 1.2$.

Figure 2.1 describes the ZND profiles for this simple reaction model. We notice that at the end of the computation $Y_{\mathcal{B}} = 0.9999$.

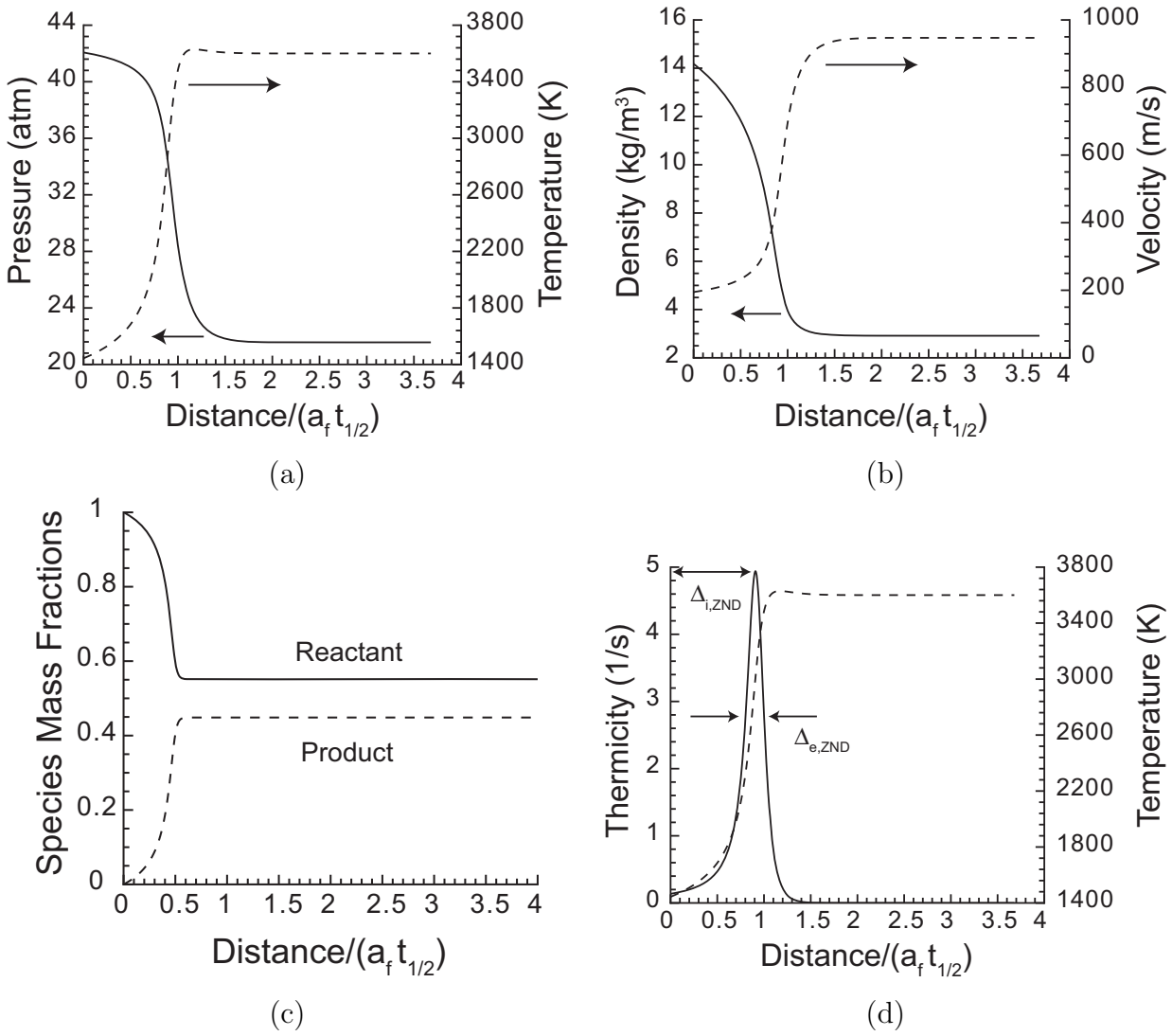

Figure 2.1: ZND profiles for one-step irreversible mechanism. In this case, $\Delta_{i,ZND}/(a_{f1}t_{1/2}) = 0.91$ and $\Delta_{e,ZND}/(a_{f1}t_{1/2}) = 0.22$.

2.2 One-Step Reversible Perfect Gas Analysis

The new model that we present is somewhat similar to the one-step irreversible model discussed in Section 2.1. Again, we have two generic species with equal and constant specific heats and molecular weights ($W = W_{\mathrm{Ar}} = 39.9$) and a single reaction. In this case, our reaction is reversible, i.e., a mixture of reactant and product exists at

equilibrium.

$$\mathcal{A} \overset{k_f,k_r}{\leftrightarrow} \mathcal{B} \tag{2.2.1}$$

As discussed below, the equilibrium ratio is controlled by the difference in the entropy constants of the two species. We have chosen to create a family of reversible mechanisms with varying equilibrium ratios but equivalent CJ temperatures, T_{CJ}.

Regarding the thermodynamic data necessary for the `cti` file, the expressions for the specific heat (2.1.3), enthalpy (2.1.6), and entropy (2.1.13) are given in Section 2.1. The five polynomial coefficients and the enthalpy constant are also determined by the methods described in Section 2.1. For $\tilde{\beta} = \tilde{E_a} = 50$ and $\gamma = 1.2$,

$$a_{0\mathcal{A}} = a_{0\mathcal{B}} = 6.0 \tag{2.2.2}$$

$$a_{k\mathcal{A}} = a_{k\mathcal{B}} = 0 \quad k = \{1, 2, 3, 4\} \tag{2.2.3}$$

$$a_{5\mathcal{A}} = -1.8 \cdot 10^3 \tag{2.2.4}$$

$$a_{5\mathcal{B}} = -1.68 \cdot 10^4. \tag{2.2.5}$$

The reaction data discussed in Section 2.1 that pertains to the forward reaction specifies A, n, and E_a. The values of n and E_a are determined in the same fashion as for the one-step irreversible reaction.

$$n = 0 \tag{2.2.6}$$

$$E_a = 3 \cdot 10^4 \text{ cal/mol} \tag{2.2.7}$$

"A" is also calculated similarly, but instead of aligning $t = 1$ s with $Y_{\mathcal{B}} = 0.5$, we assure that $Y_{\mathcal{B}} = 0.5 Y_{\mathcal{B}}^{eq}$ when $t = 1$ s.

In the case of a single irreversible reaction (Section 2.1),

$$\mathcal{A} \overset{k_f}{\rightarrow} \mathcal{B}, \tag{2.2.8}$$

we can set the standard state entropy of both species to that of argon because Cantera does not evaluate the equilibrium constant to find the backward reaction rate. On the other hand, in the case of a single reversible reaction,

$$\mathcal{A} \overset{k_f,k_r}{\leftrightarrow} \mathcal{B}, \tag{2.2.9}$$

the principle of detailed balance allows us to determine the reverse reaction rate from the forward reaction rate and equilibrium constant.

$$k_r = \frac{k_f}{K_C(T)} \tag{2.2.10}$$

where

$$K_C = K_P \left(\frac{P_o}{\mathcal{R}T}\right)^{\Delta\nu}. \tag{2.2.11}$$

The condition for chemical equilibrium of the reaction

$$\sum_{i\ (sp)} \nu_i \mu_i = 0 \tag{2.2.12}$$

defines K_P, such that

$$K_P = \prod_{i\ (sp)} P_i^{\nu_i} = \exp\left(-\frac{\nu_i \left[h_i(T) - T s_i^\circ(T)\right]}{RT}\right). \tag{2.2.13}$$

For the one-step reversible model, K_P is

$$\ln K_P = \ln\left(\frac{P_\mathcal{B}}{P_\mathcal{A}}\right) = -\left[\left(\frac{h_\mathcal{B}(T)}{RT} - \frac{h_\mathcal{A}(T)}{RT}\right) - \left(\frac{s_\mathcal{B}^\circ(T)}{R} - \frac{s_\mathcal{A}^\circ(T)}{R}\right)\right]. \tag{2.2.14}$$

By incorporating (2.1.6) and (2.1.13), K_C becomes

$$K_C = \exp\left[(a_{6\mathcal{B}} - a_{6\mathcal{A}}) - \left(\frac{a_{5\mathcal{B}} - a_{5\mathcal{A}}}{T}\right)\right] = \exp\left(\Delta a_6 - \frac{\Delta a_5}{T}\right). \tag{2.2.15}$$

With this expression for K_C we can determine the Arrhenius rate parameters for the backward reaction in terms of a_5 and a_6.

$$k_r = A' \exp\left(-\frac{E'_a}{RT}\right) = [A \exp(-\Delta a_6)] \exp\left(-\frac{(E_a - \Delta a_5)}{RT}\right). \tag{2.2.16}$$

We have already determined that Δa_5 is computed from the desired heat release. Now the only free parameter governing k_r is Δa_6, the entropy difference between the two species. We see that as we decrease the entropy constant of the products while holding the entropy of the reactant constant, we can vary the extent of reaction or $Y_{\mathcal{B}}^{eq}$.

2.2.1 Family of Reversible Models with Constant CJ Temperature

In previous implementations, the one-step irreversible model 2.1 has been hard-coded and the user provides several parameters. Most researchers have confirmed the correctness their implementations by comparing with Erpenbeck's case: nondimensional activation energy $\tilde{E}_a = 50$, nondimensional heat release $\tilde{\beta} = 50$, ratio of specific heats $\gamma = 1.2$, and overdrive $f = (\mathrm{U}/\mathrm{U}_{CJ})^2 = 1.2$. Using Cantera, we are able to create an input file that mimics this case. In addition, we have the flexibility to specify a reversible reaction and vary the amount of reversibility by adjusting the entropy difference between the reactant and product species. We have chosen to create a family of reaction models each with a single reversible reaction where the Chapman-Jouguet temperature T_{CJ} remains constant. To achieve this, we specify the desired entropy difference ($\Delta s/R = \Delta a_6$) and desired T_{CJ} and solve for the required heat release ($\Delta h/R = \Delta a_5$). Table 2.1 and Figure 2.2 describe the family of models that we have created for initial conditions $T_1 = 300$ K, $P_1 = 1$ atm, $Y_{\mathcal{A}1} = 1$, and $Y_{\mathcal{B}1} = 0$. We see that the $\Delta s/R = 0$ case is comparable to the irreversible

$\Delta s/R$	$\Delta h/(RT_1)$	U_{CJ}	M_{CJ}	T_2	$\theta = E_a/(RT_2)$	$Y_{\mathcal{B}}^{eq}$
0	50.705	1701.15	6.21	1443.5	10.39	0.986
-1	51.737	1700.30	6.21	1442.35	10.40	0.965
-2	53.932	1699.00	6.20	1440.61	10.41	0.924
-3	57.781	1697.56	6.20	1438.66	10.43	0.860
-4	63.351	1696.42	6.19	1437.12	10.44	0.782
-5	70.342	1695.66	6.19	1436.1	10.44	0.703
-6	78.380	1695.20	6.19	1435.47	10.45	0.630
-7	87.167	1694.91	6.19	1435.08	10.45	0.566
-8	96.497	1694.72	6.19	1434.83	10.45	0.510

Table 2.1: Reversibility parameters for $T_{CJ} = 3599.29$ K.

case.

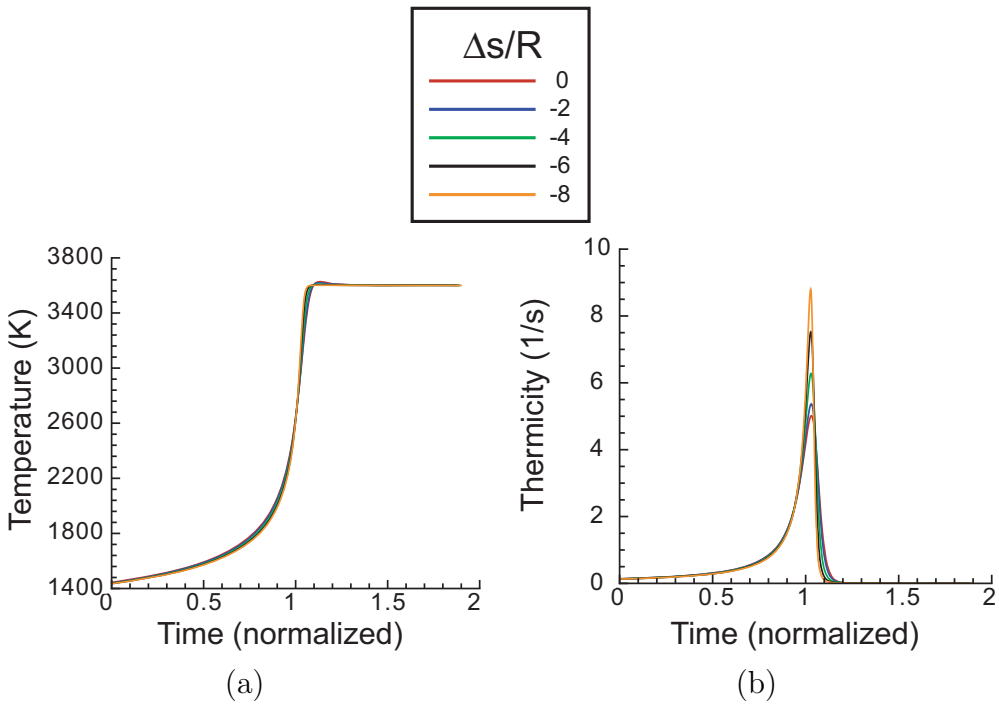

(a) (b)

Figure 2.2: Family of constant T_{CJ} solutions ($T_{CJ} = 3599.29$ K) for initial conditions $T_1 = 300$ K, $P_1 = 1$ atm, $Y_{\mathcal{A}1} = 1$, and $Y_{\mathcal{B}1} = 0$. (a) Temperature profiles (b) Thermicity profiles

Chapter 3

Linear Stability Analysis

In the following chapter, we present a method for characterizing the linear stages of the detonation instability with an arbitrary chemistry model. First in Section 3.1, we transform our problem to a new reference frame, then in Section 3.2, we linearly perturb the reactive Euler equations. Sections 3.3 and 3.4 discuss the necessary boundary conditions for the two-point boundary value problem. We describe the shooting method we use to solve the problem in Section 3.5, and finally in Section 3.6 we explain how the output is normalized. The following formulation is presented in two dimensions ($k_y \neq 0$) and allows for an arbitrary chemistry model.

3.1 Coordinate Transformation

The reactive Euler equations (1.1.1)–(1.1.4) presented in Section 1.1 are in the *laboratory frame*, an inertial reference frame in which both the shock and flow are moving. In order to carry out analyses of the basic steady reaction zone structure and the instability, the equations of motion need to be transformed to a *flat-shock-fixed frame*. This is accomplished by the following change of variables which places the shock at the origin of the coordinate system as depicted in Figure 3.1. In the following discussion, the laboratory coordinates will be designated by a superscript L.

As depicted in Figure 3.1a, the unsteady shock velocity D is the mean shock velocity in the laboratory frame U plus a perturbation $\psi(y^L, t^L)$. The location of the shock in

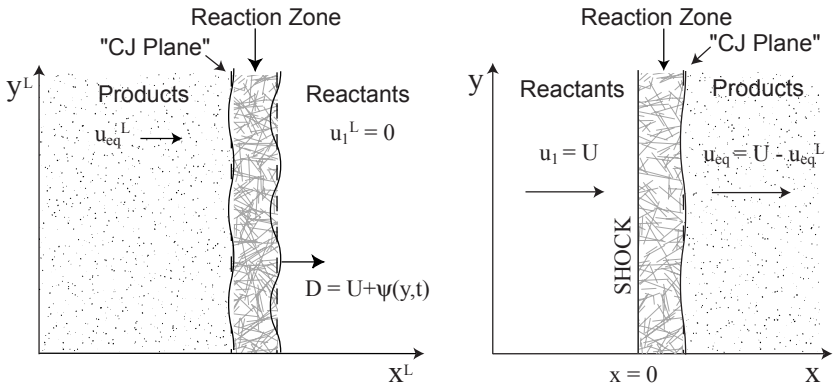

Figure 3.1: Cartoons of the two frames of reference discussed in this section: (a) Laboratory Frame and (b) Flat-Shock-Fixed Frame.

the laboratory frame is

$$x^L_{shock} = \int^{t^L} \mathrm{D}dt = \mathrm{U}t^L + \psi(y^L, t^L). \tag{3.1.1}$$

We are interested in measuring distance relative to x^L_{shock}, so our new coordinate, x, is

$$x = x^L_{shock} - x^L = \left[\mathrm{U}t^L + \psi(y^L, t^L)\right] - x^L. \tag{3.1.2}$$

The other independent variables, vertical distance y and time t, are unchanged in the new coordinate system.

The fluctuations in the dependent variables, velocity, and thermodynamic variables, are the quantities of interest in this problem. Thermodynamic variables are invariant with respect to coordinate system transformations. On the other hand, the unperturbed velocity components must be transformed to the flat-shock-fixed frame. This only applies to the velocity component normal to the shock, u, because the mean shock velocity in the direction tangential to the shock is zero.

$$\mathrm{u} = \mathrm{U} - \mathrm{u}^L \tag{3.1.3}$$

It is important to note that the transformation of u does not contain ψ because we are interested in solving for fluctuations in u. If we had accounted for ψ in the transformation of u as we have in the transformation of x, u would be a constant quantity as x is.

In the new frame of reference, the reactive Euler equations for an ideal gas in two-dimensions become

$$v_{,t} + (\mathrm{u} + \psi_{,t} + \mathrm{v}\psi_{,y})v_{,x} + \mathrm{v}v_{,y} = v(\mathrm{u}_{,x} + \mathrm{v}_{,y} + \psi_{,y}\mathrm{v}_{,x}) \tag{3.1.4}$$

$$\mathrm{u}_{,t} + (\mathrm{u} + \psi_{,t} + \mathrm{v}\psi_{,y})\mathrm{u}_{,x} + \mathrm{v}\mathrm{u}_{,y} = -vP_{,x} \tag{3.1.5}$$

$$\mathrm{v}_{,t} + (\mathrm{u} + \psi_{,t} + \mathrm{v}\psi_{,y})\mathrm{v}_{,x} + \mathrm{v}\mathrm{v}_{,y} = -v(P_{,y} + \psi_{,y}P_{,x}) \tag{3.1.6}$$

$$P_{,t} + (\mathrm{u} + \psi_{,t} + \mathrm{v}\psi_{,y})P_{,x} + \mathrm{v}P_{,y} + \rho a_f^2(\mathrm{u}_{,x} + \mathrm{v}_{,y} + \psi_{,y}\mathrm{v}_{,x}) = -\frac{G}{v}\sum_{i=1}^{N_Y} e_{,Y_i}\dot{\Omega}_i \tag{3.1.7}$$

$$Y_{i,t} + (\mathrm{u} + \psi_{,t} + \mathrm{v}\psi_{,y})Y_{i,x} + \mathrm{v}Y_{i,y} = \dot{\Omega}_i. \tag{3.1.8}$$

The details of this transformation are discussed in Appendix B.2. The reactive Euler equations in one and two dimensions are summarized for both reference frames in Appendices A.1.1 and A.1.2.

3.2 Linear Stability Equations

In order to examine the linear stability of the steady ZND solution, consider small variations of each variable about the steady values, $(\ )^o$, obtained from the solution of the ZND model (see Section 1.2).

$$\mathrm{u}(x,y,t) = \mathrm{u}^o(x) + \mathrm{u}'(x,y,t) \tag{3.2.1}$$

$$\mathrm{v}(x,y,t) = \mathrm{v}'(x,y,t) \tag{3.2.2}$$

$$P(x,y,t) = P^o(x) + P'(x,y,t) \tag{3.2.3}$$

$$v(x,y,t) = v^o(x) + v'(x,y,t) \tag{3.2.4}$$

$$Y_i(x,y,t) = Y_i^o(x) + Y_i'(x,y,t) \tag{3.2.5}$$

The shock position is assumed to undergo small oscillations about the steady position. In two dimensions, oscillations also occur in the y direction.

$$\psi = \psi^1 \exp(\omega t) \exp(ik_y y) \tag{3.2.6}$$

where ω is the growth rate and k_y is the transverse wave number. We will assume that a regular perturbation expansion exists, the solution vector $\mathbf{z}$ of the perturbation quantities,

$$\mathbf{z} = [v, \mathrm{u}, \mathrm{v}, P, Y_1, Y_2, \ldots, Y_N]^T, \tag{3.2.7}$$

is of the same order as the shock disturbance amplitude ψ^1, and has the form

$$\mathbf{z}' = \mathbf{z}^1(x) \exp(\omega t) \exp(ik_y y). \tag{3.2.8}$$

ψ^1 can be any constant and we choose

$$\psi^1 = \frac{-1}{\omega}. \tag{3.2.9}$$

Substituting this expansion into (3.1.4)–(3.1.8) yields a linear differential eigenvalue equation for $\mathbf{z}$ which can be written (following Short, 1997) as

$$\mathbf{A}^o \mathbf{z}^1_{,x} + (\omega \mathbf{I} + \mathbf{C}^o + ik_y \mathbf{B}^o)\, \mathbf{z}^1 + (\omega \mathbf{I} + ik_y \mathbf{B}^o)\mathbf{b}^o \psi^1 = 0 \tag{3.2.10}$$

where, if we assume the base flow is one dimensional ($\mathrm{v}^o = 0$), $\mathbf{b} = \mathbf{z}_{,x}$ and the matrices are

$$\mathbf{A} = \begin{pmatrix} \mathrm{u} & -v & 0 & 0 & 0 & 0 & \dots \\ 0 & \mathrm{u} & 0 & v & 0 & 0 & \dots \\ 0 & 0 & \mathrm{u} & 0 & 0 & 0 & \dots \\ 0 & \rho a_f^2 & 0 & \mathrm{u} & 0 & 0 & \dots \\ 0 & 0 & 0 & 0 & \mathrm{u} & 0 & \dots \\ 0 & 0 & 0 & 0 & 0 & \mathrm{u} & \dots \\ \dots & & & & & & \end{pmatrix} \qquad \mathbf{B} = \begin{pmatrix} 0 & 0 & -v & 0 & 0 & 0 & \dots \\ 0 & 0 & 0 & 0 & 0 & 0 & \dots \\ 0 & 0 & 0 & v & 0 & 0 & \dots \\ 0 & 0 & \rho a_f^2 & 0 & 0 & 0 & \dots \\ 0 & 0 & 0 & 0 & 0 & 0 & \dots \\ 0 & 0 & 0 & 0 & 0 & 0 & \dots \\ \dots & & & & & & \end{pmatrix} \tag{3.2.11}$$

and

$$\mathbf{C} = \begin{pmatrix} -\mathrm{u}_{,x} & v_{,x} & 0 & 0 & 0 & 0 & \dots \\ P_{,x} & \mathrm{u}_{,x} & 0 & 0 & 0 & 0 & \dots \\ 0 & 0 & 0 & 0 & 0 & 0 & \dots \\ (\rho a_f^2)_{,v}\mathrm{u}_{,x} - Z_{,v} & P_{,x} & 0 & (\rho a_f^2)_{,P}\mathrm{u}_{,x} - Z_{,P} & (\rho a_f^2)_{,Y_1}\mathrm{u}_{,x} - Z_{,Y_1} & (\rho a_f^2)_{,Y_2}\mathrm{u}_{,x} - Z_{,Y_2} & \dots \\ -\dot{\Omega}_{1,v} & Y_{1,x} & 0 & -\dot{\Omega}_{1,P} & -\dot{\Omega}_{1,Y_1} & -\dot{\Omega}_{2,Y_1} & \dots \\ -\dot{\Omega}_{2,v} & Y_{2,x} & 0 & -\dot{\Omega}_{2,P} & -\dot{\Omega}_{1,Y_2} & -\dot{\Omega}_{2,Y_2} & \dots \\ \dots & & & & & & \end{pmatrix}. \tag{3.2.12}$$

Here we have used a pseudo-thermodynamic function defined as

$$Z(P, v, \mathbf{Y}) = -\frac{G}{v}\sum_{i=1}^{N_Y} e_{,Y_i}\dot{\Omega}_i. \tag{3.2.13}$$

Because the inverse of $\mathbf{A}$ will be necessary in the code, it is presented here

$$\mathbf{A}^{-1} = \begin{pmatrix} \frac{1}{\mathrm{u}} & \frac{v}{\mathrm{u}^2 - a_f^2} & 0 & -\frac{v^2}{\mathrm{u}(\mathrm{u}^2 - a_f^2)} & 0 & 0 & \dots \\ 0 & \frac{\mathrm{u}}{\mathrm{u}^2 - a_f^2} & 0 & -\frac{v}{\mathrm{u}^2 - a_f^2} & 0 & 0 & \dots \\ 0 & 0 & \frac{1}{\mathrm{u}} & 0 & 0 & 0 & \dots \\ 0 & -\frac{\rho a_f^2}{\mathrm{u}^2 - a_f^2} & 0 & \frac{\mathrm{u}}{\mathrm{u}^2 - a_f^2} & 0 & 0 & \dots \\ 0 & 0 & 0 & 0 & \frac{1}{\mathrm{u}} & 0 & \dots \\ 0 & 0 & 0 & 0 & 0 & \frac{1}{\mathrm{u}} & \dots \\ \dots & & & & & & \end{pmatrix}. \tag{3.2.14}$$

To clarify for future discussions, (3.2.10) is a differential eigenvalue problem where ω is the eigenvalue. The necessary right boundary condition discussed in Section 3.4 requires the solution of an algebraic eigenvalue problem with eigenvalue c. These two problems are related but distinct.

If $k_y = 0$, the above equations reduce to one dimension. These expressions have been compared with Lee and Stewart (1990) and Short (1997) (see Appendix E.1 and E.2). In addition, a discussion of how the energy equation was linearized is presented in Appendix B.4.

The equations described above are solved in a finite domain. Conditions at the left and right boundaries of this domain are required to adequately specify the problem. The left boundary is immediately to the right of the flattened shock, $x = 0$ (see Figure 3.1b). At this boundary, the independent variables must satisfy the shock jump conditions in the flat-shock-fixed frame. Expressions for the independent variables at this boundary are presented in Section 3.3.

The right boundary is imposed far from the reaction zone at x_R. In true reactive systems, the composition does not come to equilibrium until infinitely far from the reaction zone. Unfortunately, a finite boundary must be imposed for computational purposes. This artificially imposed boundary can reflect a portion of the solution into the domain

of interest. We have devised a *radiation condition* presented briefly in Section 3.4 to assure that our right boundary is nonreflective. The radiation condition is discussed in detail in Chapter 4.

3.3 Left Boundary: Jump Conditions

We start with the frozen shock jump conditions (1.2.17)–(1.2.19). Now we perturb the shock velocity ($\mathrm{D} \to \mathrm{U} + \psi_{,t}$) and, as a consequence, the post-shock quantities. Recall that these jump conditions are in an instantaneous shock-fixed frame which is an intermediate frame that fixes the shock location at $x = 0$, but focuses on one moment in time. To determine the jump conditions in the flat-shock-fixed reference frame, we must first transform u^L, the velocity in the laboratory frame, to w, the velocity in the instantaneous shock-fixed frame, and then again to u, the velocity in the flat-shock-fixed frame discussed in Section 3.1. Thermodynamic quantities remain independent of the frame of reference as discussed in Section 3.1. We perturb (1.2.17)–(1.2.19), incorporate some thermodynamic identities (see Appendices C and B.5) and solve for $\rho^1(0^+)$, $P^1(0^+)$, and $\mathrm{w}^1(0^+)$ defined by (3.2.7) and (3.2.8).

$$\rho^1(0^+) = \rho_1 \omega \psi^1 \left(\frac{\frac{\rho_2}{\rho_1} G\mathrm{U} - 2\mathrm{U}[G+1] + \mathrm{w}_2[G+2]}{(a_f^2)_2 (M_2^2 - 1)} \right) \tag{3.3.1}$$

$$v^1(0^+) = -v_2^2 \rho^{1L} \to v^{1L} = -\frac{v_2^2}{v_1} \omega \psi^1 \left(\frac{\frac{v_1}{v_2} G\mathrm{U} - 2\mathrm{U}[G+1] + \mathrm{w}_2[G+2]}{(a_f^2)_2 (M_2^2 - 1)} \right) \tag{3.3.2}$$

$$P^1(0^+) = \frac{\omega \psi^1}{v_1} \left[2(\mathrm{U} - \mathrm{w}_2) + \mathrm{w}_2^2 \left(\frac{\frac{v_1}{v_2} G\mathrm{U} - 2\mathrm{U}[G+1] + \mathrm{w}_2[G+2]}{(a_f^2)_2 (M_2^2 - 1)} \right) \right] \tag{3.3.3}$$

$$\mathrm{w}^1(0^+) = \frac{v_2}{v_1} \omega \psi^1 \left[1 - \mathrm{w}_2 \left(\frac{\frac{v_1}{v_2} G\mathrm{U} - 2\mathrm{U}[G+1] + \mathrm{w}_2[G+2]}{(a_f^2)_2 (M_2^2 - 1)} \right) \right] \tag{3.3.4}$$

These expressions are in the instantaneous shock-fixed frame. To find the velocity in the flat-shock-fixed frame of reference we transform with the following transformation (see Appendix B.5):

$$\mathrm{u}' = -\mathrm{u}'^{L} = \mathrm{w}' - \psi_{,t}. \tag{3.3.5}$$

The expression for the velocity in the flat-shock-fixed frame is

$$\mathrm{u}^1(0^+) = -\omega\psi^1 \left[1 - \frac{v_2}{v_1}\left(1 - \mathrm{u}_2\left(\frac{\frac{v_1}{v_2}G\mathrm{U} - 2\mathrm{U}[G+1] + \mathrm{w}_2[G+2]}{(a_f^2)_2(M_2^2-1)}\right)\right)\right]. \tag{3.3.6}$$

In two dimensions, we can decompose w into u and v using the geometry depicted in Fig. 3.2.

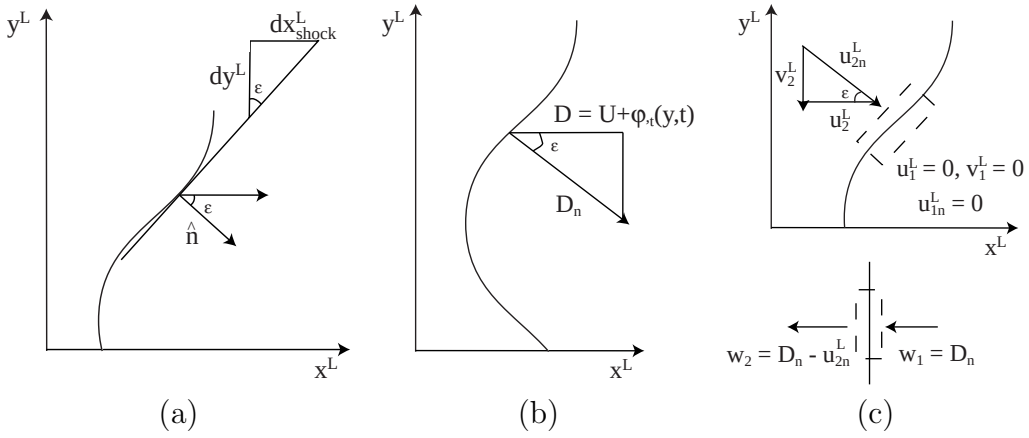

Figure 3.2: Perturbed shock front in the laboratory frame.

$$\mathrm{u}_2 = \mathrm{w}_2 \quad \mathrm{u}' = \mathrm{w}' - \psi_{,t} \tag{3.3.7}$$

$$\mathrm{v}_2 = 0 \quad \mathrm{v}' = -(\mathrm{U} - \mathrm{w}_2)\psi_{,y}. \tag{3.3.8}$$

A detailed derivation is given in Appendix B.6.

3.4 Right Boundary: Radiation Condition

Far downstream the system is almost in equilibrium. We want the radiation condition to be such that no acoustic waves travel toward the shock, i.e., that all of the waves travel out of the domain. In order to determine the criteria for this, assume that we are very far downstream (x_R) and close to the constant equilibrium state. Now, we perturb (3.1.4)–(3.1.8) about the near-equilibrium state ($\mathbf{z} = \mathbf{z}|_{x_R} + \mathbf{z}'$) with the same method discussed in Section 3.2.

In two dimensions,

$$\left(\mathbf{z}'_{,t} + \mathbf{A}\mathbf{z}'_{,x} + \mathbf{B}\mathbf{z}'_{,y} + \mathbf{C}\mathbf{z}'\right)_{x_R} = 0. \tag{3.4.1}$$

$\mathbf{A}$ is given by (3.2.11), and assuming that the base flow is one dimensional, $\mathbf{B}$ can be expressed by (3.2.11). In the near-equilibrium limit, $\mathbf{C}$ becomes

$$\mathbf{C}|_{x_R} = \begin{pmatrix} 0 & 0 & 0 & 0 & 0 & 0 & \dots \\ 0 & 0 & 0 & 0 & 0 & 0 & \dots \\ 0 & 0 & 0 & 0 & 0 & 0 & \dots \\ -Z_{,v}]|_{x_R} & 0 & 0 & -Z_{,P}|_{x_R} & -Z_{,Y_1}|_{x_R} & -Z_{,Y_2}|_{x_R} & \dots \\ -\dot{\Omega}_{1,v}\Big|_{x_R} & 0 & 0 & -\dot{\Omega}_{1,P}\Big|_{x_R} & -\dot{\Omega}_{1,Y_1}\Big|_{x_R} & -\dot{\Omega}_{1,Y_2}\Big|_{x_R} & \dots \\ -\dot{\Omega}_{2,v}\Big|_{x_R} & 0 & 0 & -\dot{\Omega}_{2,P}\Big|_{x_R} & -\dot{\Omega}_{2,Y_1}\Big|_{x_R} & -\dot{\Omega}_{2,Y_2}\Big|_{x_R} & \dots \\ \dots & & & & & & \end{pmatrix}. \tag{3.4.2}$$

Equation 3.4.1 is linear, and therefore, we can express the solution as a linear superposition

$$\mathbf{z}' = \sum_k a_k \mathbf{n}_k. \tag{3.4.3}$$

In order to solve (3.4.1), we make two assumptions. First, we assume the functional form of $\mathbf{z}'$ is the same in the tail as it is in the main reaction zone.

$$\mathbf{z}'|_{x_R} = \mathbf{z}^1(x_R) \exp\left(\omega t + i k_y y\right) \tag{3.4.4}$$

Now (3.4.1) simplifies to

$$\mathbf{z}^1_{,x}\big|_{x_R} + \left[\mathbf{A}^{-1}(\omega\mathbf{I} + ik_y\mathbf{B} + \mathbf{C})\right]_{x_R} \mathbf{z}^1\big|_{x_R} = 0. \tag{3.4.5}$$

Second we assume that $\mathbf{N}|_{x_R}$,

$$\mathbf{N}|_{x_R} = \left[\mathbf{A}^{-1}(\omega\mathbf{I} + ik_y\mathbf{B} + \mathbf{C})\right]_{x_R}, \tag{3.4.6}$$

is non-singular such that there are $4 + N_Y$ independent solutions to (3.4.1). In the case of a frozen outflow condition with positive u, $\mathbf{N}$ is non-singular (Rowley and Colonius, 2000). If there are $4+N_Y$ independent solutions, then there exists an algebraic eigenvalue equation which will allow us to diagonalize the operator and decouple the equations.

$$\left(\mathbf{L}\mathbf{z}^1\right)_{,x}\Big|_{x_R} + \left(\mathbf{L}\mathbf{N}\mathbf{z}^1\right)_{x_R} = \left(\mathbf{L}\mathbf{z}^1\right)_{,x}\Big|_{x_R} + \mathbf{\Lambda}_{\mathbf{N}|_{x_R}} \left(\mathbf{L}\mathbf{z}'\right)_{x_R} = 0 \tag{3.4.7}$$

In the decoupled system, $\left(\mathbf{L}\mathbf{z}^1\right)_{x_R}$ is the vector of eigenvariables, and if $\left(\mathbf{L}\mathbf{z}^1\right)_{x_R} = \mathbf{g}$, (3.4.7) becomes

$$g_{k,x} + \lambda_{k\mathbf{N}|_{x_R}} g_k = 0. \tag{3.4.8}$$

The solution to each one-dimensional ordinary differential equation is

$$g_k(x) = \exp\left(-\lambda_{k\mathbf{N}|_{x_R}} x\right). \tag{3.4.9}$$

Finally, we transform back to $\mathbf{z}^1$.

$$\mathbf{z}^1\big|_{x_R} = \mathbf{L}^{-1}\big|_{x_R} \exp\left(-\mathbf{\Lambda}_{\mathbf{N}|_{x_R}} x\right) \tag{3.4.10}$$

The algebraic eigenvalue equation that allowed us to diagonalize (3.4.1) is in terms

of the left eigenvectors

$$\left(\mathbf{m}_k^T \mathbf{N}\right)_{x_R} = \lambda_{k\mathbf{N}|_{x_R}} \, \mathbf{m}_k^T\big|_{x_R} \tag{3.4.11}$$

where $\mathbf{m}_k|_{x_R}$ is a left eigenvector of $\mathbf{N}|_{x_R}$ and $\lambda_{k\mathbf{N}|_{x_R}}$ is an eigenvalue of $\mathbf{N}|_{x_R}$. We can also create a matrix of left eigenvectors of $\mathbf{N}|_{x_R}$, $\mathbf{L}|_{x_R}$, and a matrix of eigenvalues of $\mathbf{N}|_{x_R}$, $\mathbf{\Lambda}_{\mathbf{N}|_{x_R}}$, and re-express the algebraic eigenvalue equation as

$$(\mathbf{LN})_{x_R} = \mathbf{\Lambda}_{\mathbf{N}|_{x_R}} \mathbf{L}|_{x_R}. \tag{3.4.12}$$

Although $\mathbf{N}|_{x_R}$ is not real or symmetric, the right ($\{\mathbf{n}\}_{x_R}$) and left ($\{\mathbf{m}\}|_{x_R}$) eigenvectors are orthogonal with respect to each other, i.e.,

$$\left(\mathbf{m}_k^T \mathbf{n}_j\right)_{x_R} = 0 \quad (\text{if } k \neq j). \tag{3.4.13}$$

This also indicates that the product of the matrices of left and right eigenvectors is diagonal. Because $\mathbf{N}$ is non-singular and there are $4 + N_Y$ distinct eigenvectors, the eigenvectors for a complete basis for the space, and we can express $\mathbf{z}^1$ as a superposition of right eigenvectors.

$$\mathbf{z}^1\big|_{x_R} = \sum_k a_k \, \mathbf{n}_k|_{x_R} \exp\left(-\lambda_{k\mathbf{N}|_{x_R}} x\right) \tag{3.4.14}$$

Finally, we recognize that $\exp\left(-\Lambda_{\mathbf{N}|_{x_R}} x\right) \neq 0$, and we can express $\mathbf{z}'|_{x_R}$ as

$$\mathbf{z}'|_{x_R} = \sum_k \hat{z}_k|_{x_R} \exp\left(\omega t + i k_y y - \lambda_{k\mathbf{N}|_{x_R}} x\right) \tag{3.4.15}$$

where

$$\hat{\mathbf{z}}|_{x_R} = \sum_k a_k \, \mathbf{n}_k|_{x_R}. \tag{3.4.16}$$

The radiation condition requires that the projection of the solution along any incoming eigenvectors must be zero. We will show in Chapter 4 that for all chemical models we have investigated, there is only one eigenvalue with a negative real component. Mathematically the radiation condition requires that

$$a_j = 0, \quad \mathcal{R}e(\lambda_{j\mathbf{N}|_{x_R}}) < 0. \tag{3.4.17}$$

This is equivalent to requiring that the projection $\mathbf{z}^1$ onto its incoming left eigenvector be zero.

$$\left(\mathbf{m}_j^T \hat{\mathbf{z}}\right)_{x_R} = 0 \quad \mathcal{R}e(\lambda_{j\mathbf{N}|_{x_R}}) < 0 \tag{3.4.18}$$

Using the orthogonality of the left and right eigenvectors, the left-hand side of (3.4.14) becomes

$$\sum_k a_k \left(\mathbf{m}_j^T \mathbf{n}_k\right)_{x_R} = a_j (\mathbf{m}_j^T \mathbf{n}_j)_{x_R}. \tag{3.4.19}$$

For this to be zero, a_j must be zero.

It is important to clarify again that the linear stability problem involves two eigenvalue equations: (3.2.10) and (3.4.11). We will show in Chapter 4, that the eigenvalues of the second equation ($\{\lambda_{\mathbf{N}|_{x_R}}\}$), discussed above, are analogous to the characteristic speeds of the solution vector at the right boundary. The eigenvalue of the first equation (ω) is the desired growth rate of the instability. The radiation condition (3.4.18) is also the eigenvalue selection criterion required to determine ω with a shooting algorithm, i.e.,

$$\mathcal{H}(\omega) = \left(\mathbf{m}_j^T \hat{\mathbf{z}}\right)_{x_R} = 0 \quad (\mathcal{R}e(\lambda_{j\mathbf{N}|_{x_R}}) < 0). \tag{3.4.20}$$

The shooting method is described in Section 3.5.

3.5 Shooting Algorithm

We use a shooting method to solve (3.2.10). This is accomplished by first specifying a value of k_y and guessing a value of ω, then using (3.3.2), (3.3.3), and (3.3.6) as initial conditions, integrating through the domain, and finally evaluating an eigenvalue (ω) selection criterion $\mathcal{H}(\omega)$ at the right boundary. If the value of $\mathcal{H}(\omega)$ is not sufficiently close to zero, we use a root-finding iterative scheme to determine a new guess for ω, re-evaluate (3.3.2), (3.3.3), and (3.3.6), and integrate through the domain again. This process is repeated until $\mathcal{H}(\omega)$ is sufficiently close to zero.

The eigenvalue selection criterion must be evaluated sufficiently far from the main reaction zone to assure that the composition is near equilibrium. On the other hand, an unstable mode grows exponentially with distance and, far from the main reaction zone, will approach infinity. We found that if we evaluated the eigenvalue selection criterion too far from the main reaction zone, we were not able to satisfy the criterion within the desired tolerance due to the exponential growth. A reasonable distance for evaluating the eigenvalue selection criterion is ten reaction zone lengths from the main reaction zone. This distance is a parameter in the input file and in further investigations can be adjusted.

There are some limitations of the shooting method. As the mode number or frequency of oscillation increases, it becomes more difficult to obtain the same tolerance on $\mathcal{H}(\omega)$. In some of the cases discussed in Chapters 5, 6, and 7, $\mathcal{H}(\omega)$ may not have met our tolerance, but the difference in ω from one iteration to the next, i.e.,

$$\omega_{i+1} - \omega_i, \tag{3.5.1}$$

was on the order of machine precision.

We use the stiff integration option of the CVODE integration library (Cohen and Hindmarsh, 1996) which uses a variable step size. We also normalize the pressure and velocity values by their post-shock value so that all of the quantities passed to the solver are of the same order.

The appropriate complex eigenvalue selection criterion $\mathcal{H}(\omega) = \mathcal{H}_\mathcal{R} + i\mathcal{H}_\mathcal{I}$ (3.4.20) was presented in Section 3.4, and two root-finding iterative schemes are discussed in this section. The first is a traditional two-variable Newton-Raphson scheme (Section 3.5.1) and the second is Muller's method (Section 3.5.2) which is particularly useful for complex numbers.

3.5.1 Newton-Raphson Iteration Scheme

For the Newton-Raphson scheme, two guesses, ω_a and ω_b form a rectangular domain that initializes the search. This is depicted in Figure 3.3. The solution occurs when both $\mathcal{H}_\mathcal{R}$

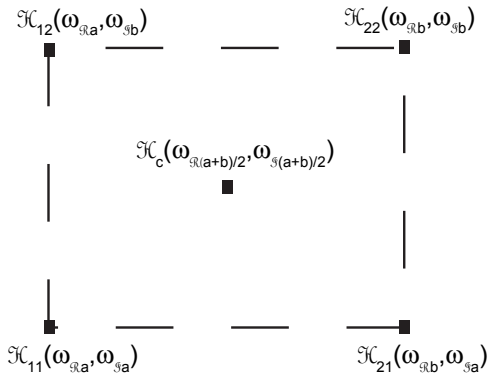

Figure 3.3: Cartoon of the initial domain created for the Newton-Raphson solver by the initial guesses for the growth rate.

and $\mathcal{H}_\mathcal{I}$ are identically zero. We can construct a matrix equation that gives $\mathcal{H}_\mathcal{R}$ and $\mathcal{H}_\mathcal{I}$ as functions of $\omega_\mathcal{R}$ and $\omega_\mathcal{I}$.

$$\begin{pmatrix} \delta\mathcal{H}_\mathcal{R} \\ \delta\mathcal{H}_\mathcal{I} \end{pmatrix} = \begin{pmatrix} \dfrac{\partial\mathcal{H}_\mathcal{R}}{\partial\omega_\mathcal{R}} & \dfrac{\partial\mathcal{H}_\mathcal{R}}{\partial\omega_\mathcal{I}} \\ \dfrac{\partial\mathcal{H}_\mathcal{I}}{\partial\omega_\mathcal{R}} & \dfrac{\partial\mathcal{H}_\mathcal{I}}{\partial\omega_\mathcal{I}} \end{pmatrix} \begin{pmatrix} \delta\omega_\mathcal{R} \\ \delta\omega_\mathcal{I} \end{pmatrix} \tag{3.5.2}$$

The idea is to use this equation to determine corrections, $\delta\omega_{\mathcal{R}}$ and $\delta\omega_{\mathcal{I}}$, that cause $\mathcal{H}_{\mathcal{R}}$ and $\mathcal{H}_{\mathcal{I}}$ to be made as close to zero as desired. To accomplish this, we must invert the Jacobian and solve for $\delta\omega_{\mathcal{R}}$ and $\delta\omega_{\mathcal{I}}$ given $\mathcal{H}_{\mathcal{R}}$ and $\mathcal{H}_{\mathcal{I}}$.

$$\mathbf{J} = \begin{pmatrix} \frac{\partial \mathcal{H}_{\mathcal{R}}}{\partial \omega_{\mathcal{R}}} & \frac{\partial \mathcal{H}_{\mathcal{R}}}{\partial \omega_{\mathcal{I}}} \\ \frac{\partial \mathcal{H}_{\mathcal{I}}}{\partial \omega_{\mathcal{R}}} & \frac{\partial \mathcal{H}_{\mathcal{I}}}{\partial \omega_{\mathcal{I}}} \end{pmatrix} \tag{3.5.3}$$

$$\begin{pmatrix} \delta\omega_{\mathcal{R}} \\ \delta\omega_{\mathcal{I}} \end{pmatrix} = \mathbf{J}^{-1} \begin{pmatrix} \delta\mathcal{H}_{\mathcal{R}} \\ \delta\mathcal{H}_{\mathcal{I}} \end{pmatrix} \tag{3.5.4}$$

Numerically, these derivatives are

$$\frac{\partial \mathcal{H}_{\mathcal{R}}}{\partial \omega_{\mathcal{R}}} = \frac{1}{\omega_{\mathcal{R}b} - \omega_{\mathcal{R}a}} \left[\frac{(\mathcal{H}_{\mathcal{R}21} - \mathcal{H}_{\mathcal{R}11}) + (\mathcal{H}_{\mathcal{R}22} - \mathcal{H}_{\mathcal{R}12})}{2} \right] \tag{3.5.5}$$

$$\frac{\partial \mathcal{H}_{\mathcal{R}}}{\partial \omega_{\mathcal{I}}} = \frac{1}{\omega_{\mathcal{I}b} - \omega_{\mathcal{I}a}} \left[\frac{(\mathcal{H}_{\mathcal{R}12} - \mathcal{H}_{\mathcal{R}11}) + (\mathcal{H}_{\mathcal{R}22} - \mathcal{H}_{\mathcal{R}21})}{2} \right] \tag{3.5.6}$$

$$\frac{\partial \mathcal{H}_{\mathcal{I}}}{\partial \omega_{\mathcal{R}}} = \frac{1}{\omega_{\mathcal{R}b} - \omega_{\mathcal{R}a}} \left[\frac{(\mathcal{H}_{\mathcal{I}21} - \mathcal{H}_{\mathcal{I}11}) + (\mathcal{H}_{\mathcal{I}22} - \mathcal{H}_{\mathcal{I}12})}{2} \right] \tag{3.5.7}$$

$$\frac{\partial \mathcal{H}_{\mathcal{I}}}{\partial \omega_{\mathcal{I}}} = \frac{1}{\omega_{\mathcal{I}b} - \omega_{\mathcal{I}a}} \left[\frac{(\mathcal{H}_{\mathcal{I}12} - \mathcal{I}_{\mathcal{R}11}) + (\mathcal{H}_{\mathcal{I}22} - \mathcal{I}_{\mathcal{R}21})}{2} \right] \tag{3.5.8}$$

and

$$\delta\mathcal{H}_{\mathcal{R}} = -\mathcal{H}_{\mathcal{R}c} \tag{3.5.9}$$

$$\delta\mathcal{H}_{\mathcal{I}} = -\mathcal{H}_{\mathcal{I}c}. \tag{3.5.10}$$

3.5.2 Muller's Method

This method is outlined in Stoer and Bulirsch (1983). Muller's method employs Newton's interpolation formula, which depends on divided differences. In this case, the necessary quadratic polynomial is

$$\mathcal{H}[\omega_k] + \mathcal{H}[\omega_{k-1}, \omega_k](\omega - \omega_k) + \mathcal{H}[\omega_{k-2}, \omega_{k-1}, \omega_k](\omega - \omega_{k-1})(\omega - \omega_k) \tag{3.5.11}$$

where the coefficients are divided differences given by the recursive formulas

$$\mathcal{H}[\omega_{k-1},\omega_k] = \frac{\mathcal{H}[\omega_k] - \mathcal{H}[\omega_{k-1}]}{\omega_k - \omega_{k-1}} \tag{3.5.12}$$

$$\mathcal{H}[\omega_{k-2},\omega_{k-1},\omega_k] = \frac{\mathcal{H}[\omega_{k-1},\omega_k] - \mathcal{H}[\omega_{k-2},\omega_{k-1}]}{\omega_k - \omega_{k-2}}. \tag{3.5.13}$$

Completing the square and solving for ω, the quadratic polynomial becomes

$$a(\omega - \omega_k)^2 + 2b(\omega - \omega_k) + c \tag{3.5.14}$$

where

$$a = \mathcal{H}[\omega_{k-2},\omega_{k-1},\omega_k] \tag{3.5.15}$$

$$b = \frac{1}{2}\left(\mathcal{H}[\omega_{k-1},\omega_k] + \mathcal{H}[\omega_{k-2},\omega_{k-1},\omega_k](\omega_k - \omega_{k-1})\right) \tag{3.5.16}$$

$$c = \mathcal{H}[\omega_k]. \tag{3.5.17}$$

We look for the smallest root of this equation and add this to the current guess to get the next guess. According to Stoer and Bulirsch

> In order to express the smaller root of a quadratic equation in a numerically stable fashion, the reciprocal of the standard solution formula for quadratic equations should be used.

I.e.,

$$\omega_{k+1} = \omega_k - \frac{c_k}{b_k \pm \sqrt{b_k^2 - a_k c_k}}. \tag{3.5.18}$$

We assure that we have chosen the smallest root by choosing the sign of the square-root to maximize the denominator. For the next iteration we only calculate $\mathcal{H}[\omega]$ for the new guess, ω_{k+1}.

3.6 Output

When we write our eigenfunctions to a file, there are several normalization options. We could output physical dimensional quantities, normalize by the pre-shock state, or normalize by the post-shock state. Lee and Stewart (1990) normalize by the post-shock state, and Ng and Lee (2003) normalize by the pre-shock state.

In our implementation, we have provided the option to normalize by either the post shock state, i.e., at the left boundary

$$\tilde{P} = \tilde{v} = 1 \tag{3.6.1}$$

$$\tilde{u} = u/a_{f2}. \tag{3.6.2}$$

or by the pre-shock state, i.e., at the left boundary

$$\tilde{P} = P/P_1 \tag{3.6.3}$$

$$\tilde{v} = v/v_1 \tag{3.6.4}$$

$$\tilde{u} = u/a_{f1}. \tag{3.6.5}$$

The results we present in Chapters 5 and 6 are normalized by the post-shock state.

Chapter 4

Radiation Condition

Chemical equilibrium is achieved infinitely far from the main reaction zone, but in order to numerically integrate, we must impose a finite domain. Unfortunately, this finite domain introduces an artificial downstream boundary in the near-equilibrium region. We must assure that no components of the solution reflect off this artificial boundary. For this reason, the necessary condition at the right boundary (x_R) is a radiation condition which was briefly discussed in Section 3.4.

The methodology for determining (3.4.20) presented in Section 3.4 was given very generally. In order to determine the exact form of (3.4.20), as we did for the base flow (Chapter 2), we must specify a chemical mechanism. In this chapter, we will present, in detail, the radiation condition first for a nonreactive system, and then for the one-step irreversible and one-step reversible chemical models defined in Sections 2.1 and 2.2. Finally we will describe the traditional formulation of the radiation condition (Lee and Stewart, 1990) and show that it gives the same $\mathcal{H}(\omega)$ as our method does.

Far from the main reaction zone is an acoustic region defined by a constant base flow and small perturbations. In this region, $\mathbf{C}$, defined by (3.2.12), simplifies greatly. The general formulation for the necessary radiation condition discussed in Section 3.4 is:

1. Diagonalize $\mathbf{N}|_{x_R}$, defined by (3.4.6), with the following algebraic eigenvalue problem.

$$\left(\mathbf{m}^T\mathbf{N}\right)_{x_R} = \lambda_{k\mathbf{N}|_{x_R}}\,\mathbf{m}^T\big|_{x_R} \tag{4.1}$$

2. Determine the eigenvalue that satisfies the following criterion.

$$\mathcal{R}e(\lambda_{j\mathbf{N}|_{x_R}}) < 0 \tag{4.2}$$

3. Find the left eigenvector that corresponds to the eigenvalue determined by the above criterion.

4. Since the left ($\{\mathbf{m}\}_{x_R}$) and right ($\{\mathbf{n}\}_{x_R}$) eigenvectors both form a complete basis for the space, we can isolate the incoming component of the solution by pre-multiplying by the transpose of the left eigenvector determined in the previous step. Assuring that this component is zero is the mathematical statement of the radiation condition, i.e.,

$$\left(\mathbf{m}_j^T \hat{\mathbf{z}}\right)_{x_R} = 0, \quad \mathcal{R}e(\lambda_{j\mathbf{N}|_{x_R}}) < 0. \tag{4.3}$$

4.1 Frozen Acoustics

For a nonreactive or frozen system, $\mathbf{C} = 0$, and $\mathbf{N}|_{x_R}$ for a one-dimensional system ($k_y = 0$) is

$$\mathbf{N}|_{x_R} = \left[\begin{array}{ccc} \dfrac{\omega}{\mathrm{u}} & -\dfrac{v\omega}{a_f^2 - \mathrm{u}^2} & \dfrac{v^2\omega}{\mathrm{u}(a_f^2 - u^2)} \\ 0 & -\dfrac{\mathrm{u}\omega}{a_f^2 - \mathrm{u}^2} & \dfrac{v\omega}{a_f^2 - \mathrm{u}^2} \\ 0 & \dfrac{a_f^2\omega}{v(a_f^2 - \mathrm{u}^2)} & -\dfrac{\mathrm{u}\omega}{a_f^2 - \mathrm{u}^2} \end{array}\right]_{x_R}. \tag{4.1.1}$$

The first step outlined above is to find the eigenvalues $\{\lambda\}_{\mathbf{N}|_{x_R}}$ of $\mathbf{N}|_{x_R}$. The equation required is

$$0 = \left[\left(\frac{\omega}{\mathrm{u}} - \lambda_{k\mathbf{N}}\right)\left((\mathrm{u}^2 - a_f^2)\lambda_{k\mathbf{N}}^2 - 2\mathrm{u}\omega\lambda_{k\mathbf{N}} + \omega^2\right)\right]_{x_R}. \tag{4.1.2}$$

The nonreactive Euler equations are strictly hyperbolic because the eigenvalues and eigenvectors of $\mathbf{N}|_{x_R}$ are strictly real. Therefore, we can solve the nonreactive Euler equations with the method of characteristics. As we will see in the next two sections, the reactive Euler equations, even with the simplest chemical model, are not strictly hyperbolic. Solving a hyperbolic system of partial differential equations with the method of characteristics provides a physical interpretation of the solution. In the nonreactive case, if we define a new variable $c_{k\mathbf{N}|_{x_R}} = \omega/\lambda_{k\mathbf{N}|_{x_R}}$, (4.1.2) becomes

$$0 = \left[(c_{k\mathbf{N}} - \mathrm{u})(c_{k\mathbf{N}} - (\mathrm{u} + a_f))(c_{k\mathbf{N}} - (\mathrm{u} - a_f))\right]_{x_R}. \tag{4.1.3}$$

The roots of (4.1.3) are identical to the characteristic speeds determined by the traditional method of characteristics

$$\{c\}_{\mathbf{N}|_{x_R}} = \{\mathrm{u},\ \mathrm{u} + a_f,\ \mathrm{u} - a_f\}_{x_R}. \tag{4.1.4}$$

This indicates that in nonreactive systems, our method is analogous to the method of characteristics. In the next two sections when we consider the radiation condition for reactive systems, we will determine complex speeds analogous to the real characteristic speeds by solving for $c_{k\mathbf{N}|_{x_R}} = \omega/\lambda_{k\mathbf{N}|_{x_R}}$ instead of $\lambda_{k\mathbf{N}|_{x_R}}$.

The second step in our algorithm is to find the eigenvalue with a negative real part. In this case, all the eigenvalues are real and only one has a negative value

$$\lambda_{k\mathbf{N}|_{x_R}} = \frac{\omega}{\mathrm{u}|_{x_R} - a_f|_{x_R}} \quad \text{or} \quad c_{k\mathbf{N}|_{x_R}} = \mathrm{u}|_{x_R} - a_f|_{x_R}. \tag{4.1.5}$$

The third step is to find the eigenvector corresponding to this eigenvalue. In the nonreactive case, the three real left eigenvectors are

$$\mathbf{m}_1 = \begin{pmatrix} 0 \\ -\dfrac{a_f}{2v} \\ \dfrac{1}{2} \end{pmatrix}_{x_R} \qquad \mathbf{m}_2 = \begin{pmatrix} 1 \\ 0 \\ \dfrac{v^2}{a_f^2} \end{pmatrix}_{x_R} \qquad \mathbf{m}_3 = \begin{pmatrix} 0 \\ \dfrac{a_f}{2v} \\ \dfrac{1}{2} \end{pmatrix}_{x_R} \tag{4.1.6}$$

and the one corresponding to $c_{k\mathbf{N}|_{x_R}} = \mathrm{u}|_{x_R} - a_f|_{x_R}$ is $\mathbf{m}_1$.

The final step is to assure that the component of the solution along $\mathbf{m}_1$ is zero.

$$\left(\mathbf{m}_1^T \hat{\mathbf{z}}\right)_{x_R} = 0 \tag{4.1.7}$$

In the nonreactive case, this reduces to the acoustic condition.

$$\left(\frac{a_f}{v}\right)_{x_R} \hat{\mathrm{u}} = \hat{P} \tag{4.1.8}$$

4.2 One-Step Irreversible Chemistry

Now we apply the same algorithm (Section 4.1) to the one-step irreversible chemistry model in two dimensions ($k_y \neq 0$). This model was described in detail in Section 2.1. Far from the main reaction zone, the reaction rate approaches zero as the mass fraction

of product species approaches one. In this case, $\mathbf{C}$ simplifies to

$$\mathbf{C}|_{x_R} = \begin{pmatrix} 0 & 0 & 0 & 0 & 0 & 0 \\ 0 & 0 & 0 & 0 & 0 & 0 \\ 0 & 0 & 0 & 0 & 0 & 0 \\ 0 & 0 & 0 & 0 & -Z_{,Y_{\mathcal{A}}} & -Z_{,Y_{\mathcal{B}}} \\ 0 & 0 & 0 & 0 & -\dot{\Omega}_{\mathcal{A},Y_{\mathcal{A}}} & -\dot{\Omega}_{\mathcal{B},Y_{\mathcal{A}}} \\ 0 & 0 & 0 & 0 & -\dot{\Omega}_{\mathcal{A},Y_{\mathcal{B}}} & -\dot{\Omega}_{\mathcal{B},Y_{\mathcal{B}}} \end{pmatrix}_{x_R} . \tag{4.2.1}$$

Here $Z(v, P, \mathbf{Y})$ is defined by (3.2.13). With this expression of $\mathbf{C}|_{x_R}$, $\mathbf{N}|_{x_R}$ is

$$\mathbf{N}|_{x_R} = \begin{bmatrix} \frac{1}{\mathrm{u}} & -\frac{v}{a_f^2 - \mathrm{u}^2} & \frac{ik_y \mathrm{u} v}{\omega(a_f^2 - \mathrm{u}^2)} & \frac{v^2}{\mathrm{u}(a_f^2 - u^2)} & -\frac{v^2 Z_{,Y_{\mathcal{A}}}}{\mathrm{u}\omega(a_f^2 - \mathrm{u}^2)} & -\frac{v^2 Z_{,Y_{\mathcal{B}}}}{\mathrm{u}\omega(a_f^2 - \mathrm{u}^2)} \\ 0 & -\frac{\mathrm{u}}{a_f^2 - \mathrm{u}^2} & \frac{ia_f^2 k_y}{\omega(a_f^2 - \mathrm{u}^2)} & \frac{v}{a_f^2 - \mathrm{u}^2} & -\frac{vZ_{,Y_{\mathcal{A}}}}{\omega(a_f^2 - \mathrm{u}^2)} & -\frac{vZ_{,Y_{\mathcal{B}}}}{\omega(a_f^2 - \mathrm{u}^2)} \\ 0 & 0 & \frac{1}{\mathrm{u}} & \frac{ik_y v}{\mathrm{u}\omega} & 0 & 0 \\ 0 & \frac{a_f^2}{v(a_f^2 - \mathrm{u}^2)} & -\frac{ia_f^2 k_y \mathrm{u}}{v\omega(a_f^2 - \mathrm{u}^2)} & -\frac{\mathrm{u}}{a_f^2 - \mathrm{u}^2} & \frac{\mathrm{u}Z_{,Y_{\mathcal{A}}}}{\omega(a_f^2 - \mathrm{u}^2)} & \frac{\mathrm{u}Z_{,Y_{\mathcal{B}}}}{\omega(a_f^2 - \mathrm{u}^2)} \\ 0 & 0 & 0 & 0 & \frac{\omega - \dot{\Omega}_{\mathcal{A},Y_{\mathcal{A}}}}{\mathrm{u}\omega} & -\frac{\dot{\Omega}_{\mathcal{A},Y_{\mathcal{B}}}}{\mathrm{u}\omega} \\ 0 & 0 & 0 & 0 & -\frac{\Omega_{\mathcal{B},Y_{\mathcal{A}}}}{\mathrm{u}\omega} & \frac{\omega - \Omega_{\mathcal{B},Y_{\mathcal{B}}}}{\mathrm{u}\omega} \end{bmatrix}_{x_R} . \tag{4.2.2}$$

In order to obtain a useful eigenvalue selection criterion (3.4.20), we must find expressions for the derivatives of the net production rates $\dot{\Omega}_i$ and $Z(v, P, \mathbf{Y})$ for the one-step irreversible model. As discussed in Section 2.1,

$$\dot{\Omega}_{\mathcal{A}} = -k_f Y_{\mathcal{A}} \tag{4.2.3}$$

$$\dot{\Omega}_{\mathcal{B}} = k_f Y_{\mathcal{A}} \tag{4.2.4}$$

where

$$k_f = A \exp\left(-\frac{E_a}{RT}\right) \tag{4.2.5}$$

and

$$Z(v, P, \mathbf{Y}) = -\frac{G}{v}\sum_{i=1}^{N_Y} e_{,Y_i}\dot{\Omega}_i = -\frac{\gamma-1}{v}\dot{\Omega}_{\mathcal{B}}(e_{Y_{\mathcal{B}}} - e_{Y_{\mathcal{A}}}). \tag{4.2.6}$$

Now the required derivatives are

$$\dot{\Omega}_{\mathcal{B},Y_{\mathcal{A}}}\Big|_{x_R} = -\dot{\Omega}_{\mathcal{A},Y_{\mathcal{A}}}\Big|_{x_R} = k_f|_{x_R} \tag{4.2.7}$$

$$\dot{\Omega}_{\mathcal{A},Y_{\mathcal{B}}}\Big|_{x_R} = -\dot{\Omega}_{\mathcal{B},Y_{\mathcal{B}}}\Big|_{x_R} = 0 \tag{4.2.8}$$

$$Z_{,Y_{\mathcal{B}}}|_{x_R} = 0 \quad Z_{,Y_{\mathcal{A}}}|_{x_R} = \left[-\frac{\gamma-1}{v}k_f(e_{Y_{\mathcal{B}}} - e_{Y_{\mathcal{A}}}).\right]_{x_R} \tag{4.2.9}$$

Again, we draw the analogy between the characteristic speeds of a strictly hyperbolic system and this system. Although this system is partially hyperbolic, the eigenvalues are complex indicating that it is also partially elliptic. We will specifically discuss the character of the partial differential equation in the next section. The polynomial necessary to find the complex speeds analogous to the traditional real characteristic speeds is

$$\left(\omega^2(c-\mathrm{u})^3\left[c(k_f+\omega)-\mathrm{u}\omega\right]\left[(c-\mathrm{u})^2 - a_f^2\left(1-\left[\frac{ck_y}{\omega}\right]^2\right)\right]\right)_{x_R} = 0 \tag{4.2.10}$$

giving six complex characteristic wave speeds

$$\{c\}_{\mathbf{N}|_{x_R}} = \left\{\mathrm{u}, \mathrm{u}, \mathrm{u}, \frac{\mathrm{u}\omega}{k_f+\omega}, \frac{\mathrm{u}\omega^2 \pm a_f\omega\alpha}{\omega^2 + (a_f k_y)^2}\right\}_{x_R} \tag{4.2.11}$$

where

$$\alpha = \sqrt{\omega^2 - k_y^2(\mathrm{u}^2 - a_f^2)}. \tag{4.2.12}$$

Now we must determine which of these characteristic wave speeds corresponds to the wave that propagates into our domain. Only one root c_6, the analog to $\mathrm{u} - a_f$, has a negative real part and therefore corresponds to the incoming wave. The corresponding eigenvector is

$$\mathbf{m}_6|_{x_R} = \begin{pmatrix} 0 \\ -\dfrac{a_f\omega}{2v\alpha} \\ \dfrac{ia_f k_y u}{2v\alpha} \\ \dfrac{1}{2} \\ -\left(\dfrac{\Delta e(\gamma-1)}{v}\dfrac{k_f}{2}\right)\left(\dfrac{\mathrm{u}}{2}\right)\left(\dfrac{\omega}{\alpha}\right)\left[\dfrac{k_f \mathrm{u}\frac{\alpha}{\omega} + a_f\left(k_f + \omega - \frac{(k_y u)^2}{\omega}\right)}{a_f^2\left[(k_f+\omega)^2 - (k_y\mathrm{u})^2\right] - (k_f\mathrm{u})^2}\right] \\ \left(\dfrac{\Delta e(\gamma-1)}{v}\dfrac{k_f}{2}\right)\left(\dfrac{\mathrm{u}}{2}\right)\left(\dfrac{\omega}{\alpha}\right)\left[\dfrac{k_f \mathrm{u}\frac{\alpha}{\omega} + a_f\left(k_f + \omega - \frac{(k_y u)^2}{\omega}\right)}{a_f^2\left[(k_f+\omega)^2 - (k_y\mathrm{u})^2\right] - (k_f\mathrm{u})^2}\right] \end{pmatrix}_{x_R}. \tag{4.2.13}$$

Finally we apply the radiation condition (3.4.18) to find the necessary eigenvalue selection criterion for (3.2.10)

$$\begin{aligned} \mathcal{H}(\omega) = &\left[\frac{\mathrm{u}'}{a_f}\right]_{x_R} - \left[\frac{ik_y\mathrm{u}}{\omega}\frac{\mathrm{v}'}{a_f}\right]_{x_R} - \left[\frac{\alpha}{\omega}\frac{P'}{\gamma P}\right]_{x_R} - \\ &Y'_{\mathcal{B}}\left(\frac{\mathrm{u}}{a_f}\left[\frac{\Delta e k_f(\gamma-1)}{a_f}\right]\left[\frac{k_f \mathrm{u}\frac{\alpha}{\omega} + a_f\left(k_f + \omega - \frac{(k_y u)^2}{\omega}\right)}{a_f^2\left[(k_f+\omega)^2 - (k_y\mathrm{u})^2\right] - (k_f\mathrm{u})^2}\right]\right)_{x_R}. \end{aligned} \tag{4.2.14}$$

4.2.1 Traditional Formulation

In Lee and Stewart (1990), the algorithm for determining the radiation condition was slightly different, although it yielded the same eigenvalue selection criterion for the shooting method ($\mathcal{H}(\omega)$).

1. Find the analytic solution of $\mathbf{z}'|_{x_R}$

$$\mathbf{z}'|_{x_R} = \sum_{k\,(\text{no rxn})} \mathbf{n}_k F_k(x - c_k t) + \mathbf{n}_{Y_\mathcal{B}} \exp\left[\frac{\left(\dot{\Omega}_{\mathcal{B},Y_\mathcal{B}}\Big|_{x_R} - \dot{\Omega}_{\mathcal{B},Y_\mathcal{A}}\Big|_{x_R} \right)}{a_f|_{x_R}} \tilde{\kappa} x + \left(\dot{\Omega}_{\mathcal{B},Y_\mathcal{B}}\Big|_{x_R} - \dot{\Omega}_{\mathcal{B},Y_\mathcal{A}}\Big|_{x_R} \right) \left(1 - \frac{\tilde{\kappa}}{a_f} \mathrm{u} \right)_{x_R} t \right]. \tag{4.2.15}$$

2. Find c_k with negative real part.

3. Eliminate corresponding wave function, i.e.,

$$F_k(x - c_k t) = 0, \quad \mathcal{R}e(c_k) < 0, \tag{4.2.16}$$

   which is equivalent to setting the coefficient a_j equal to zero (see (3.4.17)).

4. Create a single criterion from the system of equations (1) that is independent of wave functions F_k. This single equation is the eigenvalue selection criterion for (3.2.10).

This alternate algorithm was applied in one dimension ($k_y = 0$) in Lee and Stewart (1990) and in two dimensions ($k_y \neq 0$) in Short (1997) for and irreversible one-step chemistry model. The details are given in Appendix E.6, but the final eigenvalue selection

criterion in two dimensions ($k_y \neq 0$) with chemistry is

$$\mathcal{H}(\omega) = \left[\frac{\mathrm{u}'}{a_f}\right]_{x_R} - \left[\frac{ik_y \mathrm{u}}{\omega}\frac{\mathrm{v}'}{a_f}\right]_{x_R} - \left[\sqrt{1 - \frac{k_y^2}{\omega^2}(\mathrm{u}^2 - a_f^2)}\frac{P'}{\gamma P}\right]_{x_R} + Y'_{\mathcal{B}}\left[\tilde{\kappa}_*\left(\tilde{\kappa} + \sqrt{1 - \frac{k_y^2}{\omega^2}(\mathrm{u}^2 - a_f^2)}\right)\right]_{x_R} \tag{4.2.17}$$

where

$$\tilde{\kappa} = \frac{a_f}{\mathrm{u}}\left(1 - \frac{\omega}{\dot{\Omega}_{\mathcal{B},Y_\mathcal{B}} - \dot{\Omega}_{\mathcal{B},Y_\mathcal{A}}}\right) \tag{4.2.18}$$

$$\tilde{\kappa}_* = \frac{v}{a_f^2}\frac{(Z_{,Y_\mathcal{B}} - Z_{,Y_\mathcal{A}})}{\left(\dot{\Omega}_{\mathcal{B},Y_\mathcal{B}} - \dot{\Omega}_{\mathcal{B},Y_\mathcal{A}}\right)}\frac{1}{1 - \tilde{\kappa}^2}. \tag{4.2.19}$$

This is very similar to (4.2.14), and I believe that the discrepancy is in the choice of $\tilde{\kappa}$ which was chosen for a one-dimensional system. In either case, if $k_y = 0$ ($Y'_{\mathcal{B}} \neq 0$), this will reduce to Lee and Stewart's expression

$$\mathcal{H}(\omega) = \left[\frac{\mathrm{u}'}{a_f}\right]_{x_R} - \left[\frac{\alpha}{\omega}\frac{P'}{\gamma P}\right]_{x_R} - Y'_{\mathcal{B}}\left(\frac{\mathrm{u}}{a_f}\left[\frac{\Delta e k_f(\gamma - 1)}{a_f}\right]\left[\frac{k_f \mathrm{u}\frac{\alpha}{\omega} + a_f\,(k_f + \omega)}{a_f^2(k_f + \omega)^2 - (k_f \mathrm{u})^2}\right]\right)_{x_R} \tag{4.2.20}$$

and if $Y'_{\mathcal{B}}$ is zero ($k_y \neq 0$), it will reduce to Short's condition

$$\mathcal{H}(\omega) = \left[\frac{\mathrm{u}'}{a_f}\right]_{x_R} - \left[\frac{ik_y \mathrm{u}}{\omega}\frac{\mathrm{v}'}{a_f}\right]_{x_R} - \left[\frac{\alpha}{\omega}\frac{P'}{\gamma P}\right]_{x_R}. \tag{4.2.21}$$

4.3 One-Step Reversible Chemistry

The method discussed briefly in Section 4.2.1 and described in detail in Appendix E.6 is convenient because for irreversible kinetics, the species conservation equation decouples from the fluid mechanics equations. We have presented the alternate method (see

Section 4.2) because, in the case of reversible kinetics, the one-way coupling no longer exists.

$$\dot{\Omega}_{i,v} \neq 0 \quad \dot{\Omega}_{i,P} \neq 0 \tag{4.3.1}$$

$$Z_{,v} \neq 0 \quad Z_{,P} \neq 0 \tag{4.3.2}$$

With this slightly more complex model, $\mathbf{C}$ does not simplify as much.

$$\mathbf{C}|_{x_R} = \begin{pmatrix} 0 & 0 & 0 & 0 & 0 & 0 \\ 0 & 0 & 0 & 0 & 0 & 0 \\ 0 & 0 & 0 & 0 & 0 & 0 \\ -Z_{,v} & 0 & 0 & -Z_{,P} & -Z_{,Y_\mathcal{A}} & -Z_{,Y_\mathcal{B}} \\ -\dot{\Omega}_{\mathcal{A},v} & 0 & 0 & -\dot{\Omega}_{\mathcal{A},P} & -\dot{\Omega}_{\mathcal{A},Y_\mathcal{A}} & -\dot{\Omega}_{\mathcal{B},Y_\mathcal{A}} \\ -\dot{\Omega}_{\mathcal{B},v} & 0 & 0 & -\dot{\Omega}_{\mathcal{B},P} & -\dot{\Omega}_{\mathcal{A},Y_\mathcal{B}} & -\dot{\Omega}_{\mathcal{B},Y_\mathcal{B}} \end{pmatrix}_{x_R} \tag{4.3.3}$$

For the one-step reversible model presented in Section 2.2,

$$\dot{\Omega}_\mathcal{A} = -k_f \left(Y_\mathcal{A} - \frac{1}{K_C} Y_\mathcal{B} \right) \tag{4.3.4}$$

$$\dot{\Omega}_\mathcal{B} = k_f \left(Y_\mathcal{A} - \frac{1}{K_C} Y_\mathcal{B} \right) \tag{4.3.5}$$

where

$$k_f = A \exp\left(-\frac{E_a}{RT} \right) \tag{4.3.6}$$

$$K_C = -\left[\frac{(h_\mathcal{B} - h_\mathcal{A})}{RT} - \frac{(s^\circ_\mathcal{B} - s^\circ_\mathcal{A})}{R} \right] \tag{4.3.7}$$

and

$$Z(v, P, \mathbf{Y}) = -\frac{G}{v} \sum_{i=1}^{N_Y} e_{,Y_i} \dot{\Omega}_i = -\frac{\gamma - 1}{v} \dot{\Omega}_\mathcal{B} (e_{Y_\mathcal{B}} - e_{Y_\mathcal{A}}). \tag{4.3.8}$$

Now the required derivatives are

$$\dot{\Omega}_{\mathcal{B},v}\Big|_{x_R} = -\dot{\Omega}_{\mathcal{A},v}\Big|_{x_R} = \left(\frac{k_f}{v}\frac{E_a}{RT}\left[Y_{\mathcal{A}} + \frac{1}{K_C}\frac{1}{v}\frac{(h_{\mathcal{B}} - h_{\mathcal{A}})}{\mathcal{R}T}Y_{\mathcal{B}}\right]\right)_{x_R} \tag{4.3.9}$$

$$\dot{\Omega}_{\mathcal{B},P}\Big|_{x_R} = -\dot{\Omega}_{\mathcal{A},P}\Big|_{x_R} = \left(\frac{k_f}{P}\frac{E_a}{RT}\left[Y_{\mathcal{A}} + \frac{1}{K_C}\frac{1}{P}\frac{(h_{\mathcal{B}} - h_{\mathcal{A}})}{\mathcal{R}T}Y_{\mathcal{B}}\right]\right)_{x_R} \tag{4.3.10}$$

$$\dot{\Omega}_{\mathcal{B},Y_{\mathcal{A}}}\Big|_{x_R} = -\dot{\Omega}_{\mathcal{A},Y_{\mathcal{A}}}\Big|_{x_R} = k_f|_{x_R} \tag{4.3.11}$$

$$\dot{\Omega}_{\mathcal{A},Y_{\mathcal{B}}}\Big|_{x_R} = -\dot{\Omega}_{\mathcal{B},Y_{\mathcal{B}}}\Big|_{x_R} = \left(\frac{k_f}{K_C}\right)_{x_R} \tag{4.3.12}$$

$$Z_{,v}|_{x_R} = \left(\frac{\gamma - 1}{v}(e_{Y_{\mathcal{B}}} - e_{Y_{\mathcal{A}}})\left[\frac{\dot{\Omega}_{\mathcal{B}}}{v} - \dot{\Omega}_{\mathcal{B},v}\right]\right)_{x_R} \tag{4.3.13}$$

$$Z_{,P}|_{x_R} = -\left(\frac{\gamma - 1}{v}(e_{Y_{\mathcal{B}}} - e_{Y_{\mathcal{A}}})\dot{\Omega}_{\mathcal{B},P}\right)_{x_R} \tag{4.3.14}$$

$$Z_{,Y_{\mathcal{B}}}|_{x_R} = -\left(\frac{\gamma - 1}{v}(e_{Y_{\mathcal{B}}} - e_{Y_{\mathcal{A}}})\dot{\Omega}_{\mathcal{B},Y_{\mathcal{B}}}\right)_{x_R} \tag{4.3.15}$$

$$Z_{,Y_{\mathcal{A}}}|_{x_R} = -\left(\frac{\gamma - 1}{v}(e_{Y_{\mathcal{B}}} - e_{Y_{\mathcal{A}}})\dot{\Omega}_{\mathcal{B},Y_{\mathcal{A}}}\right)_{x_R}. \tag{4.3.16}$$

We used the van't Hoff rule (D1.15) to determine the derivatives of the equilibrium constant. Following the prescription given in Section 4.1, we attempt to analytically determine the complex wave speeds which are related to the eigenvalues of $\mathbf{N}|_{x_R}$. Unfortunately, the characteristic polynomial,

$$0 = \Big[(c - \mathrm{u})^2\left(c(2\dot{\Omega}_{\mathcal{B},Y_{\mathcal{B}}} + \omega) - \mathrm{u}\omega\right)\Big]_{x_R} \times$$
$$\left[c\left(Z_{,P}(c - \mathrm{u})^2 - v^2 Z_{,v}\left[1 + \left(\frac{ck_y}{\omega}\right)^2\right]\right) + \omega(c - \mathrm{u})\left((c - \mathrm{u})^2 - a_f^2\left[1 - \left(\frac{ck_y}{\omega}\right)^2\right]\right)\right]_{x_R} \tag{4.3.17}$$

does not have analytic roots. We must determine the roots of this equation numerically, but first it is valuable to present an alternate formulation which gives insight into the character of the system of partial differential equations.

Since we evaluate the radiation condition far from the main reaction zone where the

composition is almost in equilibrium, our problem is analogous to the chemical nonequilibrium flow example discussed in Vincenti and Kruger (1965, Chap VIII). In this analogy, Vincenti and Kruger introduce the *near-equilibrium relaxation time scale*

$$\tau|_{x_R} = \left(\dot{\Omega}_{\mathcal{B},Y_\mathcal{B}} - \dot{\Omega}_{\mathcal{B},Y_\mathcal{A}}\right)^{-1}_{x_R} \tag{4.3.18}$$

which describes how long a system that is only slightly in chemical nonequilibrium will need to return to equilibrium. They reformulate the one-dimensional equations of motion in this regime in terms of $\tau|_{x_R}$

$$\frac{\mathrm{D}\rho'}{\mathrm{D}t} = -\rho|_{x_R}\mathrm{u}'_{,x} \tag{4.3.19}$$

$$\frac{\mathrm{D}\mathrm{u}'}{\mathrm{D}t} = -\frac{P'_{,x}}{\rho|_{x_R}} \tag{4.3.20}$$

$$\frac{\mathrm{D}P'}{\mathrm{D}t} = a_f^2|_{x_R}\left(\frac{\mathrm{D}\rho'}{\mathrm{D}t} + \rho|_{x_R}\dot{\sigma}\right) \tag{4.3.21}$$

$$\frac{\mathrm{D}Y'_\mathcal{B}}{\mathrm{D}t} = \frac{Y^{*'}_\mathcal{B} - Y'_\mathcal{B}}{\tau|_{x_R}}. \tag{4.3.22}$$

In the linearized species equation (4.3.22), $Y^{*'}_\mathcal{B}$ is the equilibrium value of product species perturbation whereas $Y'_\mathcal{B}$ is the current nonequilibrium value.

With some algebraic manipulation described fully in Appendix I.2, (4.3.19)–(4.3.22) can be combined into a single wave hierarchy equation

$$\tau^*|_{x_R}\left(\frac{a_e}{a_f}\right)^2_{x_R}\frac{\mathrm{D}}{\mathrm{D}t}\left[\left(\frac{\mathrm{D}}{\mathrm{D}t}\right)^2\mathrm{u}' - a_f^2\mathrm{u}'_{,xx}\right]_{x_R} + \left[\left(\frac{\mathrm{D}}{\mathrm{D}t}\right)^2\mathrm{u}' - a_e^2\mathrm{u}'_{,xx}\right]_{x_R} = 0 \tag{4.3.23}$$

where

$$\tau^*|_{x_R} = \frac{h_{,\rho}\tau|_{x_R}}{h_{,\rho} + h_{,Y^*_\mathcal{B}}Y^*_{\mathcal{B},\rho}}. \tag{4.3.24}$$

The wave hierarchy equation consists of two wave operators with different wave speeds. Whitman (1999, Chap. 10) discusses wave hierarchy equations at length. In this case, the lower-order operator involves the equilibrium soundspeed, and the higher-order operator

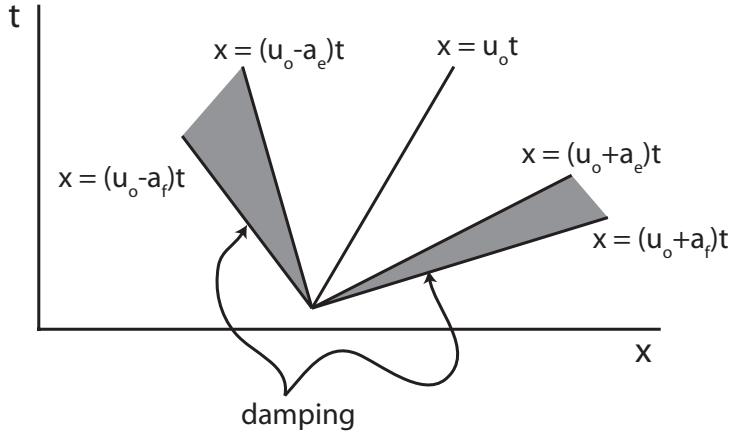

Figure 4.1: Wave decomposition schematic for flow field far from the main reaction zone in systems with reversible kinetics.

involves the frozen soundspeed. These two soundspeeds are defined and discussed in Appendix C.1. In 1920, Einstein discussed the difficulties in defining the speed of sound in dissociated gases. He recognized that high-frequency disturbances travel at the frozen soundspeed, low-frequency disturbances travel at the equilibrium soundspeed, and there exists a continuum of speeds between these two extremes.

The hierarchy equation (4.3.23) supports Einstein's argument that sound waves in partially dissociated gases are dispersive. The defining characteristic of dispersive waves is that the phase speed is a function of frequency, i.e.,

$$c_\phi = \frac{\omega}{k} = f(\omega). \tag{4.3.25}$$

Vincenti and Kruger solve (4.3.23) for the specific case of "harmonic disturbances propagating to infinity in the positive x-direction." Because their solution has complex growth rates, there is both dispersion and damping in the system. The high-frequency disturbances traveling at the frozen soundspeed are often considered "precursor waves" because they move away from the source more quickly but decay due to damping. The bulk of the energy moves with the equilibrium soundspeed. A schematic of the dispersive waves described by (4.3.23) is shown in Figure 4.1.

In an irreversible system, there is a single soundspeed far from the main reaction zone because there is no mechanism to shift the composition. In this case, the polynomial determining the complex wave speeds, (4.2.10), has analytic roots. Unfortunately, the characteristic polynomial associated with the hierarchy equation (derived in Appendix I.2)

$$-\omega\tau^*|_{x_R}\left(\frac{a_e}{a_f}\right)^2_{x_R}\left((c-\mathrm{u})\left[(c-\mathrm{u})^2-a_f^2\right]\right)_{x_R}+\left(c\left[(c-\mathrm{u})^2-a_e^2\right]\right)_{x_R}=0 \tag{4.3.26}$$

which is equivalent to (4.3.17) (see Appendix I.1) does not have analytic roots and must be solved numerically.

We see from (4.3.26) that in the limit of an irreversible reaction where there is a single soundspeed ($a_f = a_e$), (4.3.26) reduces to

$$\left[-\omega\tau^*\left(\frac{a_e}{a_f}\right)^2(c-\mathrm{u})+c\right]_{x_R}\left[(c-\mathrm{u})^2-a_f^2\right]_{x_R}=0 \tag{4.3.27}$$

which is equivalent to (4.2.10). The solution to (4.3.27) is depicted in Figure 4.2 by the open squares. When we introduce reversibility, the soundspeeds will no longer be equal ($a_f \neq a_e$), and the complex wave speeds are determined numerically from (4.3.26). The curves that extend from the squares in Figure 4.2 indicate how the roots change as reversibility is increased. We provided a detailed discussion of how we vary the reversibility in Section 2.2. The roots depicted in Figure 4.2 are labeled according to their non-reactive analogs to indicate which root should correspond to the component of the solution traveling into the domain. Based on the results depicted in Figure 4.2, only one eigenvalue consistently has a negative real part.

4.4 General Formulation — Detailed Chemistry Model

In the previous sections, we have discussed three distinct chemical scenarios: non-reactive kinetics in one dimension ($k_y = 0$), single-step irreversible kinetics in two dimensions

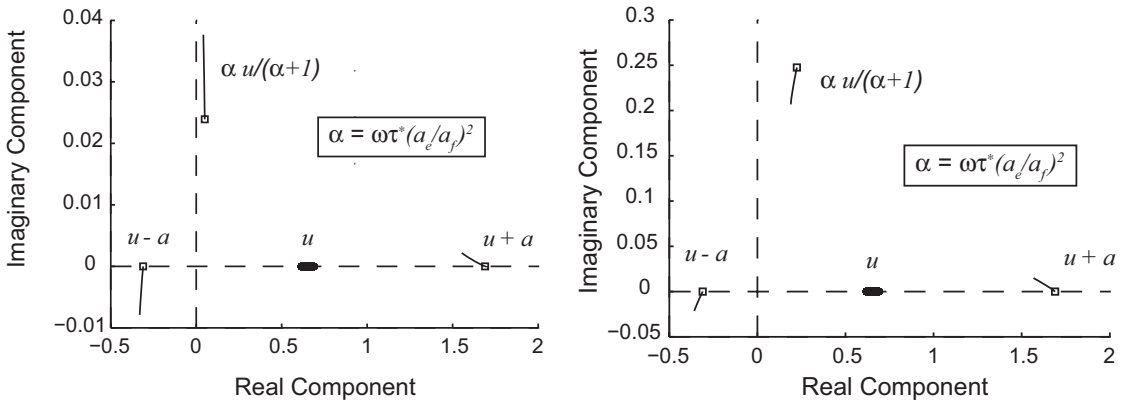

Figure 4.2: Roots (c) of (4.3.26) for the first two modes (Lee and Stewart, 1990) normalized by the frozen soundspeed a_f. (a) Mode 1 (b) Mode 2

($k_y \neq 0$), and single-step reversible kinetics in two dimensions ($k_y \neq 0$). We have indicated that the algorithm described at the beginning of the chapter is appropriate because for all cases observed there exists a single eigenvalue with a negative real part. The eigenvector corresponding to this solitary eigenvalue is the only direction along which information can propagate from our artificial boundary toward the main reaction zone.

In the general case, a detailed chemical mechanism contains many independent species governed by many reversible reactions. Clearly, it would be most useful to extend our formulation to realistic chemical models, but we have found that extension even to the simplest detailed mechanism is challenging. For detonations, the simplest detailed mechanism is the hydrogen-oxygen mechanism. In this mechanism, there are 12 species: H_2, H, O_2, O, OH, HO_2, H_2O_2, H_2O, N, N_2, NO, and Ar, as well as 24 reversible reactions given in Table 4.1. We have presented the details of how to implement a detailed mechanism in Section 1.4.

First we attempted an extension of the wave hierarchy derivation described in Section 4.3 and Appendix I.2 to multiple independent species. We assumed that each species has its own near-equilibrium relaxation time scale τ_i. Unfortunately, although the species conservation equations are decoupled in this case, each species contributes to the thermicity term in the adiabatic change equation (4.3.21). For this reason, we cannot extend

No.	**Reaction**	A	n	E_a
1	$H_2 + O_2 \leftrightarrow 2OH$	$1.70 \cdot 10^{10}$	0	47780.0
2	$OH + H_2 \leftrightarrow H_2O + H$	$1.17 \cdot 10^{06}$	1.30	3626.0
3	$O + OH \leftrightarrow O_2 + H$	$4.00 \cdot 10^{11}$	−0.50	0
4	$O + H_2 \leftrightarrow OH + H$	$5.06 \cdot 10^{01}$	2.67	6290.0
5	$H + O_2 + M \leftrightarrow HO_2 + M$	$3.61 \cdot 10^{11}$	−0.72	0
6	$OH + HO_2 \leftrightarrow H_2O + O_2$	$7.50 \cdot 10^{09}$	0	0
7	$H + HO_2 \leftrightarrow 2OH$	$1.40 \cdot 10^{11}$	0	1073.0
8	$O + HO_2 \leftrightarrow O_2 + OH$	$1.40 \cdot 10^{10}$	0	1073.0
9	$2OH \leftrightarrow O + H_2O$	$6.00 \cdot 10^{05}$	1.30	0
10	$H + H + M \leftrightarrow H_2 + M$	$1.00 \cdot 10^{12}$	−1.00	0
11	$H + H + H_2 \leftrightarrow H_2 + H_2$	$9.20 \cdot 10^{10}$	−0.60	0
12	$H + H + H_2O \leftrightarrow H_2 + H_2O$	$6.00 \cdot 10^{13}$	−1.25	0
13	$H + OH + M \leftrightarrow H_2O + M$	$1.60 \cdot 10^{16}$	−2.00	0
14	$H + O + M \leftrightarrow OH + M$	$6.20 \cdot 10^{10}$	−0.60	0
15	$O + O + M \leftrightarrow O_2 + M$	$1.89 \cdot 10^{07}$	0	−1788.0
16	$H + HO_2 \leftrightarrow H_2 + O_2$	$1.25 \cdot 10^{10}$	0	0
17	$HO_2 + HO_2 \leftrightarrow H_2O_2 + O_2$	$2.00 \cdot 10^{09}$	0	0
18	$H_2O_2 + M \leftrightarrow OH + OH + M$	$1.30 \cdot 10^{14}$	0	45500.0
19	$H_2O_2 + H \leftrightarrow HO_2 + H_2$	$1.60 \cdot 10^{09}$	0	3800.0
20	$H_2O_2 + OH \leftrightarrow H_2O + HO_2$	$1.00 \cdot 10^{10}$	0	1800.0
21	$O + N_2 \leftrightarrow NO + N$	$1.40 \cdot 10^{11}$	0	75800.0
22	$N + O_2 \leftrightarrow NO + O$	$6.40 \cdot 10^{06}$	1.00	6280.0
23	$OH + N \leftrightarrow NO + H$	$4.00 \cdot 10^{10}$	0	0
24	$N_2 + M \leftrightarrow N + N + M$	$3.71 \cdot 10^{18}$	−1.60	224928.0

Table 4.1: Reactions and Arrhenius parameters (1.4.5) for the hydrogen-oxygen mechanism. Arrhenius parameters from GRI Mech 3.0 (Smith et al., 1999).

the wave hierarchy formulation to systems with multiple independent species.

In order to use the methodology described in Chapter 3, we must determine an initial guess for the value of the growth rate ω. It is important to note that the root finding schemes associated with the shooting algorithm are sensitive to the initial guess. In the simplified mechanisms discussed in the previous sections, we were able to use the values from Lee and Stewart (1990) as initial guesses for our shooting algorithm. They determined their initial guesses via a carpet search. In the hydrogen-oxygen case, we have attempted a carpet search but not had any success.

In the one-step mechanisms, there is only one independent species and therefore only one chemical timescale. Far from the main reaction zone, this time scale is the near-equilibrium relaxation time scale (4.3.18). We have investigated the chemical time scales far from the main reaction zone in the hydrogen-oxygen case by diagonalizing the Jacobian matrix of the net production rates, i.e.,

$$J_{ij} = \frac{\partial \dot{\Omega}_i}{\partial Y_j}. \tag{4.4.1}$$

The chemical time scales, inverted eigenvalues of $\mathbf{J}$, are shown in Table 4.2. It is clear

Species	**Chemical Time Scale**	
	$2H_2 - O_2$	$2H_2 - O_2 - 3.76N_2$
H_2	$-1.576 \cdot 10^{-11}$	$-8.270 \cdot 10^{-11}$
H	$-2.506 \cdot 10^{-11}$	$-1.058 \cdot 10^{-10}$
O_2	$-2.900 \cdot 10^{-11}$	$-1.311 \cdot 10^{-10}$
O	$-2.900 \cdot 10^{-11}$	$-1.311 \cdot 10^{-10}$
OH	$-3.618 \cdot 10^{-10}$	$-1.138 \cdot 10^{-09}$
HO_2	$1.236 \cdot 10^{-08}$	$-4.650 \cdot 10^{-09}$
H_2O_2	$-2.573 \cdot 10^{04}$	$1.339 \cdot 10^{-07}$
H_2O	$-6.221 \cdot 10^{-08}$	$-3.459 \cdot 10^{-07}$
N	$-1.411 \cdot 10^{-09}$	$-2.284 \cdot 10^{-06}$
N_2	$-1.987 \cdot 10^{08}$	$6.265 \cdot 10^{07}$
NO	$-3.301 \cdot 10^{-05}$	$-5.063 \cdot 10^{09}$
Ar	0	0

Table 4.2: Chemical time scales far from the main reaction zone for initial conditions: stoichiometric hydrogen-oxygen at 300 K and 1 atm.

from the table, that this problem is very stiff even in the near-equilibrium region. The chemical time scales range from $\approx 10^{-11}$ to $\approx 10^{9}$ which is 20 orders of magnitude. We believe that this will be an important factor in determining the value of the unstable growth rates and should be considered when making an initial guess.

We have investigated values of ω in this range of time scales by setting $\mathcal{R}e(\omega) = 0$ and $\mathcal{I}m(\omega) \in (10^{-10}, 10^{10})$. For each value of ω, we have integrated through the domain and found the eigenvalues of $\mathbf{N}$ (3.4.6) far from the reaction zone. The wave speeds are the inverse of the eigenvalues of $\mathbf{N}$ and are given in Tables 4.3–4.6. We see that while for some frequencies, there are several eigenvalues with negative real parts, one is appreciably larger than the others. For this reason, we believe that the method outlined at the beginning of this chapter will apply for detailed mechanisms as well.

$\mathcal{I}m(\omega)$ - Mixture: $2H_2$-O_2-$3.76N_2$		
10^{-10}	10^{-8}	10^{-6}
$\mathbf{-1.95 \cdot 10^{-1} - i6.28 \cdot 10^{-2}}$	$\mathbf{-8.75 \cdot 10^{-1} - i1.01 \cdot 10^{0}}$	$\mathbf{-2.87 \cdot 10^{-1} - i1.80 \cdot 10^{-1}}$
$-1.25 \cdot 10^{-4} + i8.35 \cdot 10^{-5}$	$-8.58 \cdot 10^{-3} + i1.61 \cdot 10^{-2}$	$-2.52 \cdot 10^{-15} + i1.03 \cdot 10^{-13}$
$-2.52 \cdot 10^{-19} + i1.03 \cdot 10^{-17}$	$-2.52 \cdot 10^{-17} + i1.03 \cdot 10^{-15}$	$-5.23 \cdot 10^{-24} - i6.78 \cdot 10^{-11}$
$-2.89 \cdot 10^{-25} + i1.78 \cdot 10^{-13}$	$-2.61 \cdot 10^{-23} + i1.78 \cdot 10^{-11}$	$5.50 \cdot 10^{-30} + i6.44 \cdot 10^{-14}$
$-1.22 \cdot 10^{-27} + i2.69 \cdot 10^{-14}$	$-2.34 \cdot 10^{-30} + i8.85 \cdot 10^{-15}$	$1.30 \cdot 10^{-29} + i8.22 \cdot 10^{-14}$
$-1.82 \cdot 10^{-32} + i8.85 \cdot 10^{-17}$	$4.15 \cdot 10^{-33} + i6.44 \cdot 10^{-16}$	$1.03 \cdot 10^{-27} + i8.85 \cdot 10^{-13}$
$-2.91 \cdot 10^{-35} + i6.44 \cdot 10^{-18}$	$5.19 \cdot 10^{-32} + i8.22 \cdot 10^{-16}$	$1.69 \cdot 10^{-26} + i3.61 \cdot 10^{-12}$
$5.35 \cdot 10^{-34} + i8.22 \cdot 10^{-18}$	$2.49 \cdot 10^{-31} + i3.61 \cdot 10^{-14}$	$1.11 \cdot 10^{-22} + i2.69 \cdot 10^{-10}$
$2.60 \cdot 10^{-32} + i3.61 \cdot 10^{-16}$	$2.34 \cdot 10^{-26} + i2.69 \cdot 10^{-12}$	$8.49 \cdot 10^{-21} + i1.78 \cdot 10^{-9}$
$3.98 \cdot 10^{-28} - i6.78 \cdot 10^{-15}$	$3.31 \cdot 10^{-26} - i6.78 \cdot 10^{-13}$	$2.52 \cdot 10^{-15} + i1.03 \cdot 10^{-13}$
$2.52 \cdot 10^{-19} + i1.03 \cdot 10^{-17}$	$2.52 \cdot 10^{-17} + i1.03 \cdot 10^{-15}$	$3.48 \cdot 10^{-2} + i2.19 \cdot 10^{-1}$
$6.54 \cdot 10^{-6} + i5.14 \cdot 10^{-5}$	$4.88 \cdot 10^{-4} + i5.56 \cdot 10^{-3}$	$4.27 \cdot 10^{-1} - i2.37 \cdot 10^{-1}$
$1.26 \cdot 10^{-4} - i1.57 \cdot 10^{-4}$	$7.34 \cdot 10^{-3} - i2.52 \cdot 10^{-2}$	$6.78 \cdot 10^{2} + i2.59 \cdot 10^{2}$
$4.53 \cdot 10^{-1} - i9.95 \cdot 10^{-2}$	$1.69 \cdot 10^{2} - i1.28 \cdot 10^{2}$	$7.26 \cdot 10^{2} - i6.20 \cdot 10^{1}$
$7.78 \cdot 10^{2} + i0.00 \cdot 10^{0}$	$7.78 \cdot 10^{2} + i0.00 \cdot 10^{0}$	$7.78 \cdot 10^{2} + i0.00 \cdot 10^{0}$
$7.78 \cdot 10^{2} + i0.00 \cdot 10^{0}$	$7.78 \cdot 10^{2} + i0.00 \cdot 10^{0}$	$7.78 \cdot 10^{2} + i0.00 \cdot 10^{0}$

Table 4.3: Inverse eigenvalues of $\mathbf{N}$ (3.4.6) far from the main reaction zone for initial conditions: stoichiometric hydrogen-air at 300 K and 1 atm. The eigenvalues are ordered by the real part from most negative to most positive. The eigenvalue that we believe is relevant to the radiation condition is bolded. Frequencies ($\mathcal{I}m(\omega)$) 10^{-10}, 10^{-8}, and 10^{-6} are given here.

$\mathcal{I}m(\omega)$ - Mixture: $2H_2$-O_2-$3.76N_2$		
10^{-4}	10^{-2}	10^{0}
$\mathbf{-1.36 \cdot 10^{1} - i1.71 \cdot 10^{1}}$	$\mathbf{-2.58 \cdot 10^{2} + i1.76 \cdot 10^{2}}$	$\mathbf{-6.21 \cdot 10^{2} + i2.76 \cdot 10^{0}}$
$-2.52 \cdot 10^{-13} + i1.03 \cdot 10^{-11}$	$-2.52 \cdot 10^{-11} + i1.03 \cdot 10^{-9}$	$-2.52 \cdot 10^{-9} + i1.03 \cdot 10^{-7}$
$5.32 \cdot 10^{-26} + i6.44 \cdot 10^{-12}$	$5.33 \cdot 10^{-22} + i6.43 \cdot 10^{-10}$	$5.33 \cdot 10^{-18} + i6.43 \cdot 10^{-8}$
$8.66 \cdot 10^{-26} + i8.22 \cdot 10^{-12}$	$8.70 \cdot 10^{-22} + i8.23 \cdot 10^{-10}$	$8.70 \cdot 10^{-18} + i8.23 \cdot 10^{-8}$
$1.01 \cdot 10^{-23} + i8.85 \cdot 10^{-11}$	$1.01 \cdot 10^{-19} + i8.85 \cdot 10^{-9}$	$1.01 \cdot 10^{-15} + i8.85 \cdot 10^{-7}$
$1.67 \cdot 10^{-22} + i3.61 \cdot 10^{-10}$	$1.67 \cdot 10^{-18} + i3.61 \cdot 10^{-8}$	$1.67 \cdot 10^{-14} + i3.61 \cdot 10^{-6}$
$1.89 \cdot 10^{-20} - i6.78 \cdot 10^{-9}$	$1.92 \cdot 10^{-16} - i6.78 \cdot 10^{-7}$	$1.92 \cdot 10^{-12} - i6.78 \cdot 10^{-5}$
$9.23 \cdot 10^{-19} + i2.69 \cdot 10^{-8}$	$9.22 \cdot 10^{-15} + i2.69 \cdot 10^{-6}$	$9.22 \cdot 10^{-11} + i2.69 \cdot 10^{-4}$
$4.08 \cdot 10^{-17} + i1.78 \cdot 10^{-7}$	$4.06 \cdot 10^{-13} + i1.78 \cdot 10^{-5}$	$2.52 \cdot 10^{-9} + i1.03 \cdot 10^{-7}$
$2.52 \cdot 10^{-13} + i1.03 \cdot 10^{-11}$	$2.52 \cdot 10^{-11} + i1.03 \cdot 10^{-9}$	$4.06 \cdot 10^{-9} + i1.78 \cdot 10^{-3}$
$4.81 \cdot 10^{0} + i1.32 \cdot 10^{1}$	$3.03 \cdot 10^{2} - i3.35 \cdot 10^{2}$	$7.78 \cdot 10^{2} - i1.79 \cdot 10^{-3}$
$2.65 \cdot 10^{1} - i7.24 \cdot 10^{1}$	$7.69 \cdot 10^{2} + i1.85 \cdot 10^{1}$	$7.78 \cdot 10^{2} + i1.03 \cdot 10^{-5}$
$7.78 \cdot 10^{2} - i7.07 \cdot 10^{-1}$	$7.78 \cdot 10^{2} - i1.19 \cdot 10^{-3}$	$7.78 \cdot 10^{2} + i0.00 \cdot 10^{0}$
$7.78 \cdot 10^{2} + i0.00 \cdot 10^{0}$	$7.78 \cdot 10^{2} + i0.00 \cdot 10^{0}$	$7.78 \cdot 10^{2} + i0.00 \cdot 10^{0}$
$7.78 \cdot 10^{2} + i0.00 \cdot 10^{0}$	$7.78 \cdot 10^{2} + i0.00 \cdot 10^{0}$	$7.78 \cdot 10^{2} + i4.36 \cdot 10^{-3}$
$8.54 \cdot 10^{2} + i8.48 \cdot 10^{1}$	$7.79 \cdot 10^{2} - i3.66 \cdot 10^{-1}$	$2.18 \cdot 10^{3} - i2.50 \cdot 10^{1}$

Table 4.4: Inverse eigenvalues of $\mathbf{N}$ (3.4.6) far from the main reaction zone for initial conditions: stoichiometric hydrogen-air at 300 K and 1 atm. The eigenvalues are ordered by the real part from most negative to most positive. The eigenvalue that we believe is relevant to the radiation condition is bolded. Frequencies ($\mathcal{I}m(\omega)$) 10^{-4}, 10^{-2}, and 10^{0} are given here.

$\mathcal{I}m(\omega)$ - Mixture: $2H_2$-O_2-$3.76N_2$		
10^2	10^4	10^6
$\mathbf{-6.21 \cdot 10^2 + i3.41 \cdot 10^{-3}}$	$\mathbf{-6.21 \cdot 10^2 - i6.88 \cdot 10^{-1}}$	$\mathbf{-6.02 \cdot 10^2 - i6.60 \cdot 10^1}$
$-2.52 \cdot 10^{-7} + i1.03 \cdot 10^{-5}$	$-2.52 \cdot 10^{-5} + i1.03 \cdot 10^{-3}$	$-2.51 \cdot 10^{-3} + i1.03 \cdot 10^{-1}$
$5.33 \cdot 10^{-14} + i6.43 \cdot 10^{-6}$	$5.33 \cdot 10^{-10} + i6.44 \cdot 10^{-4}$	$5.33 \cdot 10^{-6} + i6.44 \cdot 10^{-2}$
$8.70 \cdot 10^{-14} + i8.23 \cdot 10^{-6}$	$8.70 \cdot 10^{-10} + i8.22 \cdot 10^{-4}$	$8.70 \cdot 10^{-6} + i8.22 \cdot 10^{-2}$
$1.01 \cdot 10^{-11} + i8.85 \cdot 10^{-5}$	$1.01 \cdot 10^{-7} + i8.85 \cdot 10^{-3}$	$1.01 \cdot 10^{-3} + i8.85 \cdot 10^{-1}$
$1.67 \cdot 10^{-10} + i3.61 \cdot 10^{-4}$	$1.67 \cdot 10^{-6} + i3.61 \cdot 10^{-2}$	$2.53 \cdot 10^{-3} + i1.03 \cdot 10^{-1}$
$1.92 \cdot 10^{-8} - i6.78 \cdot 10^{-3}$	$2.52 \cdot 10^{-5} + i1.03 \cdot 10^{-3}$	$1.67 \cdot 10^{-2} + i3.61 \cdot 10^{0}$
$2.52 \cdot 10^{-7} + i1.03 \cdot 10^{-5}$	$1.92 \cdot 10^{-4} - i6.78 \cdot 10^{-1}$	$2.09 \cdot 10^{0} - i6.85 \cdot 10^{1}$
$9.22 \cdot 10^{-7} + i2.69 \cdot 10^{-2}$	$9.23 \cdot 10^{-3} + i2.69 \cdot 10^{0}$	$8.28 \cdot 10^{1} + i2.40 \cdot 10^{2}$
$4.06 \cdot 10^{-5} + i1.78 \cdot 10^{-1}$	$4.06 \cdot 10^{-1} + i1.78 \cdot 10^{1}$	$6.53 \cdot 10^{2} + i2.86 \cdot 10^{2}$
$7.78 \cdot 10^{2} - i3.97 \cdot 10^{-6}$	$7.78 \cdot 10^{2} + i1.89 \cdot 10^{-7}$	$7.78 \cdot 10^{2} + i2.68 \cdot 10^{-9}$
$7.78 \cdot 10^{2} - i2.80 \cdot 10^{-7}$	$7.78 \cdot 10^{2} - i5.27 \cdot 10^{-8}$	$7.78 \cdot 10^{2} - i5.07 \cdot 10^{-10}$
$7.78 \cdot 10^{2} + i0.00 \cdot 10^{0}$	$7.78 \cdot 10^{2} + i9.85 \cdot 10^{-10}$	$7.78 \cdot 10^{2} + i7.59 \cdot 10^{-12}$
$7.78 \cdot 10^{2} + i0.00 \cdot 10^{0}$	$7.78 \cdot 10^{2} + i0.00 \cdot 10^{0}$	$7.78 \cdot 10^{2} + i0.00 \cdot 10^{0}$
$7.78 \cdot 10^{2} + i2.68 \cdot 10^{-5}$	$7.78 \cdot 10^{2} + i0.00 \cdot 10^{0}$	$7.78 \cdot 10^{2} + i0.00 \cdot 10^{0}$
$2.18 \cdot 10^{3} - i3.48 \cdot 10^{-2}$	$2.18 \cdot 10^{3} + i1.96 \cdot 10^{-1}$	$2.17 \cdot 10^{3} + i1.95 \cdot 10^{1}$

Table 4.5: Inverse eigenvalues of $\mathbf{N}$ (3.4.6) far from the main reaction zone for initial conditions: stoichiometric hydrogen-air at 300 K and 1 atm. The eigenvalues are ordered by the real part from most negative to most positive. The eigenvalue that we believe is relevant to the radiation condition is bolded. Frequencies ($\mathcal{I}m(\omega)$) 10^2, 10^4, and 10^6 are given here.

$\mathcal{I}m(\omega)$ - Mixture: $2H_2$-O_2-$3.76N_2$	
10^8	10^{10}
$\mathbf{-3.93 \cdot 10^2 - i5.40 \cdot 10^0}$	$\mathbf{-3.99 \cdot 10^2 - i1.60 \cdot 10^0}$
$-1.14 \cdot 10^{-1} + i1.03 \cdot 10^1$	$3.16 \cdot 10^2 + i3.82 \cdot 10^2$
$5.33 \cdot 10^{-2} + i6.43 \cdot 10^0$	$4.11 \cdot 10^2 + i3.88 \cdot 10^2$
$8.70 \cdot 10^{-2} + i8.22 \cdot 10^0$	$4.91 \cdot 10^2 + i3.65 \cdot 10^2$
$3.90 \cdot 10^{-1} + i1.03 \cdot 10^1$	$4.96 \cdot 10^2 + i3.84 \cdot 10^2$
$9.94 \cdot 10^0 + i8.74 \cdot 10^1$	$7.72 \cdot 10^2 + i6.77 \cdot 10^1$
$1.38 \cdot 10^2 + i2.97 \cdot 10^2$	$7.77 \cdot 10^2 + i1.67 \cdot 10^1$
$7.71 \cdot 10^2 - i7.17 \cdot 10^1$	$7.78 \cdot 10^2 - i7.24 \cdot 10^{-1}$
$7.77 \cdot 10^2 + i2.24 \cdot 10^1$	$7.78 \cdot 10^2 + i2.25 \cdot 10^{-1}$
$7.78 \cdot 10^2 + i3.40 \cdot 10^0$	$7.78 \cdot 10^2 + i3.40 \cdot 10^{-2}$
$7.78 \cdot 10^2 - i5.63 \cdot 10^{-12}$	$7.78 \cdot 10^2 + i4.13 \cdot 10^{-14}$
$7.78 \cdot 10^2 + i2.43 \cdot 10^{-11}$	$7.78 \cdot 10^2 + i1.93 \cdot 10^{-12}$
$7.78 \cdot 10^2 + i2.11 \cdot 10^{-13}$	$7.78 \cdot 10^2 - i8.42 \cdot 10^{-14}$
$7.78 \cdot 10^2 + i0.00 \cdot 10^0$	$7.78 \cdot 10^2 + i0.00 \cdot 10^0$
$7.78 \cdot 10^2 + i0.00 \cdot 10^0$	$7.78 \cdot 10^2 + i0.00 \cdot 10^0$
$1.95 \cdot 10^3 + i2.62 \cdot 10^1$	$1.95 \cdot 10^3 + i3.34 \cdot 10^0$

Table 4.6: Inverse eigenvalues of $\mathbf{N}$ (3.4.6) far from the main reaction zone for initial conditions: stoichiometric hydrogen-air at 300 K and 1 atm. The eigenvalues are ordered by the real part from most negative to most positive. The eigenvalue that we believe is relevant to the radiation condition is bolded. Frequencies ($\mathcal{I}m(\omega)$) 10^8 and 10^{10} are given here.

Chapter 5

Linear Stability Results

In this chapter, we present results obtained using the methods described in Chapters 2–4. Throughout this discussion, we will compare our results with the results from Lee and Stewart (1990). First in Section 5.1, we illustrate the shape of the base flow and how the length scales change with increasing reversibility. Following the base flow discussions, we present the unstable eigenvalues (ω) determined for each degree of reversibility $\Delta s/R$, overdrive f, and transverse wave number k_y in Section 5.2. As a reference, we have compared the unstable eigenvalues for $\Delta s/R = 0$ with Lee and Stewart's results. In addition to the eigenvalues, we give some further discussion strictly about one-dimensional results ($k_y = 0$). In Section 5.2, will give the shape of some representative eigenfunctions ($\mathbf{z}^1(x)$). In Section 5.3 we will compare relevant time scales. In Section 5.4, we will discuss the neutral stability curves. Finally in Section 5.6, we give tabular data corresponding to the figures.

5.1 Base Flow

Using the methodology explained in Chapter 3 and the family of single-step reactions with constant T_{CJ} described in Section 2.2.1, we have investigated the unstable eigenvalues for nine extents of reversibility

$$\Delta s/R = 0, -1, -2, -3, -4, -5, -6, -7, -8. \tag{5.1}$$

The base flow, described fully in Chapter 2, is the ZND model of a steady one-dimensional detonation. Figure 5.2 depicts the base flow profiles normalized by the post-shock state for the two extreme cases ($\Delta s/R = 0$ and $\Delta s/R = -8$). As given in Table 2.1, $\Delta s/R = 0$ corresponds to an irreversible reaction where the reactant is completely consumed at equilibrium. $\Delta s/R = -8$ corresponds to a case where approximately half of the reactant is consumed at equilibrium.

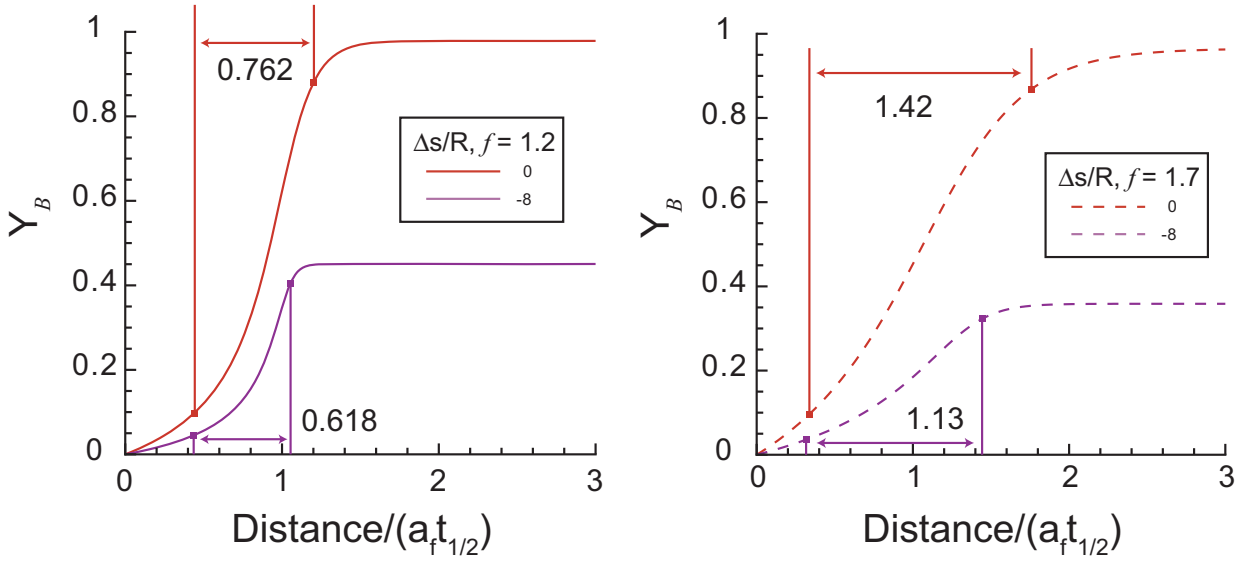

Figure 5.1: Comparison of product profiles for varying overdrive and reversibility. Distances indicated are measured from $0.1Y_{\mathcal{B}}^{eq}$ to $0.9Y_{\mathcal{B}}^{eq}$. (a) $f = 1.2$ (b) $f = 1.7$

The ZND structure has two relevant length scales which we discussed in Section 1.2.3, the induction length $\Delta_{i,ZND}$ and the energy release pulse width $\Delta_{e,ZND}$. The most visible difference in the ZND profiles is in the energy pulse width $\Delta_{e,ZND}$. As the reaction becomes more reversible, the energy release zone becomes more concentrated, i.e., $\Delta_{e,ZND}$ decreases. Table 5.1 gives the values of the relevant length scales $\Delta_{i,ZND}$ and $\Delta_{e,ZND}$ for each degree of reversibility for $f = 1.2$, and Table 5.2 provides a comparison of the length scales for varying overdrive. Ng et al. (2005b) found that their parameter $\chi = \theta \dfrac{\Delta_{i,ZND}}{\Delta_{e,ZND}}$ correlates with the extent of detonation instability as measured by the irregularity of experimental soot foil traces (discussed in Section 3.2). Tables 5.1 and 5.2 show how

this parameter increases with increasing reversibility because $\Delta_{e,ZND}$ decreases. $\Delta_{e,ZND}$ decreases due the fact that less distance is required to transition from $0.1Y_{\mathcal{B}}^{eq}$ to $0.9Y_{\mathcal{B}}^{eq}$ for more reversible cases, as shown in Figure 5.1. Figure 5.1 shows that more distance is required for higher overdrive values.

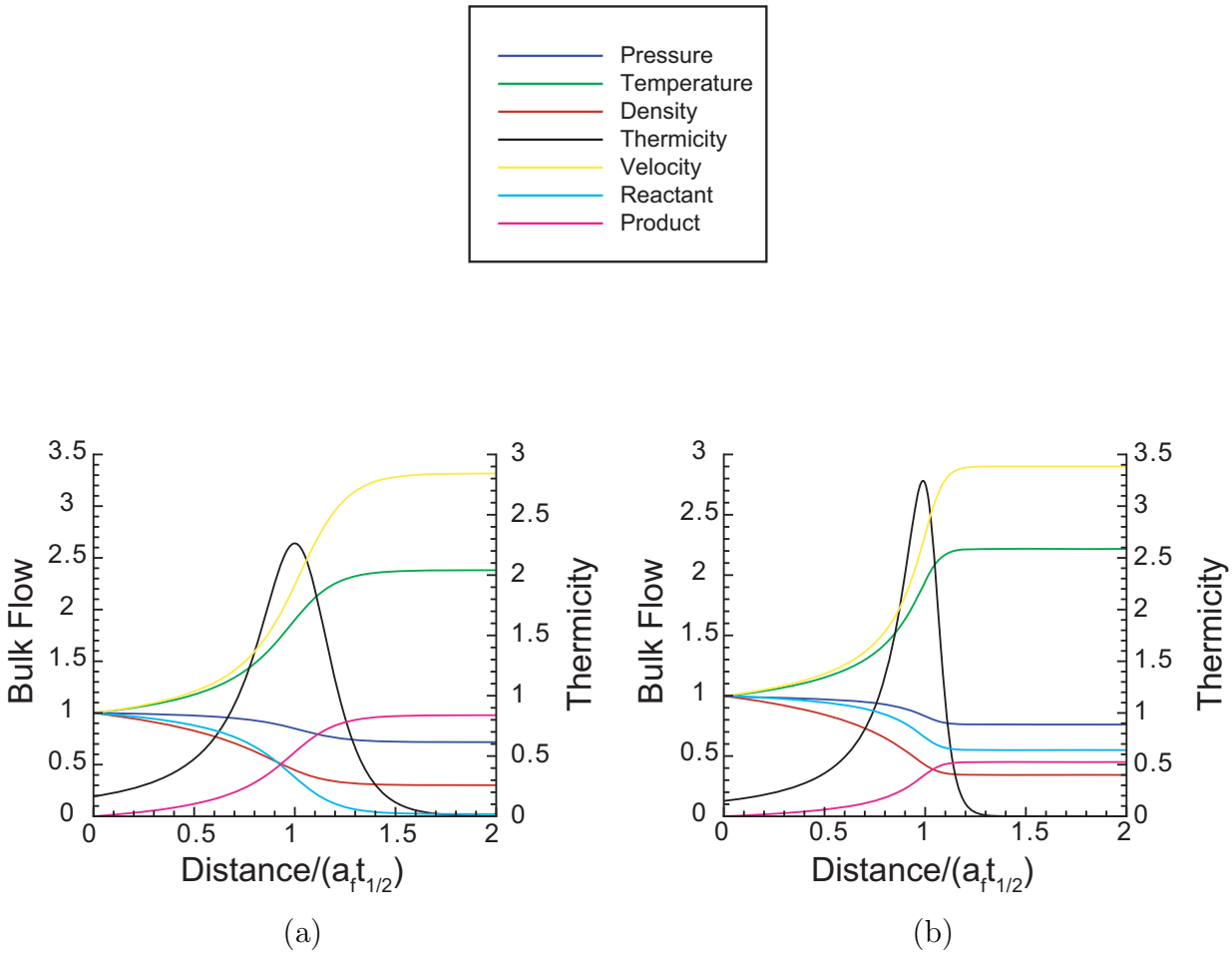

Figure 5.2: ZND structure for two extents of reversibility (a) $\Delta s/R = 0$ (b) $\Delta s/R = -8$ normalized by the post-shock state. The distance is normalized by the pre-shock sound speed a_{f1} and the half reaction time scale $t_{1/2}$. $t_{1/2} = 1$ in our normalization.

$\Delta s/R$	f	$\Delta_{i,ZND}/(a_{f1}t_{1/2})$	$\Delta_{e,ZND}/(a_{f1}t_{1/2})$	$\theta = E_a/RT_2$	$\theta\Delta_{i,ZND}/\Delta_{e,ZND}$
0	1.2	0.9973	0.4514	8.964	19.80
-1	1.2	0.9981	0.4349	8.971	20.59
-2	1.2	0.9985	0.4099	8.982	21.88
-3	1.2	0.9985	0.3837	8.995	23.41
-4	1.2	0.9964	0.3461	9.005	25.93
-5	1.2	0.9942	0.3162	9.011	28.34
-6	1.2	0.9912	0.2899	9.016	30.82
-7	1.2	0.9905	0.2632	9.018	33.94
-8	1.2	0.9895	0.2438	9.020	36.61

Table 5.1: $\Delta_{i,ZND}$ and $\Delta_{e,ZND}$ normalized by the initial frozen sound speed for all extents of reversibility and overdrive $f = 1.2$.

$\Delta s/R$	f	$\Delta_{i,ZND}/(a_{f1}t_{1/2})$	$\Delta_{e,ZND}/(a_{f1}t_{1/2})$	$\theta = E_a/RT_2$	$\theta\Delta_{i,ZND}/\Delta_{e,ZND}$
0	1.2	0.9973	0.4514	8.964	19.80
0	1.3	1.034	0.5896	8.387	14.70
0	1.4	1.068	0.7461	7.881	11.28
0	1.5	1.076	0.9088	7.414	8.774
0	1.6	1.096	1.084	7.032	7.114
0	1.7	1.104	1.273	6.672	5.784
-8	1.2	0.9895	0.2438	9.020	36.61
-8	1.3	1.035	0.3343	8.441	26.13
-8	1.4	1.075	0.4494	7.932	18.97
-8	1.5	1.107	0.5816	7.480	14.24
-8	1.6	1.137	0.7377	7.078	10.91
-8	1.7	1.160	0.9068	6.716	8.590

Table 5.2: $\Delta_{i,ZND}$ and $\Delta_{e,ZND}$ normalized by the initial frozen sound speed for $\Delta s/R = 0$ and $\Delta s/R = -8$ with varying overdrive f.

5.2 Unstable Eigenvalues

The quantities of interest resulting from the linear stability calculation are the stable and unstable eigenmodes and the corresponding complex growth rate ω which appears as an eigenvalue in (3.2.10). As described in Chapter 3, (3.2.10) is a two-point boundary value problem that we have solved with a shooting algorithm. Due to the difficulties described in Sharpe (1997), we have avoided the CJ case and investigated strictly overdriven ($f > 1$) cases.

We have considered the single-step reversible chemistry model with nine extents of reversibility in one ($k_y = 0$) and two dimensions ($k_y \neq 0$). In one dimension, we have computed the first four modes of instability corresponding to those previously computed by Lee and Stewart (1990) (Section 5.2.1). In two dimensions, we have computed the first three modes of instability corresponding to those previously computed by Short and Stewart (1998) (Section 5.2.1). Sections 5.2.3 shows eigenfunction profiles in one dimension.

5.2.1 One Dimension

For the family of reaction mechanisms discussed in Section 2.2.1, the frequency of the successive one-dimensional modes ($k_y = 0$) is separated by approximately four in nondimensional variables (discussed in Section 3.6), i.e.,

$$\mathcal{I}m(\omega)_{\mathrm{mode}_{k_y=0}\ i+1} - \mathcal{I}m(\omega)_{\mathrm{mode}_{k_y=0}\ i} \approx 4. \tag{5.2}$$

For each extent of reversibility, we have started with an overdrive of 1.2 and solved for a discrete set of unstable eigenvalues corresponding to increasing overdrive until we find a stable eigenvalue ($\mathcal{R}e(\omega) < 0$). We define neutral stability in one dimension ($k_y = 0$) as the point where the real part of ω is zero ($\mathcal{R}e(\omega) = 0$) and determine the approximate overdrive value by linear interpolation between adjacent stable and unstable modes. The results of this investigation are given numerically in Tables 5.7–5.15 and graphically

in Figure 5.3. As the mode number increases, the number of unstable eigenvalues with $\mathcal{R}e(\omega) > 0$ decreases for a given extent of reversibility which agrees with Lee and Stewart's results.

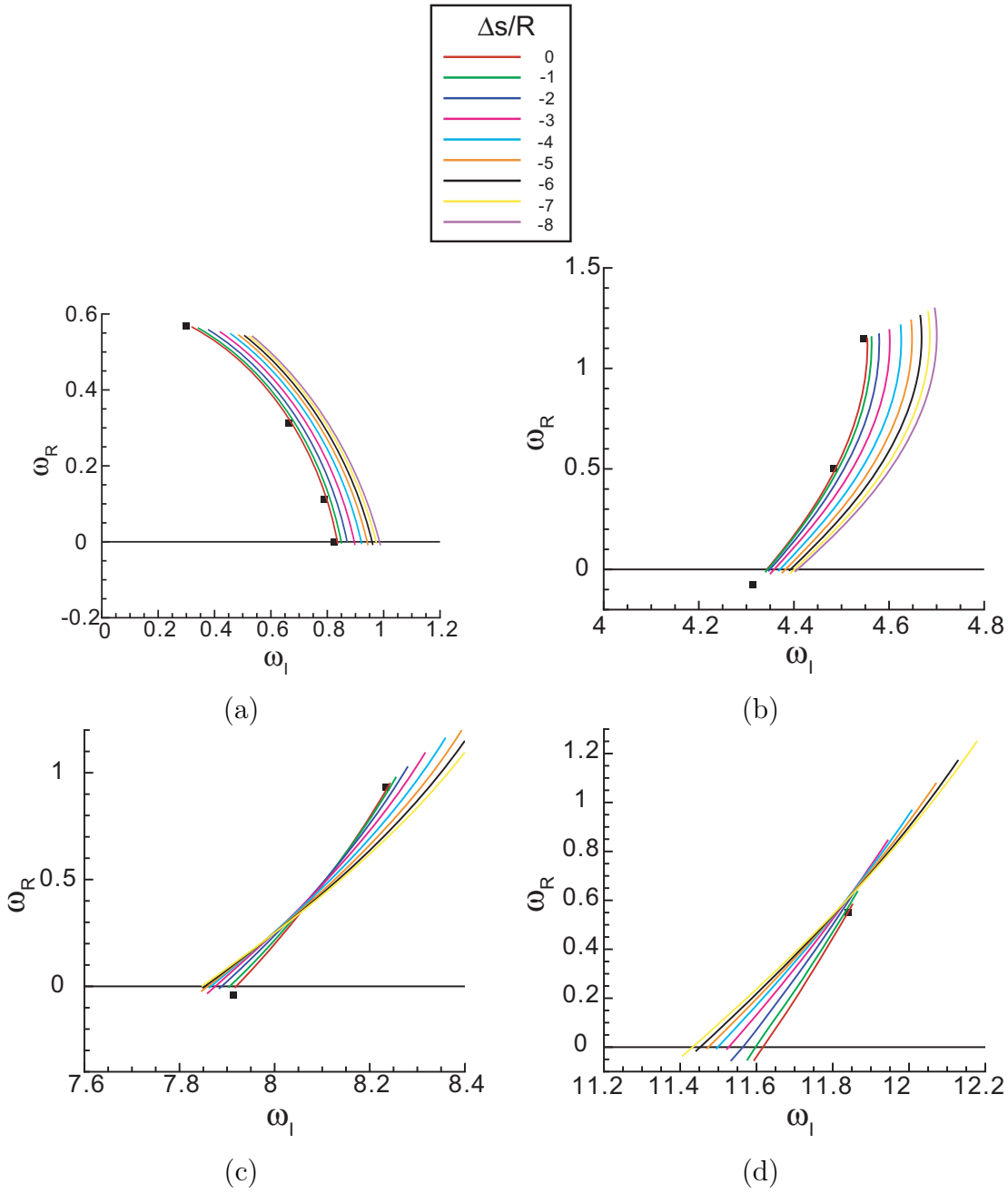

Figure 5.3: Unstable eigenvalues for the first four modes ($k_y = 0$). The real part of the eigenvalue $\omega_{\mathcal{I}}$ is plotted on the x-axis and the imaginary part $\omega_{mathcalR}$ is plotted on the y-axis. (a) Mode 1 ($k_y = 0$) (b) Mode 2 ($k_y = 0$) (c) Mode 3 ($k_y = 0$) (d) Mode 4 ($k_y = 0$)

f	Mode ($k_y = 0$)	$\Delta s/R = 0$	Lee & Stewart	% Difference
1.20	1	$0.564 + i0.341$	$0.569 + i0.300$	$0.88 + i12.0$
1.20	2	$1.160 + i4.563$	$1.148 + i4.547$	$1.0 + i0.35$
1.20	3	$0.981 + i8.256$	$0.933 + i8.234$	$5.1 + i0.27$
1.20	4	$0.638 + i11.866$	$0.550 + i11.84$	$16.0 + i0.22$
1.40	1	$0.304 + i0.692$	$0.313 + i0.664$	$2.9 + i4.0$
1.40	2	$0.526 + i4.499$	$0.504 + i4.484$	$4.4 + i0.33$
1.40	3	$0.039 + i7.924$	$-0.041 + i7.913$	$195.1 + i0.14$
1.60	1	$0.100 + i0.816$	$0.112 + i0.789$	$10.7 + i3.3$
1.71	1	$0.004 + i0.848$		
1.72	1	$-0.005 + i0.851$		
1.731	1		$0.000 + i0.825$	

Table 5.3: Comparison between data calculated in this study for $\Delta s/R = 0$ and data reported in Lee and Stewart (1990).

Also shown in Figure 5.3 as black squares are the results given in Lee and Stewart (1990). We see that these results lie very close to the $\Delta s/R = 0$ curve, which is red in the figures. Table 5.3 gives a comparison of the values we find for $\Delta s/R = 0$ and those reported in Lee and Stewart. There are several differences between the methodology we have used and the methodology in Lee and Stewart. First, they analytically calculated the Chapman-Jouguet detonation velocity, and we used the numerical method described in Browne et al. (2007a). Secondly, Lee and Stewart (1990) algebraically calculated the base state, and we have solved the ZND differential equations alongside the eigenvalue equation (3.2.10). Finally, the reaction used in Lee and Stewart (1990) was truly irreversible where our reaction is reversible with a value of $\Delta s/R$ sufficiently large that the equilibrium value of the product is 0.986. The values of ω we compute are within five percent of the Lee and Stewart values for most cases, and the greater differences may be attributed to the differences in methodologies. The large difference (195%) for mode 3 and $f = 1.4$ is due to the fact that it is very close to the stability boundary. Lee and Stewart (1990) find that this case is stable and we report that this case is unstable.

5.2.2 Two Dimensions

We have investigated the first three two-dimensional modes as a function of the transverse wave number for three of the nine extents of reversibility and two overdrive values. Again, for each extent of reversibility, we have specified an overdrive value, varied k_y, and solved for a discrete set of unstable eigenvalues. We vary k_y between zero and the value of k_y corresponding to neutral stability. To determine the value of k_y that gives neutral stability, we linearly interpolate.

First we verified that we could reproduce the results presented in Short and Stewart (1998). Short uses a different normalization than that used in Lee and Stewart (1990). In their two-dimensional calculations, they chose the reference length scale such that $\tilde{x}_{1/2} = \dfrac{x}{x_c} = a_{f2} \cdot t_c$ and the reference time scale $t_c = 1$ where a_{f2} is the frozen post-shock sound speed. The formula for normalizing the pre-exponential A (2.1.20) then becomes

$$\tilde{A} = A t_c \frac{x_{Y_{\mathcal{B}=0.5}}}{\tilde{x}_{1/2}}. \tag{5.3}$$

For $\tilde{\beta} = \tilde{E}_a = 50$ and $\gamma = f = 1.2$,

$$\tilde{x}_{1/2} = 646.66 \quad \tilde{t}_{1/2} = 2.5616 \quad \tilde{A} = 3.364753 \cdot 10^2. \tag{5.4}$$

In addition to choosing the correct parameters for the Cantera input file, we needed to compute the CJ velocity U_{CJ} analytically to correctly compare our computations with those from Short and Stewart. For all computations other than this comparison, we have used the algorithms from the Shock and Detonation Toolbox (Browne et al., 2007b) to calculate U_{CJ}. To compute U_{CJ} analytically, we use the following formulas (Thompson, 1988)

$$M_{CJ} = \sqrt{\frac{(\gamma^2 - 1)\tilde{\beta}}{2\gamma} + 1} + \sqrt{\frac{(\gamma^2 - 1)\tilde{\beta}}{2\gamma}} \tag{5.5}$$

$$U_{CJ} = M_{CJ} \cdot a_{f1}. \tag{5.6}$$

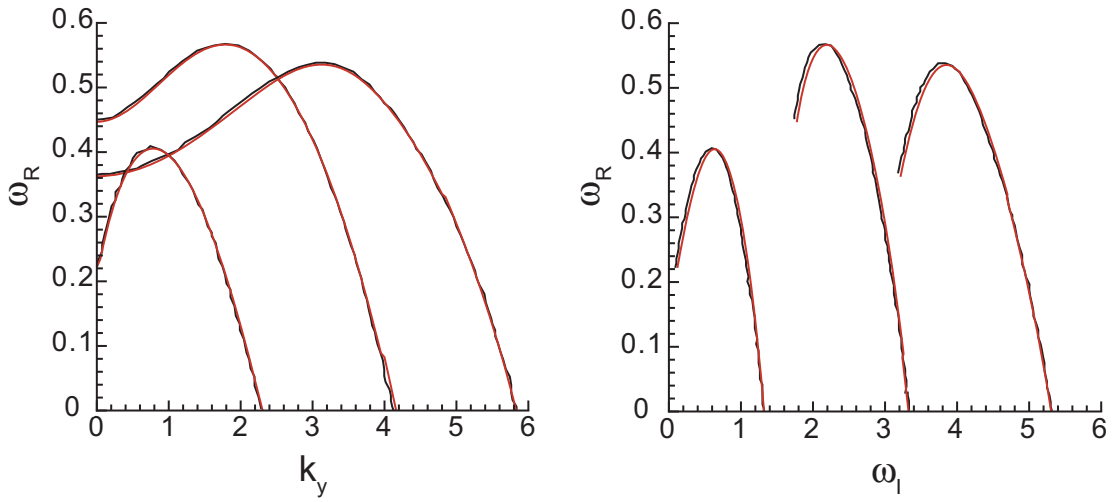

Figure 5.4: Comparison of two-dimensional results from Short and Stewart (1998) (black curves) with results from the current study (red curves). $\tilde{E}_a = \tilde{\beta} = 50$, $\gamma = f = 1.2$, irreversible kinetics.

Figure 5.4 graphically compares the results presented in Short and Stewart and the present study. Because Short and Stewart only provide graphical results, we have digitized their graph to get values for quantitative comparison. Figure 5.5 shows the relative percent difference corresponding to the data shown in Figure 5.4. The differences are between one and ten percent with a few exceptions. Some of the large differences may be due to the digitization of Short and Stewart's data.

We then proceeded to investigate the effects of reversibility on the two-dimensional problem. The results of this investigation are given numerically in Tables 5.16–5.21 and graphically in Figure 5.7. We see that the ordering of the dependence on $\Delta s/R$ is opposite for mode one than for modes two and three. For mode one, the lowest curve corresponds to $\Delta s/R = -8$ while for modes two and three, $\Delta s/R = -8$ corresponds to the highest curve.

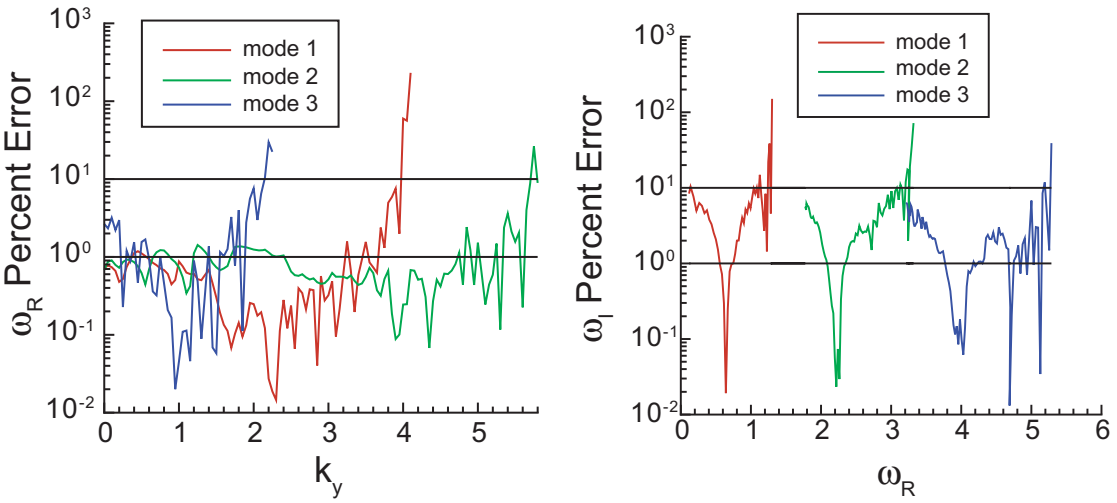

Figure 5.5: Relative percent difference between digitized data from Short and Stewart (1998) and data from the current study. $\tilde{E}_a = \tilde{\beta} = 50$, $\gamma = f = 1.2$, irreversible kinetics. Black lines indicate 1% and 10% difference.

5.2.3 Eigenfunctions

Figure 5.8a and b show eigenfunction profiles $\mathbf{z}^1(x)$ (3.2.8) for the two extreme cases ($\Delta s/R = 0$ and $\Delta s/R = -8$) at the lowest overdrive value ($f = 1.2$) and mode number (mode 1) in one dimension ($k_y = 0$). The complex growth rates for these eigenfunctions are $\omega = 0.566 + i0.318$ and $\omega = 0.543 + i0.533$, respectively. Qualitatively, the eigenfunction profiles are similar. There appears to be one-half wave length of oscillation in the perturbation values within the reaction zone. Quantitatively, as the energy pulse width ($\Delta_{e,ZND}$) of the base flow decreases, the eigenvalue peak narrows. The energy pulse width of the base flow thermicity is shown in Figure 5.8.

Figure 5.8a, c, and d also illustrate the how the eigenfunction profiles change with mode number. These three figures are for $\Delta s/R = 0$ and $f = 1.2$. The imaginary portion of the eigenfunctions describes the oscillatory behavior of the perturbation. We see that as the mode number increases, the number of nodes in the reaction zone increases. In general, the region of energy release in the reaction zone creates a variation of flow properties that partially reflects and transmits the perturbations. This is schematically

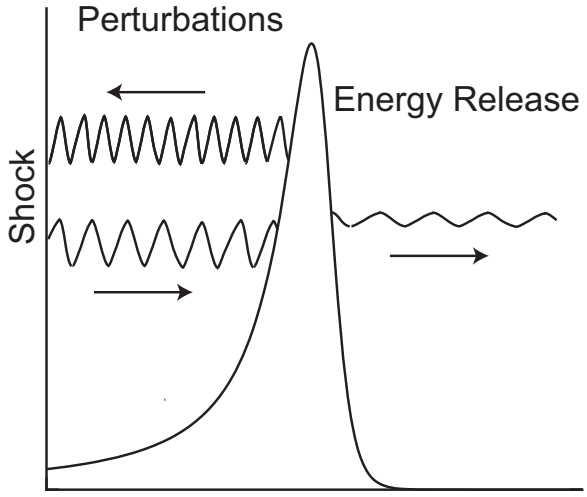

Figure 5.6: Schematic of acoustic resonance between the shock front and the energy release zone.

depicted in Figure 5.6. If we assume a constant frequency for all three waves depicted, the following approximate relationships exist between the wave lengths:

$$\lambda_{\text{upstream}} \approx \frac{\text{u} - a_f}{\text{u} + a_f}\lambda_{\text{downstream}} \approx \frac{1}{2}\lambda_{\text{downstream}} \tag{5.7}$$

$$\lambda_{\text{tail}} \approx \frac{\text{u} + a_f|_{x_R}}{\text{u} + a_f}\lambda_{\text{downstream}} \approx \frac{3}{2}\lambda_{\text{downstream}}. \tag{5.8}$$

The perturbations can be thought of as generalized acoustic disturbances that propagate upstream and downstream between the oscillating shock and energy release zone. We speculate that discrete unstable modes exist due to a resonance between the shock oscillations and the upstream propagating waves (see Sections 5.5 and 7.2.2). The spatial wave length of the unstable modes appears to be an integral fraction of the reaction zone length.

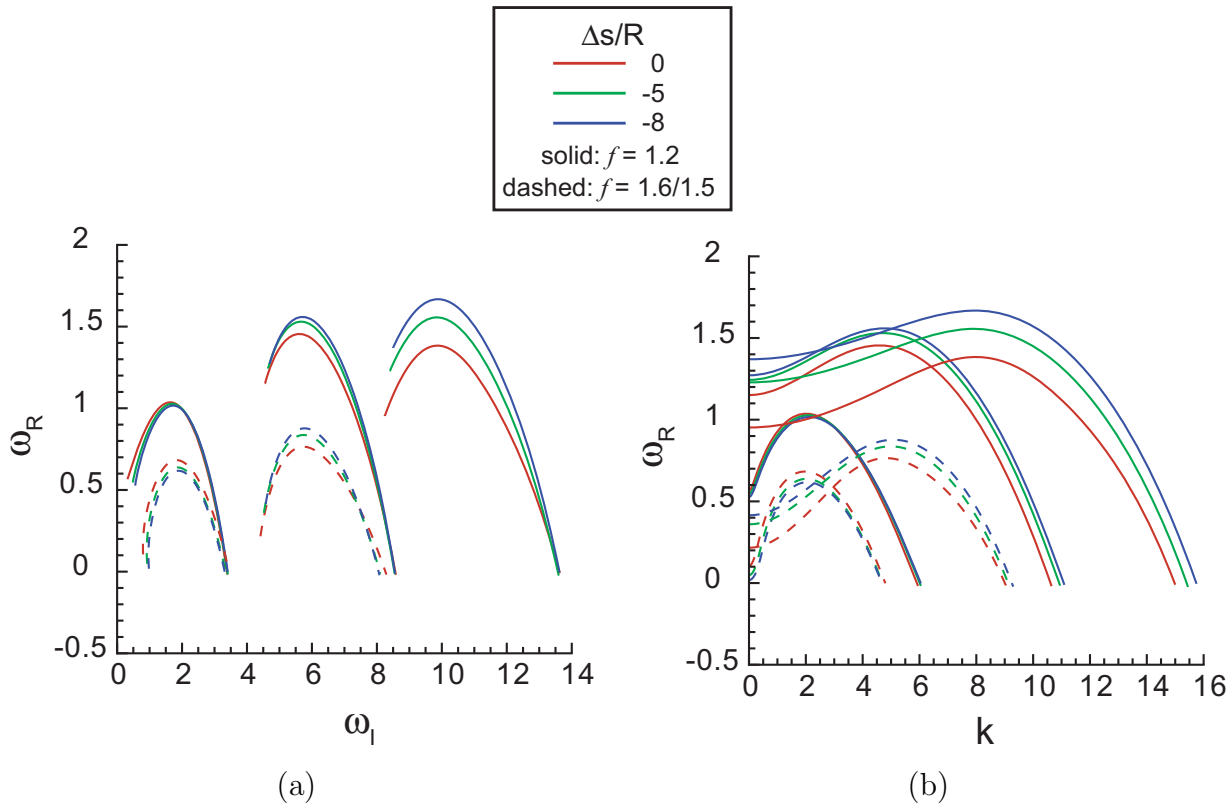

Figure 5.7: Unstable modes for three extents of reversibility ($\Delta s/R = 0, -5, -8$) varying transverse wave number k_y. Mode 1 ($k_y = 0$): $f = 1.2$ (solid), $f = 1.6$ (dashed), Mode 2 ($k_y = 0$): $f = 1.2$ (solid), $f = 1.5$ (dashed), and Mode 3 ($k_y = 0$): $f = 1.2$ (solid)

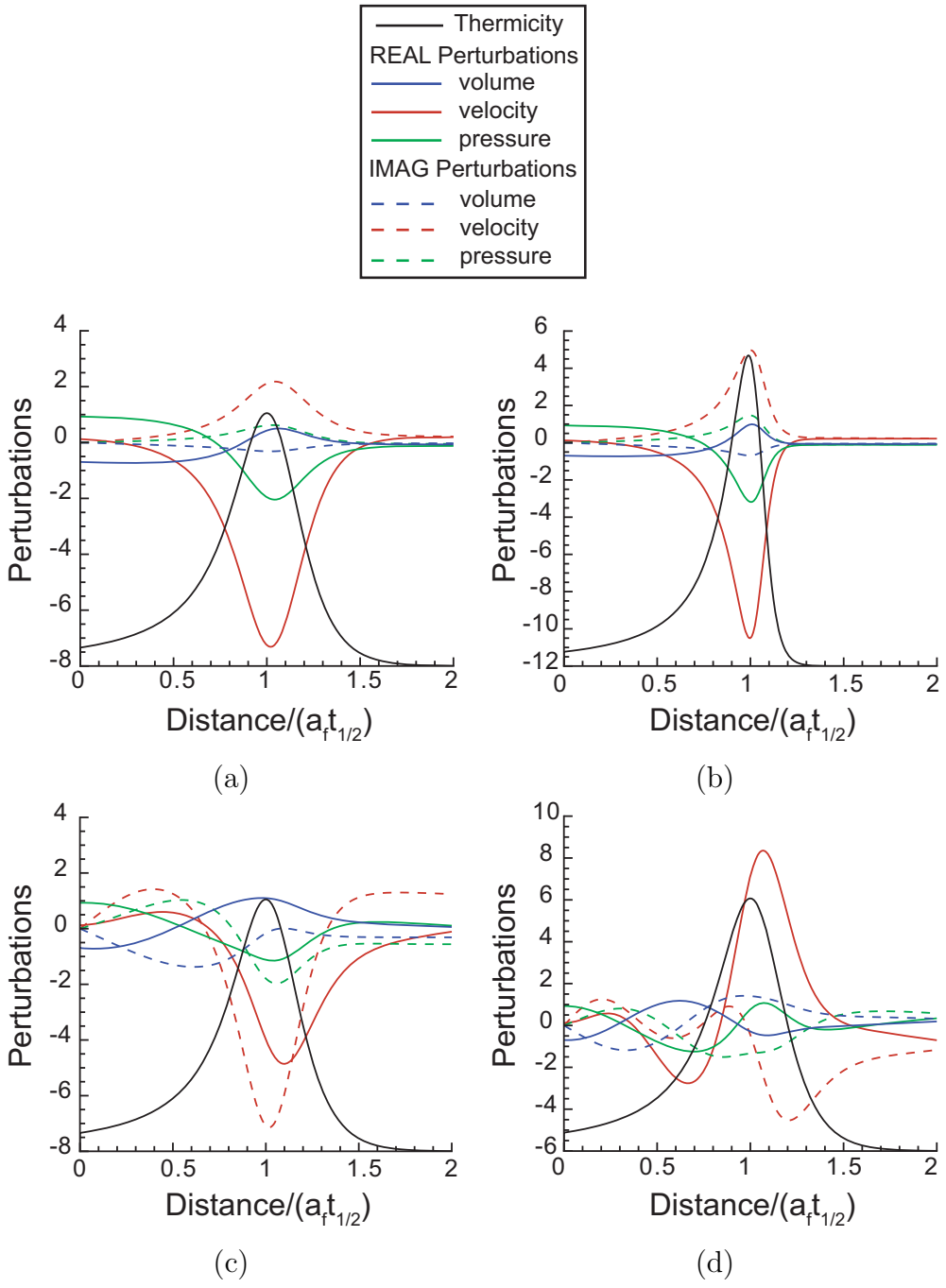

Figure 5.8: Eigenfunction profiles $\mathbf{z}^1(x)$ (3.2.8) for $f = 1.2$ and (a) Mode 1 ($k_y = 0$), $\Delta s/R = 0$, (b) Mode 1 ($k_y = 0$), $\Delta s/R = -8$, (c) Mode 2 ($k_y = 0$), $\Delta s/R = 0$, (d) Mode 3 ($k_y = 0$), $\Delta s/R = 0$.

$\Delta s/R$	$\tau\|_{x_R}$ (s)	$\tau^*\|_{x_R}$ (s)	$\tau_{i,ZND}$	$\tau_{e,ZND}$	$2\pi/\mathcal{I}m(\omega)$ $(k_y = 0)$			
					Mode 1	Mode 2	Mode 3	Mode 4
0	0.0497	0.04730	1.049	0.2873	19.758	1.3797	0.7622	0.5301
-2	0.0514	0.0404	1.054	0.2621	16.666	1.3722	0.7588	0.5282
-4	0.0548	0.0301	1.059	0.2223	13.809	1.3588	0.7516	0.5232
-6	0.0580	0.0223	1.061	0.1866	12.442	1.3469	0.7446	0.5180
-8	0.0604	0.0172	1.063	0.1560	11.788	1.3380	0.7394	0.5142

Table 5.4: Time scale comparisons for varying extents of reversibility. Complex growth rates for modes one and four are given for the lowest overdrive value ($f = 1.2$).

5.3 Perturbation Regime

Now that we have presented our results and compared them with previous work, it is interesting to compare relevant time scales both within and far from the reaction zone. The results given in this section are in one dimension ($k_y = 0$).

5.3.1 Far from the Reaction Zone

As we discussed in Section 4.3, the characteristic polynomial of the algebraic eigenvalue problem necessary to determine the radiation condition can be derived from the wave hierarchy equation,

$$\tau^*|_{x_R} \left(\frac{a_e}{a_f}\right)^2_{x_R} \frac{\mathrm{D}}{\mathrm{D}t}\left[\left(\frac{\mathrm{D}}{\mathrm{D}t}\right)^2 \mathrm{u}' - a_f^2 \mathrm{u}'_{,xx}\right]_{x_R} + \left[\left(\frac{\mathrm{D}}{\mathrm{D}t}\right)^2 \mathrm{u}' - a_e^2 \mathrm{u}'_{,xx}\right]_{x_R} = 0. \tag{5.9}$$

It is of interest to investigate how the perturbation time scales are related to the characteristic relaxation time scales and if the perturbations correspond more to one operator than the other. There are two limiting behaviors of this expression. As $-\omega\tau^*|_{x_R} (a_e/a_f)^2_{x_R}$ approaches zero, the equation reduces to an equilibrium wave equation,

$$\left(\frac{\mathrm{D}}{\mathrm{D}t}\right)^2 \mathrm{u}' - a_e|^2_{x_R} \mathrm{u}'_{,xx} = 0, \tag{5.10}$$

and as $-\omega\tau^*|_{x_R}\,(a_e/a_f)^2_{x_R}$ approaches infinity, the equation is a frozen wave equation,

$$\left(\frac{\mathrm{D}}{\mathrm{D}t}\right)^2 \mathrm{u}' - a_f|^2_{x_R}\mathrm{u}'_{,xx} = 0. \tag{5.11}$$

If our problem lies in either of these limiting regimes, the boundary condition simplifies. If $-\omega\tau^*|_{x_R}\,(a_e/a_f)^2_{x_R}$ is order one, both wave operators will be important.

We may achieve these limiting behaviors because the equilibration time scale remains constant as ω varies. When the time scale of the perturbation ($2\pi/\mathcal{I}m(\omega)$) is smaller than the chemical equilibrium time scale, the perturbations will be frozen ($\mathbf{Y}' = \mathbf{0}$) because there will not be sufficient time to come to equilibrium. On the other hand, if the time scale of the perturbation becomes greater than the equilibration time scale, the system will have time to equilibrate, $\mathbf{Y}' = \mathbf{Y}'_{eq}(T', P')$. We expect that low-order modes with large perturbation time scales will be in equilibrium and as we increase the mode number, and decrease the perturbation time scale, we will eventually achieve a frozen situation.

Figure 5.9 shows how $-\omega\tau^*|_{x_R}\,(a_e/a_f)^2_{x_R}$ varies with overdrive for four different cases in one dimension ($k_y = 0$). We see that for all cases, the real part of the $-\omega\tau^*|_{x_R}\,(a_e/a_f)+{x_R}^2$ remains $\ll 1$, but as we increase the mode number the imaginary part approaches one. Theoretically if we increase the mode number further, we will approach $\mathcal{I}m(-\omega\tau^*|_{x_R}\,(a_e/a_f)+{x_R}^2) \gg 1$.

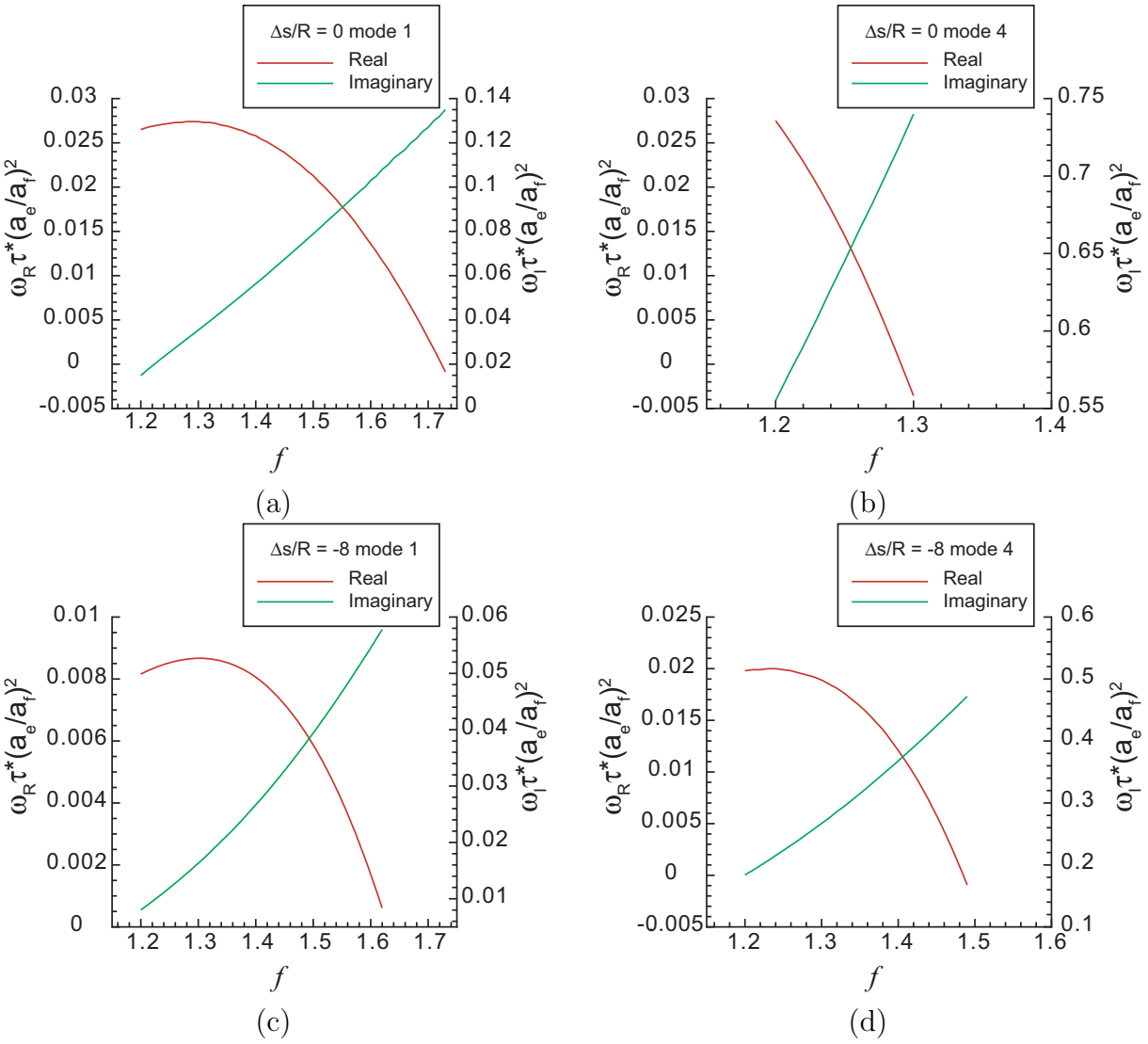

Figure 5.9: $-\omega\tau^*|_{x_R}\,(a_e/a_f) + {x_R}^2$ as a function of overdrive for four cases (a) Mode 1 ($k_y = 0$), $\Delta s/R = 0$, (b) Mode 4 ($k_y = 0$), $\Delta s/R = 0$, (c) Mode 1 ($k_y = 0$), $\Delta s/R = -8$, (d) Mode 4 ($k_y = 0$), $\Delta s/R = -8$.

It is useful to compare the chemical relaxation time scales with the perturbation time scale. We characterize the perturbation time scale as $2\pi/\mathcal{I}m(\omega)$, but there two choices for the chemical relaxation time scale: the near-equilibrium relaxation time constant ($\tau|_{x_R}$) and the function of $\tau|_{x_R}$ which appears in the hierarchy equation ($\tau^*|_{x_R}$ (4.3.24)). Table 5.4 compares these time scales. In this table, $1/\mathcal{I}m(\omega)$ is given for $f = 1.2$. It is interesting to note that because $\tau^*|_{x_R}$ also depends on derivatives of enthalpy, it decreases with increasing reversibility while $\tau|_{x_R}$ increases.

The values in Table 5.4 indicate that for mode one, the period of perturbation oscillation ($1/\mathcal{I}m(\omega)$) is three orders of magnitude greater than the chemical equilibration time scale ($\tau|_{x_R}$). For all mode numbers investigated, the perturbation time scale is greater than both $\tau|_{x_R}$ and $\tau^*|_{x_R}$ by at least one order of magnitude. This indicates that we are still in the equilibrium regime of (4.3.23), and the period of the perturbation is long enough that it allows the composition to remain in equilibrium which agrees with Figure 5.9. If we had investigated mode five, the perturbation time scale may have been on the order of both $\tau|_{x_R}$ and $\tau^*|_{x_R}$.

5.3.2 Reaction Zone

We can also compare the perturbation time scale $2\pi/\mathcal{I}m(\omega)$ to the reaction zone time scales: the induction time ($\tau_{i,ZND}$), and the energy release pulse width time ($\tau_{e,ZND}$). The perturbation time scale is greater than $\tau_{e,ZND}$ for all mode numbers in one dimension ($k_y = 0$) although it is the same order of magnitude for modes three and four. On the other hand, $2\pi/\mathcal{I}m(\omega)$ is an order of magnitude larger than $\tau_{i,ZND}$ for mode one, the same order of magnitude for mode two, slightly more than half for mode three, and approximately half for mode four.

Alpert and Toong (1972) give a discussion of the nonlinear mechanism of the longitudinal oscillation in a square-wave detonation. They observed two distinct frequencies of oscillation in hydrogen and oxygen, a low-frequency mode with period ($3.8 - 5.4\tau_{i,ZND}$) and a high-frequency mode with period ($\approx 1.6\tau_{i,ZND}$). Their low-frequency mode affects

the location of the reaction zone with respect to the shock unlike their high-frequency mode which does not. In our case, mode one has a period of $\approx 10 - 20\tau_{i,ZND}$, mode two has a period of $\approx 1.3\tau_{i,ZND}$, mode three has a period of $\approx 0.7\tau_{i,ZND}$, and mode four has a period of $\approx 0.5\tau_{i,ZND}$.

Another measure of the reaction time scale is the total reaction time, $\tau_{i,ZND} + \tau_{e,ZND}/2$, and Figure 5.10 shows how the ratio of this reaction time scale to the perturbation time scale is a function of the mode number. For $\Delta s/R = 0$,

$$\frac{\tau_{i,ZND} + \frac{\tau_{e,ZND}}{2}}{\frac{2\pi}{\mathcal{I}m(\omega)}} = 0.7269(n-1) + 0.0945 \tag{5.12}$$

and for $\Delta s/R = -8$,

$$\frac{\tau_{i,ZND} + \frac{\tau_{e,ZND}}{2}}{\frac{2\pi}{\mathcal{I}m(\omega)}} = 0.7057(n-1) + 0.1193 \tag{5.13}$$

where n is the mode number. We can relate the period of oscillation $2\pi/\mathcal{I}m(\omega)$ to the wave length of the perturbations λ,

$$\frac{\lambda}{\frac{2\pi}{\mathcal{I}m(\omega)}} = c_\phi, \tag{5.14}$$

and conclude that λ is on the order of $\dfrac{1}{n-1}$.

$$\lambda \approx \mathcal{O}\left(\frac{\tau_{i,ZND} + \frac{\tau_{e,ZND}}{2}}{n-1}\right) \tag{5.15}$$

Using this expression, we can re-evaluate why (5.2) is true.

$$\mathcal{I}m(\omega) \approx 2\pi \frac{c_\phi}{\tau_{i,ZND} + \frac{\tau_{e,ZND}}{2}}(n-1) \cdot 0.71 \tag{5.16}$$

$$\Delta\mathcal{I}m(\omega) \approx 2\pi \frac{c_\phi}{\tau_{i,ZND} + \frac{\tau_{e,ZND}}{2}} \cdot 0.71. \tag{5.17}$$

If we assume that $c_\phi/(\tau_{i,ZND} + \tau_{e,ZND}/2)$ is approximately one,

$$\Delta\mathcal{I}m(\omega) \approx 4.5. \tag{5.18}$$

Although this is an approximation, it is a reasonable approximation for the frequency spacing that we see.

The expression for the perturbation wave length (5.15) confirms that mode one behaves differently than the higher order modes. This may indicate that mode one is a quasi-steady breathing mode corresponding to Alpert and Toong's low-frequency mode and affects the length scales of the reaction zone. On the other hand, for modes two and higher, the perturbation oscillation time scale is proportional to a fraction of the reaction time which is consistent with the resonator interpretation of the instability (Chiu and Lee, 1976).

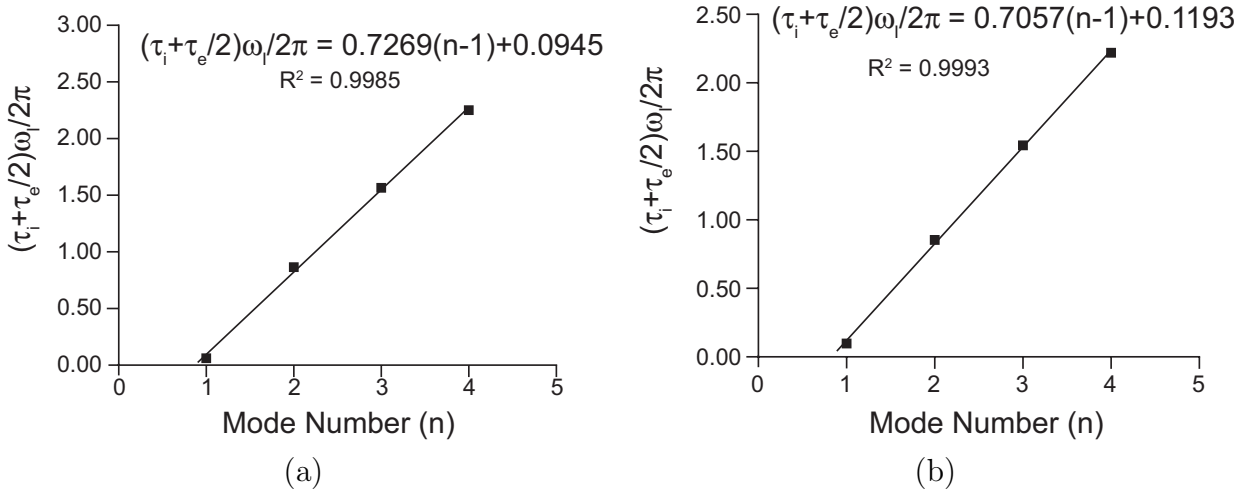

Figure 5.10: Ratio of reaction zone length $(\tau_{i,ZND} + \tau_{e,ZND}/2)$ to oscillation frequency $(2\pi/\mathcal{I}m(\omega))$ vs. one-dimensional mode number. Data corresponds to values given in Table 5.4. Linear fit equations are given for each case. (a) $\Delta s/R = 0$, $f = 1.2$ (b) $\Delta s/R = -8$, $f = 1.2$

$\Delta s/R$	$f_{\mathcal{R}e(\omega)=0}$			
	Mode 1 ($k_y = 0$)	Mode 2 ($k_y = 0$)	Mode 3 ($k_y = 0$)	Mode 4 ($k_y = 0$)
0	1.7234	1.5777	1.3985	1.2910
-1	1.7144	1.5848	1.4088	1.3016
-2	1.6990	1.5975	1.4273	1.3204
-3	1.6803	1.6111	1.4517	1.3482
-4	1.6632	1.6267	1.4781	1.3785
-5	1.6502	1.6421	1.5038	1.4085
-5.3167		1.6469		
-6	1.6410	1.6570	1.5279	1.4364
-7	1.6348	1.6712	1.5499	1.4619
-8	1.6305	1.6846	1.5702	1.4850

Table 5.5: Neutral stability ($\mathcal{R}e(\omega) = 0$) overdrive values for modes one through four with varying extents of reversibility. The approximate crossover value for modes 1 and 2 is given.

5.4 Neutral Stability

Previous research (Lee and Stewart, 1990, Short, 1997) indicates that if a detonation in sufficiently overdriven, it will be linearly stable to all perturbations. Table 5.5 and Figure 5.11 illustrate the neutral stability curves ($\mathcal{R}e(\omega) = 0$) for modes one through four from our study in one dimension ($k_y = 0$). We determined the value of f when $\mathcal{R}e(\omega) = 0$ by interpolating between the smallest unstable eigenvalue and the first stable eigenvalue. For mode one, increasing reversibility has a stabilizing effect so that, as the system becomes more reversible, the overdrive corresponding to the neutral stability decreases. On the other hand, for modes two, three, and four, reversibility has a destabilizing effect.

Similar stability exchange behavior between the modes was noted in Lee and Stewart (1990) and Short and Stewart (1998) in Figure 5.4 and Tables 5.16–5.21. In these previous studies, there were exchanges of stability due to the activation energy E_a, the isentropic coefficient γ, and the transverse wave number k_y. We see that, in one dimension, reversibility, characterized by $\Delta s/R$, is another parameter that leads to an exchange of stability.

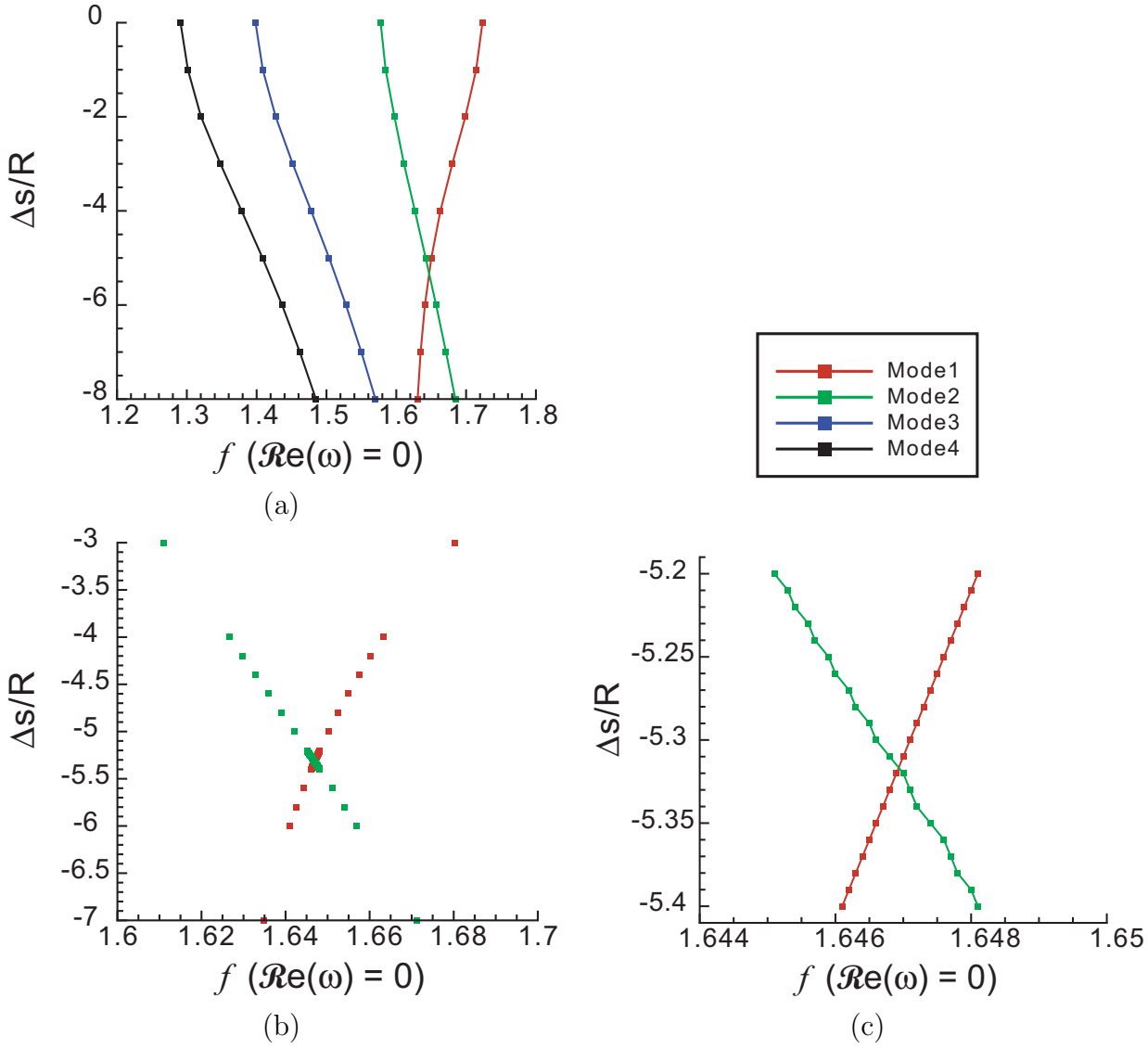

Figure 5.11: (a) Neutral stability ($\mathcal{R}e(\omega) = 0$) curves for modes one through four with varying extents of reversibility. (b) and (c) are refinements of (a) for modes 1 and 2.

5.5 Acoustic Impedance

Tumin (2007a) has suggested that chemical feedback plays a limited role in the amplification of perturbations. He proposes that the detonation instability is primarily associated with resonance of acoustic waves trapped between the shock front and the energy release zone. How effectively the reaction zone traps acoustic waves and the existence of a resonance mechanism will depend on the acoustic impedance (P'/u') of the shock front and the energy release pulse. This conjecture is based on computations in which the coupling between chemical perturbations $\mathbf{Y}'$ and physical perturbations P', u', and v' has been removed by setting the appropriate coupling terms in the linear stability equation (3.2.10) to zero. these terms appear in the $\mathbf{C}$ matrix (3.2.12).

Figure 5.12 provides a preliminary investigation of how the specific acoustic impedance (Kinsler et al., 1950)

$$\zeta = \left[\frac{P'}{u'}\right] \frac{v^o}{a_f^o} \tag{5.19}$$

varies through the domain for four cases in one dimension ($k_y = 0$). We see that as the mode number increases the number of phase oscillations through the domain also increases. Table 5.6 gives the value of ζ at the shock, at the peak thermicity, and far from the reaction zone. We also note that for three cases (Figure 5.12a,b, and c), the specific complex acoustic impedance is real at the shock and far from the reaction zone but not necessarily at the peak thermicity. In Figure 5.12d, ζ is real at the shock, but complex far from the reaction zone. This is due to the limitations of the shooting method described in Section 3.5.

The fact that $\zeta \approx 1$ and is real far from the reaction zone for all convergent cases means that the rear boundary condition is being properly implemented. The complex values of ζ within the reaction zone can be interpreted as regions of amplification and damping of the acoustic waves. The locus of $\zeta_{\mathcal{I}}$ vs. $\zeta_{\mathcal{R}}$ shows an intriguing oscillatory pattern but the interpretation of this is left to future investigations.

$\Delta s/R$	Mode	ζ		
		shock	$\dot{\sigma}_{max}$	far from rxn
0	1	-0.624	$-0.333 + i0.113$	$0.995 - i5.95 \cdot 10^{-4}$
0	4	-0.624	$-3.83 + i0.143$	$1.00 - i4.23 \cdot 10^{-3}$
-8	1	-0.624	$-0.455 + i0.089$	$0.936 - i2.79 \cdot 10^{-3}$
-8	4	-0.624	$-0.810 + i1.01$	$-0.671 - i0.429$

Table 5.6: Specific complex acoustic impedance for the cases shown in Figure 5.12 at the shock, at the thermicity peak, and far from the reaction zone.

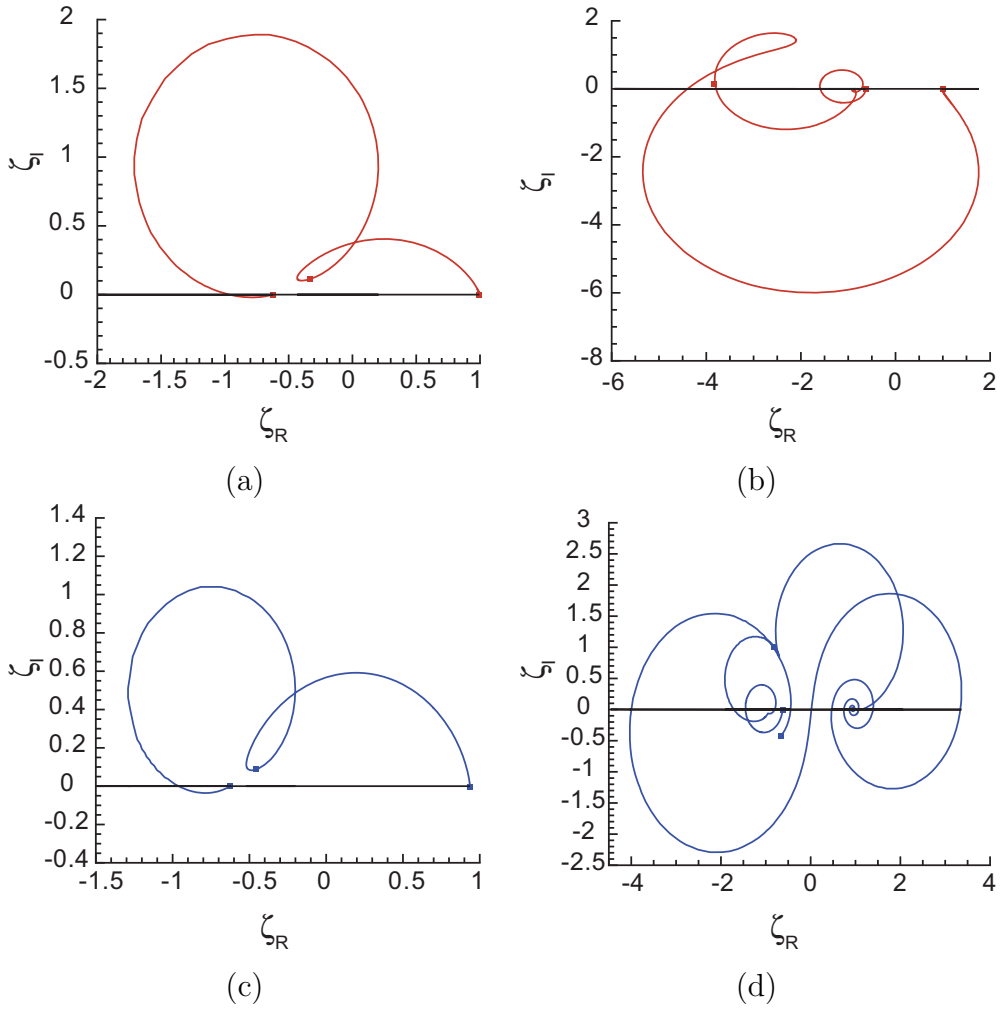

Figure 5.12: Specific complex acoustic impedance $\zeta = (P'/u')/(\rho a_f)$ for $f = 1.2$ and (a) $\Delta s/R = 0$ mode 1, (b) $\Delta s/R = 0$ mode 4, (c) $\Delta s/R = -8$ mode 1, (d) $\Delta s/R = -8$ mode 4. A line at $\zeta_{\mathcal{I}} = 0$ is provided to indicate where ζ is real.

5.6 Tabular Results

$\Delta s/R = 0$, $k_y = 0$				
f	Mode 1	Mode 2	Mode 3	Mode 4
1.20	$0.566 + i0.318$	$1.152 + i4.554$	$0.953 + i8.243$	$0.586 + i11.853$
1.29	$0.442 + i0.539$	$0.857 + i4.542$	$0.517 + i8.115$	$0.006 + i11.619$
1.30	$0.429 + i0.555$	$0.825 + i4.539$	$0.469 + i8.099$	$-0.056 + i11.593$
1.39	$0.321 + i0.667$	$0.544 + i4.496$	$0.040 + i7.936$	
1.40	$0.309 + i0.676$	$0.513 + i4.490$	$-0.007 + i7.916$	
1.50	$0.203 + i0.752$	$0.218 + i4.415$		
1.57	$0.134 + i0.788$	$0.021 + i4.351$		
1.58	$0.125 + i0.793$	$-0.006 + i4.341$		
1.60	$0.106 + i0.801$			
1.70	$0.019 + i0.831$			
1.72	$0.003 + i0.835$			
1.73	$-0.005 + i0.837$			

Table 5.7: Unstable growth rates for $\Delta s/R = 0$ with varying overdrive f for the first four one-dimensional modes ($k_y = 0$).

$\Delta s/R = -1$, $k_y = 0$				
f	Mode 1	Mode 2	Mode 3	Mode 4
1.20	$0.564 + i0.341$	$1.160 + i4.563$	$0.981 + i8.256$	$0.638 + i11.866$
1.30	$0.425 + i0.571$	$0.834 + i4.548$	$0.506 + i8.109$	$0.010 + i11.602$
1.31	$0.412 + i0.586$	$0.803 + i4.545$	$0.459 + i8.093$	$-0.055 + i11.575$
1.40	$0.304 + i0.692$	$0.526 + i4.499$	$0.039 + i7.924$	
1.41	$0.293 + i0.701$	$0.496 + i4.493$	$-0.005 + i7.903$	
1.50	$0.197 + i0.767$	$0.234 + i4.423$		
1.58	$0.118 + i0.808$	$0.013 + i4.349$		
1.59	$0.109 + i0.812$	$-0.014 + i4.339$		
1.60	$0.100 + i0.816$			
1.70	$0.012 + i0.846$			
1.71	$0.004 + i0.848$			
1.72	$-0.005 + i0.851$			

Table 5.8: Unstable growth rates for $\Delta s/R = -1$ with varying overdrive f for the first four one-dimensional modes ($k_y = 0$).

$\Delta s/R = -2$, $k_y = 0$				
f	Mode 1	Mode 2	Mode 3	Mode 4
1.20	$0.559 + i0.377$	$1.175 + i4.579$	$1.030 + i8.280$	$0.729 + i11.895$
1.30	$0.418 + i0.598$	$0.851 + i4.565$	$0.569 + i8.133$	$0.125 + i11.626$
1.32	$0.392 + i0.627$	$0.789 + i4.558$	$0.477 + i8.098$	$0.003 + i11.566$
1.33	$0.380 + i0.640$	$0.758 + i4.553$	$0.432 + i8.080$	$-0.057 + i11.532$
1.40	$0.296 + i0.717$	$0.547 + i4.516$	$0.118 + i7.945$	
1.42	$0.273 + i0.735$	$0.488 + i4.503$	$0.031 + i7.903$	
1.43	$0.262 + i0.743$	$0.459 + i4.495$	$-0.011 + i7.883$	
1.50	$0.187 + i0.792$	$0.260 + i4.440$		
1.59	$0.098 + i0.837$	$0.017 + i4.356$		
1.60	$0.088 + i0.840$	$-0.009 + i4.346$		
1.69	$0.008 + i0.868$			
1.70	$-0.001 + i0.871$			

Table 5.9: Unstable growth rates for $\Delta s/R = -2$ with varying overdrive f for the first four one-dimensional modes ($k_y = 0$).

$\Delta s/R = -3$, $k_y = 0$				
f	Mode 1	Mode 2	Mode 3	Mode 4
1.20	$0.554 + i0.418$	$1.195 + i4.601$	$1.095 + i8.317$	$0.848 + i11.946$
1.30	$0.410 + i0.631$	$0.874 + i4.588$	$0.650 + i8.170$	$0.274 + i11.676$
1.34	$0.358 + i0.684$	$0.752 + i4.573$	$0.474 + i8.100$	$0.046 + i11.553$
1.35	$0.345 + i0.696$	$0.722 + i4.568$	$0.431 + i8.081$	$-0.010 + i11.521$
1.40	$0.285 + i0.748$	$0.574 + i4.540$	$0.216 + i7.983$	
1.45	$0.228 + i0.789$	$0.431 + i4.505$	$0.007 + i7.878$	
1.46	$0.217 + i0.796$	$0.403 + i4.497$	$-0.034 + i7.858$	
1.50	$0.174 + i0.822$	$0.292 + i4.464$		
1.60	$0.073 + i0.871$	$0.029 + i4.370$		
1.61	$0.064 + i0.874$	$0.003 + i4.360$		
1.62	$0.055 + i0.878$	$-0.023 + i4.349$		
1.68	$0.000 + i0.896$			
1.69	$-0.008 + i0.898$			

Table 5.10: Unstable growth rates for $\Delta s/R = -3$ with varying overdrive f for the first four one-dimensional modes ($k_y = 0$).

$\Delta s/R = -4$, $k_y = 0$				
f	Mode 1	Mode 2	Mode 3	Mode 4
1.20	$0.549 + i0.455$	$1.219 + i4.624$	$1.164 + i8.360$	$0.971 + i12.008$
1.30	$0.402 + i0.661$	$0.901 + i4.614$	$0.733 + i8.216$	$0.425 + i11.743$
1.37	$0.312 + i0.748$	$0.691 + i4.584$	$0.439 + i8.090$	$0.046 + i11.526$
1.38	$0.299 + i0.758$	$0.662 + i4.579$	$0.397 + i8.070$	$-0.008 + i11.494$
1.40	$0.275 + i0.777$	$0.604 + i4.567$	$0.315 + i8.031$	
1.47	$0.194 + i0.833$	$0.408 + i4.517$	$0.032 + i7.883$	
1.48	$0.183 + i0.839$	$0.380 + i4.509$	$-0.008 + i7.862$	
1.50	$0.162 + i0.852$	$0.326 + i4.492$		
1.60	$0.059 + i0.900$	$0.067 + i4.397$		
1.62	$0.040 + i0.907$	$0.017 + i4.377$		
1.63	$0.031 + i0.911$	$-0.008 + i4.367$		
1.66	$0.003 + i0.920$			
1.67	$-0.006 + i0.922$			

Table 5.11: Unstable growth rates for $\Delta s/R = -4$ with varying overdrive f for the first four one-dimensional modes ($k_y = 0$).

$\Delta s/R = -5$, $k_y = 0$				
f	Mode 1	Mode 2	Mode 3	Mode 4
1.20	$0.546 + i0.484$	$1.243 + i4.646$	$1.228 + i8.401$	$1.081 + i12.072$
1.30	$0.397 + i0.686$	$0.928 + i4.638$	$0.810 + i8.262$	$0.559 + i11.813$
1.40	$0.267 + i0.802$	$0.634 + i4.593$	$0.405 + i8.080$	$0.043 + i11.503$
1.41	$0.255 + i0.811$	$0.606 + i4.587$	$0.365 + i8.060$	$-0.008 + i11.469$
1.50	$0.152 + i0.876$	$0.360 + i4.520$	$0.015 + i7.868$	
1.51	$0.141 + i0.882$	$0.333 + i4.511$	$-0.024 + i7.845$	
1.60	$0.048 + i0.925$	$0.103 + i4.425$		
1.64	$0.010 + i0.938$	$0.005 + i4.385$		
1.65	$0.000 + i0.942$	$-0.019 + i4.374$		
1.66	$-0.009 + i0.944$			

Table 5.12: Unstable growth rates for $\Delta s/R = -5$ with varying overdrive f for the first four one-dimensional modes ($k_y = 0$).

$\Delta s/R = -6$, $k_y = 0$				
f	Mode 1	Mode 2	Mode 3	Mode 4
1.20	$0.544 + i0.505$	$1.266 + i4.665$	$1.284 + i8.438$	$1.174 + i12.129$
1.30	$0.393 + i0.705$	$0.953 + i4.660$	$0.877 + i8.304$	$0.673 + i11.878$
1.40	$0.262 + i0.821$	$0.663 + i4.616$	$0.483 + i8.125$	$0.178 + i11.574$
1.43	$0.226 + i0.847$	$0.579 + i4.598$	$0.368 + i8.065$	$0.031 + i11.474$
1.44	$0.214 + i0.855$	$0.552 + i4.591$	$0.330 + i8.044$	$-0.017 + i11.440$
1.50	$0.146 + i0.896$	$0.391 + i4.545$	$0.104 + i7.915$	
1.52	$0.124 + i0.908$	$0.339 + i4.528$	$0.029 + i7.871$	
1.53	$0.113 + i0.913$	$0.313 + i4.519$	$-0.008 + i7.848$	
1.60	$0.040 + i0.945$	$0.137 + i4.451$		
1.64	$0.001 + i0.959$	$0.041 + i4.410$		
1.65	$-0.009 + i0.962$	$0.017 + i4.400$		
1.66		$-0.007 + i4.390$		

Table 5.13: Unstable growth rates for $\Delta s/R = -6$ with varying overdrive f for the first four one-dimensional modes ($k_y = 0$).

$\Delta s/R = -7$, $k_y = 0$				
f	Mode 1	Mode 2	Mode 3	Mode 4
1.20	$0.543 + i0.521$	$1.286 + i4.682$	$1.331 + i8.471$	$1.251 + i12.179$
1.30	$0.391 + i0.720$	$0.975 + i4.678$	$0.934 + i8.340$	$0.768 + i11.935$
1.40	$0.259 + i0.836$	$0.688 + i4.637$	$0.550 + i8.165$	$0.291 + i11.637$
1.46	$0.187 + i0.885$	$0.525 + i4.598$	$0.327 + i8.045$	$0.009 + i11.439$
1.47	$0.175 + i0.892$	$0.499 + i4.591$	$0.290 + i8.023$	$-0.038 + i11.405$
1.50	$0.141 + i0.912$	$0.420 + i4.567$	$0.180 + i7.958$	
1.54	$0.097 + i0.934$	$0.317 + i4.533$	$0.036 + i7.869$	
1.55	$0.086 + i0.939$	$0.292 + i4.523$	$-0.0002 + i7.847$	
1.60	$0.035 + i0.961$	$0.169 + i4.475$		
1.63	$0.005 + i0.972$	$0.097 + i4.444$		
1.64	$-0.005 + i0.975$	$0.073 + i4.434$		
1.67		$0.003 + i4.402$		
1.68		$-0.021 + i4.392$		

Table 5.14: Unstable growth rates for $\Delta s/R = -7$ with varying overdrive f for the first four one-dimensional modes ($k_y = 0$).

$\Delta s/R = -8$, $k_y = 0$				
f	Mode 1	Mode 2	Mode 3	Mode 4
1.20	$0.543 + i0.533$	$1.303 + i4.696$	$1.370 + i8.498$	$1.314 + i12.220$
1.30	$0.389 + i0.731$	$0.994 + i4.694$	$0.981 + i8.371$	$0.847 + i11.983$
1.40	$0.256 + i0.848$	$0.710 + i4.654$	$0.607 + i8.200$	$0.386 + i11.691$
1.48	$0.160 + i0.911$	$0.497 + i4.602$	$0.317 + i8.039$	$0.022 + i11.429$
1.49	$0.149 + i0.918$	$0.471 + i4.594$	$0.282 + i8.018$	$-0.023 + i11.395$
1.50	$0.138 + i0.924$	$0.445 + i4.586$	$0.246 + i7.996$	
1.57	$0.062 + i0.961$	$0.270 + i4.525$	$0.001 + i7.840$	
1.58	$0.051 + i0.966$	$0.245 + i4.515$	$-0.034 + i7.816$	
1.60	$0.031 + i0.974$	$0.197 + i4.496$		
1.63	$0.000 + i0.985$	$0.126 + i4.465$		
1.64	$-0.009 + i0.989$	$0.103 + i4.455$		
1.68		$0.011 + i4.412$		
1.69		$-0.012 + i4.402$		

Table 5.15: Unstable growth rates for $\Delta s/R = -8$ with varying overdrive f for the first four one-dimensional modes ($k_y = 0$).

$\Delta s/R = 0,\ f = 1.2,\ k_y \neq 0$			
k_y	Mode 1	Mode 2	Mode 3
0.00	$0.5657 + i0.3198$	$1.1508 + i4.5542$	$0.9523 + i8.2431$
1.00	$0.9277 + i1.0278$	$1.1875 + i4.6080$	$0.9650 + i8.2661$
2.00	$1.0367 + i1.6217$	$1.2772 + i4.7685$	$1.0018 + i8.3352$
3.00	$0.9544 + i2.1431$	$1.3760 + i5.0299$	$1.0592 + i8.4512$
4.00	$0.7268 + i2.6191$	$1.4428 + i5.3786$	$1.1322 + i8.6165$
5.00	$0.3850 + i3.0468$	$1.4482 + i5.7957$	$1.2144 + i8.8358$
5.90	$0.0048 + i3.3811$	$1.3881 + i6.2111$	$1.2878 + i9.0854$
5.95	$-0.0178 + i3.3981$	$1.3829 + i6.2350$	$1.2916 + i9.1008$
6.00		$1.3775 + i6.2589$	$1.2954 + i9.1164$
7.00		$1.2276 + i6.7499$	$1.3586 + i9.4633$
8.00		$0.9988 + i7.2575$	$1.3835 + i9.8735$
9.00		$0.6873 + i7.7714$	$1.3532 + i10.3333$
10.00		$0.2877 + i8.2750$	$1.2631 + i10.8236$
10.60		$0.0058 + i8.5615$	$1.1833 + i11.1267$
10.65		$-0.0190 + i8.5846$	$1.1759 + i11.1522$
11.00			$1.1211 + i11.3322$
12.00			$0.9349 + i11.8626$
13.00			$0.6976 + i12.4238$
14.00			$0.3905 + i13.0168$
14.95			$0.0126 + i13.5982$
15.00			$-0.0100 + i13.6288$

Table 5.16: Unstable growth rates for $\Delta s/R = 0$ and $f = 1.2$ with varying transverse wave number k_y for the first three two-dimensional modes ($k_y \neq 0$).

$\Delta s/R = -5$, $f = 1.2$, $k_y \neq 0$			
k_y	Mode 1	Mode 2	Mode 3
0.00	$0.5457 + i0.4840$	$1.2435 + i4.6462$	$1.2284 + i8.4012$
1.00	$0.9045 + i1.0662$	$1.2760 + i4.6953$	$1.2385 + i8.4227$
2.00	$1.0265 + i1.6419$	$1.3567 + i4.8416$	$1.2675 + i8.4873$
3.00	$0.9579 + i2.1528$	$1.4484 + i5.0800$	$1.3126 + i8.5951$
4.00	$0.7439 + i2.6183$	$1.5145 + i5.3999$	$1.3695 + i8.7477$
5.00	$0.4158 + i3.0341$	$1.5269 + i5.7870$	$1.4325 + i8.9482$
6.00	$0.0046 + i3.3898$	$1.4679 + i6.2231$	$1.4934 + i9.2015$
6.05	$-0.0175 + i3.4059$	$1.4629 + i6.2459$	$1.4961 + i9.2156$
7.00		$1.3301 + i6.6903$	$1.5396 + i9.5116$
8.00		$1.1113 + i7.1740$	$1.5560 + i9.8776$
9.00		$0.8097 + i7.6609$	$1.5286 + i10.2922$
10.00		$0.4240 + i8.1340$	$1.4496 + i10.7438$
10.90		$0.0089 + i8.5299$	$1.3335 + i11.1739$
10.95		$-0.0158 + i8.5507$	$1.3258 + i11.1984$
11.00			$1.3180 + i11.2229$
12.00			$1.1342 + i11.7263$
13.00			$0.8924 + i12.2540$
14.00			$0.5806 + i12.8014$
15.00			$0.1844 + i13.3543$
15.40			$0.0000 + i13.5714$
15.45			$-0.0241 + i13.5982$

Table 5.17: Unstable growth rates for $\Delta s/R = -5$ and $f = 1.2$ with varying transverse wave number k_y for the first three two-dimensional modes ($k_y \neq 0$).

$\Delta s/R = -8$, $f = 1.2$, $k_y \neq 0$			
k_y	Mode 1	Mode 2	Mode 3
0.00	$0.5264 + i0.5585$	$1.2715 + i4.6976$	$1.3699 + i8.4977$
1.00	$0.8862 + i1.0907$	$1.3028 + i4.7447$	$1.3790 + i8.5184$
2.00	$1.0150 + i1.6581$	$1.3813 + i4.8849$	$1.4054 + i8.5804$
3.00	$0.9531 + i2.1653$	$1.4720 + i5.1137$	$1.4463 + i8.6839$
4.00	$0.7457 + i2.6276$	$1.5401 + i5.4221$	$1.4979 + i8.8299$
5.00	$0.4241 + i3.0396$	$1.5574 + i5.7974$	$1.5550 + i9.0212$
6.00	$0.0197 + i3.3910$	$1.5054 + i6.2227$	$1.6099 + i9.2618$
6.05	$-0.0021 + i3.4069$	$1.5008 + i6.2450$	$1.6124 + i9.2752$
7.00		$1.3750 + i6.6803$	$1.6520 + i9.5554$
8.00		$1.1634 + i7.1544$	$1.6676 + i9.9021$
9.00		$0.8691 + i7.6310$	$1.6437 + i10.2967$
10.00		$0.4920 + i8.0931$	$1.5715 + i10.7303$
11.00		$0.0382 + i8.5200$	$1.4469 + i11.1940$
11.05		$0.0137 + i8.5401$	$1.4393 + i11.2178$
11.10		$-0.0109 + i8.5600$	$1.4315 + i11.2417$
12.00			$1.2679 + i11.6821$
13.00			$1.0298 + i12.1915$
14.00			$0.7237 + i12.7161$
15.00			$0.3391 + i13.2427$
15.70			$0.0199 + i13.6007$
15.75			$-0.0044 + i13.6257$

Table 5.18: Unstable growth rates for $\Delta s/R = -8$ and $f = 1.2$ with varying transverse wave number k_y for the first three two-dimensional modes ($k_y \neq 0$).

$\Delta s/R = 0$, $k_y \neq 0$		
k_y	Mode 1 ($f = 1.6$)	Mode 2 ($f = 1.5$)
0.00	$0.1056 + i0.8009$	$0.2163 + i4.4148$
1.00	$0.5621 + i1.2235$	$0.2739 + i4.4613$
2.00	$0.6825 + i1.8455$	$0.4171 + i4.6164$
3.00	$0.5829 + i2.4415$	$0.5932 + i4.8983$
4.00	$0.3188 + i3.0181$	$0.7263 + i5.3180$
4.75	$0.0199 + i3.4242$	$0.7644 + i5.6969$
4.80	$-0.0013 + i3.4498$	$0.7647 + i5.7235$
5.00		$0.7630 + i5.8309$
6.00		$0.6971 + i6.3845$
7.00		$0.5554 + i6.9669$
8.00		$0.3328 + i7.5915$
9.00		$0.0013 + i8.2594$
9.05		$-0.0180 + i8.2921$

Table 5.19: Unstable growth rates for $\Delta s/R = 0$ with varying transverse wave number k_y for the first two two-dimensional modes ($k_y \neq 0$).

$\Delta s/R = -5$, $k_y \neq 0$		
k_y	Mode 1 ($f = 1.6$)	Mode 2 ($f = 1.5$)
0.00	$0.0484 + i0.9247$	$0.3597 + i4.5196$
1.00	$0.5017 + i1.2494$	$0.4067 + i4.5608$
2.00	$0.6377 + i1.8527$	$0.5271 + i4.6962$
3.00	$0.5445 + i2.4313$	$0.6725 + i4.9415$
4.00	$0.2787 + i2.9839$	$0.7909 + i5.2993$
4.65	$0.0219 + i3.3163$	$0.8310 + i5.5853$
4.70	$-0.0004 + i3.3404$	$0.8325 + i5.6087$
5.00		$0.8365 + i5.7528$
6.00		$0.7870 + i6.2669$
7.00		$0.6456 + i6.8196$
8.00		$0.4073 + i7.4052$
9.00		$0.0519 + i8.0116$
9.10		$0.0088 + i8.0722$
9.15		$-0.0133 + i8.1024$

Table 5.20: Unstable growth rates for $\Delta s/R = -5$ with varying transverse wave number k_y for the first two two-dimensional modes ($k_y \neq 0$).

$\Delta s/R = -8$, $k_y \neq 0$		
k_y	Mode 1 ($f = 1.6$)	Mode 2 ($f = 1.5$)
0.00	$0.0484 + i0.9247$	$0.3597 + i4.5196$
1.00	$0.5017 + i1.2494$	$0.4067 + i4.5608$
2.00	$0.6377 + i1.8527$	$0.5271 + i4.6962$
3.00	$0.5445 + i2.4313$	$0.6725 + i4.9415$
4.00	$0.2787 + i2.9839$	$0.7909 + i5.2993$
4.65	$0.0219 + i3.3163$	$0.8310 + i5.5853$
4.70	$-0.0004 + i3.3404$	$0.8325 + i5.6087$
5.00		$0.8365 + i5.7528$
6.00		$0.7870 + i6.2669$
7.00		$0.6456 + i6.8196$
8.00		$0.4073 + i7.4052$
9.00		$0.0519 + i8.0116$
9.10		$0.0088 + i8.0722$
9.15		$-0.0133 + i8.1024$

Table 5.21: Unstable growth rates for $\Delta s/R = -8$ with varying transverse wave number k_y for the first two two-dimensional modes ($k_y \neq 0$).

Chapter 6

Direct Euler Simulation

In order to confirm the predicted complex growth rates discussed in Chapter 5, we have carried out one dimensional unsteady simulations of the Euler equations using the one-step reversible reaction model. To do this, we have used software developed by Inaba (2004). In this chapter, we present his formulation for direct Euler simulation and our confirmation results. In Section 6.1, we give the reactive Euler equations in conservative form and describe the numerical methods and boundary conditions used in the implementation. Section 6.2 describes the results from the direct Euler simulations and comparisons with the one-dimensional linear stability results presented in Chapter 3.

6.1 Implementation

Inaba (2004) developed a two-dimensional unsteady Euler solver, but we have only used the one-dimensional version of his software. The Euler equations are solved in conservative form, which can be written

$$\frac{\partial \mathbf{z}_c}{\partial t} + \frac{\partial \mathbf{F}}{\partial x} = \mathbf{S} \tag{6.1.1}$$

$$\mathbf{z}_c = \begin{pmatrix} \rho \\ \rho \mathrm{u} \\ \rho e \\ \rho Y_{\mathcal{A}} \end{pmatrix}, \quad \mathbf{F} = \begin{pmatrix} \rho \mathrm{u} \\ P + \rho \mathrm{u}^2 \\ (\rho e + P)\mathrm{u} \\ \rho Y_{\mathcal{A}} \mathrm{u} \end{pmatrix}, \quad \mathbf{S} = \begin{pmatrix} 0 \\ 0 \\ 0 \\ \rho \dot{\omega}_{\mathcal{A}} \end{pmatrix} \tag{6.1.2}$$

where $\mathbf{z}_c$ is the vector of conserved variables, $\mathbf{F}$ is the vector of fluxes, and $\mathbf{S}$ is the vector of source terms. These equations are equivalent to (1.1.1)–(1.1.4).

To be consistent with the linear stability study, the equation of state is specified by the perfect gas P-ρ-T relationship,

$$P = \rho R T \tag{6.1.3}$$

and the following expression for specific internal energy

$$e = \frac{P/\rho}{\gamma - 1} + Y_{\mathcal{A}} \Delta h + \frac{1}{2}\mathrm{u}^2 \tag{6.1.4}$$

where Δh is the heat of reaction. We have modified Inaba's software to use the one-step reversible perfect gas model described in Section 2.2 to compute $\dot{\Omega}$ using (4.3.4).

Inaba's implementation uses Yee's scheme (Yee, 1987) for spatial integration. and explicit first-order time integration. The Δt required for the time integration is determined by a user-specified CFL number. This software is validated in Inaba (2004) for several detonation problems.

The initial profile for the simulation is the steady ZND structure discussed in Section 1.2. To compute this profile, the user must provide the Chapman-Jouguet detonation velocity U_{CJ}, degree of overdrive f (see Section 1.2.1), the reaction activation energy E_a, pre-exponential constant A, degree of reversibility $\Delta s/R$, and heat of reaction $\Delta h/RT_o$ (see Section 2.2), as well as the half-reaction distance and equilibrium value of $Y_{\mathcal{B}}$.

Inaba's software has the ability to solve the equations in the laboratory frame or in the shock-fixed frame. The work presented and validated in Inaba (2004) uses the laboratory frame option. For the shock-fixed frame option, the grid moves with the shock velocity. We have modified the shock-fixed frame capability to use the shock boundary condition presented in Henrick et al. (2006). The new formulation of the shock boundary condition transforms the x-coordinate in a similar way to that discussed in Section 3.1. In this way, the shock is attached to the right boundary and the post-shock state is always the right-

most cell in the grid. The initial spatial profile, the steady ZND structure, is inherently unstable and directly leads to an unstable shock front due to numerical errors exciting the instabilities. The perturbations in the flow create perturbations in the detonation velocity through the boundary conditions at the shock front. We have used the numerical implementation of the shock change equation (Henrick et al., 2006) to determine the instantaneous value of the detonation velocity at any given time. Although the left boundary condition is not a radiation condition, Daimon and Matsuo (2003) "confirmed that no perturbations reflected from the outflow boundary reach the detonation front during the calculation time used, based on the observation of the wave propagation of the perturbations on the $x - t$ diagram."

Inaba (2004) presents a convergence study and determines that for one-dimensional simulations, 80 grid points per induction length were sufficient. Eckett (2000) also gives a refinement study and concludes that it is necessary to have "at least 50 mesh cells per half-reaction length." In the present research, there are 150 cells per half-reaction length.

We also investigated convergence of the software with the new shock boundary condition. We found that the numerical results for $\Delta s/R = 0$, $k_y = 0$, and $f = 1.72$ did not vary significantly for the following parameter space.

$$\mathrm{dx} = \{2\mathrm{dx}, \mathrm{dx}, 0.5\mathrm{dx}, 0.25\mathrm{dx}\} \tag{6.1.5}$$

$$\mathrm{CFL} = \{0.2, 0.4, 0.8\} \tag{6.1.6}$$

$$\text{entropy correction} = \{0.1, 0.01\} \tag{6.1.7}$$

6.2 Confirmation of Linear Stability Results

Inaba's software returns post-shock pressure as a function of time. Unlike the linear stability calculation, several modes may present and are coupled in this pressure history. Close to the stability boundary, where only one mode is present, we can clearly see the onset of instability. The growth (Figure 6.1a) and decay (Figure 6.1b) of perturbations on each side of the stability boundary are illustrated by Figure 6.1. Both Figure 6.1a and

Figure 6.1b are results for $\Delta s/R = 0$. The location of the neutral stability curve for the first mode in one dimension ($k_y = 0$) (Figure 5.11) is such that Figure 6.1a ($f = 1.71$) is stable while Figure 6.1b ($f = 1.74$) is unstable.

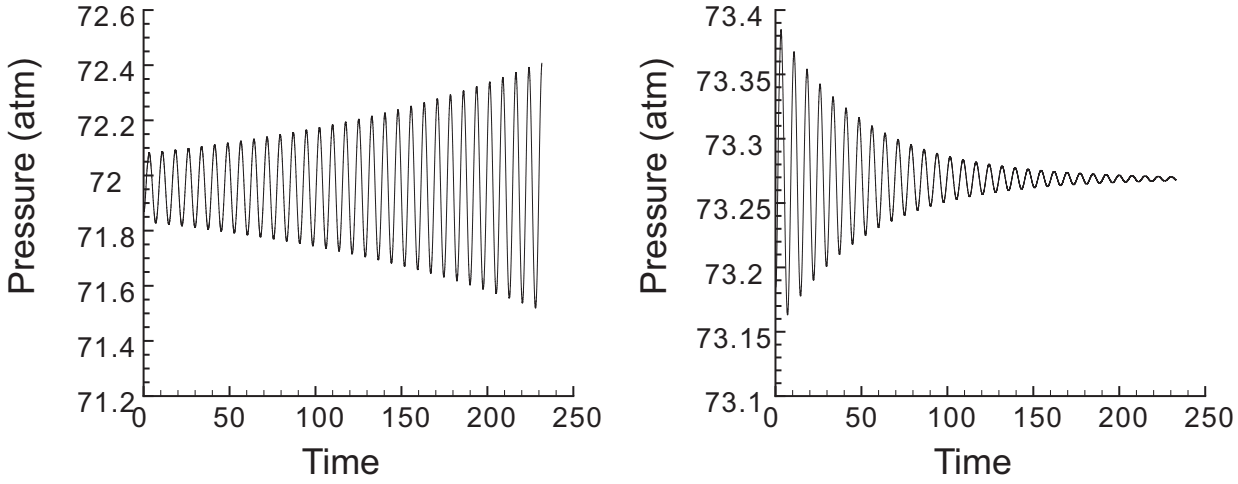

(a) (b)

Figure 6.1: Post-shock pressure vs. time for $\Delta s/R = 0$ and (a) $f = 1.7088$ (b) $f = 1.74$ generated with Inaba's software.

We can transform the post-shock pressure history from the time domain to the frequency domain in order to isolate the excited frequencies. Once we have determined these frequencies, we can compare them to $\mathcal{I}m(\omega)$ from the linear stability calculation. Using the fast Fourier transform algorithm (Frigo and Johnson, 1998) implemented in Matlab, we find the discrete Fourier transform ($\mathcal{P}$) of the post-shock pressure history. For comparison, we have also created a synthetic history which is a function of the ω from the linear stability calculation, which was based on the oscillatory portion and did not include growth or damping:

$$P_{\text{synthetic}}(m) = \sum_{k \text{ modes}} P_{\text{mode } k} \sin\left[(\omega_{\mathcal{I}})_{\text{mode } k} t(m)\right]. \tag{6.2.1}$$

Our synthetic history is evaluated at discrete points using the same array of times created by Inaba's software. To graphically compare the two histories, we find the discrete Fourier

f	LSC	DES
1.7088	0.8260	0.8326
1.74	0.82158	0.838686

Table 6.1: Frequency values determined by linear stability calculation (LSC) and direct Euler simulation (DES).

transform ($\mathcal{P}$) of our synthetic history and plot the spectral densities of both histories.

Figure 6.2 shows the spectral densities,

$$|\mathcal{P}| = \sqrt{\mathcal{P}\mathcal{P}^*}, \tag{6.2.2}$$

described for the data depicted in Figure 6.1. The results from Inaba's software are shown in black and the synthetic data is red. Although ω is determined with the methodology described in Chapter 3, $P_{\text{mode k}}$ is an arbitrary constant which we have chosen so that the amplitude of the peaks in the spectra are somewhat comparable. The values of $\omega_{\mathcal{I}}$ determined by the linear stability calculation (LSC) and the frequencies of the direct Euler simulation (DES) are given in Table 6.1.

The most interesting feature that we found in our linear stability results was the exchange of stability between modes one and two as a function of reversibility. Initially we expected that in the region between the two neutral stability curves we would see only one mode. Above the crossing point we would only see low-frequency oscillations and below we would see only the higher-frequency mode. Figure 6.3 and Table 6.2 give the cases we have investigated and a comparison of Euler results with frequencies determined by the linear stability calculations.

Figure 6.4 shows the post-shock pressure histories for Cases 1–6 and Figure 6.5 shows the corresponding spectra. We see that, as expected, four of these cases (1,4,5,6) exhibit only the lowest mode of instability. Table 6.3 indicates that the mode-one frequency values predicted by the linear stability calculation agree within 2% of the frequency of the direct Euler simulation pressure history in all but two cases. Cases 2 and 3 are farther from the mode-one stability boundary than the other cases. In these two cases,

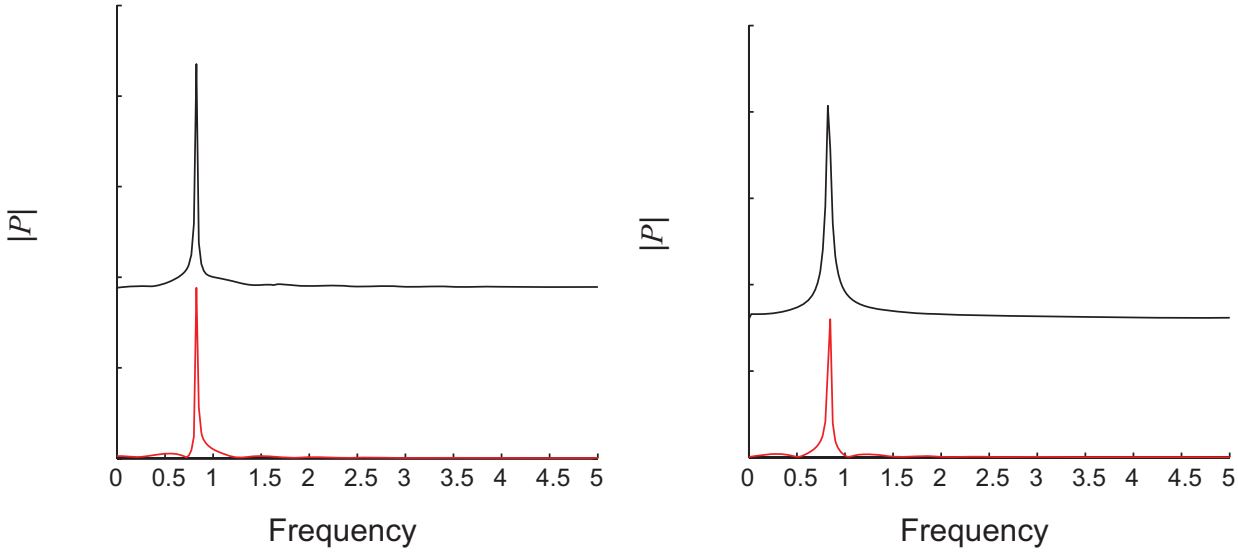

Figure 6.2: Discrete Fourier transforms (black) of post-shock pressure vs. time for $\Delta s/R = 0$ and (a) $f = 1.7088$ (b) $f = 1.74$ generated with Inaba's software. Also shown (red) are discrete Fourier transforms of synthetic histories described by (6.2.1). Spectra are displaced for clarity.

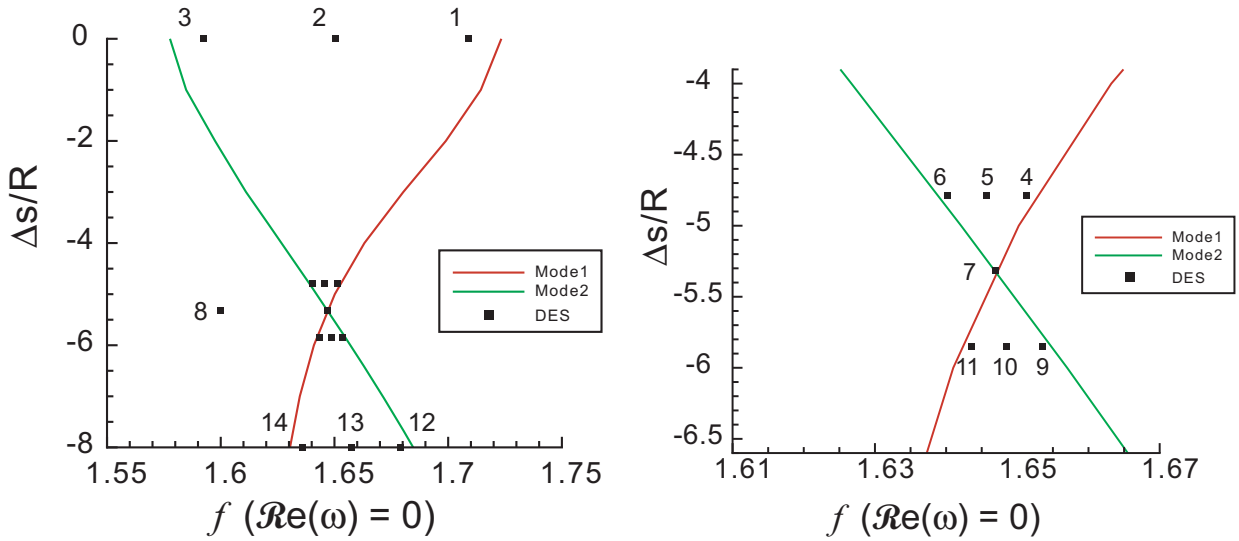

Figure 6.3: Direct Euler Simulation cases superposed as black squares on the neutral stability curves for modes one and two (see Figure 5.11). Case numbers refer to Table 6.2.

No.	$\Delta s/R$	f
1	0.0	1.7088
2	0.0	1.6506
3	0.0	1.5923
4	−4.7850	1.6513
5	−4.7850	1.6457
6	−4.7850	1.6402
7	−5.3167	1.6469
8	−5.3167	1.6
9	−5.8484	1.6535
10	−5.8484	1.6485
11	−5.8484	1.6435
12	−8.0	1.6792
13	−8.0	1.6575
14	−8.0	1.6359

Table 6.2: Direct Euler simulation cases.

we observe excited harmonics.

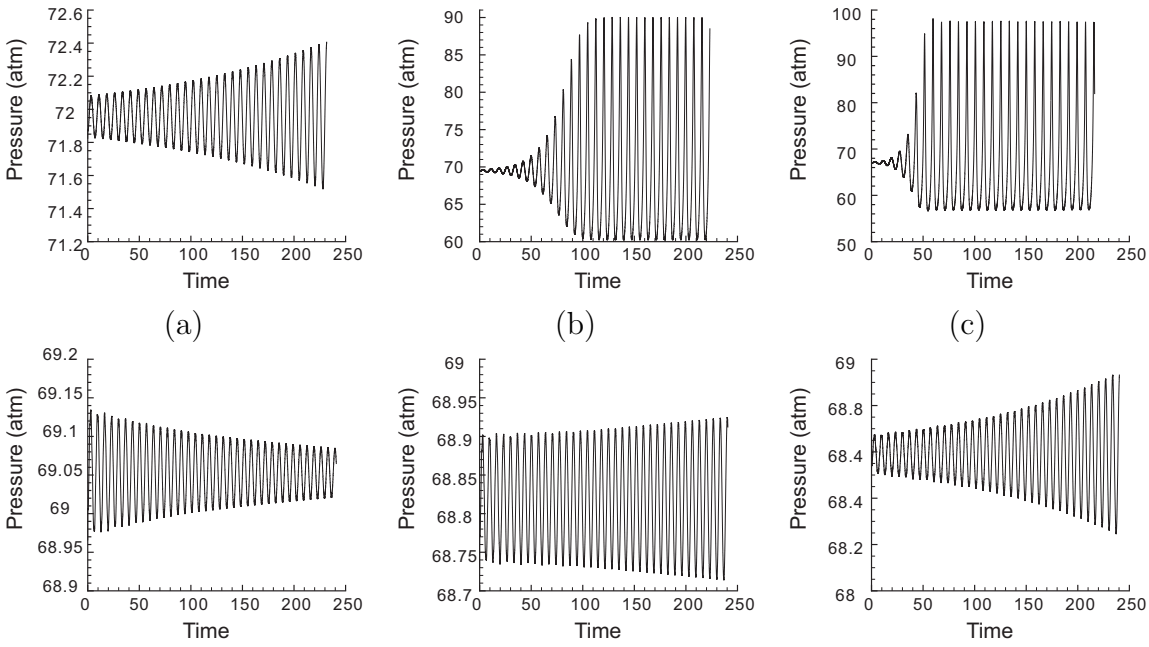

Figure 6.4: Post-shock pressure histories from direct Euler simulations. (a) Case 1, (b) Case 2, (c) Case 3, (d) Case 4, (e) Case 5, (f) Case 6

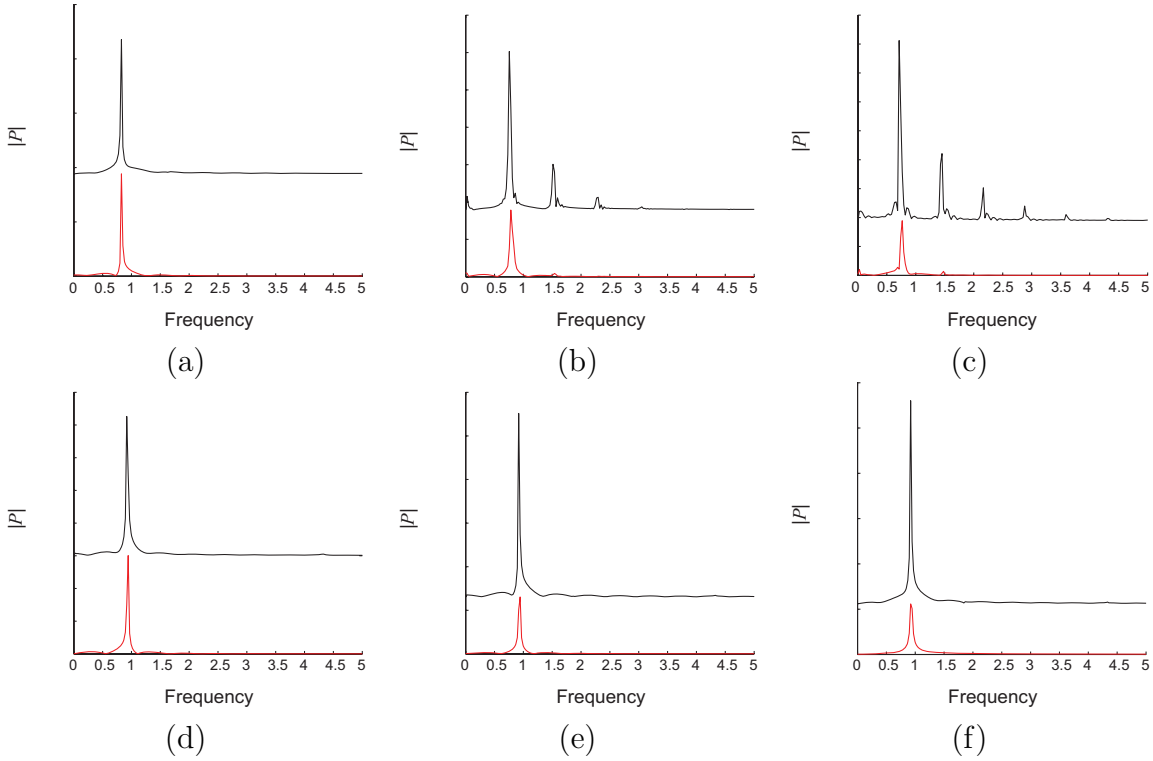

Figure 6.5: Post-shock pressure spectra from direct Euler simulations (black) and synthetic spectra using linear stability results (red). (a) Case 1, (b) Case 2, (c) Case 3, (d) Case 4, (e) Case 5, (f) Case 6. Spectra are displaced for clarity.

Below the stability exchange, Cases 9–14, we expected to see only mode 2. Instead, each simulation began with a decaying oscillation with a frequency comparable to mode 1. The mode-two oscillation begins to grow after the simulation starts and eventually dominates. The pressure histories and spectra for these cases are depicted in Figures 6.6 and 6.7. The comparison of the mode-two frequencies predicted by the linear stability calculations and obtained in the direct Euler simulations is given in Table 6.4. The largest difference is on the order of 3%.

Finally, we investigated the region near the point of stability exchange, Cases 7 and 8. As expected, to the left of the stability exchange point, Case 8, we see both modes excited. In fact, because we are far enough from the stability boundaries of modes one and two, we also see excited harmonics and some coupling between the modes. Directly at the stability exchange point, we expect a zero growth rate for both modes.

Case	$\Delta s/R$	f	DES	LSC	% diff
			$\omega_{\mathcal{I},\text{mode 1}}$	$\omega_{\mathcal{I},\text{mode 1}}$	$\omega_{\mathcal{I},\text{mode 1}}$
1	0	1.7088	0.8260	0.8326	0.79%
2	0	1.6506	0.7568	0.8177	7.46%
3	0	1.5923	0.7131	0.7976	10.60%
4	-4.7850	1.6513	0.9191	0.9369	1.91%
5	-4.7850	1.6457	0.9202	0.9353	1.61%
6	-4.7850	1.6402	0.9213	0.9336	1.31%

Table 6.3: Direct Euler simulation (DES) results compared with linear stability calculations (LSC). These cases are only unstable to Mode 1.

Case	$\Delta s/R$	f	DES	LSC	% diff
			$\omega_{\mathcal{I},\text{mode 2}}$	$\omega_{\mathcal{I},\text{mode 2}}$	$\omega_{\mathcal{I},\text{mode 2}}$
9	-5.8484	1.6535	4.3578	4.3926	0.79%
10	-5.8484	1.6485	4.3628	4.3978	0.80%
11	-5.8484	1.6435	4.3429	4.4029	1.36%
12	-8	1.6792	4.3561	4.4133	1.30%
13	-8	1.6575	4.3266	4.4363	2.47%
14	-8	1.6359	4.3291	4.4588	2.91%

Table 6.4: Direct Euler simulation (DES) results compared with linear stability calculations (LSC). These cases are only unstable to Mode 2.

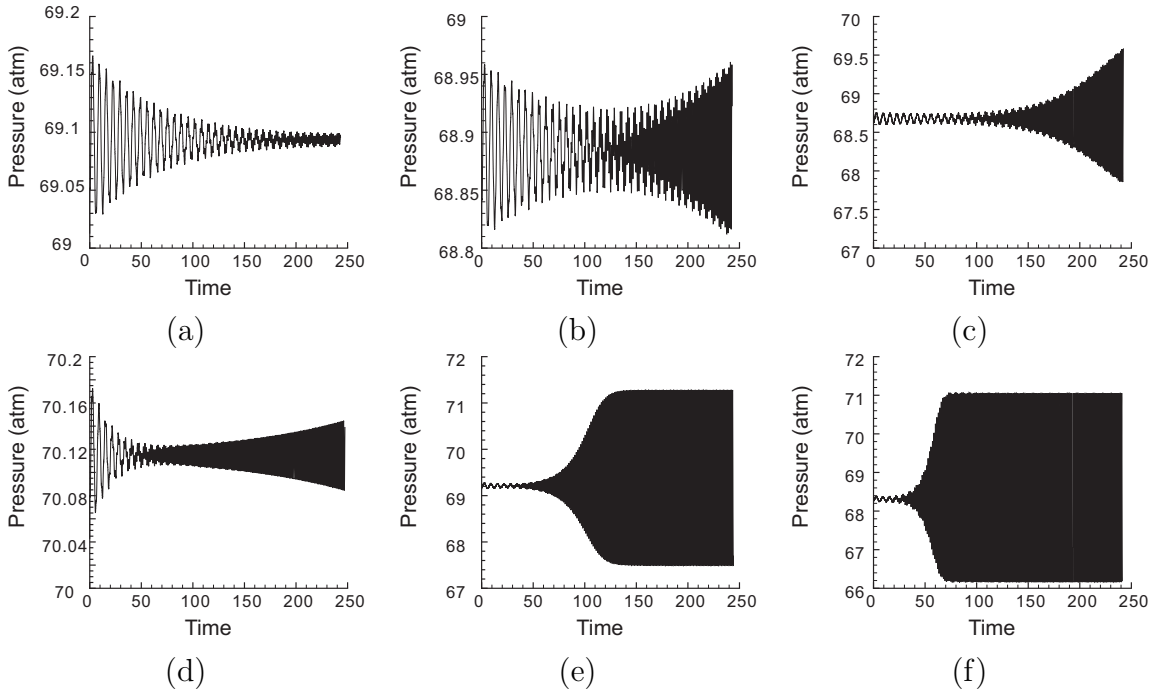

Figure 6.6: Post-shock pressure histories from direct Euler simulations. (a) Case 9, (b) Case 10, (c) Case 11, (d) Case 12, (e) Case 13, (f) Case 14

Achieving conditions close to this point requires higher precision than the present method of solution, and our Case 7 is slightly to the right of this point. Because of this, we observe a decaying post-shock pressure history. These results are shown in Figures 6.8 and 6.9, and the calculated frequencies for both modes one and two are compared in Table 6.5. The largest disagreement is slightly larger than 3%.

The comparison between the linear stability calculations and the direct Euler simulations shows modest agreement given the low-order method of solving the Euler equations. These results indicate that our new methods described in Chapter 3 are reasonable for

Case	$\Delta s/R$	f	DES		LSC		% diff	
			$\omega_{\mathcal{I},\text{mode 1}}$	$\omega_{\mathcal{I},\text{mode 2}}$	$\omega_{\mathcal{I},\text{mode 1}}$	$\omega_{\mathcal{I},\text{mode 2}}$	$\omega_{\mathcal{I},\text{mode 1}}$	$\omega_{\mathcal{I},\text{mode 2}}$
7	-5.3167	1.6469	0.9406	4.3319	0.9475	4.3858	0.72%	1.23%
8	-5.3167	1.6	0.9009	4.3044	0.9315	4.4337	3.29%	2.92%

Table 6.5: Direct Euler simulation (DES) results compared with linear stability calculations (LSC) for stability transition cases.

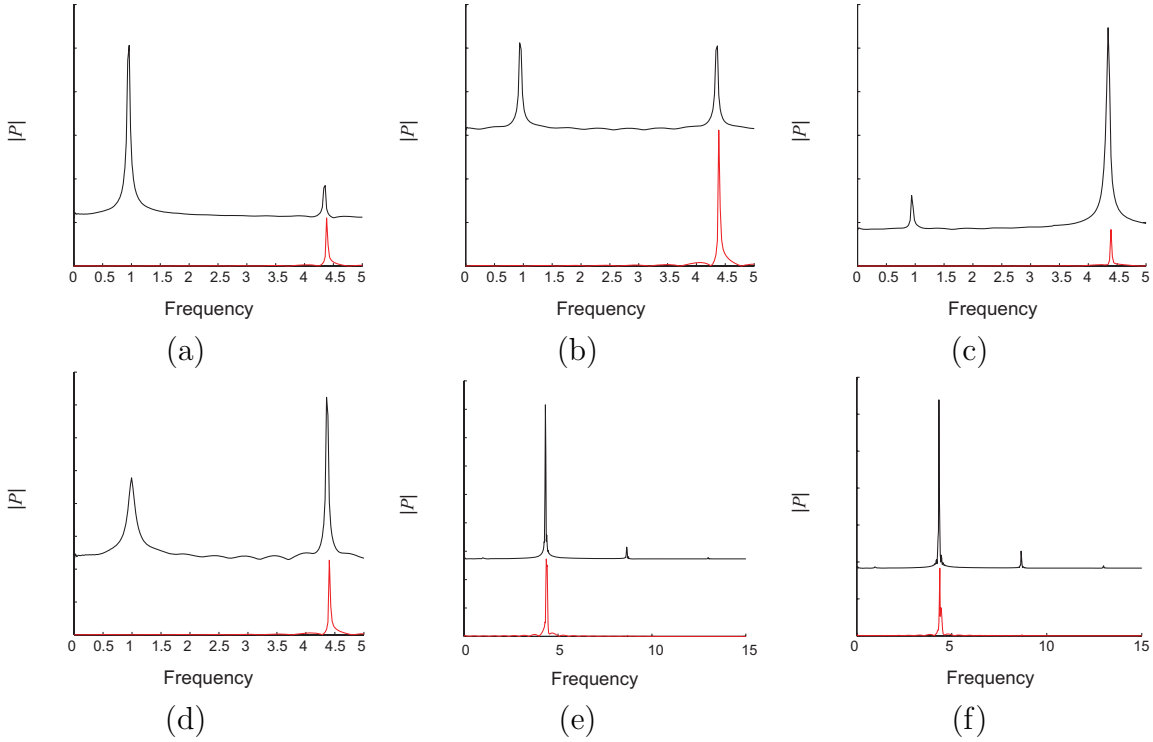

Figure 6.7: Post-shock pressure spectra from direct Euler simulations (black) and synthetic spectra using linear stability results (red). (a) Case 9, (b) Case 10, (c) Case 11, (d) Case 12, (e) Case 13, (f) Case 14. Spectra are displaced for clarity.

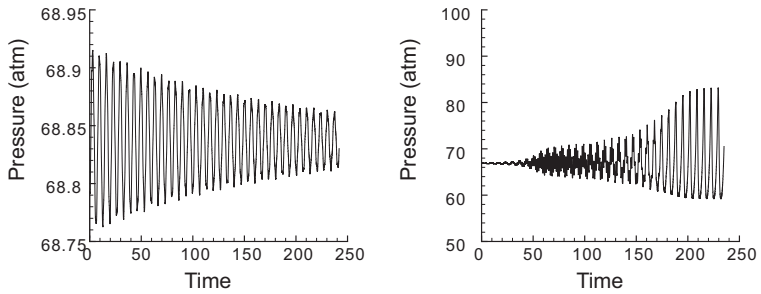

Figure 6.8: Post-shock pressure histories from direct Euler simulations. (a) Case 7 (b) Case 8

predicting the linear stability modes for a single reversible, one-step reaction. One of the key predictions of the linear instability, the exchange of mode one and mode two as the first unstable mode, is verified by the Euler simulations.

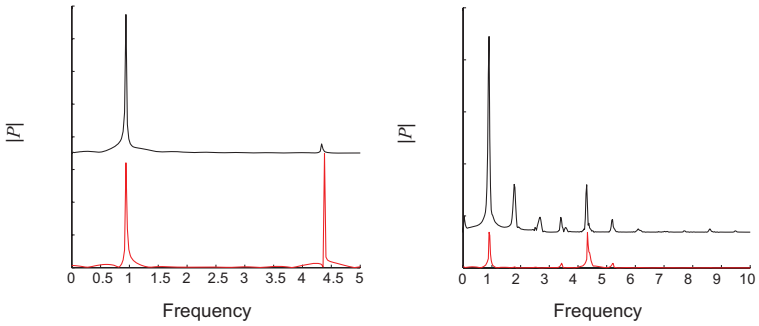

(a) (b)

Figure 6.9: Post-shock pressure spectra from direct Euler simulations (black) and synthetic spectra using linear stability results (red). (a) Case 7 (b) Case 8. Spectra are displaced for clarity.

Chapter 7

Summary

Detonations are inherently unstable. Many aspects of this instability have been investigated both experimentally and numerically, and several approximate models (Strehlow, 1979, McVey and Toong, 1971, Alpert and Toong, 1972) have been proposed to describe the physics of the instability. From a theoretical viewpoint, it is valuable to understand the specific chemical features that create the conditions necessary for the instability.

The rigorous study of linear stability of detonations started with Erpenbeck (1962) but comprehensive results were not obtained until the reformulation as a normal modes approach by Lee and Stewart (1990) and Short and Stewart (1998). This approach requires formulating a differential eigenvalue problem with two boundary conditions and is often solved with a shooting method. To date, although researchers have investigated single- and multi-step reaction schemes, detailed chemical reaction mechanisms and the effect of reversibility have not been considered in linear stability investigations.

7.1 Summary

The primary focus of this work was to investigate the role that reversibility plays in detonation instability. To this end, we generalized the equations of motion (see Chapter 1) and reformulated the normal modes approach (see Chapter 3) to allow for an arbitrary kinetics mechanism. In order to study the effects of chemical reversibility, we created a family of single-step reversible mechanisms (see Chapter 2).

When reversible reactions are included, no analytic solution for the radiation condition exists because the one-way coupling between fluid mechanics and chemistry that simplifies the irreversible case no longer exists far from the reaction zone. Also, unlike non-reactive systems, the characteristic speeds in reactive systems are complex valued. Chapter 4 explains in detail our generalized methodology for determining the necessary radiation condition that we believe is applicable for the generalized problem. This new method assures that the function space of the solution along the upstream-traveling wave is zero.

We have also shown that the equations of motion far from the reaction zone with reversible chemistry are equivalent to a single wave hierarchy equation (4.3.23). The wave hierarchy equation gives the same complex characteristic speeds as the algebraic eigenvalue problem and enables a simple physical interpretation of the flowfield far downstream from the detonation. In a situation with reversible chemistry, the wave hierarchy consists of two wave operators: an equilibrium operator and a higher-order frozen operator. For acoustic waves with frequency $2\pi/\mathcal{I}m(\omega)$, the contribution of each operator is governed by a function of the near-equilibrium relaxation time constant, $\tau|_{x_R}$ (4.3.18). As $[\tau^*|_{x_R}(a_e/a_f)^2_{x_R}] \to 0$, the equilibrium operator dominates, and as $[\tau^*|_{x_R}(a_e/a_f)^2_{x_R}] \to \infty$, the frozen operator dominates. The wave hierarchy provides an alternate interpretation of acoustic processes in the far downstream that is more physical than the algebraic eigenvalue problem.

Using this new implementation of the linear stability problem, we studied the stability characteristics of our family of detonations with reversible chemistry in one and two dimensions and discussed them in Chapter 5. We first verified that, by choosing our reversibility parameter, $\Delta s/R$, sufficiently "large," we approached the irreversible situation as a limit of our family of reversible reactions. Using this limit, we computed one-dimensional and two-dimensional results and compared them with Lee and Stewart and Short and Stewart. Following this satisfactory comparison, we investigated how the unstable eigenvalues (ω) vary with increasing reversibility and varying overdrive, f.

Increasing the reversibility affects the base flow quantitatively by decreasing the energy release pulse width, $\Delta_{e,ZND}$, but qualitatively, the character of the base flow reaction

zone remains the same. Reversibility has a similar effect on the eigenfunctions. As the reversibility increases, the quantitative shape changes, but the qualitative characteristics remain the same.

In one dimension, our results indicate that reversibility has a stabilizing effect on the lowest mode and a destabilizing effect on higher modes. Because of this, we see a stability exchange between modes one and two as we vary the reversibility. We also see an exchange of stability in our two-dimensional computations. The near-equilibrium relaxation time ($\tau|_{x_R}$) indicates that for the parameter space we have studied, the tail of the reaction remains in equilibrium, but the relationship between the period of oscillation ($2\pi/\mathcal{I}m(\omega)$) and the induction time ($\tau_{i,ZND}$) varies with the mode number. For low mode numbers, the induction time is shorter than the period of the oscillation, but as the mode number increases, the period of oscillation becomes shorter than the induction time.

Finally in Chapter 6, we confirmed our results using direct Euler simulation. By examining the unsteady pressure history in the frequency domain, we were able to compare the excited frequencies with those predicted by our one-dimensional linear stability calculations. Most of our linear stability eigenvalues were within 3% of the frequency of the direct Euler simulation post-shock pressure history. We were also able to observe the stability exchange as we increased the reversibility.

This study has provided a methodology for evaluating the linear stability characteristics of an idealized two-dimensional detonation with arbitrary chemical mechanisms. Our results indicate that reversibility does affect the character of the detonation instability. Although we have made progress toward understanding the essential chemical features contributing to the character of detonation instability, work remains to be done to improve the current implementations. As discussed in Section 3.5, the shooting method has limitations, and the root finding algorithms are sensitive to the initial guess. Also, higher-order methods in the direct Euler simulations may resolve some of the discrepancies between the linear stability eigenvalues and the frequency of the post-shock pressure histories.

7.2 Future Work

7.2.1 Effective Activation Energy

The family of reversible chemical systems that we devised in Section 2.2.1 is only one of the possible families. For a single-step reversible reaction system, there are five free parameters: γ, E_a, Δh, Δs, and A. In our family, we fixed γ, E_a, and T_{CJ} which is the same as fixing the effective energy release. We then evaluated the stability bounds as a function of the overdrive f and reversibility Δs. We could have studied the stability boundaries as a function of γ, E_a, or Δh instead of f.

As discussed in the introduction (see Section 1.3), the effective activation energy, E_a, is a figure of merit for classifying stability experimentally. Austin (2003) reported the stability curve reprinted as Figure 7.1. Figure 7.1 indicates that for a fixed overdrive, different chemical mixtures have different effective activation energies. As given in Table 2.1, all of our cases lie to the right of Austin's H_2-O_2-CO_2 case ($M_{CJ} \approx 6.2$ and $\theta \approx 10.44$). It would be interesting in the future to investigate how the effective activation energy affects the stability for a fixed overdrive value and varying reversibility.

7.2.2 Acoustics

A more fundamental question examines what essential ingredients trigger positive feedback mechanisms that lead to discrete unstable modes. For example, does chemistry play an important role at the perturbation level? Clearly, a feedback loop between chemical reaction and fluid dynamics is necessary in the base flow, but it is unclear if the chemistry influences the perturbations. We can investigate this in two ways. First, we can further examine the perturbation regime (frozen or equilibrium) far from the reaction zone. Second, we can examine the importance of the chemical-acoustic coupling in the reaction zone.

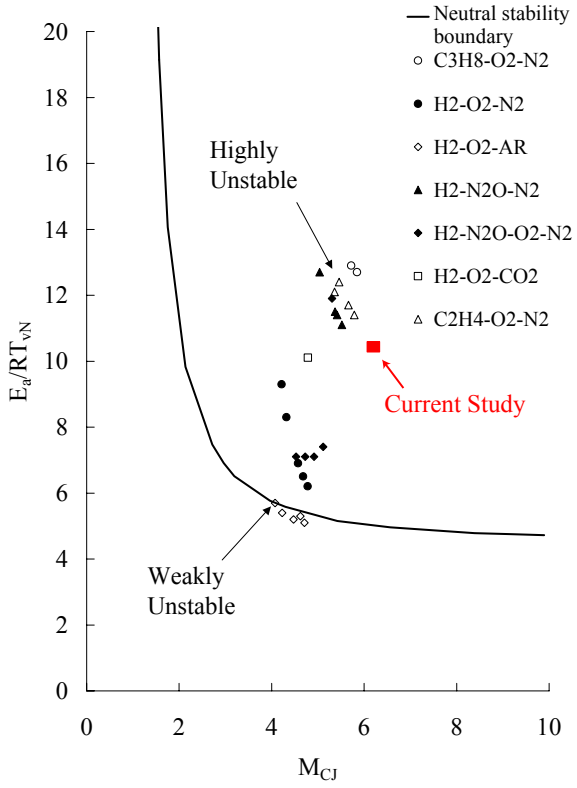

Figure 7.1: Categorization of detonation front structure from stability considerations. Parameters for mixtures considered in this study (symbols) are compared to the neutral stability boundary from Lee and Stewart (1990). Activation energy is calculated using the procedure described in Schultz and Shepherd (2000) from one-dimensional constant volume explosion assumption with detailed kinetics. M_{CJ} is calculated using STANJAN. (Reprinted with permission from Austin (2003), Figure 1.6.) Current study data (Table 2.1) included for reference.

7.2.2.1 Far from the Reaction Zone

In Section 5.3, we discussed the limiting cases of the wave hierarchy formulation. Examining both limits, equilibrium and frozen, may provide insight into how influential chemical effects are in the radiation condition formulation. In the current study, we found that as the mode number increased, the wave hierarchy equation began to transition from the equilibrium limit to the frozen limit. To fully investigate the frozen limit, future work must include computing eigenvalues for higher mode numbers.

7.2.2.2 Reaction Zone

As we discussed in Section 5.5, Tumin (2007a) has suggested that chemical-acoustic coupling at the perturbation level is not essential for detonation instability. A physical interpretation of his theory is that the shock front and energy release zone form a "leaky" resonator. The acoustic impedance of the shock front and energy release zone (shown in Figure 5.6) influence the effectiveness of this resonator. The magnitude of the base flow gradients ($\mathbf{b} = \mathbf{z}_{,x}$) also influences the effectiveness. For this reason, the shape factor proposed by Short and Sharpe (2003), Short and Quirk (1997), Ng and Lee (2003), and Ng et al. (2005b), which compares gradients in the base flow ($\propto \Delta_{e,ZND}$) with the induction length $\Delta_{i,ZND}$, is important.

Tumin has recently neglected the chemical-acoustic coupling terms at the perturbation level by using

$$\mathbf{C} = \begin{pmatrix} -\mathrm{u}_{,x} & v_{,x} & 0 & 0 & 0 & 0 & \dots \\ P_{,x} & \mathrm{u}_{,x} & 0 & 0 & 0 & 0 & \dots \\ 0 & 0 & 0 & 0 & 0 & 0 & \dots \\ (\rho a_f^2)_{,v}\mathrm{u}_{,x} - Z_{,v} & P_{,x} & 0 & (\rho a_f^2)_{,P}\mathrm{u}_{,x} - Z_{,P} & 0 & 0 & \dots \\ 0 & 0 & 0 & 0 & 0 & 0 & \dots \\ 0 & 0 & 0 & 0 & 0 & 0 & \dots \\ \dots & & & & & & \end{pmatrix} \tag{7.2.1}$$

in (3.2.10) and calculated unstable eigenvalues. We have reproduced these calculations and they are compared with the results presented in Chapter 5 in Figure 7.2 and Table 7.1. Qualitatively, these eigenvalues are comparable, although quantitatively there are large percent differences. It would be useful future work to develop a quantitative model of how the eigenvalues vary with and without chemical-acoustic coupling at the perturbation level.

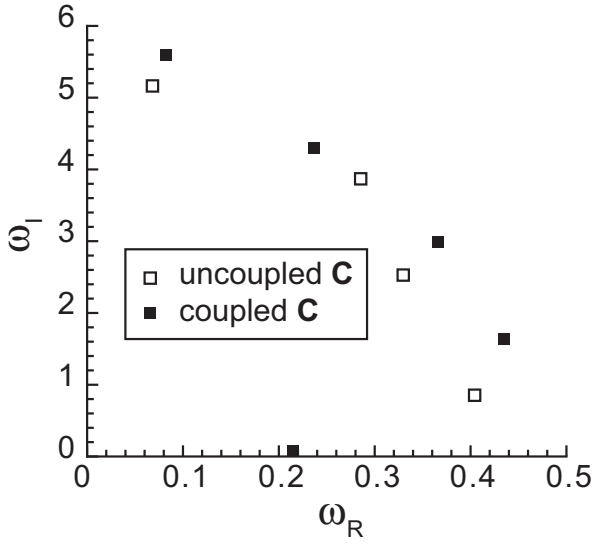

Figure 7.2: Comparison of unstable eigenvalues with uncoupled **C** (7.2.1) (open squares) and coupled **C** (3.2.12) (solid squares). Short and Stewart's normalization discussed in Section 5.2 was used.

uncoupled **C** (7.2.1)	
$\omega_{\mathcal{R}}$	$\omega_{\mathcal{I}}$
0.4042	0.8538
0.3298	2.528
0.2854	3.869
0.0682	5.164
coupled **C** (3.2.12)	
$\omega_{\mathcal{R}}$	$\omega_{\mathcal{I}}$
0.2145	0.080
0.4346	1.643
0.3662	2.982
0.2372	4.293
0.0825	5.599

Table 7.1: Comparison of unstable eigenvalues with **C** (7.2.1) and **C** (3.2.12). Short and Stewart's normalization discussed in Section 5.2 was used.

Bibliography

R. L. Alpert and T. Y. Toong. Periodicity in exothermic hypersonic flows about blunt projectiles. *Astronautica Acta*, 17:539–560, 1972.

S. Arrhenius. Uber die reaktionsgeschwindigkeit bei der inversion von rohrzucker durch sauren. *Phys. Chem.*, 4(2):226–248, 1889.

S. K. Aslanov. Criterion of instability of Chapman-Jouguet detonation in a gas. *Dokl. Akad. Nauk.*, 163:667, 1965. (English translation: *Proc. Acad. Sci. USSR, Phys. Chem. Sec.*, 163:553 1965).

J. Austin. *The Role of Instability in Gaseous Detonation*. PhD thesis, California Institute of Technology, Pasadena, CA, 2003.

J. M. Austin, F. Pintgen, and J. E. Shepherd. Reaction zones in highly unstable detonations. In *Proc. Combust. Inst.*, volume 30, pages 1849–1857, 2005.

H. O. Barthel and R. A. Strehlow. Wave propagation in one-dimensional reactive flows. *Phys. Fluids*, 9(10):1896–1904, 1966.

W. A. Bone, R. P. Fraser, and W. H. Wheeler. II-A photographic investigation of flame movements in gaseous explosions, Part VII—The phenomenon of spin in detonation. *Phil. Trans. R. Soc. Lond.* A, 235:29–68, 1935.

A. Bourlioux, A. J. Majda, and V. Roytburd. Theoretical and numerical structure for unstable one-dimensional detonations. *SIAM J. Appl. Math.*, 51(2):303–343, 1991.

S. Browne, J. Ziegler, and J. E. Shepherd. Numerical solution methods for control volume explosions and ZND detonation structure. Technical Report FM2006.007, GALCIT, 2005.

S. Browne, J. Ziegler, and J. E. Shepherd. Numerical solution methods for shock and detonation jump conditions. Technical Report FM2006.007, GALCIT, 2007a.

S. T. Browne, J. Zeigler, and J. E. Shepherd. Shock and Detonation Toolbox. http://www.galcit.caltech.edu/EDL/public/cantera/html/SD_Toolbox/index.html, 2007b.

J. D. Buckmaster and J. Neves. One-dimensional detonation stability: the spectrum of infinite activation energy. *Phys. Fluids*, 12:3571–3576, 1988.

P. B. Butler. Real gas equations of state for CHEMKIN. Technical Report SAND88-3118, Sandia National Laboratories, 1989.

C. Campbell and D. W. Woodhead. The ignition of gases by an explosion wave. I. Carbon monoxide and hydrogen mixtures. *J. Chem. Soc.*, 129:3010–3021, 1926.

D. L. Chapman. On the rate of explosion in gases. *Philos. Mag.*, 14:1091–1094, 1899.

K. W. Chiu and J. H. Lee. Simplified version of Barthel model for transverse-wave spacings in gaseous detonations. *Combust. Flame*, 26:353–361, 1976.

B. T. Chu. Vibration of the gaseous column behind a strong detonation wave. In *Gas Dynamics Symposium on Aerothermochemistry*. Northwestern University Press, Evanston, 1956.

S. D. Cohen and A. C. Hindmarsh. CVODE, a stiff/nonstiff ODE solver in C. *Computers in Physics*, 10:138–143, 1996.

Y. Daimon and A. Matsuo. Detailed features of one-dimensional detonations. *Phys. Fluids*, 15:112–122, 2003.

Y. Daimon and A. Matsuo. Unsteady features on one-dimensional hydrogen-air detonations. *Phys. Fluids*, 19, Art. No. 116101, 2007.

Y. N. Denisov and Y. K. Troshin. Pulsating and spinning detonation of gaseous mixtures in tubes. *Dokl. Akad. Nauk.*, 125:110–113, 1959.

W. Doering. On detonation processes in gases. *Ann. Phys.*, 43:421–436, 1943.

J. W. Dold and A. K. Kapila. Comparison between shock initiations of detonation using thermally-sensitive and chain-branching chemical models. *Combust. Flame*, 85:185–194, 1991.

R. E. Duff. Investigation of spinning detonation and detonation stability. *Phys. Fluids*, 4:1427–1433, 1961.

C. A. Eckett. *Numerical and analytical studies of the dynamics of gaseous detonations*. PhD thesis, California Institute of Technology, Pasadena, California, September 2000.

C. A. Eckett, J. J. Quirk, and J. E. Shepherd. The role of unsteadiness in direct initiation of gaseous detonations. *J. Fluid Mech.*, 421:147–183, 2000.

A. Einstein. Propagation of sound in partly dissociated gases. In E. Schucking, editor, *The collected papers of Albert Einstein*, number 39 in vol. 7 The Berlin Years: Writings, 1918–1921, pages 183–189. Princeton University Press, Princeton and Oxford, April 1920. (Originally in *Königlich Preußische Akademie der Wissenschaften*. Berlin. Sitzungsberichte,).

J. J. Erpenbeck. Stability of steady-state equilibrium detonations. *Phys. Fluids*, 5: 604–614, 1962.

J. J. Erpenbeck. Structure and stability of the square-wave detonation. In *9th Symp. (Intl) on Combustion*, pages 442–453, New York, 1963.

J. J. Erpenbeck. Stability of idealized one-reaction detonations: zero activation energy. *Phys. Fluids*, 8:1192–1193, 1965.

J. J. Erpenbeck. Detonation stability for disturbances of small transverse wavelength. *Phys. Fluids*, 9:1293–1306, 1966.

J. J. Erpenbeck. Theory of detonation stability. In *12th Symp. (Intl) on Combustion*, pages 711–721, Pittsburgh, 1969.

J. A. Fay. A mechanical theory of spinning detonation. *J. Comput. Phys.*, 20:942–950, 1952.

W. Fickett and W. Davis. *Detonation Theory and Experiment*. Dover Publications, INC., 1979.

W. Fickett and W. W. Wood. Flow calculation for pulsating one-dimensional detonation. *Phys. Fluids*, 9:903–916, 1966.

M. Frigo and S. G. Johnson. FFTW: An adaptive software architecture for the FFT. *Proceedings of the International Conference on Acoustics, Speech, and Signal Processing*, 3:1381–1384, 1998.

V. N. Gamezo, D. Desbordes, and E. S. Oran. Formation and evolution of two-dimensional cellular detonations. *Combust. Flame*, 116:154–165, 1999.

D. Goodwin. Cantera: object-oriented software for reacting flows. Technical report, California Institute of Technology, 2005. URL http://www.cantera.org.

W. E. Gordon, A. J. Mooradian, and S. A. Harper. Limit and spin effects in hydrogen-oxygen detonations. In *7th Symp. (Intl) on Combustion*, pages 752–759, 1959.

B. F. Gray and C. H. Yang. On the unification of the thermal and chain theories of explosion limits. *J. Phys. Chem.*, 69(8):2747–2750, 1965.

L. V. Gurvich, I. V. Veyts, and C. B. Alcock. *Thermodynamic Properties of Individual Substances, vol. 1, parts 1 and 2*. Hemisphere Publishing Corp., New York, 1989.

L. T. He and J. H. S. Lee. The dynamical limit of one-dimensional detonations. *Phys. Fluids*, 7:1151–1158, 1995.

A. K. Henrick, T. D. Aslam, and J. M. Powers. Simulations of pulsating one-dimensional detonations with true fifth order accuracy. *J. Comput. Phys.*, 213:311–329, 2006.

H. G. Hornung. Gradients at a curved shock in reacting flow. *Shock Waves*, 8:11–21, 1998.

K. Inaba and A. Matsuo. Cellular structures of planar detonations with a detailed chemical reaction model. In *39th AIAA Aerospace Sciences Meeting*, Reno, NV, 2001.

Kazuaki Inaba. *Numerical study on the dynamics of cellular structures in gaseous detonation*. PhD thesis, School of Science for Open and Environmental Systems Graudate School of Science and Technology, Yokohama, Japan, November 2004.

E. Jouguet. On the propagation of chemical reactions in gases. *J. de Mathematiques Pures et Appliquees*, 1:347–425, 1905. (Continued in 2:5–85, 1906).

A. R. Kasimov and D. S. Stewart. Spinning instability of gaseous detonations. *J. Fluid Mech.*, 466:179–203, 2002.

A. R. Kasimov and D. S. Stewart. On the dynamics of self-sustained one-dimensional detonations: A numerical study in the shock-attached frame. *Phys. Fluids*, 16(10): 3566–3578, 2004.

R. J. Kee, F. M. Rupley, and J. A. Miller. The CHEMKIN thermodynamic data base. Technical Report SAND87-8215, Sandia National Laboratories, 1987.

L. E. Kinsler, A. R. Frey, A. B. Coppens, and J. V. Sanders. *Fundamental of Acoustics*. John Wiley and Sons, 1950.

V. P. Korobeinikov, V. A. Levin, V. V. Markov, and G. G. Cher. Propagation of blast wave in combustible gas. *Astronautica Acta*, 17:529–537, 1972.

H. I. Lee and D. S. Stewart. Calculation of linear detonation instability: one-dimensional instability of plane detonation. *J. Fluid Mech.*, 216:103–132, 1990.

J. H. Lee. Dynamic parameters of gaseous detonations. *Ann. Rev. Fluid Mech.*, 16: 311–336, 1984.

M. H. Lefebvre, E. S. Oran, and K Kailasanath. Computations of detonation structure: The influence of model parameters. Technical Report NRL Memorandum Report NRL/MR/4404-92-6961, Naval Research Laboratory, 1992.

Z. Liang and L. Bauwens. Cell structure and stability of detonations with a pressure dependent chain-branching reaction rate model. *Combust. Theor. Model.*, 9:93–112, 2005.

Z. Liang, S. Browne, R. Deiterding, and J.E. Shepherd. Detonation front structure and the competition for radicals. In *31st Symp. (Intl) on Combustion*, pages 2445–2453, 2007.

J. C. Libouton, A. Jacques, and P. Van Tiggelen. Cinétique, structure et entretien des ondes de détonation. *Actes du Colloque International Berthelot-Vieille-Mallard-LeChatelier*, 2:437–442, 1981.

U. Maas and S. B. Pope. Simplifying chemical kinetics: Intrinsic low-dimensional manifolds in composition space. *Combust. Flame*, 88:239–264, 1992.

N. Manson. On the structure of so-called helical detonation waves in gaseous mixtures. *C. r. hebd. Sanc. Acad. Sci. Paris*, 222:46–51, 1946.

A. Matsuo and K. Fujii. Numerical investigation of the one-dimensional piston supported detonation waves. *Energy Conversion and Management*, 38:1283–1295, 1997.

S. McCahan. *Thermodynamic applications: rapid evaporation and reacting flow.* PhD thesis, Rensselaer Polytechnic Institute, 1992.

J. B. McVey and T. Y. Toong. Mechanism of instabilities in exothermic blunt-body flows. *Combust. Sci. Technol.*, 3:63–76, 1971.

H. D. Ng, A. J. Higgins, C. B. Kiyanda, M. I. Radulescu, and J. H. S. Lee. Nonlinear dynamics and chaos analysis of one-dimensional pulsating detonations. *Combust. Theor. Model.*, 9:159–170, 2005a.

H. D. Ng and J. H. S. Lee. Direct initiation of detonation with a multi-step reaction scheme. *J. Fluid Mech.*, 476:179–211, 2003.

H. D. Ng, M. I. Radulescu, A. J. Higgins, N. Nikiforakis, and J. H. S. Lee. Numerical investigation of the instability for one-dimensional Chapman-Jouguet detonations with chain-branching kinetics. *Combust. Theor. Model.*, 9(3):385–401, 2005b.

E. S. Oran, J. P. Boris, T. Young, M. Flanigan, T. Burks, and M. Picone. Numerical simulations of detonations in hydrogen-air and methane-air mixtures. In *18th Symp. (Intl) on Combustion*, pages 1641–1649, 1981.

E. S. Oran, J. W. Weber, Jr., E. I. Stefaniw, M. H. Lefebvre, and J. D. Anderson, Jr. A numerical study of a two-dimensional H_2–O_2–Ar detonation using a detailed chemical reaction model. *Combust. Flame*, 113:147–163, 1998.

N. Peters. Systematic reduction of flame kinetics: Principles and details. *Prog. Astronaut. Aeronaut.*, 113:67–86, 1988.

F. Pintgen. *Detonation diffraction in mixtures with various degrees of instability*. PhD thesis, California Institute of Technology, 2004.

F. Pintgen, C. A. Eckett, J. M. Austin, and J. E. Shepherd. Direct observations of reaction zone structure in propagating detonations. *Combust. Flame*, 133:211–229, 2003.

F. Pintgen and J. E. Shepherd. Pulse detonation engine impulse analysis for partially-oxidized jet fuel. Technical Report FM2003.001, GALCIT, 2003.

V. V. Pukhnachev. Stability of Chapman-Jouguet detonation. *Zh. Prikl. Mekh. i Tekhn. Fiz.*, 6:66, 1963. (English translation: *Sov. Phys. — Doklady*, 8, 338, 1963).

M. I. Radulescu, H. D. Ng, J. H. S. Lee, and B. Varatharajan. The effect of argon dilution on the stability of acetylene-oxygen detonations. In *Proc. Combust. Inst.*, volume 29, pages 2825–2831, 2002.

C. W. Rowley and T. Colonius. Discretely nonreflecting boundary conditions for linear hyperbolic systems. *J. Comput. Phys.*, 157:500–538, 2000.

G. L. Schott. Observations of structure of spinning detonations. *Phys. Fluids*, 8:850–865, 1965.

E. Schultz and J. E. Shepherd. Validation of detailed reaction mechanisms for detonation simulation. Technical Report FM99-5, GALCIT, 2000.

N. N. Semenov. *Chemical Kinetics and Chain Reactions.* Clarendon Press, Oxford, 1935.

G. J. Sharpe. Linear stability of idealized detonations. *Proc. R. Soc. Lond.* A, 453 (1967):2603–2625, 1997.

G. J. Sharpe and S. A. E. G. Falle. Two-dimensional numerical simulations of idealized detonations. *Proc. R. Soc. Lond.* A, 456:2081–2100, 2000.

K. I. Shchelkin and Y. K. Troshin. *Gasdynamics of Detonations.* Mono Book Corp., Baltimore, 1965.

J. E. Shepherd. Chemical kinetics of hydrogen–air–diluent detonations. *Prog. Astronaut. Aeronaut.*, 106:263–293, 1986.

M. Short. Multidimensional linear stability of a detonation wave at high activation energy. *SIAM J. Appl. Math.*, 57(2):307–326, 1997.

M. Short and J. J. Quirk. On the nonlinear stability and detonability limit of a detonation wave for a model three-step chain branching reaction. *J. Fluid Mech.*, 339:89–119, 1997.

M. Short and G. J Sharpe. Pulsating instability of detonations with a two-step chain-branching reaction model: theory and numerics. *Combust. Theor. Model.*, 7(2):401–416, 2003. URL http://stacks.iop.org/1364-7830/7/401.

M. Short and D. S. Stewart. Cellular detonation stability. Part 1. A normal-mode linear analysis. *J. Fluid Mech.*, 368:229–262, 1998.

G. P. Smith, D. M. Golden, M. Frenklach, N. W. Moriarty, B. Eiteneer, M. Goldenberg, C. T. Bowman, R. K. Hanson, S. Song, W. C. Gardiner, V. V. Lissianski Jr., and Z. Qin. GRI-Mechanism 3.0. http://www.me.berkeley.edu/gri_mech, 1999.

J. M. Smith, H. C. Van Hess, and M. M. Abbott. *Introduction to Chemical Engineering Thermodynamics*. McGraw-Hill, 1996.

D. S. Stewart and A. R. Kasimov. On the dynamics of self-sustained one-dimensional detonations: a numerical study in the shock-attached frame. *J. Propulsion Power*, 22: 1230–1244, 2006.

J. Stoer and R. Bulirsch. *Introduction to Numerical Analysis*. Springer-Verlag, 1983.

R. A. Strehlow. *Fundamentals of Combustion*. Robert E. Kreiger Publishing Company, Huntington, NY, 1979.

R. A. Strehlow and J. R. Biller. On the strength of transverse waves in gaseous detonations. *Combust. Flame*, 13:577–582, 1969.

R. A. Strehlow and C. D. Engel. Transverse waves in detonations .2. structure and spacing in H_2-O_2, C_2H_2-O_2, C_2H_4-O_2 and CH_4-O_2 systems. *AIAA Journal*, 7:492, 1969.

R. A. Strehlow, R. Liaugminas, R. H. Watson, and J. R. Eyman. Transverse wave structure in detonations. In *11th Symp. (Intl) on Combustion*, pages 683–391, 1967.

B. Sturtevant and V. A. Kulkarny. The focusing of weak shock waves. *J. Fluid Mech.*, 73(4):651–671, 1976.

P. A. Thompson. *Compressible–Fluid Dynamics*. Rensselaer Polytechnic Institute, 1988.

A. S. Tomlin, T. Turanyi, and M. J. Pilling. Mathematical tools for the construction, investigation, and reduction of combustion mechanisms. In M. J. Pilling, editor, *Low-temperature combustion and autoignition*, pages 293–437. Elsevier, 1997.

A. Tumin. Discussion about acoustic trapping. Personal Conversation, 2007a.

A. Tumin. Initial-value problem for small disturbances in an idealized one-dimensional detonation. *Phys. Fluids*, 19, 2007b.

V. Y. Ul'yanitskii. Role of flashing and transverse-wave collisions in the evolution of a multifrontal detonation-wave structure in gases. *Combustion Explosion and Shock Waves*, 17(2):227–232, 1981.

B. Varatharajan, M. Petrova, F. A. Williams, and V. Tangirala. Two-step chemical-kinetic description for hydrocarbon-oxygen-diluent ignition and detonation applications. In *Proc. Combust. Inst.*, volume 30, pages 1869–1877, 2005.

B. Varatharajan and F. A. Williams. Chemical-kinetic descriptions of high-temperature ignition and detonation of acetylene-oxygen-diluent systems. *Combust. Flame*, 124(4): 623–645, 2001.

W. G. Vincenti and C. H. Kruger. *Introduction to Physical Gas Dynamics*. Krieger Publishing Company, 1965.

V. V. Voevodesky and R. I. Soloukhin. On the mechanism and explosion limits of hydrogen-oxygen chain self-ignition in shock waves. In *10th Symp. (Intl) on Combustion*, pages 279–283, 1965.

J. von Neumann. Theory of detonation waves. In A. J. Taub, editor, *John von Neumann, Collected Works*. Macmillan, New York, 1942.

D. R. White. Turbulent structure of gaseous detonations. *Phys. Fluids*, 4:465–480, 1961.

G. B. Whitman. *Linear and Nonlinear Waves*. Wiley Interscience, 1999.

W. W. Wood and Z. W. Salsburg. Analysis of steady-state supported one-dimensional detonations and shocks. *Phys. Fluids*, pages 549–566, 1960.

H. C. Yee. Upwind and symmetric shock capturing schemes. Technical Report TM 89464, NASA, 1987.

S. Yungster and K. Radhakrishnan. Structure and stability of one-dimensional detonations in ethylene-air mixtures. *Shock Waves*, 2005. DOI: 10.1007/s00193-005-0242-0.

R. M. Zaidel. Stability of detonation waves in gas mixtures. *Dokl. Akad. Nauk.*, 136: 1142, 1961. (English translation: *Proc. Acad. Sci. USSR, Phys. Chem. Sec.* 136:167, 1961).

Ia. B. Zel'dovich. On the theory of the propagation of detonation in gaseous systems. *Zh. Eksp. Teor. Fiz.*, 10:542–568, 1940.

Appendix A

Summary of Equations Required for Implementation

A.1 Reactive Euler Equations

A.1.1 Shock-Fixed Frame

The one-dimensional reactive Euler equations are

$$v_{,t} + \mathrm{w}v_{,x} = v\mathrm{w}_{,x} \tag{A1.1}$$

$$\mathrm{w}_{,t} + \mathrm{w}\mathrm{w}_{,x} = -vP_{,x} \tag{A1.2}$$

$$P_{,t} + \mathrm{w}P_{,x} + \frac{a_f^2}{v}\mathrm{w}_{,x} = -\frac{G}{v}\sum_k e_{,Y_k}\dot{\Omega}_k \tag{A1.3}$$

$$Y_{i,t} + \mathrm{w}Y_{i,x} = \dot{\Omega}_i \tag{A1.4}$$

and the two-dimensional reactive Euler equations are

$$v_{,t} + \mathrm{w}v_{,x} + \mathrm{v}v_{,y} = v(\mathrm{w}_{,x} + \mathrm{v}_{,y}) \tag{A1.5}$$

$$\mathrm{w}_{,t} + \mathrm{w}\mathrm{w}_{,x} + \mathrm{v}\mathrm{w}_{,y} = -vP_{,x} \tag{A1.6}$$

$$\mathrm{v}_{,t} + \mathrm{w}\mathrm{v}_{,x} + \mathrm{v}\mathrm{v}_{,y} = -vP_{,y} \tag{A1.7}$$

$$P_{,t} + \mathrm{w}P_{,x} + \mathrm{v}P_{,y} + \frac{a_f^2}{v}(\mathrm{w}_{,x} + \mathrm{v}_{,y}) = -\frac{G}{v}\sum_k e_{,Y_k}\dot{\Omega}_k \tag{A1.8}$$

$$Y_{i,t} + \mathrm{w}Y_{i,x} + \mathrm{v}Y_{i,y} = \dot{\Omega}_i. \tag{A1.9}$$

A.1.2 Flat-Shock-Fixed Frame

The reactive Euler equations in one dimension become

$$v_{,t} + (\mathrm{u} + \psi_{,t})v_{,x} = v\mathrm{u}_{,x} \tag{A1.10}$$

$$\mathrm{u}_{,t} + (\mathrm{u} + \psi_{,t})\mathrm{u}_{,x} = -vP_{,x} \tag{A1.11}$$

$$P_{,t} + (\mathrm{u} + \psi_{,t})P_{,x} + \rho a_f^2 \mathrm{u}_{,x} = Z(P, v, \mathbf{Y}) \tag{A1.12}$$

$$Y_{i,t} + (\mathrm{u} + \psi_{,t})Y_{i,x} = \dot{\Omega}_i. \tag{A1.13}$$

The reactive Euler equations in two dimensions become

$$v_{,t} + (\mathrm{u} + \psi_{,t} + \mathrm{v}\psi_{,y})v_{,x} + \mathrm{v}v_{,y} = v(\mathrm{u}_{,x} + \mathrm{v}_{,y} + \psi_{,y}\mathrm{v}_{,x}) \tag{A1.14}$$

$$\mathrm{u}_{,t} + (\mathrm{u} + \psi_{,t} + \mathrm{v}\psi_{,y})\mathrm{u}_{,x} + \mathrm{v}\mathrm{u}_{,y} = -vP_{,x} \tag{A1.15}$$

$$\mathrm{v}_{,t} + (\mathrm{u} + \psi_{,t} + \mathrm{v}\psi_{,y})\mathrm{v}_{,x} + \mathrm{v}\mathrm{v}_{,y} = -v(P_{,y} + \psi_{,y}P_{,x}) \tag{A1.16}$$

$$P_{,t} + (\mathrm{u} + \psi_{,t} + \mathrm{v}\psi_{,y})P_{,x} + \mathrm{v}P_{,y} + \rho a_f^2(\mathrm{u}_{,x} + \mathrm{v}_{,y} + \psi_{,y}\mathrm{v}_{,x}) = Z(P, v, \mathbf{Y}) \tag{A1.17}$$

$$Y_{i,t} + (\mathrm{u} + \psi_{,t} + \mathrm{v}\psi_{,y})Y_{i,x} + \mathrm{v}Y_{i,y} = \dot{\Omega}_i \tag{A1.18}$$

where

$$Z(P, v, \mathbf{Y}) = -\frac{G}{v}\sum_k e_{,Y_k}\dot{\Omega}_k. \tag{A1.19}$$

A.2 Linear Stability Equations

$$\mathbf{A}^o\mathbf{z}^1_{,x} + (\omega\mathbf{I} + \mathbf{C}^o + ik_y\mathbf{B}^o)\,\mathbf{z}^1 + (\omega\mathbf{I} + ik_y\mathbf{B}^o)\mathbf{b}^o\psi^1 = 0 \tag{A2.1}$$

$$\mathbf{b} = \mathbf{z}_{,x} \qquad \mathbf{A} = \begin{pmatrix} \mathrm{u} & -v & 0 & 0 & 0 & 0 & \dots \\ 0 & \mathrm{u} & 0 & v & 0 & 0 & \dots \\ 0 & 0 & \mathrm{u} & 0 & 0 & 0 & \dots \\ 0 & \rho a_f^2 & 0 & \mathrm{u} & 0 & 0 & \dots \\ 0 & 0 & 0 & 0 & \mathrm{u} & 0 & \dots \\ 0 & 0 & 0 & 0 & 0 & \mathrm{u} & \dots \\ \dots & & & & & & \end{pmatrix} \tag{A2.2}$$

$$\mathbf{B} = \begin{pmatrix} 0 & 0 & -v & 0 & 0 & 0 & \dots \\ 0 & 0 & 0 & 0 & 0 & 0 & \dots \\ 0 & 0 & 0 & v & 0 & 0 & \dots \\ 0 & 0 & \rho a_f^2 & 0 & 0 & 0 & \dots \\ 0 & 0 & 0 & 0 & 0 & 0 & \dots \\ 0 & 0 & 0 & 0 & 0 & 0 & \dots \\ \dots & & & & & & \end{pmatrix} \tag{A2.3}$$

$$\mathbf{C} = \begin{pmatrix} -\mathrm{u}_{,x} & v_{,x} & 0 & 0 & 0 & 0 & \dots \\ P_{,x} & \mathrm{u}_{,x} & 0 & 0 & 0 & 0 & \dots \\ 0 & 0 & 0 & 0 & 0 & 0 & \dots \\ (\rho a_f^2)_{,v}\mathrm{u}_{,x} - Z_{,v} & P_{,x} & 0 & (\rho a_f^2)_{,P}\mathrm{u}_{,x} - Z_{,P} & (\rho a_f^2)_{,Y_1}\mathrm{u}_{,x} - Z_{,Y_1} & (\rho a_f^2)_{,Y_2}\mathrm{u}_{,x} - Z_{,Y_2} & \dots \\ -\dot{\Omega}_{1,v} & Y_{1,x} & 0 & -\dot{\Omega}_{1,P} & -\dot{\Omega}_{1,Y_1} & -\dot{\Omega}_{2,Y_1} & \dots \\ -\dot{\Omega}_{2,v} & Y_{2,x} & 0 & -\dot{\Omega}_{2,P} & -\dot{\Omega}_{1,Y_2} & -\dot{\Omega}_{2,Y_2} & \dots \\ \dots & & & & & & \end{pmatrix} \tag{A2.4}$$

$$\mathbf{A}^{-1} = \begin{pmatrix} \frac{1}{\mathrm{u}} & \frac{v}{\mathrm{u}^2 - a_f^2} & 0 & -\frac{v^2}{\mathrm{u}(\mathrm{u}^2 - a_f^2)} & 0 & 0 & \dots \\ 0 & \frac{\mathrm{u}}{\mathrm{u}^2 - a_f^2} & 0 & -\frac{v}{\mathrm{u}^2 - a_f^2} & 0 & 0 & \dots \\ 0 & 0 & \frac{1}{\mathrm{u}} & 0 & 0 & 0 & \dots \\ 0 & -\frac{\rho a_f^2}{\mathrm{u}^2 - a_f^2} & 0 & \frac{\mathrm{u}}{\mathrm{u}^2 - a_f^2} & 0 & 0 & \dots \\ 0 & 0 & 0 & 0 & \frac{1}{\mathrm{u}} & 0 & \dots \\ 0 & 0 & 0 & 0 & 0 & \frac{1}{\mathrm{u}} & 0 \\ \dots & & & & & & \end{pmatrix} \tag{A2.5}$$

A.3 Left Boundary Condition

At the shock the boundary conditions are such that the jump conditions are satisfied. The steady solution must satisfy

$$\rho_1 \mathrm{w}_1 = \rho_2 \mathrm{w}_2 \tag{A3.1}$$

$$P_1 + \rho_1 \mathrm{w}_1^2 = P_2 + \rho_2 \mathrm{w}_2^2 \tag{A3.2}$$

$$h_1 + \frac{\mathrm{w}_1^2}{2} = h_2 + \frac{\mathrm{w}_2^2}{2} \tag{A3.3}$$

and the perturbed quantities must satisfy

$$\rho_1 \mathrm{w}_1 = \rho_2^o \mathrm{w}_2^o \tag{A3.4}$$

$$P_1 + \rho_1 \mathrm{w}_1^2 = P_2^o + \rho_2^o \left(\mathrm{w}_2^2\right)^o \tag{A3.5}$$

$$h_1 + \frac{\mathrm{w}_1^2}{2} = h_2^o + \frac{\left(\mathrm{w}_2^2\right)^o}{2} \tag{A3.6}$$

$$v^1 = -\frac{v_2^2}{v_1}\omega\psi^1 \left(\frac{\frac{v_1}{v_2^o}G\mathrm{U} - 2\mathrm{U}[G+1] + \mathrm{w}_2^o[G+2]}{(a_f^2)_2(M_2^2-1)} \right) \tag{A3.7}$$

$$P^1 = \frac{\omega\psi^1}{v_1}\left[2(\mathrm{U}-\mathrm{w}_2^o) + (\mathrm{w}_2^2)^o \left(\frac{\frac{v_1}{v_2^o}G\mathrm{U} - 2\mathrm{U}[G+1] + \mathrm{w}_2^o[G+2]}{(a_f^2)_2(M_2^2-1)} \right) \right] \tag{A3.8}$$

$$\mathrm{u}^1 = -\omega\psi^1 \left[1 - \frac{v_2}{v_1}\left(1 - \left(\frac{\frac{v_1}{v_2}G\mathrm{U} - 2\mathrm{U}[G+1] + \mathrm{w}_2[G+2]}{(a_f^2)_2(M_2^2-1)} \right) \right) \right] \tag{A3.9}$$

$$\mathrm{v}_2^o = 0 \quad \mathrm{v}' = -(\mathrm{U}-\mathrm{w}_2^o) i k_y \psi^1. \tag{A3.10}$$

A.4 Radiation Condition — One-Step Irreversible Chemistry

$$\begin{aligned} &\left[\frac{\mathrm{u}'}{a_f}\right]_{x_R} - \left[\frac{ik_y\mathrm{u}}{\omega}\frac{\mathrm{v}'}{a_f}\right]_{x_R} - \left[\frac{\alpha}{\omega}\frac{P'}{\gamma P}\right]_{x_R} \\ &\qquad = Y'_{\mathcal{B}}\left(\left(\frac{q(\gamma-1)}{a_f^2} \right)(k_f\mathrm{u}) \left[\frac{k_f\mathrm{u}\frac{\alpha}{\omega} + a_f\left(k_f + \omega - \frac{(k_y\mathrm{u})^2}{\omega}\right)}{a_f^2\left[(k_f+\omega)^2 - (k_y\mathrm{u})^2\right] - (k_f\mathrm{u})^2} \right] \right)_{x_R} \end{aligned} \tag{A4.1}$$

A.5 Required Additional Derivatives

One-Step Irreversible Model

Thermodynamic Constants Section 2.1

Derivatives of $\dot{\Omega}_{\mathcal{A},Y_{\mathcal{B}}}$ and $Z(v,P,\mathbf{Y})$ (4.2.7)–(4.2.9)

A.5.1 One-Step Reversible Model

Thermodynamic Constants	Section 2.2
Derivatives of $\dot{\Omega}_{\mathcal{A},Y_{\mathcal{B}}}$ and $Z(v,P,\mathbf{Y})$	(4.3.9)–(4.3.16)

A.5.2 Detailed Chemistry Model

Thermodynamic Constants	Section 1.4
Soundspeed	Appendix C.1
Derivatives of h	Appendix C.2
Derivatives of T	Appendix C.3
Derivatives of c_{vi} and γ	Appendix C.5
Derivatives of $\dot{\Omega}_{\mathcal{A},Y_{\mathcal{B}}}$	Appendix D.2
Derivatives of $Z(v,P,\mathbf{Y})$	Appendix D.3

Appendix B

Transformations

B.1 Energy Equation

We transform the energy equation (1.1.3) to a more convenient form by first expanding the internal energy as a function of the independent variables.

$$\mathrm{d}e = \left.\frac{\partial e}{\partial P}\right|_{v,\mathbf{Y}} \mathrm{d}P + \left.\frac{\partial e}{\partial v}\right|_{P,\mathbf{Y}} \mathrm{d}v + \sum_{k=1}^{N} \left.\frac{\partial e}{\partial Y_k}\right|_{P,v,Y_{j\neq k}} \dot{\Omega}_k \tag{B1.1}$$

The thermodynamic derivatives can be simplified using the fundamental relation of thermodynamics and Maxwell's identities to obtain (for fixed composition)

$$\left.\frac{\partial e}{\partial P}\right|_{v} = \frac{v}{G} \tag{B1.2}$$

$$\left.\frac{\partial e}{\partial v}\right|_{P} = \frac{c_P}{v\alpha_T} - P \tag{B1.3}$$

where G is the Grüneisen coefficient, α_T is the coefficient of thermal expansion, and c_P is the specific heat capacity at constant pressure.

$$G \equiv v \left.\frac{\partial P}{\partial e}\right|_v \tag{B1.4}$$

$$\alpha_T \equiv \frac{1}{v} \left.\frac{\partial v}{\partial T}\right|_P \tag{B1.5}$$

$$c_P \equiv \left.\frac{\partial h}{\partial T}\right|_P \qquad h = e + Pv \tag{B1.6}$$

Substituting the expansion (B1.1) and above relationships into (1.1.3), we obtain the following energy equation:

$$\frac{\mathrm{D}P}{\mathrm{D}t} + \frac{a_f^2}{v}\boldsymbol{\nabla}\cdot\mathbf{u} = -\frac{G}{v}\sum_{k=1}^{N} \left.\frac{\partial e}{\partial Y_k}\right|_{P,v,Y_{j\neq k}} \dot{\Omega}_k. \tag{B1.7}$$

In deriving this, we have used the thermodynamic identity

$$\frac{Gc_P}{\alpha_T} = a_f^2 \tag{B1.8}$$

where a_f is the frozen soundspeed discussed in Appendix C.1.

B.2 Flat-Shock-Fixed Frame

In this appendix we explicitly discuss how we transformed the coordinate system from the laboratory frame to the flat-shock-fixed frame.

B.2.1 One-D Transformation

The derivatives below must remain invariant with respect to coordinate system transformations. To transform correctly, assume we have a function $f(x^L, t^L)$ that can be

expressed in either reference frame such that

$$f(x^L, t^L) = f(x^L(x,t), t^L(x,t)). \tag{B2.1}$$

The derivatives of f in the flat-shock-fixed frame are

$$\frac{\partial f}{\partial x} = \frac{\partial f}{\partial x^L}\frac{\partial x^L}{\partial x} + \frac{\partial f}{\partial t^L}\frac{\partial t^L}{\partial x}, \quad \frac{\partial f}{\partial t} = \frac{\partial f}{\partial x^L}\frac{\partial x^L}{\partial t} + \frac{\partial f}{\partial t^L}\frac{\partial t^L}{\partial t} \tag{B2.2}$$

$$\frac{\mathrm{D}f}{\mathrm{D}t^L} = \frac{\partial f}{\partial t^L} + \mathrm{u^L}\frac{\partial f}{\partial x^L}. \tag{B2.3}$$

With (3.1.2), the independent variables in the laboratory frame are

$$x^L = (\mathrm{U}t + \psi(t)) - x, \quad t^L = t. \tag{B2.4}$$

Incorporating these definitions of $x(x^L, t^L)$ and $t(x^L, t^L)$, the derivatives of f become

$$\frac{\partial f}{\partial x} = \frac{\partial f}{\partial x^L}(-1) + \frac{\partial f}{\partial t^L}(0), \quad \frac{\partial f}{\partial t} = \frac{\partial f}{\partial x^L}(\mathrm{U} + \psi_{,t}) + \frac{\partial f}{\partial t^L}(1) \tag{B2.5}$$

$$\frac{\mathrm{D}f}{\mathrm{D}t^L} = \frac{\partial f}{\partial t} + (\mathrm{U} + \psi_{,t})\frac{\partial f}{\partial x} - (\mathrm{U} - \mathrm{u})\frac{\partial f}{\partial x}. \tag{B2.6}$$

So the final expressions for the derivatives in the new reference frame are

$$\frac{\partial}{\partial x^L} = -\frac{\partial}{\partial x} \tag{B2.7}$$

$$\frac{\partial}{\partial t^L} = \frac{\partial}{\partial t} + (\mathrm{U} + \psi_{,t})\frac{\partial}{\partial x} \tag{B2.8}$$

$$\frac{\mathrm{D}}{\mathrm{D}t^L} = \frac{\partial}{\partial t} + (\mathrm{u} + \psi_{,t})\frac{\partial}{\partial x}. \tag{B2.9}$$

B.2.2 Two-D Transformation

In two spatial dimensions, assume we have a function $f(x^L, y^L, t^L)$ that can be expressed in either reference frame such that

$$f(x^L, y^L, t^L) = f(x^L(x, y, t), y^L(x, y, t), t^L(x, y, t)). \tag{B2.10}$$

The derivatives of f in the flat shock fixed frame are

$$\frac{\partial f}{\partial x} = \frac{\partial f}{\partial x^L}\frac{\partial x^L}{\partial x} + \frac{\partial f}{\partial y^L}\frac{\partial y^L}{\partial x} + \frac{\partial f}{\partial t^L}\frac{\partial t^L}{\partial x} \tag{B2.11}$$

$$\frac{\partial f}{\partial y} = \frac{\partial f}{\partial x^L}\frac{\partial x^L}{\partial y} + \frac{\partial f}{\partial y^L}\frac{\partial y^L}{\partial y} + \frac{\partial f}{\partial t^L}\frac{\partial t^L}{\partial y} \tag{B2.12}$$

$$\frac{\partial f}{\partial t} = \frac{\partial f}{\partial x^L}\frac{\partial x^L}{\partial t} + \frac{\partial f}{\partial y^L}\frac{\partial y^L}{\partial t} + \frac{\partial f}{\partial t^L}\frac{\partial t^L}{\partial t} \tag{B2.13}$$

$$\frac{\mathrm{D}f}{\mathrm{D}t^L} = \frac{\partial f}{\partial t^L} + \mathrm{u^L}\frac{\partial f}{\partial x^L} + \mathrm{v^L}\frac{\partial f}{\partial y^L}. \tag{B2.14}$$

With (3.1.2), the independent variables in the laboratory frame are

$$x^L = (\mathrm{U}t + \psi(y, t)) - x \tag{B2.15}$$

$$y^L = y, \quad t^L = t. \tag{B2.16}$$

Incorporating these definitions of $x(x^L, y^L, t^L)$, $y(x^L, y^L, t^L)$, and $t(x^L, y^L, t^L)$, the derivatives of f become

$$\frac{\partial f}{\partial x} = \frac{\partial f}{\partial x^L}(-1) + \frac{\partial f}{\partial y^L}(0) + \frac{\partial f}{\partial t^L}(0) \tag{B2.17}$$

$$\frac{\partial f}{\partial y} = \frac{\partial f}{\partial x^L}(\psi_{,y}) + \frac{\partial f}{\partial y^L}(1) + \frac{\partial f}{\partial t^L}(0) \tag{B2.18}$$

$$\frac{\partial f}{\partial t} = \frac{\partial f}{\partial x^L}(\mathrm{U} + \psi_{,t}) + \frac{\partial f}{\partial y^L}(0) + \frac{\partial f}{\partial t^L}(1) \tag{B2.19}$$

$$\frac{\mathrm{D}f}{\mathrm{D}t^L} = \frac{\partial f}{\partial t} + (\mathrm{U} + \psi_{,t})\frac{\partial f}{\partial x} - (\mathrm{U} - \mathrm{u})\frac{\partial f}{\partial x} + \mathrm{v}\left(\frac{\partial f}{\partial y} + (\psi_{,y})\frac{\partial f}{\partial x}\right). \tag{B2.20}$$

So the final expressions for the derivatives in the new reference frame are

$$\frac{\partial}{\partial x^L} = -\frac{\partial}{\partial x} \tag{B2.21}$$

$$\frac{\partial}{\partial y^L} = \frac{\partial}{\partial y} + (\psi_{,y})\frac{\partial}{\partial x} \tag{B2.22}$$

$$\frac{\partial}{\partial t^L} = \frac{\partial}{\partial t} + (\mathrm{U} + \psi_{,t})\frac{\partial}{\partial x} \tag{B2.23}$$

$$\frac{\mathrm{D}}{\mathrm{D}t^L} = \frac{\partial}{\partial t} + (\mathrm{u} + \psi_{,t} + \mathrm{v}\psi_{,y})\frac{\partial}{\partial x} + \mathrm{v}\frac{\partial}{\partial y}. \tag{B2.24}$$

B.3 Thermicity Equations

In order to derive the expressions for the ZND equations given in Fickett and Davis (1979), we use the steady form of (1.1.3) instead of (1.2.4) for ease. It is important to note that the coordinate transformation introduces only time derivatives, and in the steady case, all time derivatives go to zero. For this reason the steady form of (1.1.3),

$$e_{,x} = -Pv_{,x} \tag{B3.1}$$

is equivalent to (1.2.4). Equation B3.1 can be expressed in terms of enthalpy in the following way

$$e_{,x} + (Pv)_{,x} = -Pv_{,x} + (Pv)_{,x} \tag{B3.2}$$

$$h_{,x} = vP_{,x} \tag{B3.3}$$

and using (1.2.3)

$$h_{,x} = -\mathrm{ww}_{,x}. \tag{B3.4}$$

Now we use the definition of enthalpy,

$$h_{,x} = \left(\sum_k h_k Y_k \right)_{,x} = T_{,x} \sum_k Y_k c_{Pk} + \sum_k h_k Y_{k,x} \tag{B3.5}$$

combine (B3.5) with (1.2.5) and solve for the temperature gradient,

$$T_{,x} = \frac{1}{c_P} \left(h_{,x} - \frac{1}{\mathrm{w}} \sum_k h_k \dot{\Omega}_k \right) \tag{B3.6}$$

and combine (B3.6) with (B3.4) to eliminate the enthalpy gradient

$$T_{,x} = -\frac{1}{c_P} \left(\mathrm{ww}_{,x} + \frac{1}{\mathrm{w}} \sum_k h_k \dot{\Omega}_k \right). \tag{B3.7}$$

We differentiate the ideal gas equation of state, (1.1.11), and simplify with the derivative of the mass dependent gas constant,

$$R_{,x} = \mathcal{R} \sum_k \frac{1}{W_k} Y_{k,x}, \tag{B3.8}$$

to find an alternate expression for the temperature gradient

$$T_{,x} = T \left(\frac{1}{P} P_{,x} - \frac{1}{\rho} \rho_{,x} - \frac{1}{R} R_{,x} \right) \tag{B3.9}$$

$$= T \left(\frac{1}{P} P_{,x} - \frac{1}{\rho} \rho_{,x} \right) - T \overline{W} \sum_k \frac{\dot{\Omega}_k}{\mathrm{w} W_k}. \tag{B3.10}$$

By equating (B3.7) and (B3.10),

$$-\frac{1}{c_P} \left(\mathrm{ww}_{,x} + \frac{1}{\mathrm{w}} \sum_k h_k \dot{\Omega}_k \right) = T \left(\frac{1}{P} P_{,x} - \frac{1}{\rho} \rho_{,x} \right) - T \overline{W} \sum_k \frac{\dot{\Omega}_k}{\mathrm{w} W_k}, \tag{B3.11}$$

and using (1.2.2) and (1.2.3) to express everything in terms of $\mathrm{u}_{,x}$, we find

$$-\frac{1}{c_P}\left(\mathrm{w}\mathrm{w}_{,x}+\frac{1}{\mathrm{w}}\sum_k h_k\dot{\Omega}_k\right)=T\left(-\frac{\rho\mathrm{w}}{P}\mathrm{w}_{,x}+\frac{1}{\mathrm{w}}\mathrm{w}_{,x}\right)-T\overline{W}\sum_k\frac{\dot{\Omega}_k}{\mathrm{w}W_k}. \tag{B3.12}$$

To simplify, we apply the ideal gas equation of state and the ideal gas specific heat definitions:

$$-\frac{\gamma-1}{\gamma RT}\left(\mathrm{w}\mathrm{w}_{,x}+\frac{1}{\mathrm{w}}\sum_k h_k\dot{\Omega}_k\right)=-\frac{\mathrm{w}}{RT}\mathrm{w}_{,x}+\frac{1}{\mathrm{w}}\mathrm{w}_{,x}-\overline{W}\sum_k\frac{\dot{\Omega}_k}{\mathrm{w}W_k}. \tag{B3.13}$$

Finally we solve for $\mathrm{u}_{,x}$ and use the definitions of $\dot{\sigma}$, (1.2.11), and the sonic parameter,

$$\eta=1-M^2, \tag{B3.14}$$

to determine the final expression for $\mathrm{u}_{,x}$

$$\mathrm{w}_{,x}=\frac{1}{1-M^2}\sum_k\left(\frac{\overline{W}}{W_k}-\frac{h_k}{c_PT}\right)\dot{\Omega}_k=\frac{\dot{\sigma}}{\eta}. \tag{B3.15}$$

From this we can determine the thermicity form of the other equations (1.2.13)–(1.2.16).

B.4 Linear Perturbation of the Energy Equation

Linear perturbation of the mass and momentum equations is fairly straightforward, but the energy equation requires some special care. If we start with (A1.12), ρa_f^2 and $G\rho\sum_k e_{Y_k}\dot{\Omega}_i$ are thermodynamic quantities that can be expressed in terms of $\mathbf{z}$, our vector of independent variables. With this in mind, we can perturb the energy equation, subtract the steady equation, (A1.12), and express the perturbed energy equation as

follows

$$\begin{aligned}\omega P^1 + P^o_{,x}\mathrm{u}^1 + \mathrm{u}^o_{,x}\left[(\rho a_f^2)_{,v}v^1 + (\rho a_f^2)_{,P}P^1 + \sum_k (\rho a_f^2)_{,Y_k}Y_k^1\right] \\ + \mathrm{u}^o P^1_{,x} + \rho^o a_f^2 \mathrm{u}^1_{,x} + \omega\psi^1 P^o_{,x} = \left[Z_{,v}v^1 + Z_{,P}P^1 + \sum_k Z_{,Y_k}Y_k^1\right]\end{aligned} \tag{B4.1}$$

where $Z(P, v, \mathbf{Y})$ is defined by (3.2.13). The final expression of the energy equation which leads to the elements of $\mathbf{A}$, $\mathbf{b}$, and $\mathbf{C}$ is

$$\begin{aligned}&\left[\left[(\rho a_f^2)_{,v}\mathrm{u}^o_{,x} - Z_{,v}v^1\right]v^1 + \left[(\rho a_f^2)_{,P}\mathrm{u}^o_{,x} - Z_{,P}P^1\right]P^1 + \sum_k \left[(\rho a_f^2)_{,Y_k}\mathrm{u}^o_{,x} - Z_{,Y_k}Y_k^1\right]Y_k^1\right] \\ &\omega P^1 + P^o_{,x}\mathrm{u}^1 + \left[\mathrm{u}^o P^1_{,x} + \rho^o a_f^2 \mathrm{u}^1_{,x}\right] + \omega\psi^1 P^o_{,x} = 0.\end{aligned} \tag{B4.2}$$

B.5 Linear Perturbation of the Shock Jump Conditions

Starting with the shock jump conditions (1.2.17)–(1.2.19), (1.2.17) becomes

$$\rho_1(\mathrm{U} + \psi_{,t}) = (\rho_2 + \rho')(\mathrm{w}_2 + \mathrm{w}'). \tag{B5.1}$$

By neglecting products of perturbations and grouping terms of equal order, (B5.1) becomes

$$[\rho_1 \mathrm{U}] + \rho_1\psi_{,t} = [\rho_2 \mathrm{w}_2] + \mathrm{w}_2\rho' + \rho_2\mathrm{w}'. \tag{B5.2}$$

The zero-order terms in (B5.2) are exactly (1.2.17), and the remaining terms give the following criterion.

$$\rho_1\psi_{,t} = \mathrm{w}_2\rho' + \rho_2\mathrm{w}'. \tag{B5.3}$$

Following similar derivations for (1.2.18) and (1.2.19), the other criteria become

$$P' = 2\rho_1 \mathrm{U}\psi_{,t} - 2\rho_2 \mathrm{w}_2 \mathrm{w}' - \mathrm{w}_2^2 \rho' \tag{B5.4}$$

$$\mathrm{U}\psi_{,t} = h' + \mathrm{w}_2 \mathrm{w}'. \tag{B5.5}$$

To first order, h' in terms of P and ρ is

$$h' = \left.\frac{\partial h}{\partial P}\right|_2 P' + \left.\frac{\partial h}{\partial \rho}\right|_2 \rho' = h_{2,P} P' + h_{2,\rho} \rho' \tag{B5.6}$$

and (B5.5) becomes

$$\mathrm{U}\psi_{,t} = h_{2,P} P' + h_{2,\rho} \rho' + \mathrm{w}_2 \mathrm{w}'. \tag{B5.7}$$

Solving (B5.3), (B5.4), and (B5.7) for ρ', P', and w' gives

$$\rho' = \rho_2 \psi_{,t} \left[\frac{\mathrm{U} - 2\rho_1 h_{2,P}(\mathrm{U} - \mathrm{w}_2) - \mathrm{w}_2 \frac{\rho_1}{\rho_2}}{h_{2,P}\rho_2 \mathrm{w}_2^2 + \rho_2 h_{2,\rho} - \mathrm{w}_2^2} \right] \tag{B5.8}$$

$$P' = \psi_{,t} \left[2\rho_1(\mathrm{U} - \mathrm{w}_2) + \rho_2 \mathrm{w}_2^2 \left(\frac{\mathrm{U} - 2\rho_1 h_{2,P}(\mathrm{U} - \mathrm{w}_2) - \mathrm{w}_2 \frac{\rho_1}{\rho_2}}{h_{2,P}\rho_2 \mathrm{w}_2^2 + \rho_2 h_{2,\rho} - \mathrm{w}_2^2} \right) \right] \tag{B5.9}$$

$$\mathrm{w}' = \psi_{,t} \left[\frac{\rho_1}{\rho_2} - \mathrm{w}_2 \left(\frac{\mathrm{U} - 2\rho_1 h_{2,P}(\mathrm{U} - \mathrm{w}_2) - \mathrm{w}_2 \frac{\rho_1}{\rho_2}}{h_{2,P}\rho_2 \mathrm{w}_2^2 + \rho_2 h_{2,\rho} - \mathrm{w}_2^2} \right) \right]. \tag{B5.10}$$

With some thermodynamics, the derivatives of enthalpy are (see Appendix C.2)

$$h_{2,P} = \frac{1}{\rho_2} \frac{G+1}{G} \tag{B5.11}$$

$$h_{2,\rho} = -\frac{(a_f^2)_2}{\rho_2} \frac{1}{G}. \tag{B5.12}$$

Inserting (B5.11) and (B5.12) into (B5.8)–(B5.10), defining $M_2 = \mathrm{w}_2/(a_f)_2$, and incorporating (3.2.6), the final expressions for $\rho^1(0^+)$, $P^1(0^+)$, and $\mathrm{w}^1(0^+)$ are

$$\rho^1(0^+) = \rho_1 \omega \psi^1 \left(\frac{\frac{\rho_2}{\rho_1} G\mathrm{U} - 2\mathrm{U}[G+1] + \mathrm{w}_2[G+2]}{(a_f^2)_2 (M_2^2 - 1)} \right) \tag{B5.13}$$

$$v^1(0^+) = -v_2^2 \rho^{1L} \rightarrow v^{1L} = -\frac{v_2^2}{v_1} \omega \psi^1 \left(\frac{\frac{v_1}{v_2} G\mathrm{U} - 2\mathrm{U}[G+1] + \mathrm{w}_2[G+2]}{(a_f^2)_2 (M_2^2 - 1)} \right) \tag{B5.14}$$

$$P^1(0^+) = \frac{\omega \psi^1}{v_1} \left[2(\mathrm{U} - \mathrm{w}_2) + \mathrm{w}_2^2 \left(\frac{\frac{v_1}{v_2} G\mathrm{U} - 2\mathrm{U}[G+1] + \mathrm{w}_2[G+2]}{(a_f^2)_2 (M_2^2 - 1)} \right) \right] \tag{B5.15}$$

$$\mathrm{w}^1(0^+) = \frac{v_2}{v_1} \omega \psi^1 \left[1 - \mathrm{w}_2 \left(\frac{\frac{v_1}{v_2} G\mathrm{U} - 2\mathrm{U}[G+1] + \mathrm{w}_2[G+2]}{(a_f^2)_2 (M_2^2 - 1)} \right) \right]. \tag{B5.16}$$

These expressions are in the instantaneous shock-fixed frame. To find the velocity in the flat-shock-fixed frame of reference first we transform to the lab frame.

$$\mathrm{u}_2^L = \mathrm{D} - \mathrm{w}_2 \tag{B5.17}$$

$$(\mathrm{u}_2^o)^L + \mathrm{u}'^L = \mathrm{U} + \psi_{,t} - \mathrm{w}_2^o - \mathrm{w}' \tag{B5.18}$$

$$\mathrm{u}'^L = \psi_{,t} - \mathrm{w}' \tag{B5.19}$$

Now we can transform u'^L to the perturbation fixed frame according to (3.1.3).

$$\mathrm{u}_2^o + \mathrm{u}' = \mathrm{U} - (\mathrm{u}_2^o)^L - \mathrm{u}'^L \tag{B5.20}$$

$$\mathrm{u}' = -\mathrm{u}'^L = \mathrm{w}' - \psi_{,t} \tag{B5.21}$$

The expression for the velocity in the perturbation fixed frame is

$$\mathrm{u}^1(0^+) = -\omega \psi^1 \left[1 - \frac{v_2}{v_1} \left(1 - \mathrm{u}_2 \left(\frac{\frac{v_1}{v_2} G\mathrm{U} - 2\mathrm{U}[G+1] + \mathrm{w}_2[G+2]}{(a_f^2)_2 (M_2^2 - 1)} \right) \right) \right]. \tag{B5.22}$$

B.6 Decomposition of w

First we determine the value of ϵ in terms of ψ (see Figure 3.2a).

$$\epsilon \approx \tan(\epsilon) \tag{B6.1}$$

$$= \frac{\mathrm{d}x^L_{shock}}{\mathrm{d}y^L} \tag{B6.2}$$

$$\frac{\mathrm{d}x^L_{shock}}{\mathrm{d}y^L} = \frac{\mathrm{d}(\mathrm{U}t + \psi(y,t))}{\mathrm{d}y} + \psi_{,y}\frac{\mathrm{d}(\mathrm{U}t + \psi(y,t))}{\mathrm{d}x} = \psi_{,y} \tag{B6.3}$$

Next, we need to determine the component of the shock velocity normal to the shock front (see Figure 3.2b).

$$\mathrm{D}_n \approx \mathrm{D}_n \cos(\epsilon) = \mathrm{D} = \mathrm{U} + \psi_{,t} \tag{B6.4}$$

Above, we have solved for w_2 which we can transform to u_{2n} and decompose into u_2 and v_2 according to Figure 3.2c.

$$\mathrm{u}^L_{2n} = \mathrm{D}_n - \mathrm{w}_2 = \mathrm{U} + \psi_{,t} - \mathrm{w}_2 \tag{B6.5}$$

$$\mathrm{u}^L_2 = \mathrm{u}^L_{2n}\cos(\epsilon) \approx \mathrm{u}^L_{2n} = \mathrm{U} + \psi_{,t} - \mathrm{w}_2 \tag{B6.6}$$

$$\mathrm{v}^L_2 = \mathrm{u}^L_{2n}\sin(\epsilon) \approx \mathrm{u}^L_{2n}\epsilon = (\mathrm{U} + \psi_{,t} - \mathrm{w}_2)\psi_{,y} \tag{B6.7}$$

We then transform u^L_2 to the perturbation fixed frame discussed in Section 3.1.

$$\mathrm{u}_2 = \mathrm{U} - \mathrm{u}^L_2 = \mathrm{w}_2 - \psi_{,t} \tag{B6.8}$$

$$\mathrm{u}_2 + \mathrm{u}' = \mathrm{w}_2 + \mathrm{w}' - \psi_{,t} \rightarrow \mathrm{u}_2 = \mathrm{w}_2 \quad \mathrm{u}' = \mathrm{w}' - \psi_{,t} \tag{B6.9}$$

$$\mathrm{v}_2 + \mathrm{v}' = -(\mathrm{U} + \psi_{,t} - \mathrm{w}_2 - \mathrm{w}')\psi_{,y} \rightarrow \mathrm{v}_2 = 0 \quad \mathrm{v}' = -(\mathrm{U} - \mathrm{w}_2)\psi_{,y} \tag{B6.10}$$

B.7 Adiabatic Change Relation

The adiabatic change relation is an alternate expression of the energy equation. We could use

$$\frac{\mathrm{D}h'}{\mathrm{D}t} = \frac{1}{\rho_o}\frac{\mathrm{D}P'}{\mathrm{D}t} \tag{B7.1}$$

in the wave hierarchy methodology discussed in Appendix I.2. Instead we use the adiabatic change equation. First we re-express $Y'_{\mathcal{B}}$ in terms of the expressions for the sound-speed (see Appendix C.1)

$$Y'_{\mathcal{B}} = \frac{1}{h_{,Y_{\mathcal{B}}}}\left(h' - h_{,\rho}\rho' - h_{,P}P'\right) \tag{B7.2}$$

which gives us an expression for the left-hand side of (I1.5)

$$\frac{\mathrm{D}Y'_{\mathcal{B}}}{\mathrm{D}t} = \frac{1}{h_{,Y_{\mathcal{B}}}}\left(\frac{\mathrm{D}h'}{\mathrm{D}t} - h_{,\rho}\frac{\mathrm{D}\rho'}{\mathrm{D}t} - h_{,P}\frac{\mathrm{D}P'}{\mathrm{D}t}\right). \tag{B7.3}$$

We now use the energy equation (I1.4) to eliminate h'

$$\frac{\mathrm{D}Y'_{\mathcal{B}}}{\mathrm{D}t} = \frac{1}{h_{,Y_{\mathcal{B}}}}\left(\frac{1}{\rho_o}\frac{\mathrm{D}P'}{\mathrm{D}t} - h_{,\rho}\frac{\mathrm{D}\rho'}{\mathrm{D}t} - h_{,P}\frac{\mathrm{D}P'}{\mathrm{D}t}\right) \tag{B7.4}$$

$$= \frac{h_{,\rho}}{h_{,Y_{\mathcal{B}}}}\left(\frac{\frac{1}{\rho_o} - h_{,P}}{h_{,\rho}}\frac{\mathrm{D}P'}{\mathrm{D}t} - \frac{\mathrm{D}\rho'}{\mathrm{D}t}\right). \tag{B7.5}$$

The modified energy equation is now

$$\frac{\mathrm{D}Y'_{\mathcal{B}}}{\mathrm{D}t} = \frac{h_{,\rho}}{h_{,Y_{\mathcal{B}}}}\left(\frac{1}{a_f^2}\frac{\mathrm{D}P'}{\mathrm{D}t} - \frac{\mathrm{D}\rho'}{\mathrm{D}t}\right) \tag{B7.6}$$

which is identical to the adiabatic change equation

$$\frac{\mathrm{D}P'}{\mathrm{D}t} = a_f^2 \left(\frac{\mathrm{D}\rho'}{\mathrm{D}t} + \rho_o \dot{\sigma} \right) \tag{B7.7}$$

if

$$\rho_o \dot{\sigma} = \frac{h_{,Y_\mathcal{B}}}{h_{,\rho}} \frac{\mathrm{D}Y'_\mathcal{B}}{\mathrm{D}t} \tag{B7.8}$$

or

$$\rho_o \sigma = \frac{h_{,Y_\mathcal{B}}}{h_{,\rho}}. \tag{B7.9}$$

Appendix C

Thermodynamics

We will be using the following notation for partial derivatives evaluated at a specific state.

$$\left[\left.\frac{\partial f}{\partial x}\right|_m\right]_y = f_{m,x}|_y \tag{C1}$$

where f is a function of x and y and m is the state where we evaluate the derivative. If none of the independent variables are specifically held constant, we assume that all but the variable we are taking the derivative with respect to are held constant.

C.1 Soundspeed

It will be useful to express the frozen and equilibrium sound speeds in terms of derivatives of enthalpy. First we expand the enthalpy as a function of P, ρ, and $Y_{\mathcal{B}}$

$$dh = h_{,Y_{\mathcal{B}}} dY_{\mathcal{B}} + h_{,\rho} d\rho + h_{,P} dP. \tag{C1.1}$$

We know that $Y_{\mathcal{B}}$ is a thermodynamic function as well and can be expressed in terms of P and ρ

$$dY_{\mathcal{B}} = Y_{\mathcal{B},\rho} d\rho + Y_{\mathcal{B},P} dP. \tag{C1.2}$$

Using Gauss' equation,

$$dh = Tds + \frac{dP}{\rho}. \tag{C1.3}$$

Soundspeed, a, is defined as the isentropic ($ds = 0$) derivative of pressure with respect to density. Frozen refers to holding the composition fixed ($dY_{\mathcal{B}} = 0$) and equilibrium refers to taking the derivative at equilibrium conditions ($dY_{\mathcal{B}} = dY^*_{\mathcal{B}}$ where $dY^*_{\mathcal{B}}$ is the equilibrium value of $dY_{\mathcal{B}}$).

$$\frac{dP}{\rho_o} = h_{,Y_{\mathcal{B}}} dY_{\mathcal{B}} + h_{,\rho} d\rho + h_{,P} dP \tag{C1.4}$$

$$\left.\frac{\partial P}{\partial \rho}\right|_s = \frac{h_{,\rho} + h_{,Y_{\mathcal{B}}} Y_{\mathcal{B},\rho}}{\frac{1}{\rho} - h_{,P} - h_{,Y_{\mathcal{B}}} Y_{\mathcal{B},P}} \tag{C1.5}$$

C.1.1 Frozen Soundspeed

The frozen soundspeed, a_f, is

$$a_f^2 = \left.\frac{\partial P}{\partial \rho}\right|_{s,dY_{\mathcal{B}}=0} = \frac{h_{,\rho}}{\frac{1}{\rho} - h_{,P}}. \tag{C1.6}$$

C.1.2 Equilibrium Soundspeed

The equilibrium soundspeed, a_e, is defined as

$$a_e^2 = \left.\frac{\partial P}{\partial \rho}\right|_{s,Y_{\mathcal{B}}=Y^*_{\mathcal{B}}} = \frac{h_{,\rho} + h_{,Y^*_{\mathcal{B}}} Y^*_{\mathcal{B},\rho}}{\frac{1}{\rho} - h_{,P} - h_{,Y^*_{\mathcal{B}}} Y^*_{\mathcal{B},P}}. \tag{C1.7}$$

We can use the adiabatic change equation (B7.6) to find an alternate expression for the equilibrium soundspeed. At equilibrium

$$d\dot{\Omega} = \dot{\Omega}_{,\rho} d\rho + \dot{\Omega}_{,P} dP + \dot{\Omega}_{,Y^*_{\mathcal{B}}} dY^*_{\mathcal{B}} = 0 \tag{C1.8}$$

which can be rearranged such that

$$dY_{\mathcal{B}}^{*} = -\frac{\dot{\Omega}_{,\rho} d\rho + \dot{\Omega}_{,P} dP}{\dot{\Omega}_{,Y_{\mathcal{B}}^{*}}}. \tag{C1.9}$$

If we insert this into (B7.6),

$$-\dot{\Omega}_{,\rho} \frac{\mathrm{D}\rho}{\mathrm{D}t} - \dot{\Omega}_{,P} \frac{\mathrm{D}P}{\mathrm{D}t} = \frac{\dot{\Omega}_{,Y_{\mathcal{B}}^{*}}}{\rho\sigma} \left(\frac{1}{a_f^2} \frac{\mathrm{D}P}{\mathrm{D}t} - \frac{\mathrm{D}\rho}{\mathrm{D}t} \right) \tag{C1.10}$$

which leads to the alternate formulation of the equilibrium soundspeed

$$a_e^2 = a_f^2 \left(\frac{1 - \rho\sigma \frac{\dot{\Omega}_{,\rho}}{\dot{\Omega}_{,Y_{\mathcal{B}}^{*}}}}{1 + a_f^2 \rho\sigma \frac{\dot{\Omega}_{,P}}{\dot{\Omega}_{,Y_{\mathcal{B}}^{*}}}} \right). \tag{C1.11}$$

C.2 Enthalpy Derivatives

We would like to express the derivatives of enthalpy as functions of quantities that we can determine so that we can evaluate the derivatives of pressure. To determine these derivatives of enthalpy we need two fundamental equations as well as the definitions of the Grüneisen Coefficient, G, and the equilibrium soundspeed, a_e (C1.7).

$$dh = Tds + vdP \tag{C2.1}$$

$$Tds = de + Pdv \tag{C2.2}$$

$$G = v\, P_{,e}\big|_{v} \tag{C2.3}$$

First we will evaluate the first-order partial derivatives of enthalpy

$$h_{,P}|_v = e_{,P}|_v + (Pv)_{,P}|_v \tag{C2.4}$$
$$= e_{,P}|_v + v \tag{C2.5}$$
$$= \frac{v}{G} + v \tag{C2.6}$$
$$h_{,P}|_v = v\frac{G+1}{G}. \tag{C2.7}$$

Similarly

$$h_{,v}|_P = Ts_{,v}|_P + vP_{,v}|_P \tag{C2.8}$$
$$= Ts_{,v}|_P \tag{C2.9}$$
$$= -\,Ts_{,P}|_v\, P_{,v}|_s \tag{C2.10}$$
$$= -\,e_{,P}|_v\, P_{,v}|_s \tag{C2.11}$$
$$= -\left(\frac{v}{G}\right)\left(\frac{-a_e^2}{v^2}\right) \tag{C2.12}$$
$$h_{,v}|_P = \frac{a_e^2}{v}\frac{1}{G}. \tag{C2.13}$$

C.3 Derivatives of Temperature

Since we will be using the chain rule to determine many of our derivatives, we first find the derivatives of temperature with respect to our independent variables v, P, and $\mathbf{Y}$.

$$\left.\frac{\partial T}{\partial v}\right|_{P,\mathbf{Y}} = \left.\frac{\partial \frac{Pv}{R}}{\partial v}\right|_{P,\mathbf{Y}} = \frac{P}{R} = \frac{T}{v} \tag{C3.1}$$
$$\left.\frac{\partial T}{\partial P}\right|_{v,\mathbf{Y}} = \left.\frac{\partial \frac{Pv}{R}}{\partial P}\right|_{v,\mathbf{Y}} = \frac{v}{R} = \frac{T}{P} \tag{C3.2}$$
$$\left.\frac{\partial T}{\partial Y_i}\right|_{P,v,Y_{k\neq i}} = \left.\frac{\partial \frac{Pv}{R}}{\partial Y_i}\right|_{P,v,Y_{k\neq i}} = \frac{Pv}{\mathcal{R}}\left.\frac{\partial \overline{W}}{\partial Y_i}\right|_{P,v,Y_{k\neq i}} = \frac{Pv}{\mathcal{R}}\overline{W}_{Y_i} \tag{C3.3}$$

C.4 Pseudo-Thermodynamic Function Derivatives — Detailed Chemistry

Now, we determine $e_{,Y_i}$. For an ideal gas, the specific energy is strictly a function of temperature.

$$e_{,Y_i} = \left.\frac{\partial e}{\partial Y_i}\right|_{P,v,Y_{k\neq i}} = \left.\frac{\partial \sum_k e_k Y_k}{\partial Y_i}\right|_{P,v,Y_{k\neq i}} = e_i + \sum_k Y_k \left.\frac{\partial e_k}{\partial Y_i}\right|_{P,v,Y_{k\neq i}} \tag{C4.1}$$

$$= e_i + \sum_k Y_k \frac{\mathrm{d}e_k}{\mathrm{d}T}\left.\frac{\partial T}{\partial Y_i}\right|_{P,v,Y_{k\neq i}} \tag{C4.2}$$

By definition,

$$\frac{\mathrm{d}e_k}{\mathrm{d}T} = c_{vk}, \tag{C4.3}$$

now $e_{,Y_i}$ becomes

$$\left.\frac{\partial e}{\partial Y_i}\right|_{P,v,Y_{k\neq i}} = e_i + \sum_k Y_k c_{vk}\left(\frac{Pv}{\mathcal{R}}\overline{W}_{Y_i}\right) = e_i + \frac{Pv}{\mathcal{R}}\overline{W}_{Y_i}\sum_k Y_k c_{vk} \tag{C4.4}$$

$$= e_i + c_v\frac{Pv}{\mathcal{R}}\overline{W}_{Y_i}. \tag{C4.5}$$

Derivatives of the pseudo-thermodynamic function also require derivatives of

$$e_i + c_v\frac{Pv}{\mathcal{R}}\overline{W}_{Y_i}. \tag{C4.6}$$

First we will take the derivative with respect to a dummy variable, x, and then specialize to the independent variables

$$\begin{aligned}\frac{\partial}{\partial x}\left(e_i + \frac{c_v P v}{\mathcal{R}}\overline{W}_{Y_i}\right) &= \frac{\mathrm{d}e_i}{\mathrm{d}T}\frac{\partial T}{\partial x} + \frac{\overline{W}_{Y_i}}{\mathcal{R}}\left[\frac{\partial c_v}{\partial x}Pv + c_v v\frac{\partial P}{\partial x} + c_v P\frac{\partial v}{\partial x}\right] \\ &\quad + \frac{c_v P v}{\mathcal{R}}\frac{\partial \overline{W}_{Y_i}}{\partial x} \\ &= c_{vi}\frac{\partial T}{\partial x} + \frac{\overline{W}_{Y_i}}{\mathcal{R}}\left[Pv\sum_k\left(\frac{\mathrm{d}c_{vk}}{\mathrm{d}T}\frac{\partial T}{\partial x}Y_k + c_{vk}\frac{\partial Y_k}{\partial x}\right)\right] \\ &\quad + \frac{\overline{W}_{Y_i}}{\mathcal{R}}\left[c_v v\frac{\partial P}{\partial x} + c_v P\frac{\partial v}{\partial x}\right] + \frac{c_v P v}{\mathcal{R}}\frac{\partial \overline{W}_{Y_i}}{\partial x}.\end{aligned} \tag{C4.7}$$

(C4.8)

If $x = v$,

$$\left.\frac{\partial}{\partial v}\left(e_i + \frac{c_v P v}{\mathcal{R}}\overline{W}_{Y_i}\right)\right|_{P,\mathbf{Y}} = c_{vi}\frac{T}{v} + \frac{P\overline{W}_{Y_i}}{\mathcal{R}}\left(T\sum_k Y_k\frac{\mathrm{d}c_{vk}}{\mathrm{d}T} + c_v\right) \tag{C4.9}$$

$$= \frac{P}{\mathcal{R}}\left[c_{vi}\overline{W} + \overline{W}_{Y_i}\left(c_v + T\sum_k Y_k\frac{\mathrm{d}c_{vk}}{\mathrm{d}T}\right)\right]. \tag{C4.10}$$

If $x = P$,

$$\left.\frac{\partial}{\partial P}\left(e_i + \frac{c_v P v}{\mathcal{R}}\overline{W}_{Y_i}\right)\right|_{v,\mathbf{Y}} = c_{vi}\frac{T}{P} + \frac{v\overline{W}_{Y_i}}{\mathcal{R}}\left(T\sum_k Y_k\frac{\mathrm{d}c_{vk}}{\mathrm{d}T} + c_v\right) \tag{C4.11}$$

$$= \frac{v}{\mathcal{R}}\left[c_{vi}\overline{W} + \overline{W}_{Y_i}\left(c_v + T\sum_k Y_k\frac{\mathrm{d}c_{vk}}{\mathrm{d}T}\right)\right]. \tag{C4.12}$$

If $x = Y_j$,

$$\frac{\partial}{\partial Y_j}\left(e_i + \frac{c_v P v}{\mathcal{R}}\overline{W}_{Y_i}\right)\bigg|_{P,v,Y_{k\neq j}} = \frac{c_{vi} P v \overline{W}_{Y_i}}{\mathcal{R}} + \frac{P v \overline{W}_{Y_i}}{\mathcal{R}}\sum_k \left(\frac{P v \overline{W}_{Y_i}}{\mathcal{R}} Y_k \frac{\mathrm{d}c_{vk}}{\mathrm{d}T} + c_{vk}\right) + \frac{c_v P v}{\mathcal{R}}\left.\frac{\partial \overline{W}_{Y_i}}{\partial Y_j}\right|_{P,v,Y_{k\neq j}} \tag{C4.13}$$

$$= \frac{P v}{\mathcal{R}}\left[\overline{W}_{Y_i}\left(c_{vi} + \sum_k \left[\frac{P v \overline{W}_{Y_i}}{\mathcal{R}} Y_k \frac{\mathrm{d}c_{vk}}{\mathrm{d}T} + c_{vk}\right]\right)\right] + \frac{P v c_v}{\mathcal{R}}\left[\left.\frac{\partial \overline{W}_{Y_i}}{\partial Y_j}\right|_{P,v,Y_{k\neq j}}\right]. \tag{C4.14}$$

C.5 Specific Heat Derivatives — Detailed Chemistry

Several additional thermodynamic derivative expressions will be necessary to implement the equations discussed.

$$\frac{\mathrm{d}c_{vi}}{\mathrm{d}T}, \quad \left.\frac{\partial \gamma}{\partial v}\right|_{P,\mathbf{Y}}, \quad \left.\frac{\partial \gamma}{\partial P}\right|_{v,\mathbf{Y}}, \quad \left.\frac{\partial \gamma}{\partial Y_i}\right|_{P,v,Y_{j\neq i}} \tag{C5.1}$$

Again, in the case of a perfect gas, the specific heats are strictly functions of temperature. We can easily relate $\dfrac{\mathrm{d}c_{vi}}{\mathrm{d}T}$ to $\dfrac{\mathrm{d}c_{Pi}}{\mathrm{d}T}$

$$\frac{\mathrm{d}c_{vi}}{\mathrm{d}T} = \frac{\mathrm{d}}{\mathrm{d}T}\left(c_{Pi} - \frac{\mathcal{R}}{W_i}\right) = \frac{\mathrm{d}c_{Pi}}{\mathrm{d}T}. \tag{C5.2}$$

We determine $\frac{\mathrm{d}c_{Pi}}{\mathrm{d}T}$ from the polynomial input that Cantera uses. The form of this polynomial is discussed in Section 2.1. Using this polynomial form, $\frac{\mathrm{d}c_{Pi}}{\mathrm{d}T}$ is

$$\frac{\mathrm{d}c_{Pi}}{\mathrm{d}T} = \frac{\mathcal{R}}{W_i}\frac{\mathrm{d}}{\mathrm{d}T}\left(\frac{c_{Pi}}{R_i}\right) \tag{C5.3}$$

$$= \frac{\mathcal{R}}{W_i}\left(a_{2i} + 2a_{3i}T + 3a_{4i}T^2 + 4a_{5i}T^3\right). \tag{C5.4}$$

Finally we relate derivatives of γ to $\frac{\mathrm{d}c_{Pi}}{\mathrm{d}T}$

$$\frac{\partial\gamma}{\partial x} = \frac{1}{c_v}\left(\frac{\partial c_P}{\partial x} - \gamma\frac{\partial c_v}{\partial x}\right) \tag{C5.5}$$

$$= \frac{1}{c_v}\left[\sum_k\left(Y_k\frac{\partial c_{Pk}}{\partial x} + c_{Pk}\frac{\partial Y_k}{\partial x}\right) - \gamma\sum_k\left(Y_k\frac{\partial c_{Pk}}{\partial x} + c_{vk}\frac{\partial Y_k}{\partial x}\right)\right] \tag{C5.6}$$

$$= \frac{1}{c_v}\left[(1-\gamma)\sum_k Y_k\frac{\mathrm{d}c_{Pk}}{\mathrm{d}T}\frac{\partial T}{\partial x} - \sum_k\left(c_{Pk} - \gamma c_{vk}\right)\frac{\partial Y_k}{\partial x}\right] \tag{C5.7}$$

$$\left.\frac{\partial\gamma}{\partial v}\right|_{P,\mathbf{Y}} = \frac{(1-\gamma)}{c_v}\frac{T}{v}\sum_k Y_k\frac{\mathrm{d}c_{Pk}}{\mathrm{d}T} \tag{C5.8}$$

$$\left.\frac{\partial\gamma}{\partial P}\right|_{v,\mathbf{Y}} = \frac{(1-\gamma)}{c_v}\frac{T}{P}\sum_k Y_k\frac{\mathrm{d}c_{Pk}}{\mathrm{d}T} \tag{C5.9}$$

$$\left.\frac{\partial\gamma}{\partial Y_i}\right|_{P,v,Y_{j\neq i}} = \frac{1}{c_v}\left[(1-\gamma)\sum_k Y_k\frac{\mathrm{d}c_{Pk}}{\mathrm{d}T}\frac{Pv\overline{W}_{Y_i}}{\mathcal{R}} - \left(c_{Pi} - \gamma c_{vi}\right)\right]. \tag{C5.10}$$

Appendix D

Chemistry Implementation

In the software that accompanies this document, the user can specify the chemical model of their choice. Although we have presented results for strictly one-step models, both irreversible and reversible, this appendix describes precisely how the chemistry is implemented in the source code and how the general expressions reduce to the expressions given in Sections 2.1, 2.2, 4.2, and 4.3.

As described in Section 1.1, even though the common independent thermodynamic variables in fluid mechanics are $(v, P, \mathbf{Y})$, thermodynamic quantities for ideal gases are most often specified in terms of T. For this reason, we first generally discuss derivatives of $Z(P, v, \mathbf{Y})$ defined by (3.2.13) and $\dot{\Omega}$ defined by (1.1.6) in terms of the independent variable set $(v, T, \mathbf{Y})$. All of the mechanisms discussed rely on the ideal gas equation of state which is hardcoded into the implementation.

We assume that $e = e(T, \mathbf{Y})$ and that all dependence on P and v is specified by the ideal gas equation of state. First we generally discuss kinetics models and give general expressions for the net production rate (Appendix D.2) and pseudo-thermodynamic function (Appendix D.3). Derivatives of basic thermodynamic quantities are discussed in detail in Appendix C.3. Then we briefly discuss the specifics for detailed chemical models, and finally present some specifics about the one-step models that were not included in Sections 2.1 and 2.2.

D.1 Kinetics Models

Generically, a reaction can be written as

$$\sum_{k\ (sp)} \nu'_k \frac{P_k}{\mathcal{R}T} = \sum_{k\ (sp)} \nu''_k \frac{P_k}{\mathcal{R}T} \tag{D1.1}$$

and the following notation is used.

$$\Delta\nu_i = \nu''_i - \nu'_i \tag{D1.2}$$

$$\Delta\nu = \sum \nu''_k - \sum \nu'_k. \tag{D1.3}$$

Cantera implements three body reactions involving a chaperon molecule M by including a reaction type flag in the `xml` file. In general, $[M]$ and its derivatives are

$$[M] = \frac{P}{\mathcal{R}T} \sum_{k\ (sp)} \epsilon_k X_k = \frac{1}{v} \sum_{k\ (sp)} \epsilon_k \frac{Y_k}{W_k} \tag{D1.4}$$

$$\left.\frac{\partial[M]}{\partial T}\right|_{v,\mathbf{Y}} = 0 \tag{D1.5}$$

$$\left.\frac{\partial[M]}{\partial v}\right|_{T,\mathbf{Y}} = -\frac{1}{v^2} \sum_{k\ (sp)} \epsilon_k \frac{Y_k}{W_k} \tag{D1.6}$$

$$\left.\frac{\partial[M]}{\partial Y_j}\right|_{v,T,Y_{k\neq j}} = \frac{\epsilon_j}{W_j v} \tag{D1.7}$$

where k_f is the Arrhenius reaction rate coefficient

$$k_f = AT^n \exp\left(\frac{-E_a}{RT}\right) \tag{D1.8}$$

and the molar production rate of species i is

$$\begin{aligned}\dot{\omega}_i = &\sum_{p\ (rxns)} (\Delta\nu_i)_p\, k_{fp}[M] \left(v^{-\sum \nu'_k}\right)_p \left[\prod_{k\ (sp)} \left(\frac{Y_k}{W_k}\right)^{\nu'_k}\right]_p \\ &- \sum_{p\ (rxns)} (\Delta\nu_i)_p\, k_{rp}[M] \left(v^{-\sum \nu''_k}\right)_p \left[\prod_{k\ (sp)} \left(\frac{Y_k}{W_k}\right)^{\nu''_k}\right]_p .\end{aligned} \tag{D1.9}$$

The principle of detailed balance allows us to determine the reverse reaction rate from the forward reaction rate and equilibrium constant.

$$k_r = \frac{k_f}{K_C(T)} \tag{D1.10}$$

where

$$K_C = K_P \left(\frac{P_o}{\mathcal{R}T}\right)^{\Delta\nu} = \left[\prod_{k\ (sp)} \left(\frac{P_k}{P_o}\right)^{\nu_k}\right] \left(\frac{P_o}{\mathcal{R}T}\right)^{\Delta\nu} . \tag{D1.11}$$

We determine K_P from the condition for chemical equilibrium in a given reaction

$$\sum_{k\ (sp)} \nu_k \mu_k = 0 \tag{D1.12}$$

$$\mu_i = g_i = [h_i(T) - T s_i^\circ(T)] + \mathcal{R}T \ln\left(\frac{P_i}{P_o}\right). \tag{D1.13}$$

We can simplify by re-expressing $\sum_{k\ (sp)} \nu_k g_k^\circ(T)$ as $\Delta G^\circ(T)$ and with a little more work, we can express K_C in terms of the total Gibbs free energy, $\Delta G(T,P) = \Delta G^\circ(T) + \mathcal{R}T \ln\left(\frac{P}{P_o}\right)$.

$$K_C = \left(\frac{1}{\overline{W} v}\right)^{\Delta\nu} \exp\left(\frac{\Delta \overline{G}(T,P)}{\mathcal{R}T}\right) \tag{D1.14}$$

Using the van't Hoff rule,

$$\frac{1}{K_P}\frac{\mathrm{d}K_P}{\mathrm{d}T} = \frac{\Delta_R h}{\mathcal{R}T^2}, \tag{D1.15}$$

the derivative of the equilibrium constant (D1.14) becomes

$$\frac{\mathrm{d}K_C}{\mathrm{d}T} = K_C\left[\frac{\Delta_R h}{\mathcal{R}T^2} - \frac{\Delta\nu}{T}\right]. \tag{D1.16}$$

We will need the derivatives of both the forward and reverse reaction rates for the derivatives of interest.

$$\left.\frac{\partial k_{fp}}{\partial T}\right|_{v,\mathbf{Y}} = k_{fp}\left(\frac{n_p}{T} - \frac{E_{ap}}{RT^2}\right) \tag{D1.17}$$

$$\left.\frac{\partial k_{rp}}{\partial T}\right|_{v,\mathbf{Y}} = \frac{1}{K_{Cp}}\left.\frac{\partial k_{fp}}{\partial T}\right|_{v,\mathbf{Y}} - \frac{k_{fp}}{K_{Cp}^2}\left.\frac{\partial K_{Cp}}{\partial T}\right|_{v,\mathbf{Y}} \tag{D1.18}$$

Finally, the derivatives of the net production rate with respect to T, Y_i, and v are

$$\begin{aligned}
\left.\frac{\partial \dot{\omega}_i}{\partial T}\right|_{v,\mathbf{Y}} &= \sum_{p\,(rxns)} (\Delta\nu_i)_p \left.\frac{\partial k_{fp}}{\partial T}\right|_{v,\mathbf{Y}} [M] \left(v^{-\sum \nu'_k}\right)_p \left[\prod_{k\,(sp)} \left(\frac{Y_k}{W_k}\right)^{\nu'_k}\right]_p \\
&\quad - \sum_{p\,(rxns)} (\Delta\nu_i)_p \left.\frac{\partial k_{rp}}{\partial T}\right|_{v,\mathbf{Y}} [M] \left(v^{-\sum \nu''_k}\right)_p \left[\prod_{k\,(sp)} \left(\frac{Y_k}{W_k}\right)^{\nu''_k}\right]_p
\end{aligned} \tag{D1.19}$$

$$\begin{aligned}
\left.\frac{\partial \dot{\omega}_i}{\partial Y_j}\right|_{v,T,Y_{k\neq j}} &= \sum_{p\,(rxns)} (\Delta\nu_i)_p\, k_{fp} \left(v^{-\sum \nu'_k}\right)_p \left[\frac{\nu'_j[M]}{Y_j} \prod_{k\,(sp)} \left(\frac{Y_k}{W_k}\right)^{\nu'_k}\right]_p \\
&\quad + \sum_{p\,(rxns)} (\Delta\nu_i)_p\, k_{fp} \left(v^{-\sum \nu'_k}\right)_p \left[\left.\frac{\partial [M]}{\partial Y_j}\right|_{v,T,Y_{k\neq j}} \prod_{k\,(sp)} \left(\frac{Y_k}{W_k}\right)^{\nu'_k}\right]_p \\
&\quad - \sum_{p\,(rxns)} (\Delta\nu_i)_p\, k_{rp} \left(v^{-\sum \nu''_k}\right)_p \left[\frac{\nu''_j[M]}{Y_j} \prod_{k\,(sp)} \left(\frac{Y_k}{W_k}\right)^{\nu''_k}\right]_p \\
&\quad - \sum_{p\,(rxns)} (\Delta\nu_i)_p\, k_{rp} \left(v^{-\sum \nu''_k}\right)_p \left[\left.\frac{\partial [M]}{\partial Y_j}\right|_{v,T,Y_{k\neq j}} \prod_{k\,(sp)} \left(\frac{Y_k}{W_k}\right)^{\nu''_k}\right]_p
\end{aligned} \tag{D1.20}$$

$$\begin{aligned}
\left.\frac{\partial \dot{\omega}_i}{\partial v}\right|_{T,\mathbf{Y}} &= \sum_{p\,(rxns)} (\Delta\nu_i)_p\, k_{fp} \left(v^{-\sum \nu'_k}\right)_p \left[\left.\frac{\partial [M]}{\partial v}\right|_{T,\mathbf{Y}} \prod_{k\,(sp)} \left(\frac{Y_k}{W_k}\right)^{\nu'_k}\right]_p \\
&\quad - \sum_{p\,(rxns)} (\Delta\nu_i)_p\, k_{fp} \left(v^{-\sum \nu'_k}\right)_p \left[\frac{[M]}{v} \sum_{k\,(sp)} \nu'_k \prod_{k\,(sp)} \left(\frac{Y_k}{W_k}\right)^{\nu'_k}\right]_p \\
&\quad - \sum_{p\,(rxns)} (\Delta\nu_i)_p\, k_{rp} \left(v^{-\sum \nu''_k}\right)_p \left[\left.\frac{\partial [M]}{\partial v}\right|_{T,\mathbf{Y}} \prod_{k\,(sp)} \left(\frac{Y_k}{W_k}\right)^{\nu''_k}\right]_p \\
&\quad + \sum_{p\,(rxns)} (\Delta\nu_i)_p\, k_{rp} \left(v^{-\sum \nu''_k}\right)_p \left[\frac{[M]}{v} \sum_{k\,(sp)} \nu''_k \prod_{k\,(sp)} \left(\frac{Y_k}{W_k}\right)^{\nu''_k}\right]_p .
\end{aligned} \tag{D1.21}$$

We can use (D1.19), (D1.20), and (D1.21) as general expressions if we choose $[M] = 1$ ($\partial[M] = 0$) for reactions where all participant molecules are specified.

D.2 Net Production Rate Derivatives

Described above are derivatives of the molar net production rate $\dot{\omega}$ as a function of T, v, and $\mathbf{Y}$. To implement the equations discussed in Section 3.2, we must determine derivatives of $\dot{\Omega}$ as a function of v, P, and $\mathbf{Y}$. This can be accomplished with two methods, both discussed below. First we expand $\dot{\Omega}(v, T, \mathbf{Y})$ and $T(v, P, \mathbf{Y})$.

$$d\dot{\Omega}_i(v,T,\mathbf{Y}) = \left.\frac{\partial\dot{\Omega}_i}{\partial T}\right|_{v,\mathbf{Y}} dT + \left.\frac{\partial\dot{\Omega}_i}{\partial v}\right|_{T,\mathbf{Y}} dv + \sum_j \left.\frac{\partial\dot{\Omega}_i}{\partial Y_j}\right|_{v,T,Y_{k\neq j}} dY_j \tag{D2.1}$$

$$dT(v,P,\mathbf{Y}) = \left.\frac{\partial T}{\partial P}\right|_{v,\mathbf{Y}} dP + \left.\frac{\partial T}{\partial v}\right|_{P,\mathbf{Y}} dv + \sum_j \left.\frac{\partial T}{\partial Y_j}\right|_{v,P,Y_{k\neq j}} dY_j \tag{D2.2}$$

and insert (D2.2) into (D2.1).

$$\begin{aligned} d\dot{\Omega}_i(v,T,\mathbf{Y}) = {} & \left.\frac{\partial\dot{\Omega}_i}{\partial T}\right|_{v,\mathbf{Y}} \left.\frac{\partial T}{\partial P}\right|_{v,\mathbf{Y}} dP + \left[\left.\frac{\partial\dot{\Omega}_i}{\partial T}\right|_{v,\mathbf{Y}} \left.\frac{\partial T}{\partial v}\right|_{P,\mathbf{Y}} + \left.\frac{\partial\dot{\Omega}_i}{\partial v}\right|_{T,\mathbf{Y}}\right] dv \\ & + \sum_j \left[\left.\frac{\partial\dot{\Omega}_i}{\partial T}\right|_{v,\mathbf{Y}} \left.\frac{\partial T}{\partial Y_j}\right|_{v,P,Y_{k\neq j}} + \left.\frac{\partial\dot{\Omega}_i}{\partial Y_j}\right|_{v,T,Y_{k\neq j}}\right] dY_j \end{aligned} \tag{D2.3}$$

Eq. (D2.3) implies that

$$\left.\frac{\partial\dot{\Omega}_i}{\partial v}\right|_{P,\mathbf{Y}} = \left.\frac{\partial T}{\partial v}\right|_{P,\mathbf{Y}} \left.\frac{\partial\dot{\Omega}_i}{\partial T}\right|_{v,\mathbf{Y}} + \left.\frac{\partial\dot{\Omega}_i}{\partial v}\right|_{T,\mathbf{Y}} = \frac{T}{v} \left.\frac{\partial\dot{\Omega}_i}{\partial T}\right|_{v,\mathbf{Y}} + \left.\frac{\partial\dot{\Omega}_i}{\partial v}\right|_{T,\mathbf{Y}} \tag{D2.4}$$

$$\left.\frac{\partial\dot{\Omega}_i}{\partial P}\right|_{v,\mathbf{Y}} = \left.\frac{\partial T}{\partial P}\right|_{v,\mathbf{Y}} \left.\frac{\partial\dot{\Omega}_i}{\partial T}\right|_{v,\mathbf{Y}} = \frac{v}{R} \left.\frac{\partial\dot{\Omega}_i}{\partial T}\right|_{v,\mathbf{Y}} \tag{D2.5}$$

$$\left.\frac{\partial\dot{\Omega}_i}{\partial Y_j}\right|_{v,P,Y_{k\neq j}} = \left.\frac{\partial\dot{\Omega}_i}{\partial T}\right|_{v,\mathbf{Y}} \left.\frac{\partial T}{\partial Y_j}\right|_{v,P,Y_{k\neq j}} + \left.\frac{\partial\dot{\Omega}_i}{\partial Y_j}\right|_{v,T,Y_{k\neq j}}. \tag{D2.6}$$

Numerical Derivatives

Numerical derivatives with respect to P and v are straightforward centered differences, but

$$\left.\frac{\partial \dot{\Omega}_i}{\partial Y_j}\right|_{v,T,Y_{k\neq j}} \tag{D2.7}$$

presents a challenge. We must use the Cantera function `setMassFraction_NoNorm` which allows the user to specify the mass fractions and not enforce $\sum Y_i = 1$ to compute this derivative (D2.7) numerically.

Analytical Derivatives

It will be more accurate to implement all of the derivatives analytically in Cantera. This is slightly more involved but can be expressed analytically for a given chemical kinetics mechanism. Equation 1.1.6 simplifies the derivatives of interest to

$$\left.\frac{\partial \dot{\Omega}_i}{\partial T}\right|_{v,\mathbf{Y}} = W_i v \left.\frac{\partial \dot{\omega}_i}{\partial T}\right|_{v,\mathbf{Y}} \tag{D2.8}$$

$$\left.\frac{\partial \dot{\Omega}_i}{\partial v}\right|_{T,\mathbf{Y}} = W_i \left[\dot{\omega}_i + v \left.\frac{\partial \dot{\omega}_i}{\partial v}\right|_{T,\mathbf{Y}}\right] \tag{D2.9}$$

$$\left.\frac{\partial \dot{\Omega}_i}{\partial Y_j}\right|_{v,T,Y_{k\neq j}} = W_i v \left.\frac{\partial \dot{\omega}_i}{\partial Y_j}\right|_{v,T,Y_{k\neq j}}. \tag{D2.10}$$

We can use (D1.19)–(D1.21) to evaluate these expressions analytically.

D.3 Pseudo-Thermodynamic Function

For an ideal gas, $G = \gamma(T) - 1$, and $Z(v, P, \mathbf{Y})$ becomes

$$Z(v, P, \mathbf{Y}) = -\frac{\gamma(T) - 1}{v} \sum_k \dot{\Omega}_k \left(e_k + c_v \overline{W}_{Y_k} \frac{Pv}{\mathcal{R}}\right). \tag{D3.1}$$

We will first take the derivative with respect to a dummy variable, x, and then specialize to the independent variables

$$\begin{aligned}\frac{\partial Z}{\partial x} &= \left[\frac{\gamma(T)-1}{v^2}\frac{\partial v}{\partial x} - \frac{1}{v}\frac{\partial \gamma}{\partial x}\right]\sum_k \dot{\Omega}_k\left(e_k + c_v\overline{W}_{Y_k}\frac{Pv}{\mathcal{R}}\right)\\ &- \frac{\gamma(T)-1}{v}\sum_k \dot{\Omega}_{k,x}\left(e_k + c_v\overline{W}_{Y_k}\frac{Pv}{\mathcal{R}}\right)\\ &- \frac{\gamma(T)-1}{v}\sum_k \dot{\Omega}_k\frac{\partial}{\partial x}\left(e_k + c_v\overline{W}_{Y_k}\frac{Pv}{\mathcal{R}}\right).\end{aligned} \tag{D3.2}$$

If $x = v$,

$$\begin{aligned}\left.\frac{\partial Z}{\partial v}\right|_{P,\mathbf{Y}} &= \left(\frac{\gamma(T)-1}{v^2} - \frac{1}{v}\left.\frac{\partial \gamma}{\partial v}\right|_{P,\mathbf{Y}}\right)\sum_k \dot{\Omega}_k\left(e_k + c_{vk}\overline{W}_{Y_i}\frac{Pv}{\mathcal{R}}\right)\\ &- \frac{\gamma(T)-1}{v}\sum_k \dot{\Omega}_{k,v}\left(e_k + c_v\overline{W}_{Y_k}\frac{Pv}{\mathcal{R}}\right)\\ &- \frac{\gamma(T)-1}{v}\sum_k \dot{\Omega}_k\left.\frac{\partial}{\partial v}\left(e_k + c_v\overline{W}_{Y_k}\frac{Pv}{\mathcal{R}}\right)\right|_{P,\mathbf{Y}}.\end{aligned} \tag{D3.3}$$

If $x = P$,

$$\begin{aligned}\left.\frac{\partial Z}{\partial P}\right|_{v,\mathbf{Y}} &= -\frac{1}{v}\left.\frac{\partial \gamma}{\partial P}\right|_{v,\mathbf{Y}}\sum_k \dot{\Omega}_k\left(e_k + c_v\overline{W}_{Y_k}\frac{Pv}{\mathcal{R}}\right)\\ &- \frac{\gamma(T)-1}{v}\sum_k \dot{\Omega}_{k,P}\left(e_k + c_v\overline{W}_{Y_k}\frac{Pv}{\mathcal{R}}\right)\\ &- \frac{\gamma(T)-1}{v}\sum_k \dot{\Omega}_k\left.\frac{\partial}{\partial P}\left(e_k + c_v\overline{W}_{Y_k}\frac{Pv}{\mathcal{R}}\right)\right|_{v,\mathbf{Y}}.\end{aligned} \tag{D3.4}$$

If $x = Y_i$,

$$\begin{aligned}\left.\frac{\partial Z}{\partial Y_i}\right|_{v,P,Y_{k\neq i}} &= -\frac{1}{v}\left.\frac{\partial \gamma}{\partial Y_i}\right|_{P,v,Y_k\neq i}\sum_k \dot{\Omega}_k\left(e_k + c_v\overline{W}_{Y_k}\frac{Pv}{\mathcal{R}}\right)\\ &- \frac{\gamma(T)-1}{v}\sum_k \dot{\Omega}_{k,Y_i}\left(e_k + c_v\overline{W}_{Y_k}\frac{Pv}{\mathcal{R}}\right)\\ &- \frac{\gamma(T)-1}{v}\sum_k \dot{\Omega}_k\left.\frac{\partial}{\partial Y_i}\left(e_k + c_v\overline{W}_{Y_k}\frac{Pv}{\mathcal{R}}\right)\right|_{P,v,Y_{j\neq i}}.\end{aligned} \tag{D3.5}$$

See Appendix C.4 for more detail on the implementation of these derivatives.

D.4 Detailed Kinetics Model

The first mechanism type that we present is the detailed kinetics model. A detailed reaction mechanism is a collection of elementary reactions which represent molecular collisions. This is the most realistic model used in numerical simulations. An example is the hydrogen-oxygen mechanism which contains eight species and twenty reversible reactions.

In an ideal gas, the specific heats are a function of temperature and the mean molecular weight, $\overline{W}$ is a function of the species. With this model,

$$\left.\frac{\partial \overline{W}}{\partial Y_i}\right|_{P,v,Y_{k\neq i}} = -\frac{\overline{W}^2}{W_i} \tag{D4.1}$$

and

$$\frac{\partial}{\partial Y_j}\left[\left.\frac{\partial \overline{W}}{\partial Y_i}\right|_{P,v,Y_{k\neq i}}\right]_{P,v,Y_{m\neq j}} = 2\frac{\overline{W}^3}{W_i W_j}. \tag{D4.2}$$

The derivatives that have been presented above (see Appendices D.1–D.3) apply directly for this model.

D.5 One-Step Irreversible Model

In a perfect gas, the specific heats are constant, but the mean molecular weight is still generally a function of the species. With this model, (D4.1) remains valid. In the discussion below, we make a further simplification that all of the molecular weights are equal. In this case, the mean molecular weight $\overline{W}$ is a constant, so

$$\left.\frac{\partial \overline{W}}{\partial Y_i}\right|_{P,v,Y_{k\neq i}} = 0. \tag{D5.1}$$

With this model, the derivatives of the net production rates reduce to those given in Section 4.2.

D.5.1 Democratic Method

In Sections 2.1 and 4.2, we assumed that the net rates of production are strictly functions of the reactant species. In the original formulation (Lee and Stewart, 1990), this was sufficient because one progress variable, $Y_{\mathcal{B}}$, was used to describe the chemistry. By using Cantera, we must have two species, reactant and product, and conservation equations for each. Because the mass fractions must always add to one, i.e.,

$$\sum_i Y_i = 1, \tag{D5.2}$$

the two species equations are not independent. This leads to many definitions of the net rates of production.

$$\dot{\Omega}_{\mathcal{A},\mathcal{B}} = \mp k_f Y_{\mathcal{A}} \tag{D5.3}$$

$$= \mp k_f (1 - Y_{\mathcal{B}}) \tag{D5.4}$$

$$= \mp k_f \sqrt{Y_{\mathcal{A}}(1 - Y_{\mathcal{B}})} \tag{D5.5}$$

The first expression has been used in Sections 2.1 and 4.2. The second equation is strictly a function of the product species. The third expression is the *democratic* expression as it incorporates both species. With this definition, the derivatives of $\dot{\Omega}_i$ become

$$\left.\frac{\partial \dot{\Omega}_{\mathcal{A},\mathcal{B}}}{\partial Y_{\mathcal{A}}}\right|_{v,P,Y_{\mathcal{B}}} = \mp\frac{k_f}{2} \tag{D5.6}$$

$$\left.\frac{\partial \dot{\Omega}_{\mathcal{A},\mathcal{B}}}{\partial Y_{\mathcal{B}}}\right|_{v,P,Y_{\mathcal{A}}} = \pm\frac{k_f}{2}. \tag{D5.7}$$

D.5.2 Pseudo-Thermodynamic Function Derivative

For the perfect gas, c_v and γ are constants, and for the one-step reaction, there are two species, $\mathcal{A}$ and $\mathcal{B}$, with equal specific heats, equal molecular weights, and equal and opposite production rates, i.e.,

$$\dot{\Omega}_{\mathcal{A}} = -\dot{\Omega}_{\mathcal{B}}. \tag{D5.8}$$

Additionally, the internal energies of each species is specified as

$$e_{\mathcal{A}} = c_v T \tag{D5.9}$$

$$e_{\mathcal{B}} = c_v T - \Delta e. \tag{D5.10}$$

Now we can evaluate each of the sums in the derivatives of $Z(P, v, \mathbf{Y})$ (see Appendix D.3).

$$\sum_k \dot{\Omega}_{k,x} e_k = -\dot{\Omega}_{\mathcal{B},x} c_v T + \dot{\Omega}_{\mathcal{B},x}(c_v T - \Delta e) = -\dot{\Omega}_{\mathcal{B},x}\Delta e \tag{D5.11}$$

$$\sum_k \dot{\Omega}_k c_{vk} T = -\dot{\Omega}_{\mathcal{B}} c_v T + \dot{\Omega}_{\mathcal{B}} c_v T = 0 \tag{D5.12}$$

$$\sum_k \dot{\Omega}_{k,x}\frac{\overline{W}}{W_k} = \sum_k \dot{\Omega}_k \frac{\overline{W}}{W_k} = 0 \tag{D5.13}$$

This simplifies the derivatives of $Z(P, v, \mathbf{Y})$ further

$$\left.\frac{\partial Z}{\partial v}\right|_{P,\mathbf{Y}} = \frac{\gamma - 1}{v}\Delta e\left(\frac{\dot{\Omega}_{\mathcal{B},v}}{v} - \dot{\Omega}_{\mathcal{B}}\right) \tag{D5.14}$$

$$\left.\frac{\partial Z}{\partial P}\right|_{v,\mathbf{Y}} = \frac{\gamma - 1}{v}\Delta e\dot{\Omega}_{\mathcal{B},P} \tag{D5.15}$$

$$\left.\frac{\partial Z}{\partial Y_j}\right|_{v,P,y_{k\neq j}} = \frac{\gamma - 1}{v}\Delta e\dot{\Omega}_{\mathcal{B},Y_j} \tag{D5.16}$$

which are exactly the dimensional versions of the expressions given in Lee and Stewart. A more detailed comparison of the above expressions with those of Lee and Stewart is presented in Appendix E.5

D.6 One-Step Reversible Model

In the irreversible case, the net production rate is equivalent to the forward reaction rate, i.e.,

$$\dot{\Omega}_{\mathcal{B}} = k_f Y_{\mathcal{A}}. \tag{D6.1}$$

In the reversible case,

$$\dot{\Omega}_{\mathcal{B}} = k_f Y_{\mathcal{A}} - k_r Y_{\mathcal{B}} = k_f\left(Y_{\mathcal{A}} - \frac{1}{K_P}Y_{\mathcal{B}}\right) \tag{D6.2}$$

where k_f is the forward reaction rate coefficient and K_P is the equilibrium constant of the reaction. We also recognize that this can also be written as

$$\dot{\Omega}_{\mathcal{B}} = Y_{\mathcal{A}} A\exp\left(-\frac{E_a}{RT}\right) - Y_{\mathcal{B}}\left[A\exp\left(\frac{\Delta s^o}{\tilde{R}}\right)\right]\left[\exp\left(-\frac{(E_a - q)}{\tilde{R}T}\right)\right] \tag{D6.3}$$

$$= Y_{\mathcal{A}} A\exp\left(-\frac{E_a}{RT}\right) - Y_{\mathcal{B}} A'\exp\left(-\frac{E'_a}{\tilde{R}T}\right). \tag{D6.4}$$

To determine the derivatives of $\dot{\Omega}_{\mathcal{B}}$, we use the derivatives of temperature given in

Appendix C.3 along with the discussion of k_f and the van't Hoff rule (Appendix D.1) to find the derivatives of k_f and K_P.

$$k_f = A \exp\left(\frac{-E_a}{RT}\right) \tag{D6.5}$$

$$\left.\frac{\partial k_f}{\partial T}\right|_{v,\mathbf{Y}} = k_f \frac{E_a}{RT}\frac{1}{T} \tag{D6.6}$$

$$\left.\frac{\partial k_f}{\partial v}\right|_{P,\mathbf{Y}} = k_f \frac{E_a}{RT}\frac{1}{v} \tag{D6.7}$$

$$\left.\frac{\partial k_f}{\partial P}\right|_{v,\mathbf{Y}} = k_f \frac{E_a}{RT}\frac{1}{P} \tag{D6.8}$$

In this case, T is not a function of $\mathbf{Y}$ because all of the molecular weights are equal.

$$\left.\frac{\partial k_f}{\partial Y_i}\right|_{P,v,Y_{k\neq i}} = 0 \tag{D6.9}$$

We use the van't Hoff rule to find the derivatives of K_C

$$\left.\frac{\partial K_C}{\partial T}\right|_{v,\mathbf{Y}} = K_C\left(\frac{\Delta_R h}{\tilde{R}T^2} - \frac{\Delta\nu}{T}\right) \tag{D6.10}$$

$$\left.\frac{\partial K_C}{\partial v}\right|_{P,\mathbf{Y}} = \frac{K_C}{v}K_C\left(\frac{\Delta_R h}{\tilde{R}T^2} - \frac{\Delta\nu}{T}\right) \tag{D6.11}$$

$$\left.\frac{\partial K_C}{\partial P}\right|_{v,\mathbf{Y}} = \frac{K_C}{P}K_C\left(\frac{\Delta_R h}{\tilde{R}T^2} - \frac{\Delta\nu}{T}\right) \tag{D6.12}$$

$$\left.\frac{\partial K_C}{\partial Y_i}\right|_{P,v,Y_{k\neq i}} = 0. \tag{D6.13}$$

Now the general derivatives of $\dot{\Omega}_{\mathcal{B}}$ are

$$\left.\frac{\partial \dot{\Omega}_{\mathcal{B}}}{\partial T}\right|_{v,\mathbf{Y}} = k_f \left[\frac{E_a}{RT^2}\left(1 - Y_{\mathcal{B}}\left[1 + \frac{1}{K_P}\right]\right) - \frac{Y_{\mathcal{B}}}{K_P}\frac{\Delta_R h}{\tilde{R}T^2}\right] \tag{D6.14}$$

$$= k_f \frac{E_a}{RT^2}(1 - Y_{\mathcal{B}}) - k_r \frac{E_a'}{\tilde{R}T^2} Y_{\mathcal{B}} \tag{D6.15}$$

$$\left.\frac{\partial \dot{\Omega}_{\mathcal{B}}}{\partial v}\right|_{P,\mathbf{Y}} = \frac{k_f}{v}\left[\frac{E_a}{RT}\left(1 - Y_{\mathcal{B}}\left[1 + \frac{1}{K_P}\right]\right) - \frac{Y_{\mathcal{B}}}{K_P}\frac{\Delta_R h}{\tilde{R}T}\right] \tag{D6.16}$$

$$= \frac{k_f}{v}\frac{E_a}{RT}(1 - Y_{\mathcal{B}}) - \frac{k_r}{v}\frac{E_a'}{\tilde{R}T} Y_{\mathcal{B}} \tag{D6.17}$$

$$\left.\frac{\partial \dot{\Omega}_{\mathcal{B}}}{\partial P}\right|_{v,\mathbf{Y}} = \frac{k_f}{P}\left[\frac{E_a}{RT}\left(1 - Y_{\mathcal{B}}\left[1 + \frac{1}{K_P}\right]\right) - \frac{Y_{\mathcal{B}}}{K_P}\frac{\Delta_R h}{\tilde{R}T}\right] \tag{D6.18}$$

$$= \frac{k_f}{P}\frac{E_a}{RT}(1 - Y_{\mathcal{B}}) - \frac{k_r}{P}\frac{E_a'}{\tilde{R}T} Y_{\mathcal{B}} \tag{D6.19}$$

$$\left.\frac{\partial \dot{\Omega}_{\mathcal{B}}}{\partial Y_i}\right|_{P,v,Y_{k\neq i}} = -k_f \left[\frac{E_a}{RT}\left(1 - Y_{\mathcal{B}}\left[1 + \frac{1}{K_P}\right]\right) - \frac{Y_{\mathcal{B}}}{K_P}\frac{\Delta_R h}{\tilde{R}T}\right] - k_f\left(1 + \frac{1}{K_P}\right) \tag{D6.20}$$

$$= -k_f \frac{E_a}{RT}(1 - Y_{\mathcal{B}}) + k_r \frac{E_a'}{\tilde{R}T} Y_{\mathcal{B}}. \tag{D6.21}$$

Far from the main reaction zone, the magnitude of the forward and reverse reaction rates are approximately equal. From this, we can determine a relationship between k_f and k_r far from the main reaction zone (x_R) which is where we plan to evaluate the radiation condition discussed in Section 3.4 and Chapter 4.

$$\left(k_f(1 - Y_{\mathcal{B}})\right]_{x_R} = \left[k_r Y_{\mathcal{B}}\right]_{x_R} \tag{D6.22}$$

$$k_r|_{x_R} = \left[k_f \frac{1 - Y_{\mathcal{B}}}{Y_{\mathcal{B}}}\right]_{x_R} \tag{D6.23}$$

Therefore, at x_R the derivative of k_r with respect to temperature is

$$\left[\left.\frac{\partial k_r}{\partial T}\right|_{v,\mathbf{Y}}\right]_{x_R} = \left[\left.\frac{\partial k_f}{\partial T}\right|_{v,\mathbf{Y}} \frac{1 - Y_{\mathcal{B}}}{Y_{\mathcal{B}}}\right]_{x_R} = \left[k_f \frac{E_a}{R(T)^2}\frac{1 - Y_{\mathcal{B}}}{Y_{\mathcal{B}}}\right]_{x_R}. \tag{D6.24}$$

Now, the derivatives of $\dot{\Omega}_{\mathcal{B}}$ in the acoustic regime are

$$\left[\left.\frac{\partial\dot{\Omega}_{\mathcal{B}}}{\partial T}\right|_{v,\mathbf{Y}}\right]_{x_R} = \left[\frac{k_f}{\tilde{R}(T)^2}(E_a - E_a')(1-Y_{\mathcal{B}})\right]_{x_R} = \left[\Delta e\frac{k_f}{\tilde{R}(T)^2}(1-Y_{\mathcal{B}})\right]_{x_R} \tag{D6.25}$$

$$\left[\left.\frac{\partial\dot{\Omega}_{\mathcal{B}}}{\partial v}\right|_{P,\mathbf{Y}}\right]_{x_R} = \left[\Delta e\frac{k_f}{\tilde{R}Tv}(1-Y_{\mathcal{B}})\right]_{x_R} \tag{D6.26}$$

$$\left[\left.\frac{\partial\dot{\Omega}_{\mathcal{B}}}{\partial P}\right|_{v,\mathbf{Y}}\right]_{x_R} = \left[\Delta e\frac{k_f}{\tilde{R}TP}(1-Y_{\mathcal{B}})\right]_{x_R} \tag{D6.27}$$

$$\begin{aligned}\left[\left.\frac{\partial\dot{\Omega}_{\mathcal{B}}}{\partial Y_i}\right|_{P,v,Y_{k\neq i}}\right]_{x_R} &= \left[-k_f\frac{E_a}{RT}(1-Y_{\mathcal{B}}) + k_f\frac{E_a}{R(T)^2}\frac{1-Y_{\mathcal{B}}}{Y_{\mathcal{B}}}Y_{\mathcal{B}}T - k_f - k_r\right]_{x_R} \\ &= -\left[\frac{k_f}{Y_{\mathcal{B}}}\right]_{x_R}.\end{aligned} \tag{D6.28}$$

This shows that the derivatives of the net production rate do not go to zero far from the main reaction zone as they do for the irreversible reaction. This is valuable because the radiation derived for the irreversible reaction cannot be applied in the reversible case. The **C** Matrix does simplify nicely and an analytic solution to the progress variable equation cannot be found. Instead we follow the eigenvalue methodology outlined in Section 3.4

D.6.1 Democratic Method

Following the method discussed into Appendix D.5.1, the net production rates can also be expressed as

$$\dot{\Omega}_{\mathcal{A},\mathcal{B}} = \mp\left[k_f\sqrt{Y_{\mathcal{A}}(1-Y_{\mathcal{B}})} - k_r\sqrt{(1-Y_{\mathcal{A}})Y_{\mathcal{B}}}\right]. \tag{D6.29}$$

Now the *democratic* derivatives of $\dot{\Omega}_{\mathcal{A},\mathcal{B}}$ are

$$\left.\frac{\partial \dot{\Omega}_{\mathcal{A},\mathcal{B}}}{\partial Y_{\mathcal{A}}}\right|_{v,P,Y_{\mathcal{B}}} = \mp\frac{k_f + k_r}{2} \tag{D6.30}$$

$$\left.\frac{\partial \dot{\Omega}_{\mathcal{A},\mathcal{B}}}{\partial Y_{\mathcal{B}}}\right|_{v,P,Y_{\mathcal{A}}} = \pm\frac{k_f + k_r}{2}. \tag{D6.31}$$

D.6.2 Pseudo-Thermodynamic Function Derivatives

Because the number of species does not change in this situation, the expressions for the derivatives of the pseudo-thermodynamic function remain the same (D5.14)–(D5.16).

Appendix E

Comparison with Previous Studies

E.1 One Dimension

Lee and Stewart (1990) have studied one-dimensional linear stability with a single-step reaction mechanism in terms of the progress variable λ. This simplification gives the following expressions for the energy and reaction rate.

$$e = \frac{Pv}{\gamma - 1} - \lambda \Delta e \tag{E1.1}$$

$$r = (1 - \lambda) A \exp(-E_a / RT). \tag{E1.2}$$

It is important to note that in a one-step irreversible model (see Section 2.1), the net production rate of the progress species is equal to the forward reaction rate. Now, (1.1.10) becomes

$$\frac{\mathrm{D}P}{\mathrm{D}t} + \frac{a_f^2}{v} \boldsymbol{\nabla} \cdot \mathbf{u} = -\frac{\gamma - 1}{v} r \Delta e. \tag{E1.3}$$

Nondimensionalizing (A1.10)–(A1.13) with respect to the post-shock state in the following way

$$\Delta h = \tilde{\beta} \mathcal{R} T_2 \quad x = \tilde{x} x_c \quad t = \tilde{t} x_c / \left(a_f\right)_2 \tag{E1.4}$$

$$\mathrm{u} = \tilde{\mathrm{u}} \left(a_f\right)_2 \quad P = \tilde{P} P_2 \quad v = \tilde{v} v_2 \tag{E1.5}$$

where $\tilde{(\,)}$ indicates a nondimensional quantity and x_c is the characteristic length scale, gives

$$\tilde{v}_{,\tilde{t}} + (\tilde{\mathrm{u}} + \tilde{\psi}_{,\tilde{t}})\tilde{v}_{,\tilde{x}} = \tilde{v}\tilde{\mathrm{u}}_{,\tilde{x}} \tag{E1.6}$$

$$\tilde{\mathrm{u}}_{,\tilde{t}} + (\tilde{\mathrm{u}} + \tilde{\psi}_{,\tilde{t}})\tilde{\mathrm{u}}_{,\tilde{x}} = -\tilde{v}\frac{\tilde{P}_{,\tilde{x}}}{\gamma} \tag{E1.7}$$

$$\tilde{P}_{,\tilde{t}} + (\tilde{\mathrm{u}} + \tilde{\psi}_{,\tilde{t}})\tilde{P}_{,\tilde{x}} + \gamma\tilde{P}\tilde{\mathrm{u}}_{,\tilde{x}} = \frac{\gamma - 1}{\tilde{v}}\tilde{\beta}\tilde{r}(\tilde{v}, \tilde{P}, \lambda) \tag{E1.8}$$

$$\lambda_{,\tilde{t}} + (\tilde{\mathrm{u}} + \tilde{\psi}_{,\tilde{t}})\lambda_{,\tilde{x}} = \tilde{r}(\tilde{v}, \tilde{P}, \lambda). \tag{E1.9}$$

The characteristic length scale given in Lee and Stewart (1990) is the steady half-reaction zone length. There are few differences between (E1.6)–(E1.9) and (A1.10)–(A1.13). The mass equation (E1.6) is identical as is the species equation (E1.9) assuming that $\tilde{r}$ is the nondimensional version of $\dot{\Omega}$. Only the right-hand side of the momentum equation (E1.7) has changed, and in the energy equation (E1.8), $\rho a_f^2 \to \gamma\tilde{P}$ and the nondimensional version of $Z(v, P, \mathbf{Y})$ is the right-hand side of (E1.8). With these changes in mind, the nondimensional derivatives of ρa_f^2 and $Z(v, P, \mathbf{Y})$ become

$$(\rho a_f^2)_{,v} \to 0 \quad (\rho a_f^2)_{,P} \to \gamma \quad (\rho a_f^2)_{,\lambda} \to 0 \tag{E1.10}$$

$$Z_{,v} \to \frac{\gamma - 1}{\tilde{v}}\tilde{\beta}\left[\tilde{r}_{,\tilde{v}} - \frac{\tilde{r}}{\tilde{v}}\right] \quad Z_{,P} \to \frac{\gamma - 1}{\tilde{v}}\tilde{\beta}\tilde{r}_{,\tilde{P}} \quad Z_{,\lambda} \to \frac{\gamma - 1}{\tilde{v}}\tilde{\beta}\tilde{r}_{,\lambda}. \tag{E1.11}$$

Finally with these simplifications if $k_y = 0$, $\tilde{\mathbf{A}}$, $\tilde{\mathbf{b}}$, and $\tilde{\mathbf{C}}$ from (3.2.10) become

$$\tilde{\mathbf{b}} = \tilde{\mathbf{z}}_{,\tilde{x}} \qquad \tilde{\mathbf{A}} = \begin{pmatrix} \tilde{\mathrm{u}} & -\tilde{v} & 0 & 0 \\ 0 & \tilde{\mathrm{u}} & \tilde{v}/\gamma & 0 \\ 0 & \gamma\tilde{P} & \tilde{\mathrm{u}} & 0 \\ 0 & 0 & 0 & \tilde{\mathrm{u}} \end{pmatrix} \tag{E1.12}$$

and

$$\tilde{\mathbf{C}} = \begin{pmatrix} -\tilde{\mathrm{u}}_{,\tilde{x}} & \tilde{v}_{,\tilde{x}} & 0 & 0 \\ \tilde{P}_{,\tilde{x}}/\gamma & \tilde{\mathrm{u}}_{,\tilde{x}} & 0 & 0 \\ -\dfrac{\gamma-1}{\tilde{v}}\tilde{\beta}[\tilde{r}_{,\tilde{v}} - \tilde{r}/\tilde{v}] & \tilde{P}_{,\tilde{x}} & \gamma\tilde{\mathrm{u}}_{,\tilde{x}} - \dfrac{\gamma-1}{\tilde{v}}\tilde{\beta}\tilde{r}_{,\tilde{P}} & -\dfrac{\gamma-1}{\tilde{v}}\tilde{\beta}\tilde{r}_{,\lambda} \\ -\tilde{r}_{,\tilde{v}} & \lambda_{,\tilde{x}} & -\tilde{r}_{,\tilde{P}} & -\tilde{r}_{,\lambda} \end{pmatrix}. \tag{E1.13}$$

The above discussion confirms that if $k_y = 0$, (3.2.11) and (3.2.12) are the dimensional equivalents of (E1.12) and (E1.13), and that our derivation is the generalized one-dimensional version of Lee and Stewart (1990).

E.2 Two Dimensions

Short (1997) has studied two-dimensional linear stability with a single-step irreversible reaction (see Section 2.1) mechanism using the same technique as Lee and Stewart (1990). Nondimensionalizing (3.1.4)–(3.1.8) as described above in (E1.4) and (E1.5) gives the following equations

$$\tilde{v}_{,\tilde{t}} + (\tilde{\mathrm{u}} + \tilde{\psi}_{,\tilde{t}} + \tilde{\mathrm{v}}\tilde{\psi}_{,\tilde{y}})\tilde{v}_{,\tilde{x}} + \tilde{\mathrm{v}}\tilde{v}_{,\tilde{y}} = \tilde{v}(\tilde{\mathrm{u}}_{,\tilde{x}} + \tilde{\mathrm{v}}_{,\tilde{y}} + \tilde{\psi}_{,\tilde{y}}\tilde{\mathrm{v}}_{,\tilde{x}}) \tag{E2.1}$$

$$\tilde{\mathrm{u}}_{,\tilde{t}} + (\tilde{\mathrm{u}} + \tilde{\psi}_{,\tilde{t}} + \tilde{\mathrm{v}}\tilde{\psi}_{,\tilde{y}})\tilde{\mathrm{u}}_{,\tilde{x}} + \tilde{\mathrm{v}}\tilde{\mathrm{u}}_{,\tilde{y}} = -\frac{\tilde{v}}{\gamma}\tilde{P}_{,\tilde{x}} \tag{E2.2}$$

$$\tilde{\mathrm{v}}_{,\tilde{t}} + (\tilde{\mathrm{u}} + \tilde{\psi}_{,\tilde{t}} + \tilde{\mathrm{v}}\tilde{\psi}_{,\tilde{y}})\tilde{\mathrm{v}}_{,\tilde{x}} + \tilde{\mathrm{v}}\tilde{\mathrm{v}}_{,\tilde{y}} = -\frac{\tilde{v}}{\gamma}(\tilde{P}_{,\tilde{y}} + \tilde{\psi}_{,\tilde{y}}\tilde{P}_{,\tilde{x}}) \tag{E2.3}$$

$$\tilde{P}_{,\tilde{t}} + (\tilde{\mathrm{u}} + \tilde{\psi}_{,\tilde{t}} + \tilde{\mathrm{v}}\tilde{\psi}_{,\tilde{y}})\tilde{P}_{,\tilde{x}} + \tilde{\mathrm{v}}\tilde{P}_{,\tilde{y}} + \gamma\tilde{P}(\tilde{\mathrm{u}}_{,\tilde{x}} + \tilde{\mathrm{v}}_{,\tilde{y}} + \tilde{\psi}_{,\tilde{y}}\tilde{\mathrm{v}}_{,\tilde{x}}) = \frac{\gamma-1}{\tilde{v}}\tilde{\beta}\tilde{r}(\tilde{v}, \tilde{P}, \lambda) \tag{E2.4}$$

$$\lambda_{,\tilde{t}} + (\tilde{\mathrm{u}} + \tilde{\psi}_{,\tilde{t}} + \tilde{\mathrm{v}}\tilde{\psi}_{,\tilde{y}})\lambda_{,\tilde{x}} + \tilde{\mathrm{v}}\lambda_{,\tilde{y}} = \tilde{r}. \tag{E2.5}$$

It is important to note that Lee and Stewart use $\tilde{a}_f^2 = \gamma\tilde{P}\tilde{v}$ while Short uses $\tilde{a}_f^2 = \tilde{P}\tilde{v}$. Again, there are few differences between (E2.1)–(E2.5) and (3.1.4)–(3.1.8). The mass equation (E2.1) is identical as is the species equation (E2.5) assuming that $\tilde{r}$ is the nondimensional version of $\dot{\Omega}$. Only the right-hand sides of the momentum equations (E2.2) and (E2.3) have changed, and in the energy equation (E2.4), $\rho a_f^2 \to \gamma\tilde{P}$ and the

nondimensional version of $Z(v, P, \mathbf{Y})$ is the right-hand side of (E2.4). These changes result in the same derivatives of ρa_f^2 and $Z(P, v, \mathbf{Y})$ given above, (E1.10)–(E1.11).

Finally $\tilde{\mathbf{A}}$, $\tilde{\mathbf{b}}$, $\tilde{\mathbf{B}}$, and $\tilde{\mathbf{C}}$ from (3.2.10) become

$$\tilde{\mathbf{b}} = \tilde{\mathbf{z}}_{,\tilde{x}} \qquad \tilde{\mathbf{A}} = \begin{pmatrix} \tilde{\mathrm{u}} & -\tilde{v} & 0 & 0 & 0 \\ 0 & \tilde{\mathrm{u}} & 0 & \tilde{v}/\gamma & 0 \\ 0 & 0 & \tilde{\mathrm{u}} & 0 & 0 \\ 0 & \gamma\tilde{P} & 0 & \tilde{\mathrm{u}} & 0 \\ 0 & 0 & 0 & 0 & \tilde{\mathrm{u}} \end{pmatrix} \tag{E2.6}$$

$$\tilde{\mathbf{B}} = \begin{pmatrix} 0 & 0 & -\tilde{v} & 0 & 0 \\ 0 & 0 & 0 & 0 & 0 \\ 0 & 0 & 0 & \tilde{v}/\gamma & 0 \\ 0 & 0 & \gamma\tilde{P} & 0 & 0 \\ 0 & 0 & 0 & 0 & 0 \end{pmatrix} \tag{E2.7}$$

and

$$\tilde{\mathbf{C}} = \begin{pmatrix} -\tilde{\mathrm{u}}_{,\tilde{x}} & \tilde{v}_{,\tilde{x}} & 0 & 0 & 0 \\ \tilde{P}_{,\tilde{x}}/\gamma & \tilde{\mathrm{u}}_{,\tilde{x}} & 0 & 0 & 0 \\ 0 & \tilde{\mathrm{v}}_{,\tilde{x}} & 0 & 0 & 0 \\ -\dfrac{\gamma-1}{\tilde{v}}\tilde{\beta}[\tilde{r}_{,\tilde{v}} - \tilde{r}/\tilde{v}] & \tilde{P}_{,\tilde{x}} & 0 & \gamma\tilde{\mathrm{u}}_{,\tilde{x}} - \dfrac{\gamma-1}{\tilde{v}}\tilde{\beta}\tilde{r}_{,\tilde{P}} & -\dfrac{\gamma-1}{\tilde{v}}\tilde{\beta}\tilde{r}_{,\lambda} \\ -\tilde{r}_{,\tilde{v}} & \lambda_{,\tilde{x}} & 0 & -\tilde{r}_{,\tilde{P}} & -\tilde{r}_{,\lambda} \end{pmatrix}. \tag{E2.8}$$

Again the above discussion confirms that (3.2.11)–(3.2.12) are the dimensional equivalents of (E2.6)–(E2.8), and that our derivation is the generalized two-dimensional version of Short (1997).

E.3 Analytic Jump Conditions for the Perfect Gas

First, we start with the analytic frozen shock jump conditions[1]

$$\frac{P_2}{P_1} = 1 + \frac{2\gamma}{\gamma+1}(M_1^2 - 1) \rightarrow P_2 - P_1 = \frac{2\gamma}{\gamma+1}\frac{P_1}{(a_f^2)_1}(\mathrm{D}^2 - (a_f^2)_1) \tag{E3.1}$$

$$\frac{\mathrm{w}_2}{(a_f)_1} = M_1 - \frac{2}{\gamma+1}\left(M_1 - \frac{1}{M_1}\right) \rightarrow (\mathrm{w}_2 - \mathrm{D})\mathrm{D} = -\frac{2}{\gamma+1}(\mathrm{D}^2 - (a_f^2)_1) \tag{E3.2}$$

$$\frac{v_2}{v_1} = 1 - \frac{2}{\gamma+1}\left(1 - \frac{1}{M_1^2}\right) \rightarrow (v_2 - v_1)\mathrm{D}^2 = -\frac{2}{\gamma+1}(\mathrm{D}^2 - (a_f^2)_1). \tag{E3.3}$$

Now we perturb the shock speed ($\mathrm{D} \rightarrow \mathrm{U} + \psi_{,t}$) and, as a consequence, the post-shock quantities. Eq. (E3.1) becomes

$$P_2 + P' - P_1 = \frac{2\gamma}{\gamma+1}\frac{P_1}{(a_f^2)_1}((\mathrm{U} + \psi_{,t})^2 - (a_f^2)_1). \tag{E3.4}$$

By neglecting products of perturbations and grouping terms of equal order, (E3.4) becomes

$$[P_2 - P_1] + P' = \left[\frac{2\gamma}{\gamma+1}\frac{P_1}{(a_f^2)_1}(\mathrm{U}^2 - (a_f^2)_1)\right] + \frac{4\gamma}{\gamma+1}\frac{P_1}{(a_f^2)_1}\mathrm{U}\psi_{,t}. \tag{E3.5}$$

The zero-order terms in (E3.5) are exactly (E3.1). Now, we use (1.2.17) to replace $\mathrm{U} = \mathrm{w}_1$, nondimensionalize the remaining terms with respect to the post-shock state, and use (3.2.6) to find $\psi_{,t}$.

$$P' = \frac{4\gamma}{\gamma+1}\frac{1}{\gamma v_1}\frac{v_1}{v_2}\mathrm{w}_2\psi_{,t} \tag{E3.6}$$

$$\frac{P'}{P_2} = \tilde{P}' = \frac{4}{\gamma+1}\frac{\gamma}{\gamma\mathcal{R}T_2}\mathrm{w}_2\psi_{,t} \tag{E3.7}$$

$$\tilde{P}^1 = \frac{4\gamma M_2}{\gamma+1}\tilde{\psi}_{,\tilde{t}} = \frac{4\gamma M_2}{\gamma+1}\tilde{\omega}\tilde{\psi}^1 \tag{E3.8}$$

[1] In Lee & Stewart and Short, M_1 =D and $M_2 = M_s$.

Eq. (E3.2) becomes

$$[(\mathrm{w}_2 - \mathrm{U})\mathrm{U}] + (\mathrm{w}_2 - \mathrm{U})\psi_{,t} + (\mathrm{w}' - \psi_{,t})\mathrm{U} = -\left[\frac{2}{\gamma+1}(\mathrm{U}^2 - (a_f^2)_1)\right] - \frac{4}{\gamma+1}\mathrm{U}\psi_{,t}. \tag{E3.9}$$

Eliminating the first-order terms and substituting the right-hand side of (E3.2) for $(\mathrm{w}_2 - \mathrm{U})$, (E3.9) becomes

$$-\frac{2}{\gamma+1}(\mathrm{U}^2 - (a_f^2)_1)\psi_{,t} + \mathrm{U}^2(\mathrm{w}' - \psi_{,t}) = -\frac{4}{\gamma+1}\mathrm{U}^2\psi_{,t}. \tag{E3.10}$$

Finally, we nondimensionalize with respect to the post-shock state and use (3.2.6) to find $\psi_{,t}$.

$$\mathrm{w}'\mathrm{U}^2 = \mathrm{U}^2\psi_{,t} - 2\frac{\psi_{,t}}{\gamma+1}(\mathrm{U}^2 + (a_f^2)_1) \tag{E3.11}$$

$$\frac{\mathrm{w}'}{(a_f)_2}\frac{\mathrm{U}^2}{(a_f^2)_1} = \tilde{\mathrm{w}}' M_1^2 = \left(M_1^2 - \frac{2}{\gamma+1}(M_1^2+1)\right)\tilde{\psi}_{,\tilde{t}} \tag{E3.12}$$

$$\tilde{\mathrm{w}}^1 = \left[1 - \frac{2(M_1^2+1)}{(\gamma+1)M_1^2}\right]\tilde{\omega}\tilde{\psi}^1 \tag{E3.13}$$

As discussed before (see Appendix B.5), we must transform from the instantaneous shock-fixed frame to the flat-shock-fixed frame. The expression for the perfect gas velocity in the perturbation fixed frame becomes

$$\tilde{\mathrm{u}}^1 = -\frac{2(M_1^2+1)}{(\gamma+1)M_1^2}\tilde{\omega}\tilde{\psi}^1. \tag{E3.14}$$

Eq. (E3.3) becomes

$$[(v_2 - v_1)\mathrm{U}^2] + 2\mathrm{U}\psi_{,t}(v_2 - v_1) + v'\mathrm{U}^2 = -\left[\frac{2}{\gamma+1}v_1(\mathrm{U}^2 - (a_f^2)_1)\right] - \frac{4}{\gamma+1}v_1\mathrm{U}\psi_{,t}. \tag{E3.15}$$

Eliminating the first-order terms and substituting the right-hand side of (E3.3) for $(v_2 - v_1)$, (E3.15) becomes

$$-\frac{4}{\gamma+1}\mathrm{U}\psi_{,t}\left(1-\frac{(a_f^2)_1}{\mathrm{U}^2}\right)+v'\mathrm{U}^2=-\frac{4}{\gamma+1}v_1\mathrm{U}\psi_{,t}. \tag{E3.16}$$

Finally, we use (1.2.17) to simplify (E3.16), nondimensionalize with respect to the post-shock state, and use (3.2.6) to find $\psi_{,t}$.

$$v'\mathrm{U}^2=\frac{4}{\gamma+1}v_1\mathrm{U}\psi_{,t}\left[1-\frac{(a_f^2)_1}{\mathrm{U}^2}-1\right] \tag{E3.17}$$

$$\frac{v'}{v_2}\frac{\mathrm{U}^2}{(a_f^2)_1}=\tilde{v}'M_1^2=-\frac{4}{\gamma+1}\frac{v_1}{v_2}\frac{\psi_{,t}}{\mathrm{U}} \tag{E3.18}$$

$$\tilde{v}'M_1^2=-\frac{4}{\gamma+1}\frac{v_1}{v_2}\frac{\psi_{,t}}{\mathrm{w}_2}\frac{v_2}{v_1} \tag{E3.19}$$

$$\tilde{v}^1=-\frac{4}{(\gamma+1)M_1^2M_2}\tilde{\omega}\tilde{\psi}^1 \tag{E3.20}$$

Equations E3.8, E3.14, and E3.20 are identical to the expressions for the jump conditions presented in Lee and Stewart if we recognize that their ψ^1 has the opposite sign of ours.

E.4 Comparison of Ideal and Perfect Gas Jump Conditions

From the jump condition for density, we can determine how the expressions for the ideal gas compare with those for the perfect gas.

$$\tilde{v}^1=-\frac{4}{(\gamma+1)M_1^2M_2}\tilde{\omega}\tilde{\psi}^1 \tag{E4.1}$$

$$=-\frac{v_2}{v_1}\tilde{\omega}\tilde{\psi}^1(a_f)_2\left(\frac{\frac{v_1}{v_2}G\mathrm{U}-2\mathrm{U}[G+1]+\mathrm{w}_2[G+2]}{(a_f^2)_2(M_2^2-1)}\right) \tag{E4.2}$$

From this equality, we know that

$$\frac{4}{(\gamma+1)M_1^2M_2} = \frac{v_2}{v_1}\left(\frac{\frac{v_1}{v_2}G\mathrm{U} - 2\mathrm{U}[G+1] + \mathrm{w}_2[G+2]}{(a_f)_2(M_2^2-1)}\right). \tag{E4.3}$$

E.5 Single Progress Variable vs. Two Species Systems

It is important to note that we cannot directly compare the derivatives with respect to mass fraction of the two species system and those of the single progress variable system.

Numerical Derivatives

In a perfect gas system where all species have equal molecular weights, if the average molecular weight is treated as a constant, i.e.,

$$\overline{W} = \left(\sum_k \frac{Y_k}{W_k}\right)^{-1} = \overline{W}\left(\sum_k Y_k\right)^{-1} = \overline{W}\,(1)^{-1} = \overline{W} \tag{E5.1}$$

then R is constant and

$$\left.\frac{\partial\dot{\Omega}_i}{\partial Y_j}\right|_{v,P,Y_{k\neq j}} = \left.\frac{\partial\dot{\Omega}_i}{\partial Y_j}\right|_{v,T,Y_{k\neq j}}. \tag{E5.2}$$

Assuming this is true, for a perfect gas, the ideal gas expression (D2.6) should reduce to (E5.2). Unfortunately, the derivative of $\overline{W}$ computed with `setMassFractions_NoNorm` is not zero. This is because `setMassFractions_NoNorm` relaxes the condition that the sum of the mass fractions equals 1. Now the finite difference becomes

$$\left.\frac{\partial\overline{W}}{\partial Y_j}\right|_{P,v,Y_{k\neq j}} = \overline{W}\left.\frac{\partial\left(\sum_i Y_i\right)^{-1}}{\partial Y_j}\right|_{P,v,Y_{k\neq j}} = -\overline{W}\frac{\left(\sum_i Y_{i+}\right)^{-1} - \left(\sum_i Y_{i-}\right)^{-1}}{\Delta Y_j} \tag{E5.3}$$

where

$$\sum_i Y_{i_+} > 1 \quad \sum_i Y_{i_-} < 1. \tag{E5.4}$$

For this reason, (D2.6) does not reduce to (E5.2).

Net Production Rate

If we want to compare the value of $\tilde{r}_{,\lambda}$ to a dimensional quantity, we must look at how $\tilde{r}_{,\lambda}$ appears in the linear stability equations. The progress variable, λ, seems to represent the mass fraction of the products, but

$$\tilde{r}_{,\lambda} \not\to \left.\frac{\partial \dot{\Omega}_i}{\partial Y_{\mathcal{B}}}\right|_{v,P,Y_{\mathcal{A}}}. \tag{E5.5}$$

If we assume a perfect gas system with two species, the second species component of (3.2.10) is

$$\mathrm{u}^o Y'_{\mathcal{B},x} + \omega Y'_{\mathcal{B}} + Y^o_{\mathcal{B},x}\omega\psi' - \left(\dot{\Omega}_{\mathcal{B},v}v' - Y^o_{\mathcal{B},x}\mathrm{u}' + \dot{\Omega}_{\mathcal{B},P}P' + \dot{\Omega}_{\mathcal{B},Y_{\mathcal{A}}}Y'_{\mathcal{A}} + \dot{\Omega}_{\mathcal{B},Y_{\mathcal{B}}}Y'_{\mathcal{B}}\right) = 0. \tag{E5.6}$$

From Lee and Stewart, the dimensionless form of this equation is

$$\tilde{\mathrm{u}}^o\lambda'_{,\tilde{x}} + \tilde{\omega}\lambda' + \lambda^o_{,\tilde{x}}\tilde{\omega}\tilde{\psi}' - \left(\tilde{r}_{,\tilde{v}}\tilde{v}' - \lambda^o_{,\tilde{x}}\tilde{\mathrm{u}}' + \tilde{r}_{,\tilde{P}}\tilde{P}' + \tilde{r}_{,\lambda}\lambda'\right) = 0. \tag{E5.7}$$

If we compare the terms in each equation, the following terms must be related

$$\tilde{r}_{,\lambda}\lambda' \to \dot{\Omega}_{\mathcal{B},Y_{\mathcal{A}}}Y'_{\mathcal{A}} + \dot{\Omega}_{\mathcal{B},Y_{\mathcal{B}}}Y'_{\mathcal{B}}. \tag{E5.8}$$

Now, we recognize that $\sum_k Y_k' = 0$

$$\tilde{r}_{,\lambda}\lambda' \rightarrow -\dot{\Omega}_{\mathcal{B},Y_{\mathcal{A}}} Y_{\mathcal{B}}' + \dot{\Omega}_{\mathcal{B},Y_{\mathcal{B}}} Y_{\mathcal{B}}'. \tag{E5.9}$$

Finally, we find the dimensional quantity appropriate to compare with $\tilde{r}_{,\lambda}$

$$\tilde{r}_{,\lambda} \rightarrow \dot{\Omega}_{\mathcal{B},Y_{\mathcal{B}}} - \dot{\Omega}_{\mathcal{B},Y_{\mathcal{A}}}. \tag{E5.10}$$

Pseudo-Thermodynamic Function

We also cannot directly compare the derivatives of the dimensional and nondimensional pseudo-thermodynamic function derivatives with respect to mass fraction. If we want to compare the dimensional derivative to nondimensional quantity, we must look at how the derivative of the pseudo-thermodynamic function appears in the linear stability equations. If we assume a perfect gas system with two species, the pressure component of (3.2.10) is

$$\begin{aligned} &\mathrm{u}^o P_{,x}' + \omega P' + P_{,x}^o \omega\psi' + \gamma P' \mathrm{u}_x^o + \gamma P \mathrm{u}_x' \\ &\quad - \left[Z_{,v} v' + Z_{,P} P' + Z_{,Y_{\mathcal{A}}} Y_{\mathcal{A}}' + Z_{,Y_{\mathcal{B}}} Y_{\mathcal{B}}'\right] = 0. \end{aligned} \tag{E5.11}$$

From Lee and Stewart, the dimensionless form of this equation is

$$\begin{aligned} &\tilde{\mathrm{u}}^o \tilde{P}_{,\tilde{x}}' + \tilde{\omega}\tilde{P}' + \tilde{P}_{,\tilde{x}}^o \tilde{\omega}\tilde{\psi}' + \gamma \tilde{P}' \tilde{\mathrm{u}}_{,\tilde{x}}^o + \gamma \tilde{P} \tilde{\mathrm{u}}_{,\tilde{x}}' \\ &\quad - \left[\left(\frac{\gamma - 1}{\tilde{v}}\tilde{\beta}\tilde{r}\right)_{,\tilde{v}} \tilde{v}' + \left(\frac{\gamma - 1}{\tilde{v}}\tilde{\beta}\tilde{r}\right)_{,\tilde{P}} \tilde{P}' + \left(\frac{\gamma - 1}{\tilde{v}}\tilde{\beta}\tilde{r}\right)_{,\lambda} \lambda'\right] = 0. \end{aligned} \tag{E5.12}$$

If we compare the terms in each equation, the following terms must be related

$$\left(\frac{\gamma - 1}{\tilde{v}}\tilde{\beta}\tilde{r}\right)_{,\lambda} \lambda' \rightarrow Z_{,Y_{\mathcal{A}}} Y_{\mathcal{A}}' + Z_{,Y_{\mathcal{B}}} Y_{\mathcal{B}}'. \tag{E5.13}$$

Again, we recognize that $\sum_k Y'_k = 0$

$$\left(\frac{\gamma-1}{\tilde{v}}\tilde{\beta}\tilde{r}\right)_{,\lambda}\lambda' \rightarrow -Z_{,Y_{\mathcal{A}}}Y'_{\mathcal{B}} + Z_{,Y_{\mathcal{B}}}Y'_{\mathcal{B}}. \tag{E5.14}$$

Finally, we find appropriate quantities to compare are

$$\left(\frac{\gamma-1}{\tilde{v}}\tilde{\beta}\tilde{r}\right)_{,\lambda} \rightarrow Z_{,Y_{\mathcal{B}}} - Z_{,Y_{\mathcal{A}}}. \tag{E5.15}$$

E.6 Radiation Condition

Here we present in detail how Lee and Stewart (1990) determine the necessary radiation condition discussed generally in Section 3.4. The algorithm that they use is outlined in Section 4.2. Because the reactant and product species are dependent, they choose to specify a single species conservation equation in terms of the product species. Now, the system is

$$\mathbf{z}'_{f,t} + \mathbf{A}_{4\times4}|_{x_R}\mathbf{z}'_{f,x} + \mathbf{B}_{4\times4}|_{x_R}\mathbf{z}'_{f,y} = \begin{pmatrix} 0 \\ 0 \\ 0 \\ Z_{,Y_{\mathcal{B}}} - Z_{,Y_{\mathcal{A}}} \end{pmatrix}_{x_R} Y'_{\mathcal{B}} \tag{E6.1}$$

$$Y'_{\mathcal{B},t} + \mathrm{u}|_{x_R}Y'_{\mathcal{B},x} = \left(\dot{\Omega}_{\mathcal{B},Y_{\mathcal{B}}} - \dot{\Omega}_{\mathcal{B},Y_{\mathcal{A}}}\right)_{x_R} Y'_{\mathcal{B}}. \tag{E6.2}$$

We see here that there exists a one-way coupling between the fluid mechanics and the chemistry. Equation E6.2 can be solved independently and then applied as a forcing function in (E6.1).

Homogeneous Solution

Following the method of characteristics outlined in Appendix H (Whitman, 1999), the homogeneous portion of (E6.1) becomes

$$|\mathbf{N}|_{x_R}| = \left|\omega\mathbf{I} - \lambda_{k\mathbf{N}|_{x_R}}\mathbf{A}_{4\times4} + ik_y\mathbf{B}_{4\times4}\right|_{x_R} = 0. \tag{E6.3}$$

Solving for the eigenvalues and left eigenvectors of $\mathbf{N}|_{x_R}$, the solution to the homogeneous portion of (E6.1) is

$$\begin{pmatrix} v' \\ \mathrm{u}' \\ \mathrm{v}' \\ P' \end{pmatrix} = \begin{pmatrix} 1 & 0 & -v/P & -v/P \\ 0 & 1 & \lambda_{3\mathbf{N}}v/(\omega - \lambda_{3\mathbf{N}}\mathrm{u}) & \lambda_{4\mathbf{N}}v/(\omega - \lambda_{4\mathbf{N}}\mathrm{u}) \\ 0 & \omega/(ik_y\mathrm{u}) & -ik_yv/(\omega - \lambda_{4\mathbf{N}}\mathrm{u}) & -ik_yv/(\omega - \lambda_{4\mathbf{N}}\mathrm{u}) \\ 0 & 0 & 1 & 1 \end{pmatrix}_{x_R} \times \begin{pmatrix} F_1(-\lambda_{1\mathbf{N}}x + ik_yy + \omega t) \\ F_2(-\lambda_{2\mathbf{N}}x + ik_yy + \omega t) \\ F_3(-\lambda_{3\mathbf{N}}x + ik_yy + \omega t) \\ F_4(-\lambda_{4\mathbf{N}}x + ik_yy + \omega t) \end{pmatrix}_{x_R} \tag{E6.4}$$

where F_i is a generic wave function which can be found by projecting the solution onto the left eigenvector $\mathbf{m}_i^{\infty}$, i.e.,

$$\left(\mathbf{m}_i^T\hat{\mathbf{z}}\right)_{x_R} = F_i(x - c_it) \tag{E6.5}$$

and

$$\lambda_{1\mathbf{N}|_{x_R}} = \lambda_{2\mathbf{N}|_{x_R}} = \frac{\omega}{\mathrm{u}|_{x_R}} \tag{E6.6}$$

$$\lambda_{3\mathbf{N}|_{x_R}}, \lambda_{4\mathbf{N}|_{x_R}} = \frac{\omega\mathrm{u}|_{x_R} \mp a_f|_{x_R}\sqrt{\omega^2 - k_y^2(\mathrm{u}^2|_{x_R} - a_f^2|_{x_R})}}{\mathrm{u}^2|_{x_R} - a_f^2|_{x_R}}. \tag{E6.7}$$

Inhomogeneous Solution

We know that the particular solution of (E6.1) will have the same form as the forcing function which is proportional to $Y'_{\mathcal{B}}$. To determine the form of $Y'_{\mathcal{B}}$, we solve the decoupled equation (E6.2) with the method of characteristics.

$$Y'_{\mathcal{B}} = \exp\left[\left(\dot{\Omega}_{\mathcal{B},Y_{\mathcal{B}}} - \dot{\Omega}_{\mathcal{B},Y_{\mathcal{A}}}\right)_{x_R} t\right] F_5(x - \mathrm{u}|_{x_R} t) \tag{E6.8}$$

where

$$F_5(x - \mathrm{u}|_{x_R} t) = \exp\left[\frac{\left(\dot{\Omega}_{\mathcal{B},Y_{\mathcal{B}}} - \dot{\Omega}_{\mathcal{B},Y_{\mathcal{A}}}\right)_{x_R}}{a_f|_{x_R}} \tilde{\kappa}(x - \mathrm{u}|_{x_R} t)\right] \tag{E6.9}$$

and

$$\tilde{\kappa} = \frac{a_f}{\mathrm{u}}\left(1 - \frac{\omega}{\dot{\Omega}^{\infty}_{\mathcal{B},Y_{\mathcal{B}}} - \dot{\Omega}^{\infty}_{\mathcal{B},Y_{\mathcal{A}}}}\right). \tag{E6.10}$$

Now the dimensional inhomogeneous solution is

$$\mathbf{z}'_I = \mathbf{n} \exp\left[\frac{\left(\dot{\Omega}_{\mathcal{B},Y_{\mathcal{B}}} - \dot{\Omega}_{\mathcal{B},Y_{\mathcal{A}}}\right)}{a_f} \tilde{\kappa} x + \left(\dot{\Omega}_{\mathcal{B},Y_{\mathcal{B}}} - \dot{\Omega}_{\mathcal{B},Y_{\mathcal{A}}}\right)\left(1 - \frac{\tilde{\kappa}}{a_f}\mathrm{u}\right) t\right]_{x_R} \tag{E6.11}$$

where $\mathbf{n}$, a vector of constants, is determined by substituting the inhomogeneous solution into (E6.1),

$$\mathbf{n} = \begin{pmatrix} -\tilde{\kappa}_* \tilde{\kappa}^2 v \\ -\tilde{\kappa}_* \tilde{\kappa} a_f \\ 0 \\ \tilde{\kappa}_* \gamma P \end{pmatrix}_{x_R}, \tag{E6.12}$$

and

$$\tilde{\kappa}_* = \frac{v}{a_f^2}\frac{(Z_{,Y_\mathcal{B}} - Z_{,Y_\mathcal{A}})}{\left(\dot{\Omega}_{\mathcal{B},Y_\mathcal{B}} - \dot{\Omega}_{\mathcal{B},Y_\mathcal{A}}\right)}\frac{1}{1-\tilde{\kappa}^2}. \tag{E6.13}$$

Eigenvalue Selection Criterion

The final analytic solution of (E6.1) and (E6.2) is

$$\begin{aligned}
\mathbf{z}' = \begin{pmatrix} v' \\ \mathrm{u}' \\ \mathrm{v}' \\ P' \\ Y'_\mathcal{B} \end{pmatrix} = &\begin{pmatrix} 1 & 0 & -\frac{v}{P} & -\frac{v}{P} & -\tilde{\kappa}_*\tilde{\kappa}^2 v \\ 0 & 1 & \frac{\lambda_{3\mathbf{N}} v}{\omega - \lambda_{3\mathbf{N}}\mathrm{u}} & \frac{\lambda_{4\mathbf{N}} v}{\omega - \lambda_{4\mathbf{N}}\mathrm{u}} & -\tilde{\kappa}_*\tilde{\kappa} a_f \\ 0 & \frac{\omega}{ik_y\mathrm{u}} & -\frac{ik_y v}{\omega - \lambda_{3\mathbf{N}}\mathrm{u}} & -\frac{ik_y v}{\omega - \lambda_{4\mathbf{N}}\mathrm{u}} & 0 \\ 0 & 0 & 1 & 1 & \tilde{\kappa}_*\gamma P \\ 0 & 0 & 0 & 0 & 1 \end{pmatrix}_{x_R} \times \\
&\begin{pmatrix} F_1(-\lambda_{1\mathbf{N}}x + ik_y y + \omega t) \\ F_2(-\lambda_{2\mathbf{N}}x + ik_y y + \omega t) \\ F_3(-\lambda_{3\mathbf{N}}x + ik_y y + \omega t) \\ F_4(-\lambda_{4\mathbf{N}}x + ik_y y + \omega t) \\ \exp\left[\frac{\left(\dot{\Omega}_{\mathcal{B},Y_\mathcal{B}} - \dot{\Omega}_{\mathcal{B},Y_\mathcal{A}}\right)}{a_f}\tilde{\kappa}x + \left(\dot{\Omega}_{\mathcal{B},Y_\mathcal{B}} - \dot{\Omega}_{\mathcal{B},Y_\mathcal{A}}\right)\left(1 - \frac{\tilde{\kappa}}{a_f}\mathrm{u}_\infty\right)t\right] \end{pmatrix}_{x_R}.
\end{aligned} \tag{E6.14}$$

In order to use (E6.14) as an eigenvalue selection condition, we must develop a criterion to apply to the solution of (3.2.10). This is determined by insisting that all waves leave the domain at infinity or setting F_4 equal to zero. F_4 specifies the waves that travel into the domain from the boundary. Now we can find a criterion that is strictly a function of P', u', v', and $Y'_\mathcal{B}$.

$$\begin{aligned}
\mathcal{H}(\omega) = &\left[\frac{\mathrm{u}'}{a_f}\right]_{x_R} - \left[\frac{ik_y\mathrm{u}}{\omega}\frac{\mathrm{v}'}{a_f}\right]_{x_R} - \left[\sqrt{1 - \frac{k_y^2}{\omega^2}(\mathrm{u}^2 - a_f^2)}\frac{P'}{\gamma P}\right]_{x_R} + \\
&Y'_\mathcal{B}\left[\tilde{\kappa}_*\left(\tilde{\kappa} + \sqrt{1 - \frac{k_y^2}{\omega^2}(\mathrm{u}^2 - a_f^2)}\right)\right]_{x_R}
\end{aligned} \tag{E6.15}$$

Appendix F

Implementing the Analytic Selection Criterion

In the code, the real and imaginary components of (E6.15) must be implemented separately. First, we let

$$\alpha = \sqrt{\omega^2 - k_y^2(\mathrm{u}^2 - a_f^2)} \tag{F1}$$

$$\Delta\dot{\Omega} = \dot{\Omega}_{\mathcal{B},Y_\mathcal{B}} - \dot{\Omega}_{\mathcal{B},Y_\mathcal{A}} \tag{F2}$$

$$\Delta Z = Z_{,Y_\mathcal{B}} - Z_{,Y_\mathcal{A}}. \tag{F3}$$

Now, (E6.15) becomes

$$\left[\frac{\omega}{\alpha}\frac{\mathrm{u}'}{a_f}\right]_{x_R} - \left[\frac{ik_y\mathrm{u}}{\alpha}\frac{\mathrm{v}'}{a_f}\right]_{x_R} - \left[\frac{P'}{\gamma P}\right]_{x_R} = -Y'_\mathcal{B}\left[\tilde{\kappa}_*\left(1+\tilde{\kappa}\frac{\omega}{\alpha}\right)\right]_{x_R}. \tag{F4}$$

We recall the definitions of $\tilde{\kappa}$ (E6.10) and $\tilde{\kappa}_*$ (E6.13)

$$\tilde{\kappa} = \tilde{\kappa}_\mathcal{R} + i\tilde{\kappa}_\mathcal{I} = \frac{a_f}{\mathrm{u}}\left[\left(1 - \frac{\omega_\mathcal{R}}{\Delta\dot{\Omega}}\right) - i\left(\frac{\omega_\mathcal{I}}{\Delta\dot{\Omega}}\right)\right] \tag{F5}$$

$$\tilde{\kappa}_* = \tilde{\kappa}_{*\mathcal{R}} + i\tilde{\kappa}_{*\mathcal{I}} = \frac{v}{a_f^2}\frac{\Delta Z}{\Delta\dot{\Omega}}\left[\frac{(1-\tilde{\kappa}_\mathcal{R}^2+\tilde{\kappa}_\mathcal{I}^2) + i\,(2\tilde{\kappa}_\mathcal{R}\tilde{\kappa}_\mathcal{I})}{(1-\tilde{\kappa}_\mathcal{R}^2+\tilde{\kappa}_\mathcal{I}^2)^2 + (2\tilde{\kappa}_\mathcal{R}\tilde{\kappa}_\mathcal{I})^2}\right]. \tag{F6}$$

We can now write (E6.15) as

$$0 = \mathcal{D} - \mathcal{E} - \frac{P'}{\gamma P_\infty} + \mathcal{F} \cdot \mathcal{G} \tag{F7}$$

where

$$\alpha = \sqrt{r}\left(\cos\tfrac{\theta}{2} + \sin\tfrac{\theta}{2}\right) \tag{F8}$$

$$r = \sqrt{\left[\omega_\mathcal{R}^2 - \omega_\mathcal{I}^2 - k_y^2(\mathrm{u}^2 - a_f^2)_{x_R}\right]^2 + \left[2\omega_\mathcal{R}\omega_\mathcal{I}\right]^2} \tag{F9}$$

$$\theta = \arctan\left(\frac{2\omega_\mathcal{R}\omega_\mathcal{I}}{\omega_\mathcal{R}^2 - \omega_\mathcal{I}^2 - k_y^2(\mathrm{u}^2 - a_f^2)_{x_R}}\right) \tag{F10}$$

$$\mathcal{C} = \frac{\omega}{\alpha} = \frac{(\alpha_\mathcal{R}\omega_\mathcal{R} + \alpha_\mathcal{I}\omega_\mathcal{I}) + i\,(\alpha_\mathcal{R}\omega_\mathcal{I} - \alpha_\mathcal{I}\omega_\mathcal{R})}{\alpha_\mathcal{R}^2 + \alpha_\mathcal{I}^2} \tag{F11}$$

$$\mathcal{D} = \frac{\omega}{\alpha}\frac{\mathrm{u}'}{a_f|_{x_R}} = \frac{1}{a_f|_{x_R}}\left[(\mathcal{C}_\mathcal{R}\mathrm{u}'_\mathcal{R} - \mathcal{C}_\mathcal{I}\mathrm{u}'_\mathcal{I}) + i\,(\mathcal{C}_\mathcal{R}\mathrm{u}'_\mathcal{I} + \mathcal{C}_\mathcal{I}\mathrm{u}'_\mathcal{R})\right] \tag{F12}$$

$$\mathcal{E} = \frac{ik_y\mathrm{u}|_{x_R}}{a_f|_{x_R}}\frac{\mathrm{v}'}{\alpha} = \frac{k_y\mathrm{u}|_{x_R}}{a_f|_{x_R}}\left[\frac{(\alpha_\mathcal{I}\mathrm{v}'_\mathcal{R} - \alpha_\mathcal{R}\mathrm{v}'_\mathcal{I}) + i\,(\alpha_\mathcal{R}\mathrm{v}'_\mathcal{R} + \alpha_\mathcal{I}\mathrm{v}'_\mathcal{I})}{\alpha_\mathcal{R}^2 + \alpha_\mathcal{I}^2}\right] \tag{F13}$$

$$\mathcal{F} = Y'_\mathcal{B}\tilde{\kappa}_* = \left(Y'_{\mathcal{B},\mathcal{I}}\tilde{\kappa}_{*\mathcal{R}} - Y'_{\mathcal{B},\mathcal{R}}\tilde{\kappa}_{*\mathcal{I}}\right) + i\left(Y'_{\mathcal{B},\mathcal{R}}\tilde{\kappa}_{*\mathcal{R}} + Y'_{\mathcal{B},\mathcal{I}}\tilde{\kappa}_{*\mathcal{I}}\right) \tag{F14}$$

$$\mathcal{G} = 1 - \tilde{\kappa}\frac{\omega}{\alpha} = (1 - \tilde{\kappa}_\mathcal{R}\mathcal{C}_\mathcal{R} - \tilde{\kappa}_\mathcal{I}\mathcal{C}_\mathcal{R}) + i\,(\tilde{\kappa}_\mathcal{I}\mathcal{C}_\mathcal{R} + \tilde{\kappa}_\mathcal{R}\mathcal{C}_\mathcal{I})\,. \tag{F15}$$

Appendix G

Example cti File

The following `cti` file corresponds to a member of our family of systems described in Section 2.2.1. Specifically, the file below is for $\Delta s/R = 0$ and $f = 1.2$.

```
units(length = "cm", time = "s", quantity = "mol", act_energy = "cal/mol")

ideal_gas(name = "FakeGas",
      elements = " Ar ",
      species = """ F1 F2 """,
      reactions = "all",
      transport = "Mix",
      initial_state = state(temperature = 300.0,
                        pressure = OneAtm)    )

#-------------------------------------------------------------------------------
#  Species data
#-------------------------------------------------------------------------------

species(name = "F1",
    atoms = " Ar:1 ",
    thermo = (
```

```
      NASA( [  300.00,  1000.00], [  6.000000000E+00,   0.000000000E+00,
               0.000000000E+00,   0.000000000E+00,   0.000000000E+00,
              -1.800000000E+03,   4.366000000E+00] ),
      NASA( [ 1000.00,  5000.00], [  6.000000000E+00,   0.000000000E+00,
               0.000000000E+00,   0.000000000E+00,   0.000000000E+00,
              -1.800000000E+03,   4.366000000E+00] )
            ),
    transport = gas_transport(
                    geom = "atom",
                    diam =     3.33,
                    well_depth =   136.50),
    note = "120186"
      )

species(name = "F2",
    atoms = " Ar:1 ",
    thermo = (
      NASA( [  300.00,  1000.00], [  6.000000000E+00,   0.000000000E+00,
               0.000000000E+00,   0.000000000E+00,   0.000000000E+00,
              -1.701150398E+04,   4.366000000E+00] ),
      NASA( [ 1000.00,  5000.00], [  6.000000000E+00,   0.000000000E+00,
               0.000000000E+00,   0.000000000E+00,   0.000000000E+00,
              -1.701150398E+04,   4.366000000E+00] )
            ),
    transport = gas_transport(
                    geom = "atom",
                    diam =     3.33,
                    well_depth =   136.50),
    note = "5"
```

```
       )

#-------------------------------------------------------------------------
#  Reaction data
#-------------------------------------------------------------------------

#  Reaction 1
reaction( "F1 <=> F2",   [7.95481146e+02, 0, 298505])
```

Appendix H

Method of Characteristics

According to Whitman (1999, p. 139), a system of the following form

$$A^m_{kj}\frac{\partial f_j}{\partial x^m} + b_k = 0 \tag{H1}$$

where $\mathbf{x}$ is the vector of independent variables and $\mathbf{A}^m$ is the matrix associated with the m^{th} independent variable can be solved with method of characteristics. He states that if the appropriate linear combination is

$$n_k A^m_{kj}\frac{\partial f_j}{\partial x^m} + n_k b_k = 0, \tag{H2}$$

the directional derivative for f_j is $n_k A^m_{kj}$. If the surface element belongs to a surface $S(\mathbf{x})$=constant, the normal vector is $\partial S/\partial x^m$, and the orthogonality requirement is

$$n_k A^m_{kj}\frac{\partial S}{\partial x^m} = 0. \tag{H3}$$

The condition for $\mathbf{n}$ to be nontrivial is that the determinant

$$\left|\frac{\partial S}{\partial x^m}\mathbf{A}^m\right| = 0. \tag{H4}$$

The solutions to (H4) are the wave speeds.

In our case, following the work of Buckmaster and Neves (1988), the derivatives of the characteristic surface, $S = k_x x + ik_y y + \omega t$, are

$$\frac{\partial S}{\partial x} = -k_x \tag{H5}$$

$$\frac{\partial S}{\partial y} = ik_y \tag{H6}$$

$$\frac{\partial S}{\partial t} = \omega. \tag{H7}$$

Appendix I

Wave Hierarchy

I.1 Alternate Eigenvector Formulation

Here we will present a second formulation of the new right boundary condition discussed in Section 3.4. Far from the reaction zone, the composition is close to equilibrium. In this regime, following Vincenti and Kruger (1965) we introduce the *near equilibrium relaxation time scale*

$$\tau|_{x_R} = \left(\dot{\Omega}_{\mathcal{B},Y_\mathcal{B}} - \dot{\Omega}_{\mathcal{B},Y_\mathcal{A}}\right)^{-1}_{x_R}. \tag{I1.1}$$

For the remainder of this formulation, we will use the equations of motion in terms of $\tau|_{x_R}$.

$$\frac{\mathrm{D}\rho'}{\mathrm{D}t} = -\rho|_{x_R}\mathrm{u}'_{,x} \tag{I1.2}$$

$$\frac{\mathrm{D}\mathrm{u}'}{\mathrm{D}t} = -\frac{P'_{,x}}{\rho|_{x_R}} \tag{I1.3}$$

$$\frac{\mathrm{D}P'}{\mathrm{D}t} = a_f^2|_{x_R}\left(\frac{\mathrm{D}\rho'}{\mathrm{D}t} + \rho|_{x_R}\dot{\sigma}\right) \tag{I1.4}$$

$$\frac{\mathrm{D}Y'_\mathcal{B}}{\mathrm{D}t} = \frac{Y^{*'}_\mathcal{B} - Y'_\mathcal{B}}{\tau|_{x_R}} \tag{I1.5}$$

We can express (I1.2)–(I1.5) in matrix form as

$$\mathbf{D}^{\infty}\mathbf{z}'_{,t} + \mathbf{A}^{\infty}\mathbf{z}'_{,x} + \mathbf{C}^{\infty}\mathbf{z}' = 0 \tag{I1.6}$$

where

$$\mathbf{D} = \begin{pmatrix} 1 & 0 & 0 & 0 \\ 0 & 1 & 0 & 0 \\ -a_f^2 & 0 & 1 & -a_f^2\rho\sigma \\ 0 & 0 & 0 & 1 \end{pmatrix} \qquad \mathbf{A} = \begin{pmatrix} \mathrm{u} & \rho & 0 & 0 \\ 0 & \mathrm{u} & 1/\rho & 0 \\ -a_f^2\mathrm{u} & 0 & \mathrm{u} & -a_f^2\rho\sigma\mathrm{u} \\ 0 & 0 & 0 & \mathrm{u} \end{pmatrix} \tag{I1.7}$$

$$\mathbf{C} = \begin{pmatrix} 0 & 0 & 0 & 0 \\ 0 & 0 & 0 & 0 \\ 0 & 0 & 0 & 0 \\ -Y^*_{\mathcal{B},\rho}/\tau & 0 & -Y^*_{\mathcal{B},P}/\tau & 1/\tau. \end{pmatrix} \tag{I1.8}$$

To solve (I1.6), we assume the following normal modes form

$$\mathbf{z}' = \hat{\mathbf{z}} \exp\left[\omega\left(\frac{x}{c} - t\right)\right], \tag{I1.9}$$

where c is a characteristic wave speed of the system. Equation I1.6 becomes an algebraic eigenvalue equation with eigenvalues $\{c_i\}$

$$\mathbf{N}|_{x_R}\hat{\mathbf{z}} = \left[\mathbf{A}^{-1}\left(\mathbf{D} - \frac{1}{\omega}\mathbf{C}\right)\right]_{x_R}\hat{\mathbf{z}} = \frac{1}{c}\hat{\mathbf{z}}. \tag{I1.10}$$

The characteristic polynomial associated with (I1.10) is

$$(c - \mathrm{u}|_{x_R})\left[-\omega\tau^*\left(\frac{a_e}{a_f}\right)^2(c-\mathrm{u})\left[(c-\mathrm{u})^2 - a_f^2\right] + c\left[(c-\mathrm{u})^2 - a_e^2\right]\right]_{x_R} = 0 \tag{I1.11}$$

where

$$\tau^*|_{x_R} = \frac{h_{,\rho}\tau|_{x_R}}{h_{,\rho} + h_{,Y^*_{\mathcal{B}}} Y^*_{\mathcal{B},\rho}}. \tag{I1.12}$$

In this formulation,

$$\mathbf{N} = \begin{pmatrix} \dfrac{\omega\tau(a_f^2 - \mathrm{u}^2) - a_f^2(\rho\sigma)Y^*_{\mathcal{B},\rho}}{\mathrm{u}\omega\tau(a_f^2 - \mathrm{u}^2)} & \dfrac{\rho}{a_f^2 - \mathrm{u}^2} & -\dfrac{\omega\tau + a_f^2(\rho\sigma)Y^*_{\mathcal{B},P}}{\mathrm{u}\omega\tau(a_f^2 - \mathrm{u}^2)} & \dfrac{a_f^2(\rho\sigma)}{\mathrm{u}\omega\tau(a_f^2 - \mathrm{u}^2)} \\ \dfrac{a_f^2(\rho\sigma)Y^*_{\mathcal{B},\rho}}{\rho\omega\tau(a_f^2 - \mathrm{u}^2)} & -\dfrac{\mathrm{u}}{a_f^2 - \mathrm{u}^2} & \dfrac{\omega\tau + a_f^2(\rho\sigma)Y^*_{\mathcal{B},P}}{\rho\omega\tau(a_f^2 - \mathrm{u}^2)} & -\dfrac{a_f^2(\rho\sigma)}{\rho\omega\tau(a_f^2 - \mathrm{u}^2)} \\ -\dfrac{\mathrm{u}a_f^2(\rho\sigma)Y^*_{\mathcal{B},\rho}}{\omega\tau(a_f^2 - \mathrm{u}^2)} & \dfrac{a_f^2\rho}{a_f^2 - \mathrm{u}^2} & -\dfrac{\mathrm{u}(\omega\tau + a_f^2(\rho\sigma)Y^*_{\mathcal{B},P})}{\omega\tau(a_f^2 - \mathrm{u}^2)} & \dfrac{\mathrm{u}a_f^2(\rho\sigma)}{\omega\tau(a_f^2 - \mathrm{u}^2)} \\ \dfrac{Y^*_{\mathcal{B},\rho}}{\mathrm{u}\omega\tau} & 0 & \dfrac{Y^*_{\mathcal{B},P}}{\mathrm{u}\omega\tau} & \dfrac{\omega\tau - 1}{\mathrm{u}\omega\tau} \end{pmatrix}. \tag{I1.13}$$

In one dimension with a single progress variable, $\mathbf{N}$ in (3.4.11) becomes

$$\mathbf{N} = \begin{bmatrix} \dfrac{\omega\tau(a_f^2 - \mathrm{u}^2) - a_f^2(\rho\sigma)Y^*_{\mathcal{B},\rho}}{\mathrm{u}\omega\tau(a_f^2 - \mathrm{u}^2)} & -\dfrac{v}{a_f^2 - \mathrm{u}^2} & \dfrac{v^2(\omega - Z_{,P}}{\mathrm{u}\omega(a_f^2 - \mathrm{u}^2)} & \dfrac{v^2(Z_{,Y_{\mathcal{B}}} - Z_{,Y_{\mathcal{A}}})}{\mathrm{u}\omega(a_f^2 - \mathrm{u}^2)} \\ -\dfrac{vZ_{,v}}{\omega(a_f^2 - \mathrm{u}^2)} & -\dfrac{\mathrm{u}}{a_f^2 - \mathrm{u}^2} & \dfrac{v(\omega - Z_{,P})}{\omega(a_f^2 - \mathrm{u}^2)} & -\dfrac{v(Z_{,Y_{\mathcal{B}}} - Z_{,Y_{\mathcal{A}}})}{\omega(a_f^2 - \mathrm{u}^2)} \\ -\dfrac{\mathrm{u}Z_{,v}}{\omega(a_f^2 - \mathrm{u}^2)} & \dfrac{a_f^2}{v(a_f^2 - \mathrm{u}^2)} & -\dfrac{\mathrm{u}(Z_{,P} - \omega)}{\omega(a_f^2 - \mathrm{u}^2)} & -\dfrac{\mathrm{u}(Z_{,Y_{\mathcal{B}}} - Z_{,Y_{\mathcal{A}}})}{\omega(a_f^2 - \mathrm{u}^2)} \\ \dfrac{\dot{\Omega}_{\mathcal{B},v}}{\mathrm{u}\omega} & 0 & \dfrac{\dot{\Omega}_{\mathcal{B},P}}{\mathrm{u}\omega} & \dfrac{\omega + (\dot{\Omega}_{\mathcal{B},Y_{\mathcal{B}}} - \dot{\Omega}_{\mathcal{B},Y_{\mathcal{A}}})}{\mathrm{u}\omega} \end{bmatrix} \tag{I1.14}$$

which is equivalent to (I1.13) if we consider that (I1.2)–(I1.5) are the acoustic limits of (1.1.1)–(1.1.4) and use the following equalities

$$Z_{,v} = a_f^2\rho\sigma\frac{Y^*_{\mathcal{B},v}}{\tau} \quad Z_{,P} = a_f^2\rho\sigma\frac{Y^*_{\mathcal{B},P}}{\tau} \quad Z_{,Y_{\mathcal{B}}} - Z_{,Y_{\mathcal{A}}} = -a_f^2\frac{\rho\sigma}{\tau} \tag{I1.15}$$

$$\dot{\Omega}_{\mathcal{B},v} = -\frac{Y^*_{\mathcal{B},v}}{\tau} \quad \dot{\Omega}_{\mathcal{B},P} = -\frac{Y^*_{\mathcal{B},P}}{\tau} \quad \dot{\Omega}_{\mathcal{B},Y_{\mathcal{B}}} - \dot{\Omega}_{\mathcal{B},Y_{\mathcal{A}}} = \frac{1}{\tau}. \tag{I1.16}$$

Due to the equality of (I1.14) and (I1.13), (I1.11) is the one-dimensional reversible equivalent of (4.2.10) and in the irreversible limit will lead to (4.2.14).

I.2 Wave Hierarchy Traditional

Equation I1.11 can also be derived from a wave hierarchy equation. The methodology presented in Vincenti and Kruger (1965) is reproduced here. First we start with the equations of motion presented in Appendix I.1.

An equilibrium thermodynamic system is a function of two independent variables. If we choose P and ρ as our independent thermodynamic variables, $Y^*_{\mathcal{B}}$ can be expressed as $Y^*_{\mathcal{B}}(P,\rho)$. In order to re-express the right-hand side of (I1.5), we define a modified near equilibrium time scale, $\tau^*|_{x_R}$

$$\tau^*|_{x_R} = \frac{h_{,\rho}\tau|_{x_R}}{h_{,\rho} + h_{,Y^*_{\mathcal{B}}} Y^*_{\mathcal{B},\rho}}. \tag{I2.1}$$

By first differentiating (I1.5) and then introducing $\tau^*|_{x_R}$, we can write the rate equation as follows

$$\left(\frac{\mathrm{D}}{\mathrm{D}t}\right)^2 Y'_{\mathcal{B}} = \frac{1}{\tau^*|_{x_R}} \frac{h_{,\rho}}{h_{,Y^*_{\mathcal{B}}}} \left[\frac{\mathrm{D}\rho'}{\mathrm{D}t} - \frac{1}{a_e^2}\frac{\mathrm{D}P'}{\mathrm{D}t}\right]_{x_R}. \tag{I2.2}$$

This modified rate equation now involves the equilibrium soundspeed a_e (see Appendix C.1).

Next we take the total derivative of the momentum equation (I1.3) and use the continuity equation (I1.2) and the adiabatic change equation (I1.4) to replace the derivatives of density and pressure. Finally we incorporate the new rate equation (I2.2) and express the equation strictly in terms of velocity

$$\tau^*|_{x_R} \left(\frac{a_e}{a_f}\right)^2_{x_R} \frac{\mathrm{D}}{\mathrm{D}t}\left[\left(\frac{\mathrm{D}}{\mathrm{D}t}\right)^2 \mathrm{u}' - a_f^2 \mathrm{u}'_{,xx}\right]_{x_R} + \left[\left(\frac{\mathrm{D}}{\mathrm{D}t}\right)^2 \mathrm{u}' - a_e^2 \mathrm{u}'_{,xx}\right]_{x_R} = 0. \tag{I2.3}$$

Equation I2.3 indicates that there is a hierarchy of wave operators in this problem. The lower-order wave operator involves the equilibrium soundspeed a_e,

$$\left(\frac{\mathrm{D}}{\mathrm{D}t}\right)^2 - a_e|^2_{x_R} \frac{\partial}{\partial x^2} \tag{I2.4}$$

while the higher-order wave operator involves the frozen soundspeed a_f

$$\left(\frac{\mathrm{D}}{\mathrm{D}t}\right)^2 - a_f|_{x_R}^2 \frac{\partial}{\partial x^2}. \tag{I2.5}$$

To solve (I2.3), we assume the following normal modes form

$$\mathrm{u}' = A \exp\left[\omega\left(\frac{x}{c} - t\right)\right], \tag{I2.6}$$

where c is a characteristic wave speed of the system. $\dfrac{\mathrm{D}}{\mathrm{D}t}$ becomes

$$\frac{\mathrm{D}u'}{\mathrm{D}t} = -\omega\left(1 - \frac{\mathrm{u}|_{x_R}}{c}\right)u' \tag{I2.7}$$

and (I2.3) becomes

$$\left(-\omega\tau^*\left(\frac{a_e}{a_f}\right)^2 (c-\mathrm{u})\left[(c-\mathrm{u})^2 - a_f^2\right] + c\left[(c-\mathrm{u})^2 - a_e^2\right]\right)_{x_R} = 0. \tag{I2.8}$$

Vincenti and Kruger (1965) discuss the limits of (I2.8). As $\tau^*|_{x_R}$ approaches zero, the time required for the composition to return to equilibrium becomes negligible and the second term in (4.2.10) $c\left[(c-\mathrm{u})^2 - a_e^2\right]_{x_R}$ dominates. In this case, the characteristic wave speeds are: $\{\mathrm{u}, \mathrm{u}+a_e, \mathrm{u}-a_e\}_{x_R}$. On the other hand, as $\tau^*|_{x_R}$ approaches infinity, the time required for the composition to return to equilibrium becomes prohibitively long and the first term in (4.2.10) $(c-\mathrm{u}|_{x_R})\left[(c-\mathrm{u})^2 - a_f^2\right]_{x_R}$ dominates. In this extreme, the characteristic wave speeds are: $\{\mathrm{u}, \mathrm{u}+a_f, \mathrm{u}-a_f\}_{x_R}$.

Equation (I2.8) contains a subset of the roots given by (I1.11) which includes the root with a negative real part. This will therefore lead to (4.2.14).